

Magnetism in Mn–Doped Chalcopyrites

by

Patrick W Mengyan, M.Sc.

A Dissertation

in

Physics

Submitted to the Graduate Faculty
of Texas Tech University in
Partial Fulfillment of
the Requirements for the Degree of

DOCTOR OF PHILOSOPHY

Roger L. Lichti
Chairperson of the Committee

David Lamp

Charles W Myles

Mahdi Sanati

Mark Sheridan
Dean of the Graduate School

May, 2014

Copyright 2014, Patrick W Mengyan

ACKNOWLEDGEMENTS

I would like to express my deepest gratitude to all of the collaborators with whom I have had the privilege of working during my time as a graduate student.

I wish to thank Dr. Roger Lichti, my advisor and friend, for his continual support, guidance and patience in these research efforts and my personal growth. The freedom he has granted me in pursuing a variety of research interests (in addition to this specific project) has allowed me to collaborate with world-class researchers who are well established in this field, present at international conferences, conduct a number of experiments at national laboratories and develop the skills necessary to become a successful physicist. I am very grateful to have been able to work with and get to know someone of his caliber and character both professionally and personally. I also wish to extend my thanks and appreciation to collaborators and friends Jess Brewer, Gurkan Celebi, Slava Storchak, Dima Eshchenko and Kim Chow with whom I have worked in varying capacities and spent countless hours learning from their combined decades of professional and personal experience. Thanks to Ross Carroll for leading the neutron based projects at ORNL and sharing his expertise as I joined the MuSR group at Texas Tech. In the MuSR community, I would like to extend thanks to all of those that not only keep the accelerator-based operations running but also continually develop the equipment to further the capabilities of this technique and contribute to a positive user experience. I wish to extend thanks to the Physics faculty from Northern Michigan University for the superb preparation and very strong encouragement to pursue advanced studies in physics.

This research project and parts therein is financially supported by the U.S. Department of Energy (Basic Energy Science grant DE-SC0001769), the Welch Foundation, the Joint Institute for Neutron Sciences and the research fund of the University of Istanbul (project IRP 19149). Part of the research conducted at ORNL's High Flux Isotope Reactor (HFIR) was sponsored by the Scientific User Facilities Division, Office of Basic Energy Sciences, US Department of Energy.

On a more personal front, I wish to dedicate this dissertation to the memory of Quinton McLean; to whom I credit my interest in motorcycles, zest for learning the details of the world around us and excitement for sharing knowledge, wisdom and experiences with anyone interested. Without further adieu and with his words, stop me if you have heard this before...



TABLE OF CONTENTS

ACKNOWLEDGEMENTS	ii
ABSTRACT	vii
LIST OF TABLES	viii
LIST OF FIGURES	ix
LIST OF ABBREVIATIONS	xi
CHAPTER 1: INTRODUCTION	1
CHAPTER 2: BACKGROUND AND MOTIVATION	4
2.1. II–IV–V ₂ Chalcopyrites: General Overview.....	6
2.2. II–IV–V ₂ Chalcopyrites: Previous Work	9
2.3. Dilute Magnetic Semiconductors: Theory	13
CHAPTER 3: EXPERIMENTAL TECHNIQUES	15
3.1. Muon Spin Research	15
3.1.1. Overview: The memoir of a synthetic muon.....	15
3.1.2. Transverse Field μ SR (TF– μ SR)	33
3.1.3. Longitudinal Field μ SR (LF– μ SR)	35
3.1.4. Zero Field μ SR (ZF– μ SR).....	36
3.2. Muon Facilities and Apparatus	36
3.2.1. TRIUMF.....	37
3.2.2. ISIS.....	40
3.3. SQUID Susceptometry.....	43
3.4. Alternating Gradient Magnetometry	45
3.5. Neutron Studies.....	47
3.5.1. Triple Axis Diffractometry (PTAX: HB–1).....	49
3.5.2. Magnetic Small Angle Neutron Scattering (GP–SANS: CG–2):	50
CHAPTER 4: EXPERIMENTAL DETAILS	51
4.1. Samples	51
4.2. Muon Spin Rotation: TF–MuSR (Hyperfine Spectroscopy)	54
4.3. Muon Spin Relaxation: LF– and ZF– MuSR (Depolarization)	55
4.4. Bulk Magnetization.....	56

4.5. Triple Axis Neutron Scattering	56
4.6. Magnetic Small Angle Neutron Scattering	57
CHAPTER 5: RESULTS AND DISCUSSION	58
5.1. Muon Spin Rotation: Hyperfine Spectroscopy (TF–MuSR)	58
5.1.1. ZnGeP ₂	58
5.1.2. CdGeAs ₂	63
5.1.3. ZnGeP ₂ :Mn.....	64
5.2. Muon Spin Relaxation: LF– and ZF–MuSR.....	68
5.2.1. ZnGeP ₂	68
5.2.2. CdGeAs ₂	71
5.2.3. Dynamics in ZnGeP ₂ :Mn.....	74
5.3. Bulk Magnetization Measurements: AGM and SQUID	79
5.4. Neutron Studies.....	81
CHAPTER 6: CONCLUSION.....	82
REFERENCES.....	89
APPENDIX A: AUTHOR RESEARCH ACTIVITY	95
A.1. Publication List	95
A.2. Experiment Proposals.....	97
A.3. Conference Presentations (Primary Author or Presenter)	98
A.4. Conference Presentations (Co–author).....	99
APPENDIX B: SELECT PAPERS.....	102
B.1. Spin–Polaron band of heavy carriers in the heavy–fermion ferromagnetic superconductor UGe ₂	102
B.1.1. UGe ₂ : Author Information and Associations	102
B.1.2. UGe ₂ : Text	102
B.1.3. Figures for Appendix C.1	130
B.1.4. References for Appendix B.1.....	135
B.2. Spin Gap in Heavy Fermion UBe ₁₃	144
B.2.1. UBe ₁₃ : Author Information and Associations	144
B.2.2. UBe ₁₃ : Text	144
B.2.3. Figures for Appendix B.2	153
B.2.4. References for Appendix B.2.....	157

B.3. Magnetic polarons in $\text{Lu}_2\text{V}_2\text{O}_7$	161
B.4. Antiferromagnetism in NaV_2O_5	166
B.5. Spin Polarons in $\text{Cd}_2\text{Re}_2\text{O}_7$	172

ABSTRACT

I report on the microscopic electronic and magnetic environments of dilute magnetic semiconducting II–IV–V₂:Mn chalcopyrite compounds as primarily investigated with muon spin rotation and relaxation measurements. Specifically, ZnGeP₂ and CdGeAs₂ are selected as representatives of the chalcopyrites and investigated with and without small concentrations (< 5 at %) of Mn, a substitutional impurity. Both ZnGeP₂ and CdGeAs₂ show ferromagnetism above temperature when weakly doped with Mn. One of the main and fundamental open questions that this project aims to address relates to how the magnetism in these materials transfers from the local moments to the bulk. A combination of the technologically relevant semiconducting properties and above room temperature ferromagnetism makes this class of materials rather appealing for practical applications such as spin-based electronics, which utilizes both the charge and spin of the carrier to store or relay data.

This study investigates pure ZnGeP₂ and CdGeAs₂ via muon spin rotation and relaxation measurements, which utilize μ^+ and Mu^0 ($\text{Mu}^0 = \mu^+ + e^-$) as experimentally accessible analogs to ionic H⁺ and atomic H in materials as well as establish a necessary understanding of the probe (μ^+) behavior for use in the Mn enriched materials. μ^+ is used in ZnGeP₂:Mn to study the local field structure and distribution. Bulk magnetization and neutron scattering measurements are also performed on the ZnGeP₂:Mn materials to aid in characterization of the magnetic properties.

The data suggests a mechanism involving a spin polaron that mediates the exchange between magnetic ions that ultimately leads to bulk magnetic phases in these materials that, unlike their transition metal doped III–V or II–VI counterparts, have too dilute of magnetic concentration for a direct-exchange and have too low conductivity to have indirect exchange via an itinerant band carrier (i.e. Zener or RKKY).

LIST OF TABLES

Table 2.1: Properties of select II–IV–V ₂ compounds	7
Table 3.1: Analytic Approximations for Dynamic Kubo–Toyabe Relaxation Function	24
Table 4.1: Samples	51

LIST OF FIGURES

Figure 2.1: II–IV–V ₂ Chalcopyrite structure with the anisotropic Mu^0_{T} site associated with the II–IV sublattice indicated.....	8
Figure 2.2: FFT of CdGeAs ₂ :Mn HTF–MuSR data	12
Figure 2.3: FFT of CdGeAs ₂ HTF–MuSR data.	12
Figure 3.1: Muon production and implantation	28
Figure 3.2: Positron emission energy and asymmetry spectra.....	29
Figure 3.3: Angular distribution of positron emission.....	29
Figure 3.4: Positron counts on individual histograms.....	30
Figure 3.5: Corrected Asymmetry.....	30
Figure 3.6: Coordinate system for muon spin.....	31
Figure 3.7: Mu^0 states	31
Figure 3.8: Breit–Rabi diagram for isotropic Mu^0_{T}	32
Figure 3.9: Typical MuSR detector configurations.....	32
Figure 3.10: HiTime and Belle sample mounting and detector configuration.....	38
Figure 3.11: TRIUMF beamline 1A.....	39
Figure 3.12: ISIS schematic with TS1 and associated beamlines [82]	41
Figure 3.13: HiFi spectrometer, design drawing [83].....	42
Figure 3.14: SQUID diagram.....	44
Figure 3.15: AGM.....	46
Figure 3.16: AGM Transducer probe.....	46
Figure 3.17: HFIR beamline and instrument layout [90].....	48
Figure 3.18: HB–1 diagram [90].....	49
Figure 3.19: CG–2 diagram [90].....	50
Figure 4.1: ZnGeP ₂ – 253 A	52
Figure 4.2: ZnGeP ₂ Mn – 146 BB.....	52
Figure 4.3: ZnGeP ₂ :Mn – 146 CC	52
Figure 4.4: ZnGeP ₂ :Mn – 146 FF	53
Figure 5.1: ZnGeP ₂ HTF spectra at T=5 K and $B_{\text{ext}} = 4\text{T}$	61

Figure 5.2: ZnGeP ₂ Hyperfine constant variation with temperature.....	61
Figure 5.3: ZnGeP ₂ Relaxation rate of $\nu_{12}(T)$	62
Figure 5.4: CdGeAs ₂ FFT at 4.8 K and 4 T	63
Figure 5.5: ZnGeP ₂ :Mn TF asymmetry trends with temperature and Mn content	67
Figure 5.6: ZnGeP ₂ :Mn 146 AA asymmetry trend with temperature	67
Figure 5.7: ZnGeP ₂ Temperature dependent μ^0 hop rates	70
Figure 5.8: CdGeAs ₂ raw data with dynamic KT fits at 3 temperatures.....	73
Figure 5.9: CdGeAs ₂ Hop rate dependence on temperature	73
Figure 5.10: ZnGeP ₂ :Mn AA Temperature dependent LF relaxation rates	78
Figure 5.11: ZnGeP ₂ :Mn AA Temperature dependent LF asymmetry.....	78
Figure 5.12: ZnGeP ₂ :Mn AGM magnetization curve	80
Figure 5.13: ZnGeP ₂ :Mn AA and CC SQUID Magnetization.....	80
Figure B1.1: Frequency spectrum of muon spin precession in UGe ₂	130
Figure B1.2: FFTs of TF–MuSR signal at various temperatures in UGe ₂	131
Figure B1.3: Temperature dependent asymmetries in UGe ₂	131
Figure B1.4: Temperature dependences of frequencies in UGe ₂	132
Figure B1.5: SP frequency splitting in UGe ₂	133
Figure B1.6: Temperature dependences of SP line width in UGe ₂	134
Figure B1.7: Temperature–pressure phase diagram of UGe ₂	134
Figure B1.8: Temperature dependence of B_{loc} and bulk magnetization in UGe ₂	135
Figure B2.1: Frequency spectrum of muon spin precession in UBe ₁₃	153
Figure B2.2: FFTs of TF–MuSR signal at various temperatures in UBe ₁₃	154
Figure B2.3: UBe ₁₃ ratio of asymmetry within doublet.....	155
Figure B2.4: UBe ₁₃ temperature dependence of frequency splitting and magnetic susceptibility	155
Figure B2.5: UBe ₁₃ Temperature dependence of SP frequency splitting	156
Figure B2.6: Temperature dependence of UBe ₁₃ electrical resistivity	157

LIST OF ABBREVIATIONS

<i>Abbreviation</i>	<i>Meaning</i>
AFM	Antiferromagnetism, antiferromagnetic
DMS	Dilute magnetic {semiconductor, semiconducting}
EMU	Low field (LF) and ZF spectrometer available at ISIS
FM	Ferromagnetism, ferromagnetic
Helios	High field (LF or TF) Spectrometer available at TRIUMF
HF	Heavy Fermion
HiFi	High Field (LF) Spectrometer available at ISIS
HiTime, Belle	High Field (TF) Spectrometer available at TRIUMF
ISIS	Actual name; Synchrotron in Didcot, UK
LF	Longitudinal Field
Mu ⁰	Muonium (μ^+ plus captured electron)
Mu ⁰ _T	Muonium at tetrahedral site
PM	Paramagnetism, paramagnetic
SP	Spin Polaron
T	Tetrahedral site
TF	Transverse Field
TRIUMF	Actual name; Cyclotron in Vancouver, CA
ZF	Zero Field

CHAPTER 1: INTRODUCTION

One of the main and fundamental open questions this project aims to address relates to how the magnetism in dilute magnetic semiconducting II–IV–V₂ chalcopyrites transfers from the local moments to the bulk.

Previous studies have shown that ferromagnetism exists in Mn doped II–IV–V₂ chalcopyrites, however, a detailed understanding of how the magnetism is distributed throughout the material has yet to be achieved (i.e. magnetism distributed uniformly or confined to small regions). In order for uniform ferromagnetism to extend throughout a sample with low concentrations of local moments, the magnetism must transfer to charge carriers; holes, in the case of Mn doped II–IV–V₂ materials. Details of the interactions between the holes and Mn²⁺ local moments remain an open question. For isolated, randomly distributed Mn²⁺ ions, the minimum concentration capable of providing a fully ferromagnetically ordered material is not yet known. Even if, at low Mn concentration, the ferromagnetism originates from small clusters of Mn ions, or a MnP phase, the magnetism may still transfer to the charge carriers thereby providing bulk FM properties despite the second chemical phase. This leaves the questions as to whether hole (carrier) polarization actually occurs and whether there is a single ferromagnetic regime present or patchwork of small ferromagnetic regions imbedded in an otherwise paramagnetic background.

Models that currently attempt to describe magnetic interactions in dilute magnetic semiconducting systems [1,2] are limited to transition metal doped III–V and II–VI systems. While the transition metal doped II–IV–V₂ chalcopyrite systems are related to the III–V and II–VI systems, differences in overall behavior of the systems (e.g. transition metal solubility; transition temperature dependencies on carrier concentration, lattice parameter or magnetic ion concentration; stability of various magnetic phases) clearly show that the current models for the related systems do not accurately describe the II–IV–V₂ chalcopyrite systems; e.g. [3,4].

This project takes an experimental journey through local and bulk magnetic features of Mn doped II–IV–V₂ Chalcopyrites primarily utilizing muon spin rotation and relaxation measurements supplemented by neutron scattering and basic bulk characterization measurements. Specifically, this in depth study aims to develop a higher understanding of the internal magnetic field structure (i.e. microscopic distributions of local fields), how magnetism is distributed throughout the materials, the mechanism responsible for transferring the magnetism from the local magnetic moments to the bulk, magnetic moment fluctuation regimes (e.g. near and through transitions) and any other associated properties and characteristics of these dilute magnetic semiconducting systems. A thorough understanding of these various magnetic properties and the DMS systems, in general, may aid in bridging the gap between theory and application for technologies such as spin–based electronics.

Work by our collaboration relating to the use the muon spin research technique to investigate various properties of dilute magnetic semiconducting II–IV–V₂ chalcopyrite systems officially began with initial measurements performed on various CdGeAs₂:Mn samples [5] at PSI and TRIUMF in 2005. This preliminary look at a few samples (containing different Mn concentrations) established the muon is sensitive to some of the existing local features and that a detailed study on this class of materials would be required to understand the existing mechanisms, characteristics and associated features. An experiment designed to characterize the properties and behavior of an implanted μ^+ within the undoped II–IV–V₂ and I–III–V₂ chalcopyrite semiconducting compounds [6] was proposed and accepted, by the experimental evaluation committee for TRIUMF (Vancouver, Canada) in the spring of 2008. I joined the research group, lead by Dr. Roger Lichti at Texas Tech University (TTU), in fall of 2008. The first experiment on the undoped chalcopyrites was conducted at TRIUMF in October of 2008. This is also the first experiment in which I was actively involved. Since then, work on both these undoped and Mn doped materials continued, using a variety of techniques and is the primary focus of this dissertation. I have been heavily involved in all aspects of this project since the initial experiment time in

October of 2008. My contributions include aspects such as writing experiment proposals to the facilities at which the experiments take place, experimental setup, conducting the actual experiments, data analysis, interpretation, follow up reports and presenting the results. While the primary focus of this dissertation is on the magnetism in Mn doped Chalcopyrites, I have been active in a variety of other projects with both our local group and our international collaborators. A much more detailed accounting of my research activities is in appendix A.

This dissertation will layout and discuss the current status of this project, what questions remain and suggestions as to how to proceed. Specifically, Chapter 2 introduces the particular relevance and main goals of this project as well as provides background information on all aspects of the work except for specific details of the experimental setup. Chapter 3 provides the reader with some background on the experimental technique utilized in this project. Chapter 4 discusses the specific experimental details. Chapter 5 presents and discusses the data collected as described in chapter 4 and our interpretations thereof. Finally, chapter 6 gives a very brief summary of the discussion in chapter 5, lays out some of the remaining open questions and provides some suggestions as to the direction for which this work may continue.

CHAPTER 2: BACKGROUND AND MOTIVATION

Work in the field of semiconductor-based electronics continually focuses on developing devices that are smaller, faster and more efficient than the previous generations. The vast majority of current devices only utilize the charge of a carrier (e^- or h^+) where the developing field of spin-based electronics [7,8] is working on harnessing the spin of the carrier. The ability to use the spin, or the combination of charge and spin, to relay or store data in a device opens up a plethora of possibilities with respect to potential device designs including properties such as higher density storage, faster processing, lower power draw, less heat generation and higher energy efficiency. Read heads in magnetic discs (giant magneto resistive based spin-valve) or spin-based magnetic field sensors are examples of some early applications of spin based electronic devices [9,10,11]. Spin based Hall Effect transistors [12,13], field effect transistors [14], spin polarized light emitting diodes [15,16,17], magnetic tunnel junctions [18,19,20], optical switches and encoders are just a few more examples of devices that can be revolutionized by exploiting the advantages presented by the additional degree of freedom that spin provides [8].

The ideal material for many of the desired spin-based applications is one that is highly spin polarized and exhibits the appropriate electronic properties for the particular desired application. Ferromagnetic semiconductors have been known to be highly spin polarized since the 60s [21]; however, a ferromagnetic phase that is stable above room temperature is required for any large-scale impact to ensue. The development and discovery of ferromagnetism in Mn doped III-V materials, such as InAs:Mn and GaAs:Mn, in the late 80s instigated a significant effort to understand these materials, the fundamental mechanisms therein and further tune the electronic and magnetic properties for device applications [22,23,24]. In principle, Mn doped III-V compounds seem attractive for use in spin-based devices as they can be easily incorporated into existing semiconductor heterostructure systems for a variety of envisioned optical and electronic applications. For example, $In_{1-x}Mn_xAs$ based field

effect devices have been produced that show electrically tunable ferromagnetism [25]. Despite the enormous effort to understand and develop these materials, a T_c above 185K has yet to be achieved [26], which is a major limitation that must be addressed for practical implementation of any Mn doped III–V envisioned devices to occur. T_c being highly correlated to the carrier concentration in GaAs:Mn has been well established [27,28] and is a direct result of the hole mediated ferromagnetic interaction between the open d shells in the Mn atoms. The hole excess is generated by the Mn impurity acting as an acceptor when substitutionally incorporated on Ga sites within the GaAs system. The maximum carrier concentration (and hence T_c) is currently limited by the low Mn solubility in these compounds [1]. That is, phase segregation that occurs when more than several percent of Mn is incorporated into GaAs (as in other III–V compounds) leads to a separate Mn chemical phase within the bulk III–V material instead of replacing the group III element and thereby destroys properties, such as the FM interactions, that are so highly sought out.

The II–VI based compounds are another group of materials that have been heavily researched [2], alongside the III–V systems, for the potential tunability of the lattice constant, band parameters, electroluminescence and magnetic effects. Unlike the III–V materials that are limited somewhere between 7% and 12.5%, the II–VI compounds can accept up to nearly 77% Mn content before experiencing any type of chemical phase separation. Mn^{2+} substitutes isovalently for the group II ion which is responsible for the ease of substitution and results in an AFM coupling between ions with an overall paramagnetic, antiferromagnetic or spin–glass like (diluted AFM) behavior [2]. Many studies of these systems have been quite productive in furthering the fundamental understanding of various mechanisms (e.g. superexchange, etc) however, very few applications have been developed for them since they tend to be room temperature PM and have a low temperature AFM or spin–glassy state.

In light of these difficulties in developing a III–V or II–VI material with a FM T_c suitable for widespread implementation, it is beneficial to broaden the scope of candidate materials in which one searches for such applications.

2.1. II–IV–V₂ CHALCOPYRITES: GENERAL OVERVIEW

Current work on the II–IV–V₂ chalcopyrite systems is not nearly as comprehensive or extensive as their III–V and II–VI counterparts; however, electronic and magnetic features of the II–IV–V₂:Mn chalcopyrites (e.g. high carrier mobility, band gaps from ~0.2 eV to ~5 eV and FM above room temperature) are quite appealing to the spin–based electronics community. The II–IV–V₂ chalcopyrite materials were originally developed for their IR active non–linear optical properties in the early 70s (i.e.: [29]) extending through the 90s. While many properties of these materials are well known, they have yet to be fully optimized for their semiconducting properties. A new interest in these chalcopyrite materials has surfaced since the more recent discovery of bulk FM order at room temperature in Mn doped II–IV–V₂ compounds [4,30,31,32,33,34,35,36,37,38].

II–IV–V₂ chalcopyrites have a structure related to their III–V zincblende counterparts, where the group III elements are replaced by a mix of group II (Be, Mg, Zn, Cd) and IV (C, Si, Ge, Sn) elements, which forces a doubled unit cell ($c/a \approx 2$) along the crystallographic 001 direction (Figure 2.1). These particular systems tend to have significant disorder (i.e. [3,39]) in the II–IV sublattice as there is little energy advantage to any specific arrangement of group II and IV atoms, even in high purity single crystal samples. In addition to the disorder, vacancy impurities with very low formation energies also significantly contribute to the electronic properties in the II–IV sublattice. For example, in ZnGeP₂, Zn and P vacancies are predominantly acceptor and donor impurities, respectively [39]. The Ge vacancy has not been directly observed. However, some experimental data support the existence of an additional shallow acceptor consistent with the expected properties for such a vacancy [39,40,41]. Predicted bandgaps range from ~0.2 eV to ~5 eV. Table 2.1 presents measured gaps, lattice constants, transparency range and FM transition temperature (when Mn doped) for a relevant subset of these materials [30,35,38,42,43,44].

When appropriately doped with a transition metal, such as Mn²⁺, several of the II–IV–V₂ materials show bulk magnetic properties [4]. Mn²⁺ can substitute isovalently

in the group II cation site and as a double acceptor at the group IV site [34,4,45]. In the II–IV–V₂ systems, the excess of holes generated by the Mn²⁺ substitution on the group IV site, contributes to the Mn 3d band and provides sufficient carrier concentration to mediate interactions between the local magnetic moments that can lead to an overall FM coupling. The ability to introduce both a high concentration of magnetic ions (via the isovalent group–II substitution) and acceptor doping (hole excess via group–IV substitution) provide a very distinct advantage over their binary counterparts (III–V and II–VI compounds). Magnetic and non–magnetic semiconducting properties in these compounds have yet to be optimized for practical applications since the fundamental mechanisms that govern many of the electronic and magnetic properties have yet to be fully understood if at all. Such is the case for the mechanism responsible for transferring the magnetism from the local moments to the bulk.

Table 2.1: Properties of select II–IV–V₂ compounds

<i>Compound</i>	<i>Energy Gap</i> (eV)	<i>Lattice Constants</i> (Å)	<i>Transparency</i> Range (μm)	<i>T_c</i> (K) (Mn-doped)
ZnGeP ₂ [30,35,36,43,46]	1.99	<i>a</i> = 5.463; <i>c</i> = 10.74	1 – 12	~312–350
CdGeP ₂ [34,43,46]	1.72	<i>a</i> = 5.740; <i>c</i> = 10.776	0.9 – 11	~320–350
CdGeAs ₂ [31,32,33,42,43,46]	0.57–0.67	<i>a</i> = 5.943; <i>c</i> = 11.22	2.4 – 18	~320–355
ZnGeAs ₂ [43,44,46]	0.85	<i>a</i> = 5.671; <i>c</i> = 11.153	<i>Data not available</i>	~367
ZnSnAs ₂ [38,43,46]	0.65	<i>a</i> = 5.852; <i>c</i> = 11.703	<i>Data not available</i>	~329–350
ZnSiAs ₂ [43,46]	~2.12	<i>a</i> = 5.606; <i>c</i> = 10.886	<i>Data not available</i>	~325–337
ZnSi _x Ge _{1-x} N ₂ [43]	<i>x</i> dependent	<i>varies</i>	<i>varies</i>	200–280

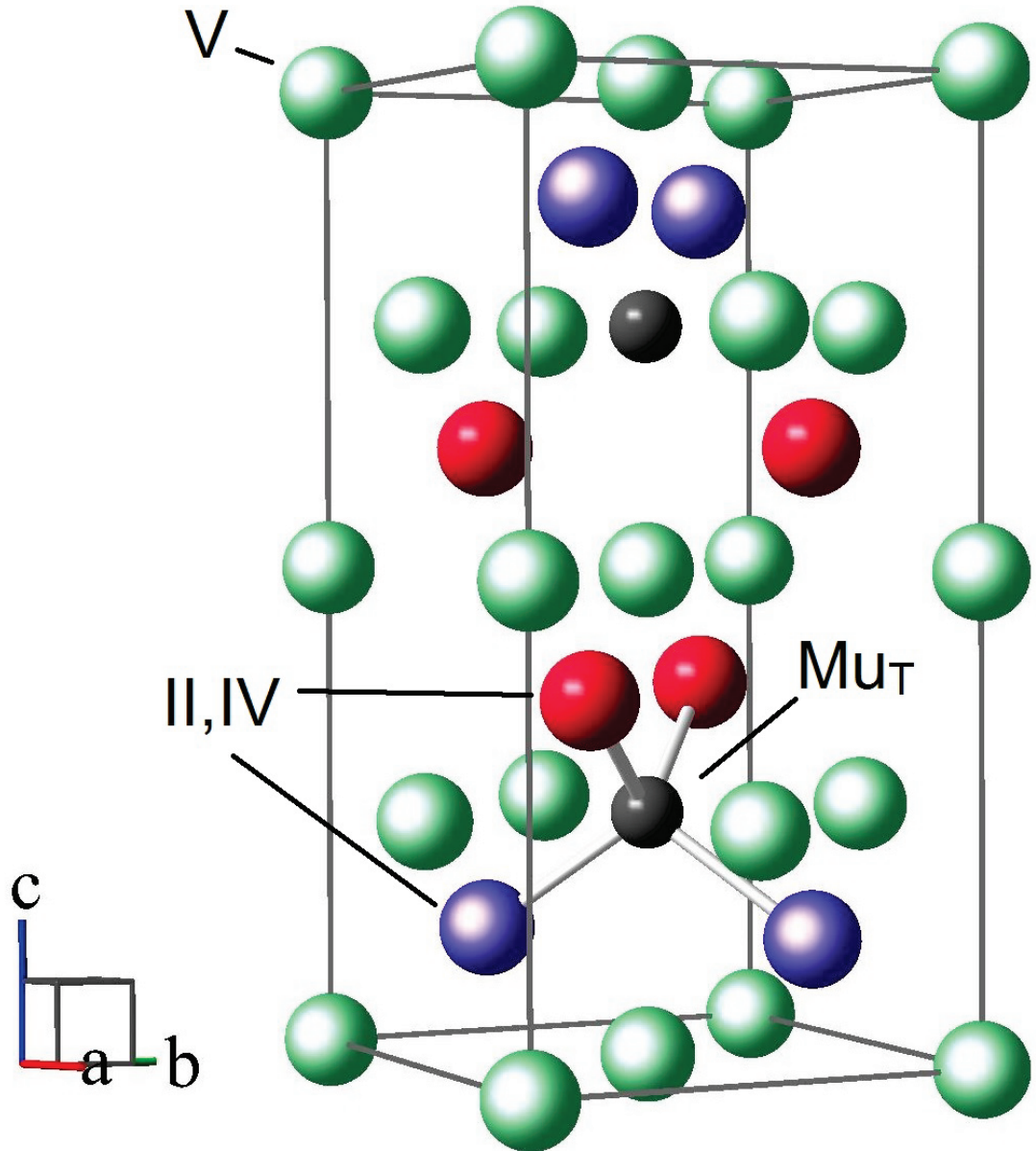


Figure 2.1: II-IV-V₂ Chalcopyrite structure with the anisotropic Mu_T⁰ site associated with the II-IV sublattice indicated

2.2. II–IV–V₂ CHALCOPYRITES: PREVIOUS WORK

Measurements such as electron paramagnetic resonance (EPR), electron–nuclear double resonance (ENDOR), X–ray diffraction (XRD), optical absorption, SQUID magnetization and nuclear magnetic resonance (NMR) were performed by various collaborations to further characterize the II–IV–V₂:Mn chalcopyrites. EPR and ENDOR studies were conducted in an effort to characterize isolated Mn²⁺ ions in bulk ZnGeP₂ single crystal materials and have provided information on the spin density and distribution of Mn²⁺ ions replacing the group–II element [47]. XRD data on ZnGeP₂:Mn clearly illustrates that the tetrahedral chalcopyrite structure is maintained but there is a slight increase in lattice parameters as the Mn content is increased; i.e. ~0.34% increase for 0 Mn incorporation to 5.6 at% Mn [30]. Optical absorption data indicate that the energy gap decreases slightly as the manganese concentration increases; which is typical of heavily *n*– or *p*– type semiconductors. Specifically, the gap for pure ZnGeP₂ is $E_g = 2.0$ eV compared to the energy gap of 1.9 eV and 1.83 eV for 1.3 at% Mn and 3.0 at% Mn in ZnGeP₂:Mn respectively [30]. Temperature dependent magnetization measurements (via SQUID Susceptometer) performed on bulk samples with a variety of Mn concentrations [30] show a ferromagnetic region between 47 K and 312 K for $0.013 \leq x \leq 0.2$ and a paramagnetic state above 312 K. Samples with concentrations below Mn_{0.05} reportedly show a mix of antiferromagnetic and paramagnetic phases below 47 K, contrasting to the pure antiferromagnetic phase reported in samples with concentrations above Mn_{0.05}. These authors (Cho, et al) argue that above $x = 0.05$, the Mn ions are very closely packed and ordered, most likely at group–II sites. Mn substitution is thus claimed to be highly non–uniform and either strong clustering of Mn ions or formation of a second structural phase (e.g. MnP) can be inferred from the growth conditions used for those particular samples. Powder XRD results produced by a different group [48], specifically investigating CdSnP₂:Mn which is closely related to ZnGeP₂:Mn and a good representative compound of the II–IV–V₂:Mn chalcopyrites, suggest a second

ordering transition. Comparing their results to those for $\text{ZnGeP}_2\text{:Mn}$ and bulk MnP, they found the characteristic ferromagnetic behavior of MnP to be very close to that of the Mn doped chalcopyrites. Despite the lack of peaks in the XRD data that caused some groups to argue against MnP as a magnetic impurity, the bulk-phase of MnP at these low concentrations may be under the detection limits of XRD; therefore, one cannot conclude from XRD, with certainty, whether or not small inclusions of MnP dominate the magnetic features. Results of a NMR study on $\text{ZnMnGeP}_2\text{:Mn}$ [49] suggest that more than 90% of the Mn atoms were in a MnP impurity phase with cluster sizes on the order of nanometers from Mn concentrations from $x = 0.08$ to 0.15. Existing data, as outlined above, suggests that separation of a MnP secondary phase likely occurs for $x > 0.05$.

Some of our collaboration's earlier TF-MuSR work (performed in 2005 at TRIUMF in Vancouver, Canada [50,51]) on the Mn doped II-IV-V₂ chalcopyrite compound, $\text{CdGeAs}_2\text{:Mn}(3\%)$, has demonstrated that these materials do exhibit some FM order above room temperature. This is shown in a spectra collected at $T=300$ K with an applied field of $\mathbf{B}_{\text{TF}} = 1$ T (Figure 2.2) the μ^+ precession frequency from within the sample is clearly shifted to a lower frequency as compared to the μ^+ precession frequency from within a CaCO_3 sample. The μ^+ precesses at the Larmor frequency, $\omega_\mu = \gamma_\mu B_{\text{eff}}$, determined by the gyromagnetic ratio of the muon ($\gamma_\mu=135.54$ MHz/T) and the effective magnetic field at the site in which the muon resides (B_{eff}). The reference sample is mounted behind the sample of interest so that any muons that miss the sample will be implanted into the nonmagnetic CaCO_3 with the positron emission data recorded in a completely separate set of histograms. This configuration provides a direct measure of the magnetic field at the sample area while actual sample data is collected. By comparing the two measured μ^+ frequencies, one can easily determine the total effective field at the muon site in the sample (for a more complete discussion of the TF-MuSR technique, see section 3.1.2). The broad form of the signal from the Mn doped sample is very different from that of the very sharp peak present in an undoped CdGeAs_2 sample [6] (Figure 2.3). A coarse temperature scan has been

completed on a few different CdGeAs₂:Mn materials with concentrations between 3 % and 6 % and this broad feature presents itself in the other Mn doped samples as well [50,51]. These measurements were performed in a survey of many materials, and there is far too little data from these measurements to conclude anything other than there is definitely a feature in the Mn doped samples, not present in the undoped samples. These earlier data clearly show that MuSR can be used as an effective tool to further develop the understanding of the local magnetic properties within these materials. CdGeAs₂:Mn and ZnGeP₂:Mn have nearly identical structures (different lattice parameters) and share many other electrical and magnetic properties with each other and also ought to serve as good representatives of the other dilute magnetic II–IV–V₂ Chalcopyrites.

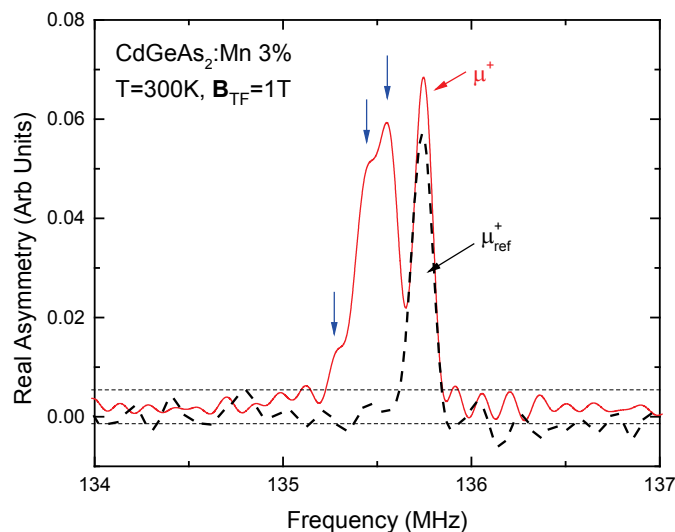


Figure 2.2: FFT of CdGeAs₂:Mn HTF-MuSR data .

The solid red line is the real component of the FFT from a CdGeAs₂:Mn 3 at% sample taken at room temperature and $B_{\text{ext}} = 1$ T. The black dashed line is the real asymmetry from a purely diamagnetic reference sample functioning as a measure of the magnetic field at the sample. Note the amplitude of the reference signal is increased by a factor of 30 to clearly indicate the *frequency* matching. The relative differences in *asymmetry* between the sample and reference samples is irrelevant for this purpose.

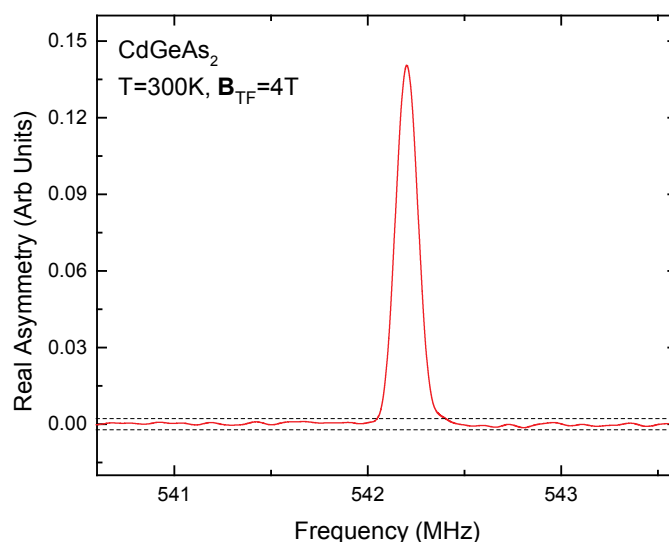


Figure 2.3: FFT of CdGeAs₂ HTF-MuSR data.

In direct contrast to Figure 2.2, this shows the real component of the FFT from a pure CdGeAs₂ that only shows μ^+ precession at the Larmor frequency given $B_{\text{ext}} = 4$ T.

2.3. DILUTE MAGNETIC SEMICONDUCTORS: THEORY

A key ingredient to the widespread application of a magnetic semiconductor based on a II–IV–V₂ chalcopyrite compound is a comprehensive understanding of the magnetic, structural and electronic properties and how they vary with respect to real world and potential device parameters. Unfortunately, a comprehensive understanding of how some of the most basic properties of these dilute magnetic materials are related does not exist [52]. That is, there is not a model that describes how characteristics of a doped material such as the transition temperatures and band gap relate to basic structural or electronic properties of the undoped material or even how relevant properties vary with magnetic ion content.

However, there has been a tremendous effort to understand the ferromagnetism in the peripherally related III–V and II–VI dilute magnetic systems (see [1,53] and references therein for a nice review). There are two models that seem to be predominant for these other systems. Both claim exchange coupling between charge carriers and local moments (partially filled 3*d* orbitals) result in ferromagnetic interactions and are parameterized with an exchange energy term, J . The Zener model [54,55] is used in the weak coupling ($J < E_F$) regime whereas the double–exchange mechanism [56] tends to be used in the strong coupling limit. In the Zener model (equivalent to the RKKY model in the mean–field limit for DMS), band [itinerant] carriers become polarized (exchange couple to a local moment) then migrate a considerable distance while keeping their spin polarization independent of other local moments encountered along the way. FM occurs when the spins of the itinerant carriers and local moments are aligned. In the double–exchange picture, the charge carriers still mediate the interactions between local moments but does so through indirect coupling to neighboring ions, (opposed to the conduction or impurity band as in the former model) since the distance between local moments is, by definition, far greater than the extent of the magnetic ions’ wavefunction. In the most simplified double–exchange picture, two magnetic ions are separated by a non–magnetic ion and

the carrier from the first magnetic ion will hop to the non-magnetic ion while an identical carrier hops from the non-magnetic ion to the second magnetic ion. The lowest overall energy configuration for this transaction to take place requires that the two magnetic ions have spins parallel since a carrier spin-flip costs energy.

As previously discussed, there are considerable distinctions between the III-V and II-VI materials as compared to the II-IV-V₂ chalcopyrite compounds. The most notable distinction has to do with the way that Mn substitutes into the II-IV sublattice. Unlike the III-V or II-VI materials where Mn only substitutes in one form (either a donor or isovalently, respectively), the ability for Mn to easily substitute on both the group II and group IV sites clearly result in very different electronic and magnetic properties (including overall Mn solubility). Moreover, when applied to the II-IV-V₂ Chalcopyrites, the respective calculations for properties such as magnetic transition temperatures do not vary with bandgap or lattice constant as one would expect with the double-exchange and Zener models, respectively [3] and therefore leaves these specific dilute magnetic semiconducting chalcopyrite systems without a consistent model.

CHAPTER 3: EXPERIMENTAL TECHNIQUES

3.1. MUON SPIN RESEARCH

The muon spin research (MuSR) technique utilizes 100% spin polarized muons ($m_\mu \approx 1/9 m_{\text{electron}}$; $S = 1/2$; $\gamma_\mu = 2\pi \times 135.54 \text{ MHz/T}$; $\tau_\mu \approx 2.2 \text{ } \mu\text{s}$) implanted into a sample where the time evolution of the muon's spin polarization function is monitored to reveal electronic and magnetic information from the local environment for which the muon is a direct probe. The MuSR technique has some distinct advantages over other techniques since the muon itself is the probe and therefore it does not rely on scattering techniques or additional trickery (e.g. strong magnetic field pulses) to modify and hence probe the environment of interest (e.g. X-ray diffraction and neutron scattering or electron spin resonance and nuclear magnetic resonance, respectively). The positive muon is very sensitive to magnetic fields and attracted to areas of high electron density making it a viable probe for applications such as investigating magnetism (e.g. local field distributions, electronic structure, ordering, dynamics), superconductivity (e.g. coexistence of superconductivity and magnetism, magnetic penetration depth, coherence length), defect states in semiconductors (where muonium, $\text{Mu}^0 = \mu^+ e^-$, functions as an experimentally accessible analog to hydrogen), quantum diffusion in metals (μ^+ c.f. H^+) and quantum diffusion in non-metals (Mu^0 c.f. H). A much more complete description of the MuSR technique is found in references such as [57,58,59,60]. The following introductory information comes straight from these references, personal conversations with the onsite scientists, my experience with the equipment and a few additional sources explicitly indicated within the subsequent text.

3.1.1. Overview: The memoir of a synthetic muon

While muons are found, naturally occurring, in cosmic rays that can be detected at sea level, among many other practical limitations, the approximate flux of ~ 1 muon per square cm every minute (incident on the Earth's surface) [61] is far too

low for efficient use for use as an experimental condensed matter probe. Additionally, these types of experiments require relatively low energy muons (~ 4 MeV) to allow for a reasonable sized sample to actually stop a muon with minimal disturbance to the material that is under investigation. For this application, muons are manufactured through a process involving a few steps. First, a 500 MeV proton beam, from cyclotrons or synchrotrons, interact with a target (typically graphite or Beryllium) producing pions (π^\pm). These pions decay after their characteristic lifetime ($\tau_\pi = 26$ ns) into a muon (μ^\pm) and the associated neutrino (ν_μ) or antineutrino ($\bar{\nu}_\mu$).

$$\pi^+ \rightarrow \mu^+ + \nu_\mu \text{ and } \pi^- \rightarrow \mu^- + \bar{\nu}_\mu \quad (3.1)$$

Since the net spin of the π^+ is zero and, in the energy range relevant to MuSR, the neutrino is produced with its spin antiparallel to its momentum (i.e. negative helicity), conservation of both linear and angular momentum force the μ^+ to also have its spin antiparallel to its momentum. Similarly for the π^- , with the exception that the antineutrino has its spin parallel to its momentum (i.e. positive helicity) and therefore the μ^- also has positive helicity. Note that this assumes the π is at rest. In the case of μ^+ sources that are functioning today, these μ^+ beams are emitted from the π^+ that are at rest near the surface of the production target. The other decay mode produces μ^+ with positive helicity and μ^- with negative helicity but these μ^\pm are at much higher energies. A different process is required for developing a beam of μ^- since the π^- is quickly captured within the primary target and hence requires a very different μ extraction configuration that is beyond the scope of this project. In light of this, any additional reference to MuSR, the muon and so forth will be referring to the positively charged muon, μ^+ , unless otherwise explicitly stated. A direct result of choosing the pions that decay from rest near the surface of the target for one's source is that the muons emerge 100% spin polarized (with momentum = 29.79 MeV/c and kinetic energy = 4.119 MeV). Once departing the proton target, the muon beam can be cleaned up and implanted directly into a sample. This implantation process reduces the initial ~ 4 MeV muon beam to the order of a few eV within the first ~ 1 ns of implantation due to the initial interactions with the local environment including the ionization of atoms and

scattering with electrons that are directly in the implantation path (known as the ionization track) followed by the capture and release of electrons (either free electrons within the system or electrons freed along the ionization track) until finally reaching an energy on the order of meV where the muon interacts with the host material but is typically rather non-invasive. The interactions occurring during implantation are all Coulombic and very rapid thereby not contributing the depolarization of the muon itself. The majority of the energy is transferred from the muon to the host material early in the implantation process and the last damage and initial μ^+ stopping site are separated by ~ 100 nm. Therefore, there should be no interaction between the thermalized muon and ionization track (i.e. vacancies or interstitial defects produced directly via the ionization track). Figure 3. depicts the process from μ^+ implantation through thermalization.

Once implanted and sufficiently slowed, the muon interacts with the local environment and decay after a characteristic time, $t \sim \exp[-t/\tau_\mu]$ where the muon lifetime (τ_μ) is 2.2 μ s. Upon decay, the muon emits a positron (e^+) in a direction preferential to the muon spin at the time of decay, along with the associated positron neutrino (ν_e) and muon antineutrino ($\bar{\nu}_\mu$) as



The emitted positrons are tracked by scintillation detectors positioned in various geometries around the sample area, depending on the particular type of measurement. The probability of the muon decay (P) and positron energy (ϵ_e) are related by the energy spectrum ($E(x)$) and asymmetry factor (a); written as [57]

$$dP(x, \theta) = E(x)(1 + a(x) \cos(\theta)) dx d(\cos[\theta]) \quad (3.3)$$

$$a(x) = \frac{2x - 1}{3 - 2x} \quad (3.4)$$

$$E(x) = 2x^2(3 - 2x) \quad (3.5)$$

parameterized by $x = \epsilon_e/\epsilon_{\max}$, and a maximum positron energy of $\epsilon_{\max} = 52.83$ MeV. The asymmetry (a) is a measure of how closely the muon spin and positron momentum align. Figure 3.2 and Figure 3.3 illustrate these relations. Note that when

the positron energy is below 50% of the maximum energy, the asymmetry is zero or less. This indicates little to no correlation of the emitted positron with muon spin direction. However, at this limit, one should also note that the angular distribution of positron emission is perfectly symmetric, the importance of which will be apparent during later discussion of detector configuration. Additionally, positrons with such low energies are not usually detected anyway.

Detector configurations vary with parameters such as primary goals of the experiment, available apparatus and specific type of MuSR experiment. Regardless of the specific arrangement, the scintillation detectors provide the same basic function; tracking the time evolution of spin polarization for an implanted muon by monitoring an ensemble of positron decay events. In the time differential (TD) mode, a clock is started upon muon implantation in the material and then stopped when a corresponding event (positron from the muon decay) is detected by one of the scintillation counters. Typically ensembles containing anywhere from $\sim 10^6$ to $\sim 10^8$ events are collected at a given temperature and field to constitute a single data point. The number of positrons recorded by a counter can be expressed as

$$N(t) = N_o \exp\left(-\frac{t}{\tau_{mu}}\right) (1 + A(t)) + B \quad (3.6)$$

where the time (t) from implantation to decay is measured and muon lifetime ($\tau_{\mu}=2.2 \mu\text{s}$) is known. However, overall normalization (N_o) and the time independent background (B) cannot be determined experimentally with only one detector. The asymmetry spectra can be numerically determined by solving equation (3.6), provided one has a model describing the time dependence so that both N_o and B are known. In practice, multiple counters are utilized to eliminate the need for such a model. By using a pair of opposing counters (180 degrees apart with respect to the frame of a 2-dimensional rotating body) and combining the individual positron counts, an experimental asymmetry can be expressed as

$$a_0(t) = \frac{(N_1(t) - B_1) - (N_2(t) - B_2)}{(N_1(t) - B_1) + (N_2(t) - B_2)} \quad (3.7)$$

Where the terms are the same as defined in equation (3.6) but now indexed by detector number 1 or 2. To account for differences between the physical detectors (e.g. counter efficiency and solid angle coverage) we define the two adjustment parameters

$$\alpha \equiv \epsilon_2/\epsilon_1 \quad (3.8)$$

and

$$\beta \equiv A_2/A_1 \quad (3.9)$$

The time dependent muon polarization, as seen by each counter is

$$p_{1,2}(t) = \cos(\omega_\mu t + \phi_{1,2}) \quad (3.10)$$

This can be written with respect to a single counter by recognizing that

$$\cos(\omega t + \theta) = (-1)^n \cos(\omega t + \theta + n\pi) \quad |n \in \mathbb{Z} \quad (3.11)$$

and that geometry dictates $|\phi_1 - \phi_2| = \pi$

$$p_1(t) = -p_2(t) \quad (3.12)$$

and then rewrite equation (3.7) as

$$a(t) = \frac{((1 - \alpha) + (1 + \alpha\beta)A_1p(t))}{((1 + \alpha) + (1 - \alpha\beta)A_1p(t))} \quad (3.13)$$

Experimentally determining α and β is straightforward. In a normally functioning experimental setup, β is very close to 1 and is not dependent on sample geometry or positioning. α , on the other hand, is highly dependent on these parameters and therefore is determined for each experiment by applying a weak transverse field and determining a value (of α) such that the resulting oscillating signal is centered around zero. An example of raw counts in two opposing counters and the corresponding corrected asymmetry is shown in Figure 3.4 and Figure 3.5, respectively.

Once fully implanted in a material, the muon will precess in the effective magnetic field of the local environment (\mathbf{B}_{loc}) at the Larmor frequency ($\omega_\mu = \gamma_\mu B = 135.54 \text{ MHz/T}$) until it decays, emitting the positron. For comparison, precession frequencies for the proton, electron and neutron are 42.577 MHz/T, 28,025 MHz/T and 29.165 MHz/T, respectively. The large magnetic moment of the muon is what allows it to be used as a very sensitive magnetic probe and hence detection of fields down to the order of $\sim 10^{-5} \text{ T}$.

This effective magnetic field (\mathbf{B}_{eff}) at the site of the muon can be generally written in the form

$$\mathbf{B}_{eff} = \mathbf{B}_{ext} + \mathbf{B}_{dip} + \mathbf{B}_{hyp} + \mathbf{B}_{fermi} + \delta\mathbf{B}_{loc} \quad (3.14)$$

where \mathbf{B}_{ext} is an externally applied magnetic field. \mathbf{B}_{dip} encompasses the dipolar field contribution that is a sum of localized moments over the entire crystal including site-to-site differences. \mathbf{B}_{hyp} is the field contribution from short range magnetic interaction between the μ^+ and local electronic moments (e.g. wavefunction overlap), commonly referred to as the hyperfine interaction. \mathbf{B}_{fermi} includes contributions from the Fermi contact interaction (between μ^+ and a carrier) which can be the magnetic interaction of μ^+ and e^- spins, for s - and p - electron metals (i.e. Li, Be, Na, Mg, Al etc); RKKY (indirect exchange) between μ^+ and unpaired electrons via the conduction (itinerant) electrons, for some d - and f - materials; or in insulators, the transferred hyperfine field which is the μ^+ and electron wavefunction overlap. $\delta\mathbf{B}_{loc}$ contains contributions related to fluctuations of the neighboring moments. Throughout this work, the *local magnetic environment* typically refers to the effective field as if no external magnetic field were applied (i.e.: $\mathbf{B}_{loc} \equiv \mathbf{B}_{eff} - \mathbf{B}_{ext}$).

To connect the experimental measurements with reality, a model of the time dependent muon spin polarization function for a particular mechanism is developed. The most straight forward and non-trivial case is for an implanted μ^+ to remain static (with respect to motion about the host material) and have a constant \mathbf{B}_{loc} such that the field direction is perpendicular to the initial spin polarization direction. In this case, the muon will happily precess at the Larmor frequency ($\omega_\mu = \gamma_\mu B = 135.54 \text{ [MHz/T]} \cdot B$) for its entire life. That is, one can write the muon spin polarization function in the following form

$$P(t) = A_0 G(t) \cos(\omega t + \phi) \quad (3.15)$$

where the initial polarization (A_0), relaxation envelope function ($G(t)$), precession frequency (ω) and phase (ϕ) are directly fit to the $P(t)$ data. With a non-relaxing and purely diamagnetic state, as described here, $G(t) = 1$ [unit less]. Figure 3.5 shows a real example of a non-relaxing diamagnetic μ^+ in silver with a magnetic field of

$B_{ext} \approx 100$ G, applied perpendicular to the initial spin polarization of the implanted muons, along with parameters found by fitting the data with equation (3.15). This very clean μ^+ behavior is why Ag is often used for calibration purposes.

In this simple system, the muon spin polarization function can be determined by considering how a magnetic moment behaves in an applied field. With the geometry shown in Figure 3.6 consider a form of Newton's second law written for a rotational body

$$\frac{d}{dt}(\hbar \mathbf{S}_\mu(t)) = \mathbf{m}_\mu(t) \times \mathbf{B}_{loc}(t) \quad | \quad \mathbf{m}_\mu = \gamma_\mu \hbar \mathbf{S}_\mu \quad (3.16)$$

With the time dependent angular momenta $[\hbar \mathbf{S}_\mu(t)]$, muon magnetic moment $[\mathbf{m}_\mu(t)]$, the muon gyromagnetic ratio (γ_μ) and the \mathbf{B}_{loc} as defined in (3.14) with its only non-zero component along the $\hat{\mathbf{x}}$ -axis. By the properties of the cross product, the angular momenta is perpendicular to the effective field. If the local field is constant with time or equivalently if the period of fluctuation is large compared to the muon lifetime ($1/\nu_B \gg \tau_\mu$) then a solution to equation (3.16) is

$$\mathbf{S}_\mu(t) = S_\mu^\perp(0)(\hat{\mathbf{y}}' \cos(\omega_\mu t) - \hat{\mathbf{z}}' \sin(\omega_\mu t)) + \hat{\mathbf{x}}' S_\mu^\parallel(0) \quad (3.17)$$

And written with respect to the initial muon spin axis

$$S_\mu(t) = S_\mu(\cos(\theta)^2 + \sin(\theta)^2 \cos(\omega_\mu t)) \quad (3.18)$$

From which we can see that for a uniform field applied at $\theta = 90^\circ$, as described in the case of Ag, the origin of equation (3.15) and therefore a direct measure of the size of B_{loc} . In the case where $\theta = 0^\circ$, equation (3.18) simply goes to S_μ . This shows that there is no contribution to the change in muon spin polarization from the fraction of implanted μ^+ with \mathbf{S}_μ aligned parallel to the direction of the local field ($\mathbf{S}_\mu \parallel \mathbf{B}_{loc}$).

One can now normalize this function with $S_\mu(t)/S_\mu$, allow \mathbf{B}_{loc} to be expressed as the general distribution ($\rho(\mathbf{B}_{loc})$) and then write the overall spin polarization function in the form

$$P(t) = \int (\cos(\theta)^2 + \sin(\theta)^2 \cos(\omega_\mu t)) \rho(\mathbf{B}_{loc}) d^3 \mathbf{B}_{loc} \quad (3.19)$$

which is the statistical average over all distributions.

Let us now consider a local field distribution within an ordered magnetic material containing only one unique stopping site for the muon and a very large diffusion barrier (i.e. no μ^+ hopping after thermalization)

$$\rho(\mathbf{B}_{loc}) = \frac{\delta(B_{loc} - B_0)}{4\pi^2 B_0^2} \quad (3.20)$$

Evaluating equation (3.19) with the distribution given by equation (3.20) we see

$$P(t) = \frac{1}{3} + \frac{2}{3} \cos(\omega_\mu t) \quad (3.21)$$

In a non-magnetic material where the source of the \mathbf{B}_{loc} is related to interactions with the nuclei that surround the μ^+ site (concentrated dipole moments), the fields are taken to have a Gaussian shaped distribution and can be expressed as

$$\rho(\mathbf{B}_{loc}) = \left(\frac{1}{\Delta_G \sqrt{2\pi}} \right)^3 \exp\left(-\frac{B_{loc}^2}{2\Delta_G^2} \right) \quad (3.22)$$

where Δ_G is the second moment of the field distribution and when this distribution (equation (3.22)) is evaluated in equation (3.19) (taking the statistical average over these distributions with $\mathbf{B}_{ext} = 0$) yields the static Kubo-Toyabe function [62]

$$P_s^{KT}(t) = \frac{1}{3} + \frac{2}{3} \left(1 - (\gamma_\mu \Delta_G t)^2 \right) \exp\left(-\frac{(\gamma_\mu \Delta_G t)^2}{2} \right) \quad (3.23)$$

In the case of a purely static system, the inhomogeneity in the field distribution itself causes dephasing of the muon spin precession. If an external field, larger than $\sim 5\Delta_G$ (Δ_G typically on the order of 10s of Gauss), is applied with $\theta = 90^\circ$ (known as *transverse field* where $\mathbf{B}_{ext} \perp \mathbf{S}_\mu(0)$) then the nuclear contribution (\mathbf{B}_{dip}) is dominated by the external field and therefore the muon is only really sensitive to the field distribution along the direction of the applied field. The solution to equation (3.19) for this arrangement then becomes

$$P^{\theta=90^\circ}(t) = \exp\left(-\frac{(\gamma_\mu \Delta_G t)^2}{2} \right) \cos(\omega_\mu t) \quad (3.24)$$

If one now considers a dynamic system where there are fast fluctuations in B_{loc} (e.g. μ^+ hopping between sites with different effective fields or fluctuations from neighboring electronic moments), then the solution to equation (3.16) becomes

$$P^{\theta=90^\circ}(t) = e^{-\lambda t} \cos(\omega_\mu t) \quad (3.25)$$

where the relaxation function (i.e. $G(t)$ in equation (3.15)) is Lorentzian, in shape, and contains the spin relaxation rate (λ). A Lorentzian shaped relaxation function can also be a result of a distribution of dilute dipole moments

$$\rho(\Delta_i) = \frac{1}{\pi} \frac{\sigma}{\sigma^2 + \Delta_i} \Big| \Delta_i = \mathbf{B}_{i,loc} \quad (3.26)$$

where the width parameter of the field distribution is σ and the local field at the i^{th} muon site, not including the externally applied field is Δ_i . The resulting relaxation function is evaluated by taking a statistical average over a Gaussian distribution of field values, is then a static Lorentzian Kubo–Toyabe function

$$G(t) = \frac{1}{3} - \frac{2}{3}(1 - \gamma_\mu \sigma t)e^{\gamma_\mu \sigma t} \quad (3.27)$$

In this case, a field applied with $\theta = 0^\circ$ the resulting relaxation function is found to be

$$\begin{aligned} G(t, \omega_L) = & 1 - \frac{\gamma_\mu \sigma}{\omega_L} j_1(\omega_L t) e^{-\gamma_\mu \sigma t} \\ & - \left(\frac{\gamma_\mu \sigma}{\omega_L} \right)^2 (j_0(\omega_L t) e^{-\gamma_\mu \sigma t} - 1) \\ & - \left(1 + \left(\frac{\gamma_\mu \sigma}{\omega_L} \right)^2 \right) \gamma_\mu \sigma \int_0^t j_0(\omega_L t') e^{-\gamma_\mu \sigma t'} dt' \end{aligned} \quad (3.28)$$

where j_0 and j_1 are spherical Bessel functions.

One way to address the field fluctuations at the muon site – either from the muon sampling different sites that each a different field or by the local field itself varying with time – is to assume that \mathbf{B}_{loc} has a time dependence that is of the form

$$\mathbf{B}_{loc}(t) = e^{-\nu t} \quad (3.29)$$

where the fluctuation rate, as sampled the muon (ν), is completely independent of its past and future hops. The static Kubo–Toyabe (P_S^{KT} , equation (3.24)) is modified and becomes [62]

$$P_D^{KT}(t) = P_S^{KT}(t)e^{-vt} + v \int_0^t P_S^{KT}(t')e^{-vt'} P_D^{KT}(t-t') dt' \quad (3.30)$$

In practice, the dynamic Kubo–Toyabe function require numerical methods to solve for the resulting spin polarization function. In light of this, a variety of analytic approximations have been made to allow for more efficient data analysis but require some assumptions that correlate the fluctuation rate (ν) and local field distribution (Δ). The three main regimes and resulting form of the relaxation function ($G(t)$) are displayed in Table 3.1 where $\lambda \equiv 2\Delta^2/\nu$.

Table 3.1: Analytic Approximations for Dynamic Kubo–Toyabe Relaxation Function

<i>Assumption</i>	<i>G(t)</i>	<i>Comment</i>
$\nu/\Delta < 1$	$\frac{1}{3}e^{-\frac{2}{3}\nu t}$	Slow – only KT tail affected
$1 < \nu/\Delta < 10$	$\exp[-\lambda e^{-\nu t} - 1 + \nu t]$	Moderate – ‘Abragam’ function
$\nu/\Delta > 10$	$e^{-\lambda t}$	Fast – simple Lorentzian

A variation on the dynamic spin polarization function that is analytic and does *not* require an assumption regarding the field distribution (unlike the Kubo–Toyabe approach) is presented in [63]. This is a particularly good approximation if field fluctuations are sufficiently fast ($\nu > 10\Delta$) or one is only interested in the very early times of muon decay. The result of this method is commonly referred to as the ‘Keren function’ (published by A. Keren in 1994) that utilizes a perturbation approach where one makes an assumption about the time dependence of the field–field correlation function that allows for the expansion of the perturbative series leading to the final analytic spin polarization function. For zero applied field ($\mathbf{B}_{\text{ext}} = 0$), this function is written as

$$P(t) = P(0) \left[\frac{2\Delta^2}{v^2} \{ \exp(-vt) - 1 + vt \} \right] \quad (3.31)$$

Where $P(0)$ is the spin polarization function evaluated at the time immediately after thermalization (e.g. the ‘static’ or initial state). The fluctuation rate (v) or inverse correlation time ($\tau_c = 1/v$) relates to variations in the field at the muon site regardless of the fluctuation source – meaning this term alone cannot distinguish the field fluctuations sensed by a muon hopping between sites with different fields opposed to a stationary muon that senses fluctuations in fields due to nearby fluctuating nuclear or electronic moments. Here, Δ is still defined as the second moment of the instantaneous field distribution.

For dilute alloys [64], one can sometimes approximate the field distribution as

$$\rho(\Delta_i) = \sqrt{\frac{2}{\pi}} \frac{a}{\Delta_i^2} \exp\left(-\frac{a^2}{2\Delta_i^2}\right) \quad \Delta_i \equiv \mathbf{B}_{i,loc} \quad (3.32)$$

where Δ_i is the local field (externally applied field is *not* included) and the static width of the fluctuating field (a). Fluctuations in the field at the i^{th} μ^+ site (i.e. $\delta\mathbf{B}_{loc}$ in equation (3.14) and Δ_i in equation (3.32)) lead to a relaxation function of the form

$$G(t, \Delta, v) = \exp\left(-\frac{2\Delta^2}{v} t\right) \quad (3.33)$$

Where the rate at which the fluctuating field varies (v) is large (i.e. $v/a \geq 20$). Taking a spatial average of equation (3.33) produces the root-exponential shape that has been successful in characterizing spin glass materials and, when $\mathbf{B}_{ext} = 0$, has the form

$$G(t) = \exp\left(-\sqrt{\frac{4a^2}{v}} t\right) \quad (3.34)$$

When \mathbf{B}_{ext} is applied with $\theta = 0^\circ$ (i.e. longitudinal field; $\mathbf{B}_{ext} \parallel \mathbf{S}_\mu(0)$), and one recalls $\omega_L = \gamma_\mu B$, the relaxation function for these dilute alloy spin glasses work out to be of the form

$$G(t, \Delta, v) = \exp\left(-\frac{2\Delta^2 v}{v^2 + \omega_L^2}\right) \quad (3.35)$$

From here, one can extract that in general, the inverse relation of relaxation rate to fluctuation rate

$$\lambda \sim \frac{4a^2}{\nu} \sim \frac{2\Delta_i^2}{\nu} \quad (3.36)$$

In general, a Lorentzian distribution is much better suited than the Gaussian counterpart for describing the physical system where the stopping sites of the muon vastly differ from one another and neighboring moments are spatially far apart. For a dilute electronic spin system that produces a local field with a $1/r^3$ dependence, a Lorentzian distribution shape fits quite well.

If the thermalized muon captures an electron forming the experimentally accessible hydrogen analog, labeled muonium ($\text{Mu}^0 = \mu^+e^-$), in a semiconductor, then the \mathbf{B}_{hyp} term becomes important in equation (3.14). For isotropic muonium (for a thorough treatment see e.g. [60,65,66]), the electron Zeeman splitting is the largest term in the spin Hamiltonian. The two levels are e^- spin up and e^- spin down. The muon Zeeman interaction introduces an additional splitting of the e^- levels that is dependent on whether the e^- and μ^+ spins are aligned parallel or antiparallel. The transition rate between these two states is the hyperfine constant (A) and shows in the spin polarization spectra as an oscillating signal with either

$$f_{e\uparrow} = \omega_\mu - \frac{A}{2} \quad (3.37)$$

or

$$f_{e\downarrow} = \omega_\mu + \frac{A}{2} \quad (3.38)$$

Where, in the high field limit ($\omega_e \gg A$) these frequencies (f_e) relate to the two muon spin-flip transitions that have $\Delta m_s = 0$. The measured μ^+ precession frequency (ω_μ) is extracted directly from the spectra. Similarly for the hyperfine constant, where

$$A = f_{e\uparrow} - f_{e\downarrow} \quad (3.39)$$

and the transition frequency for each e^- state (f_e) is also directly measured from the spectra. A schematic of this is shown in Figure 3.7. One can work out the eigenvalues for these possible configurations including the field dependence of these energy levels

and transition frequencies (i.e. solve the Breit–Rabi Hamiltonian, governing the μ^+e^- spin system; e.g. [65,66]). For a Mu^0 atom sitting in a tetrahedrally coordinated center, as an example, a plot of these values are shown in Figure 3.8.

The topic of muon spin polarization functions is quite broad and continually developing to keep up with the experimental work on the wide variety of materials currently under study. Explanations with additional details as to how these are developed for particular systems or in general is beyond the scope of this project. For more than the very brief summary of the few relevant functions supplied here, I refer the reader to any number of the already cited MuSR text books and other literature (e.g. [60,59,62,63], etc).

Typical detector arrangements for use with TF–, LF– and ZF–MuSR measurements are pictured in Figure 3.9. In the two–detector configuration, use of detectors labeled 1 and 2 (c.f. equations (3.6) to (3.13)) are as straight forward as previously discussed. If $\beta = 1$, which is quite typical unless something goes seriously wrong with the scintillation detectors, then (3.13) can be re–written in the more visually friendly form

$$a(t) = \frac{N_1'(t) - \alpha N_2'(t)}{N_1'(t) + \alpha N_2'(t)} \quad (3.40)$$

where N_i' represents the i^{th} detector having already subtracted the beam–borne background counts (c.f. (3.7)). The four–detector configuration has the distinct advantage of being able to track the direction of muon spin rotation in addition to doubling the angular resolution. To process the count information and return an asymmetry, asymmetry calculations (e.g. equation (3.40)) are performed for the two sets of counters, $\{1,3\}$ and $\{2,4\}$ and saved as two separate spectra.

This project uses transverse field muon spin rotation (TF–MuSR), longitudinal field (LF–) and zero field (ZF–) muon spin relaxation to progress towards the goal of characterizing the μ^+ behavior and magnetism within the Mn doped II–IV–V₂ chalcopyrite semiconductors.

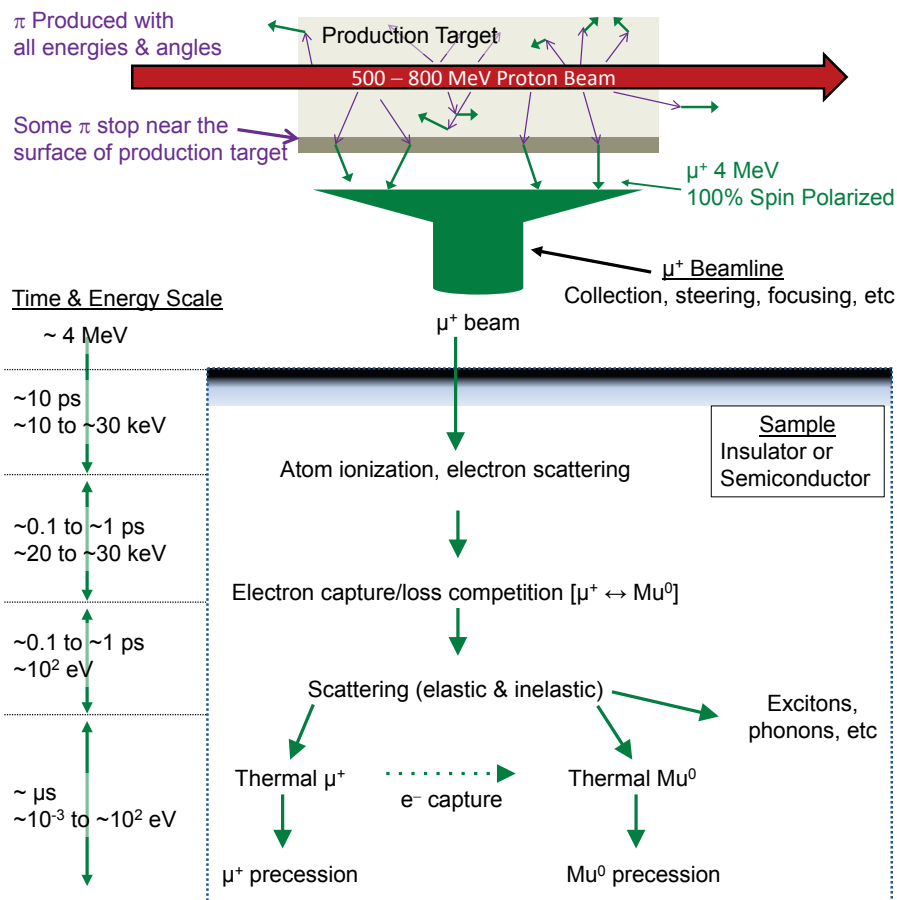


Figure 3.1: Muon production and implantation

Diagram depicting the main process of muon production from the initial proton beam and target interaction to the μ^+ implantation into an insulating or semiconducting sample. Typical time and energy scales are indicated for the process after implantation [57,67].

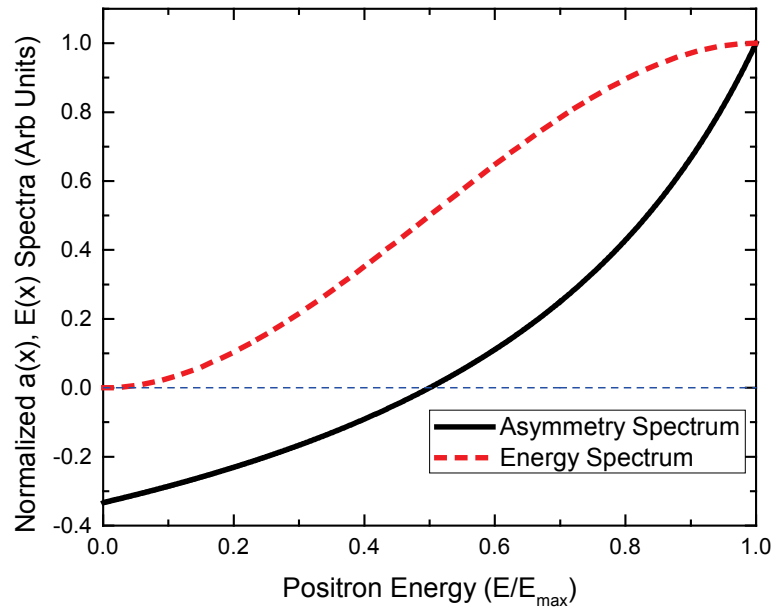


Figure 3.2: Positron emission energy and asymmetry spectra

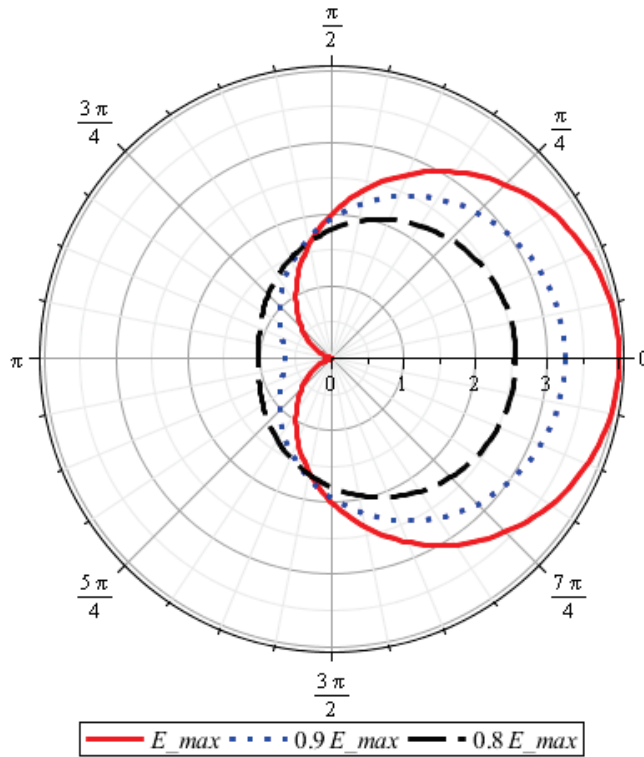


Figure 3.3: Angular distribution of positron emission

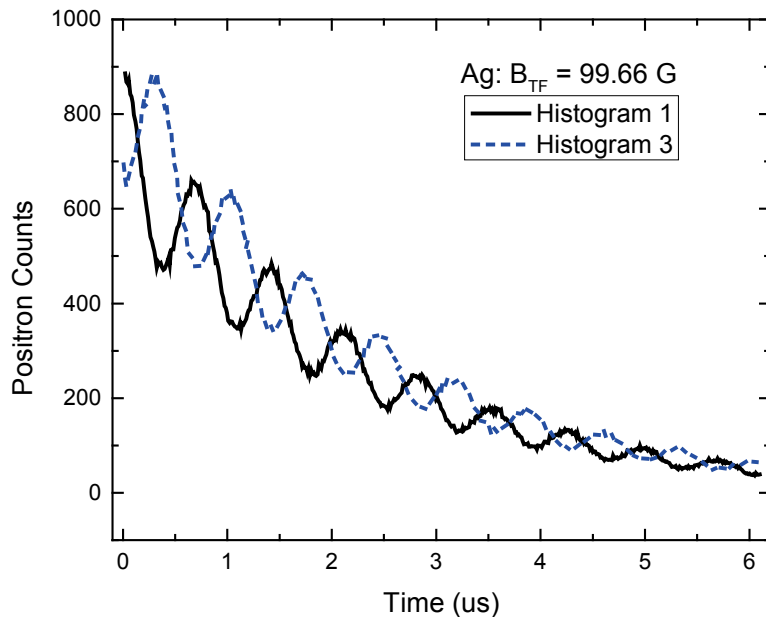


Figure 3.4: Positron counts on individual histograms

The above shows the positron counts per histogram for the front (histogram 1, solid black line) and back (histogram 3, dashed blue line) in a piece of silver at room temperature at an applied transverse field of $B_{\text{ext}} = 99.66$ G. [68]

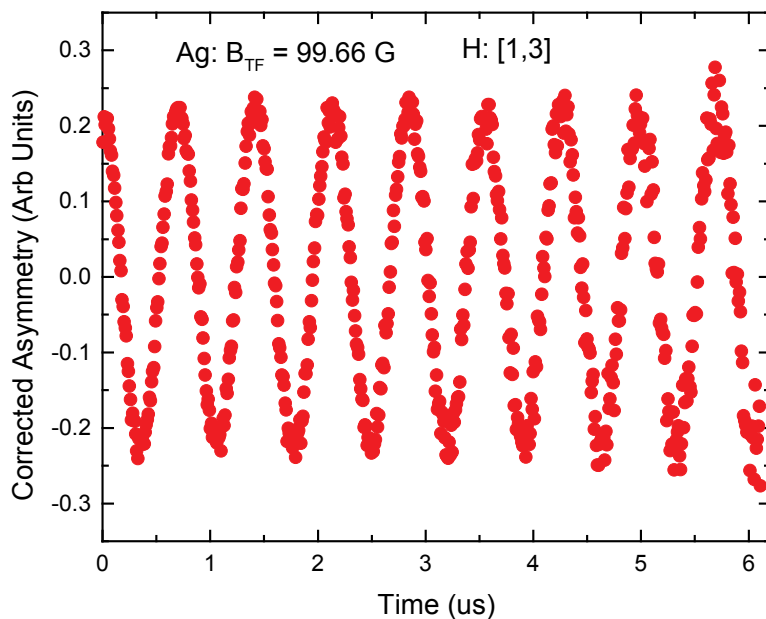


Figure 3.5: Corrected Asymmetry

Data from Figure 3.4, processed with equation (3.7).

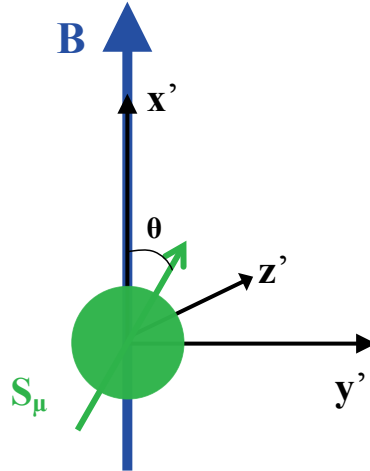


Figure 3.6: Coordinate system for muon spin

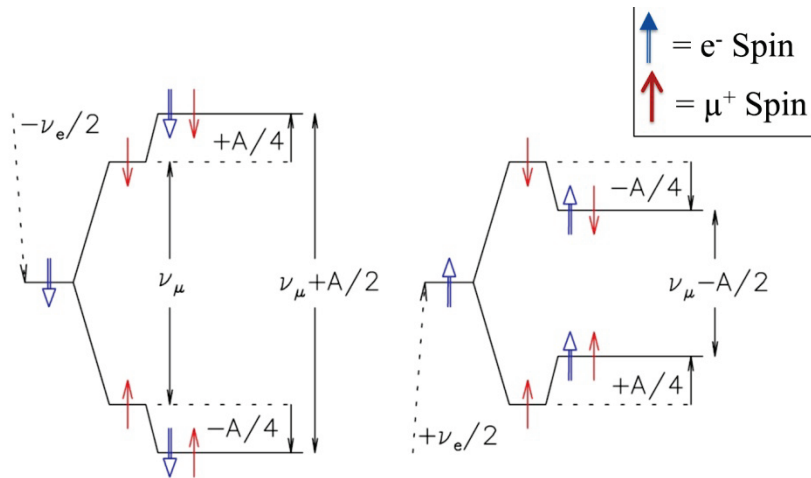


Figure 3.7: Mu^0 states

This cartoon [69] depicts an energy level diagram for the largest term in the spin Hamiltonian [electron Zeeman splitting] for Mu^0 in a high transverse field.

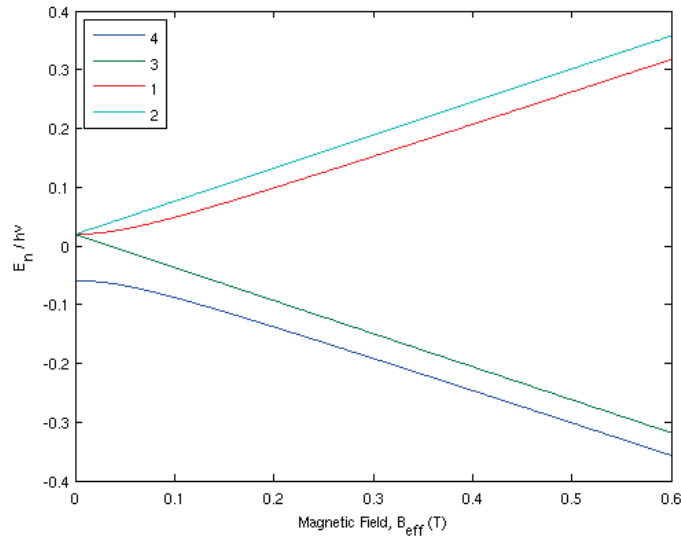


Figure 3.8: Breit-Rabi diagram for isotropic Mu^0

This depicts the energy level splitting with an applied field for a Mu^0 in a tetrahedrally coordinated site [65], with hyperfine constant $A = 1965$ MHz; which is the value determined for ZnGeP_2 (i.e. section 5.1.1). Each line depicts the energy level for a possible state as a function of field.

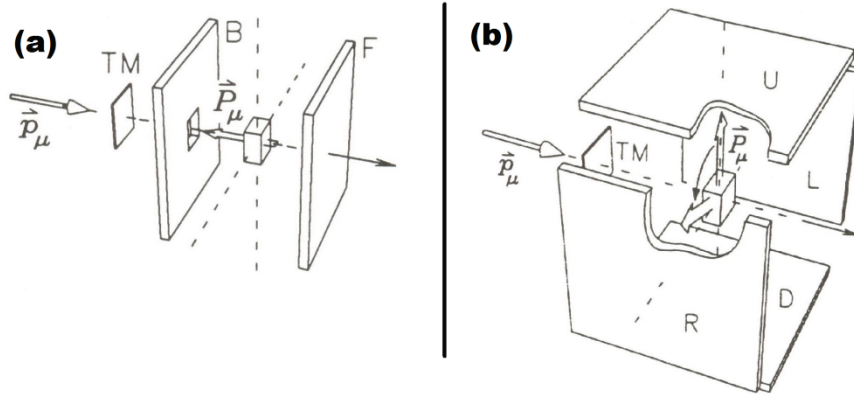


Figure 3.9: Typical MuSR detector configurations

Detector configurations [57] for typical muon spin relaxation and rotation experiments consisting of 2 and 4 detectors (a) and (b), respectively. In real application, these detectors (F, B, U, R, D or L) may be replaced with a large array of individual physical detectors, but each array is consolidated into a group with the {F, B, U, R, D or L} designation so these diagrams as a qualitative picture, are still applicable. In this paper, the {U, R, D, L} detectors are referred to as {1,2,3,4}.

3.1.2. Transverse Field μ SR (TF- μ SR)

Transverse field muon spin rotation describes the configuration where an external magnetic field (\mathbf{B}_{ext}) is applied in a direction perpendicular to the incoming muon spin polarization (i.e. $\theta = 90^\circ$) and the resulting Larmor precession (of the muon spin) about \mathbf{B}_{loc} is typically followed with a set of four detectors similar to schematic in Figure 3.9 (b). One way to obtain the transverse field orientation involves designing the magnet and detector configuration such that \mathbf{B}_{ext} is perpendicular to \mathbf{S}_μ without requiring any additional modification to the beam. The alternative method is to use a Wien filter (applies perpendicular $\vec{\mathbf{E}}$ and $\vec{\mathbf{B}}$ fields) further up the beamline so that in addition to cleaning the unwanted particles out of the beam one rotates the muon such that the \mathbf{S}_μ maintains the desired orientation upon implantation.

The four parameters of interest in a typical TF- μ SR study are frequency, asymmetry, relaxation and phase. The precession frequency (ω_μ) is a direct measure of \mathbf{B}_{loc} since $\gamma_\mu = 135.54$ MHz/T is well known, as is the Larmor relation

$$\omega_\mu = \gamma_\mu \mathbf{B}_{\text{loc}} \quad (3.41)$$

where \mathbf{B}_{loc} is the field at the muon site as described by equation (3.14). The asymmetry (amplitude) is a measure of signal intensity which is directly correlated to the probability of a muon entering a particular state – be it relative site population, μ^+ versus μ^0 fraction or even a measure of the fraction of material in a magnetic state. The relaxation rate parameter characterizes the way in which the measured oscillating signal is damped. Phase refers to the apparent initial shift of the μ^+ precession within the spectra. For very low frequency oscillations (i.e. $\mathbf{B}_{\text{loc}} < 100$ G or $\omega_\mu < 1.3554$ MHz) or spectra that contain only one or two components with sufficiently different frequencies, one can analyze time domain data relatively easily. Higher frequencies or more complicated spectra give rise to the need for a different way of analyzing the data. One way to deal with the higher frequency data is to utilize Fourier analysis to convert the time-domain data to frequency-domain. Another technique frequently utilized involves using a discrete rotating reference frame within the time-domain [70]. The rotating reference frame is a transformation from the lab frame to a rotating

observation point by subtracting the frequency of the rotating observation frame from the raw data and then repacking the processed data points to display in a time domain. Utilizing this rotating reference frame greatly improves the ability to resolve multiple high frequencies in the time domain.

A very useful application of the TF–MuSR technique is that of the ability to measure the local field with unmatched sensitivity. One can determine the magnitude of the local field by either running without an externally applied field (i.e. $\mathbf{B}_{\text{ext}} = 0$) or measure the field at the sample with the same probe one measures the field in the sample. We often choose to setup the latter by using a reference sample (CaCO_2) mounted behind the sample and a scintillator cube so that the experiment can distinguish between muons that enter the sample and those that enter the reference sample. The positron count data from the μ^+ that enter the reference sample are recorded exactly the same as the data from the sample except that they are stored in a second set of histograms. By analyzing the data set from the reference sample and comparing it to the data from the sample of interest, one can attribute nearly any shift in the internal field as to being from within the sample where the μ^+ acts as a local magnetometer. For example, Figure 2.2 is a simultaneous display of the reference spectra with the sample spectra where one can clearly see that the μ^+ signal from the spectra related to the sample is shifted from that of the reference μ^+ line thereby indicating a distinct and significant \mathbf{B}_{loc} .

Another application of the TF–MuSR technique involves identifying and characterizing Mu^0 and Mu^0 like [65,60,69,71,72,73] centers. The extreme sensitivity to local magnetic fields allow the μ^+ to probe the vortex states, magnetic penetration depth and correlation lengths within superconductors [74], local fields, electronic structure, ordering and nuclear spin dynamics. One can also study the diffusive properties of μ^+ and Mu^0 [75], which is analogous to ionic H^+ and atomic H diffusion in metals and non metals, respectively.

3.1.3. Longitudinal Field μ SR (LF- μ SR)

Longitudinal field muon spin relaxation describes the configuration where an external magnetic field (\mathbf{B}_{ext}) is applied in a direction parallel to the incoming muon spin polarization (i.e. $\theta = 0^\circ$) where time evolution of the spin polarization function in \mathbf{B}_{loc} is typically followed with a pair of counters similar to the schematic in Figure 3.9(a). Relaxation in LF- μ SR is typically caused by dynamic processes since, with the exception of some magnetic systems, \mathbf{B}_{loc} is aligned parallel with the incoming spin and therefore there is no precession and so one uses the μ^+ (probe) dephasing information from the data to understand the system. If \mathbf{B}_{ext} is significantly larger than \mathbf{B}_{hyp} and \mathbf{B}_{dip} then the relaxation processes tend to be Lorentzian in nature since the hyperfine and dipolar fields are decoupled [76] from the muon. In the case of a system where \mathbf{B}_{loc} contains a component that is not parallel to the incoming muon spin polarization, there will be precession in the local field that will ideally appear as an oscillation in the collected spectra.

Since LF data only utilizes two counters do not typically contain precession, one must calibrate the spectra by determining the appropriate value for α (c.f. equation (3.40)). Typically one utilizes a weak transverse field ($\mathbf{B}_{\text{ext}} \leq 100$ G) to force μ^+ precession and then adjusts the α parameter so that this induced precession is centered around zero asymmetry corresponding to balancing the front and back detector asymmetry. In an ideal setup where $\alpha = 1$, a sample would be perfectly centered in the sample space and the front and back detectors would be identical. Since in a real experimental configuration this symmetry is very difficult to achieve, this correction can be easily made during the analysis to balance (or weight) the asymmetry from each detector as to not distort the final asymmetry. The so-called corrected asymmetry refers to the data that has this α parameter set properly.

LF- μ SR can measure local field fluctuation rates, muonium transition rates (site to site or charge cycles), strength of nuclear and electronic coupling of the μ^+ to its local environment [77,78,79].

3.1.4. Zero Field μ SR (ZF- μ SR)

In zero field muon spin relaxation measurements, the experiment is configured such that the measured magnetic field at the sample site is zero (i.e. $\mathbf{B}_{\text{ext}} = 0$). Some ZF- μ SR setups have active ZF correction capabilities where field measurements are constantly monitored during an experiment and a series of coils are responsible for maintaining as close to zero applied field as possible. The detector configuration can be identical to either the 2 or 4 detector configuration described for LF- and TF- μ SR measurements, respectively. The choice in configuration is dictated by what one is looking to measure. If interest lies in measuring the field strength within an ordered magnetic phase, the TF-like arrangement may be preferred. However, typically a 2-detector arrangement, identical to the LF setup, is used. ZF studies excel in the ability to look at what μ^+ (or Mu^0) does in a material, measure \mathbf{B}_{loc} and characterize any dynamics that result from either μ^+ (or Mu^0) moving between sites, or fluctuations in \mathbf{B}_{loc} itself [62,80].

3.2. MUON FACILITIES AND APPARATUS

There are currently four facilities in the world that operate μ SR beamlines. The two that have been used for this work are TRIUMF (Vancouver, Canada) and STFC ISIS (Didcot, UK). Both use proton beam passing through a primary target to produce surface pions and the subsequent muons. The main difference lies in TRIUMF is a cyclotron that provides a near continuous 500 MeV ($\sim 100 - 140 \mu\text{A}$) beam of protons to the target opposed to the pair of 800 MeV (200 μA) 100 ns proton pulses, delivered at 50 Hz by the synchrotron at ISIS. While the continuous wave source at TRIUMF allows for data collection involving a single muon at a time and hence the capability of measuring very high precession frequencies and relaxation rates (with the appropriate spectrometer, of course) but at the expense of having a constant beam borne background present in the data. On the other hand, the ISIS pulsed source, delivers bunches (several thousand per bunch) of muons with a finite pulse width and so that after implantation, there is virtually no beam-borne

background but the finite bunch size imposes an intrinsic limit on the precession frequencies and relaxation rates that one can measure.

3.2.1. *TRIUMF*

The surface muon beamlines at TRIUMF used in this project are designated as *M15* and *M20*. Both can be configured for TF or LF modes and can accept the same series of spectrometers. The few differences between the beamlines are not relevant to the measurements related to this project. TF–MuSR measurements were completed using a combination of the *Belle*, *HiTime* and *HELIOS* spectrometers through different beam scheduling periods. The LF measurements completed at TRIUMF utilized *HELIOS*. *Belle* is a superconducting Helmholtz coil magnet, specifically designed for high transverse field measurements with a maximum field of 7.5 T. *HiTime* is a high field (superconducting split pair magnet) and high frequency spectrometer that replaced *Belle* and is capable of high transverse field or high longitudinal field measurements with applied fields up to 7.0 T. Sample sizes are limited to 10 mm x 10 mm x ~25 mm due to the close proximity of the detectors as required to maximize the angular resolution and minimize the effects high magnetic fields have on positrons. The sample and detector arrangement used for both *Belle* and *HiTime* is pictured in Figure 3.10. When used with the He flow cryostat, the normal operating temperature range is from ~2 K to 300 K. The high temperature limit is restricted by the plastic scintillators and light guides in the sample insert. *Helios* is a superconducting solenoid capable of applying a 6 T magnetic field across the sample space. He flow cryostat or a horizontal oven were used allowing a wide temperature range of ~2 K to upwards of 800 K. *Helios* can be used in either the LF, TF or ZF mode. While it does not contain an active ZF correction apparatus, some provisions are available to take a static measurement of the field in the sample space and manually adjust the correction field, as needed and desired. The frequency resolution in the TF mode is not nearly as good as *HiTime* as the distance from the sample to detectors is much greater but since the detectors are outside the sample space, one is not limited to 300 K.

Additional information regarding the available instruments and beamlines can be found at <http://musr.ca> or <http://www.triumf.ca>. Figure 3.11 is a schematic of the beamline relevant to the MuSR studies at TRIUMF.

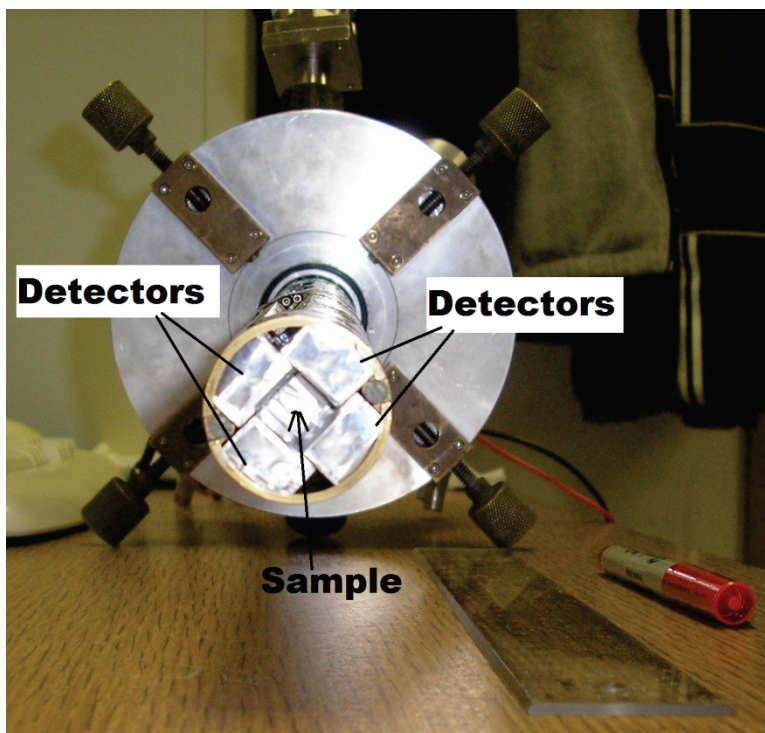


Figure 3.10: HiTime and Belle sample mounting and detector configuration

Four scintillators surround the sample which is mounted on top of an additional scintillator cube that is used to veto the positrons from muons that miss the sample and instead hit this cube. When used with a CaCO_2 reference counter, the fifth scintillator cube is replaced with an identical cube containing a thin layer of CaCO_2 behind the active part of the scintillator. This is used to trigger the timing circuitry such that a count that misses the sample but hits this reference sample will be tallied in a secondary set of histograms. This sample insert is specifically for Belle and HiTime. This picture is taken from the perspective of the incoming muons.

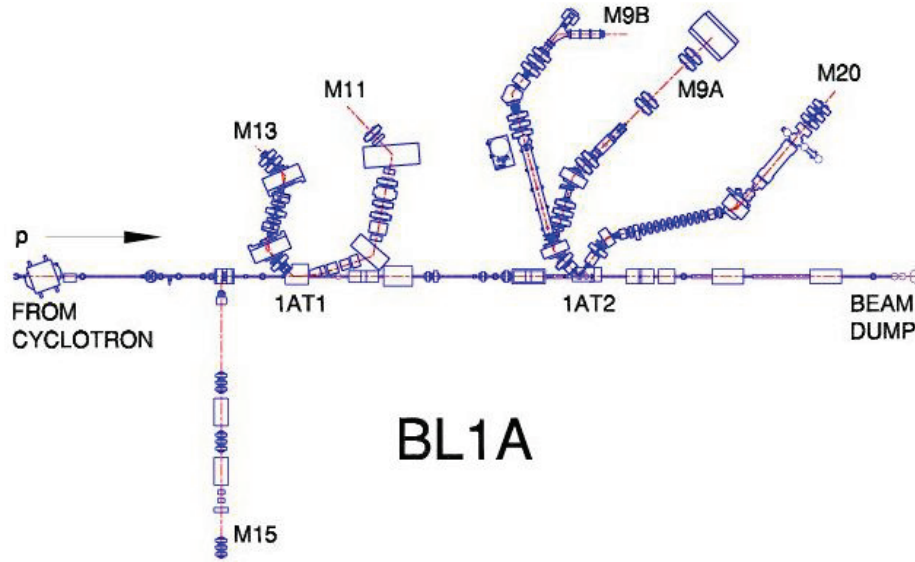


Figure 3.11: TRIUMF beamline 1A

This schematic, which was current as of 2010, shows the beamline used for muon production at TRIUMF (Vancouver, CA) [81]. The surface muon channels used at TRIUMF in this study are M15 and M20.

3.2.2. *ISIS*

The muon beamline at ISIS has three instruments permanently setup to use the muon pulse from the primary target, two of which are used for this project. Figure 3.12 is a sketch of the beamline configuration. *EMU* is a spectrometer configured with the basic 2–detector configuration but in reality uses a series of 96 scintillation counters; 48 counters constitute each front and back counter. This instrument is ideal for LF– and ZF– measurements as the pulsed source is inherently low background and is equipped with active ZF correction capabilities. The measurable temperature and fields range from 50 mK to 1500 K and 0 to 0.45 T, respectively. *HiFi* is a high field muon spectrometer that can be configured to function in the LF and ZF modes with the typical 2–detector configuration where a 32 counter array (64 total) constitutes the front and back counters. HiFi has an operational field (superconducting magnet) and temperature range of 0 to 5 T and 30 mK to 1500 K. HiFi is also configured with the active ZF correction coils. Figure 3.13 shows the design drawing for HiFi. EMU is similar in design where the differences reside in number of channels per detector array, magnet and details of the sample environment.

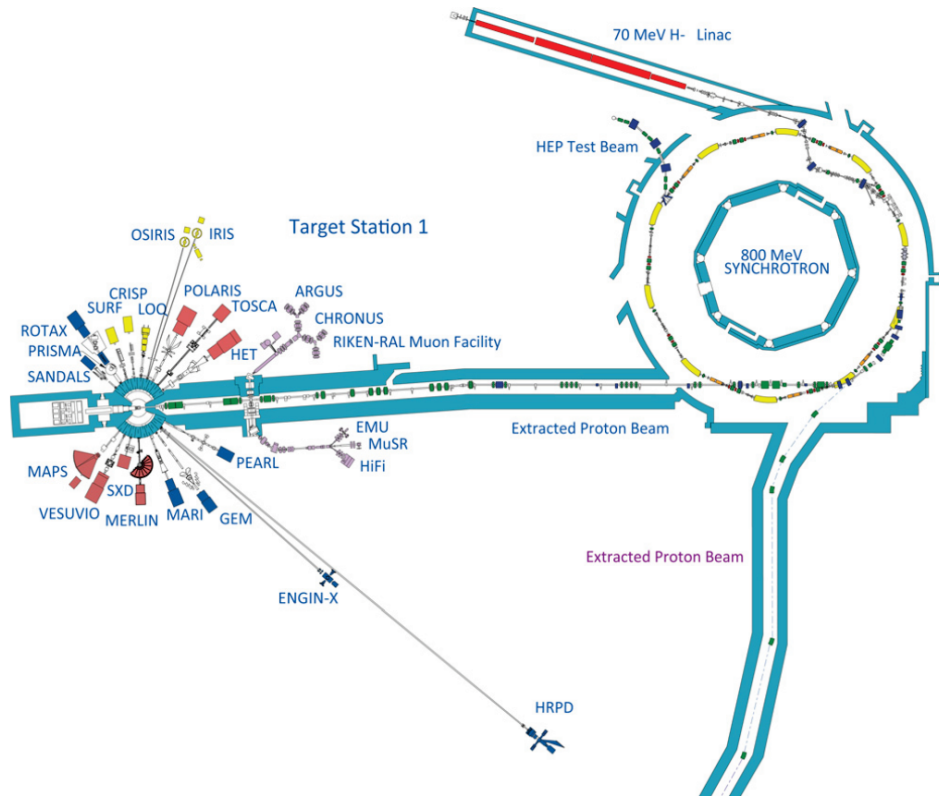


Figure 3.12: ISIS schematic with TS1 and associated beamlines [82]

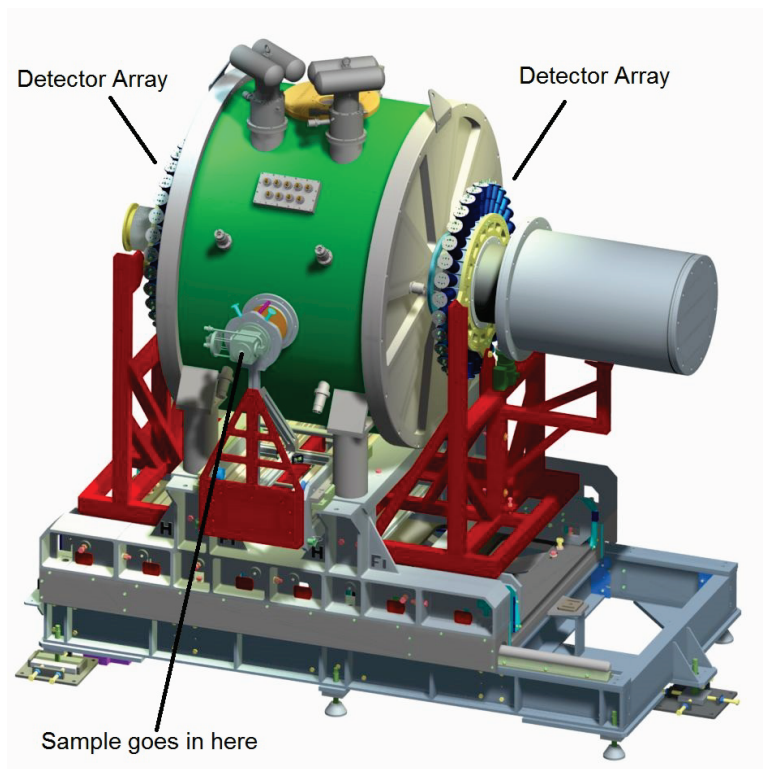


Figure 3.13: HiFi spectrometer, design drawing [83]

The HiFi spectrometer is configured with the 2-detector configuration where each detector array consists of 32 channels. The EMU spectrometer has a similar qualitative layout but with a total of 48 channels per array.

3.3. SQUID SUSCEPTOMETRY

Quantum Design commercially produces superconducting quantum interference (SQUID) based susceptometers designed to measure very small magnetic fields via variations in the current between two parallel Josephson junctions [84]. That is, two superconductors are separated by a thin insulating layer, through which Cooper pairs can tunnel, and the current within the loop is proportional to the phase shift of the wavefunctions. In a DC SQUID susceptometer, a pair of these junctions are configured with opposite polarity so that the magnetic field produced within the current carrying loops are actively canceled. A magnetic sample is then lowered at a fixed rate through these loops and the time varying magnetic field (as seen by the superconducting loops) disrupts the existing current in these loops and the resulting variation in voltage (detected via phase shifts) are measured, from which one can determine the magnitude of the magnetic field produced by the sample. In practice, it is often more practical to use a pickup coil through which one lowers the magnetic material that is then electrically connected to the superconducting detection loop where the standing current is disrupted by the induced current (from the time varying magnetic field passing through the pickup coils). Figure 3.14 shows the typical pick-up coil configuration for a DC SQUID Susceptometer. The Quantum Design DC SQUID Susceptometer used in this study (Michigan State University, Department of Physics and Astronomy, East Lansing, MI, USA) has a temperature and magnetic field range of 2 K to 350 K and ± 1 T and the capability to resolve magnetic moments as small as 10^{-8} emu.

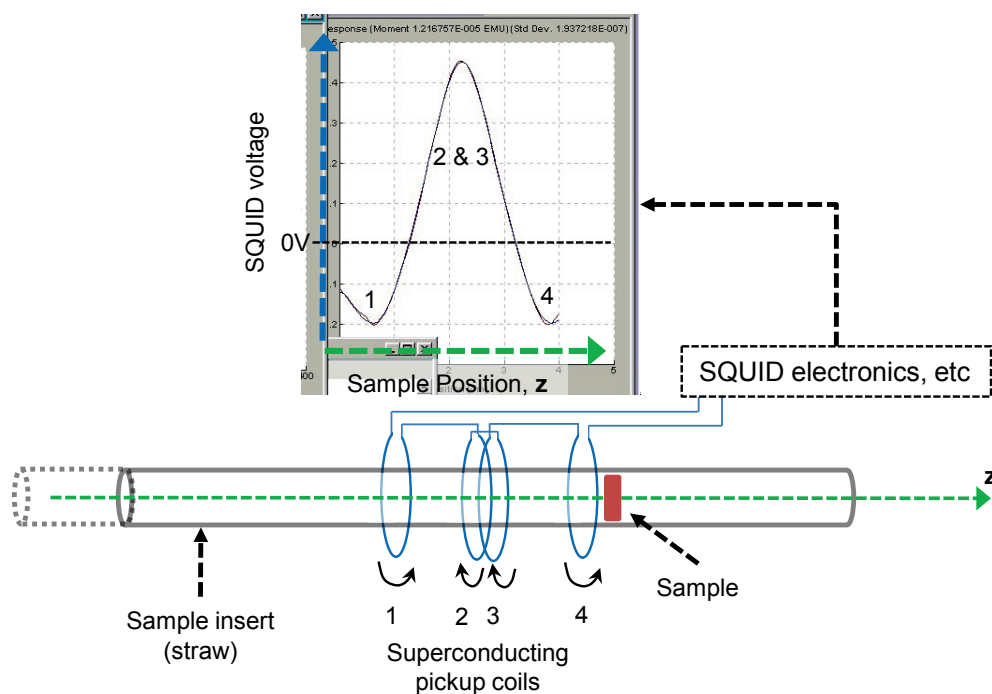


Figure 3.14: SQUID diagram

The sample passes through the pickup coils at a specified temperature and given field. The distance between coil 1 and 4 for the apparatus used in this study is approximately 3.5 cm. The pictured SQUID voltage versus sample position plot is a screen shot from a measurement on $\text{ZnGeP}_2\text{:Mn}$ [CC], showing a typical display of the raw data, as collected by the instrument. The software was configured to fit these curve and output the measured moment based on stored calibration data for each field and temperature point. Note the direction in which the wire is wound is opposite for the inner and outer pair which allows for an active background canceling and hence a more sensitive measurement. The magnetic field is typically applied along the z axis but can be configured to the user specifications.

3.4. ALTERNATING GRADIENT MAGNETOMETRY

Princeton Measurements produces an alternating gradient magnetometer (AGM) designed to perform bulk measurements on small samples [85,86]. The sample is mounted on the end of a transducer probe (with a piezoelectric element) that is then suspended in the center of an electromagnet. A DC field is applied with a small, well characterized, AC field gradient imposed on top of the existing DC field where the resulting deflection of the probe (i.e. force on the probe, F) is directly proportional to the magnetic moment of the sample.

$$F_z = m_z B_z \frac{dB_z}{dz} \quad (3.42)$$

The measured force calibration curve is established by initially measuring a well known and characterized reference material.

The AGM used in this study is a Princeton Measurements (LakeShore) MicroMag AGM 2900 with field capabilities of ± 1.5 T and a sensitivity range of 1 μ emu to 5 emu. Figure 3.15 and Figure 3.16 shows the AGM and transducer probe used in this study. The reference material is a 2.778 mg yttrium iron garnet sphere, provided by Princeton Measurements, where the magnetic moment is reported (by NIST) to be 76.67 memu.

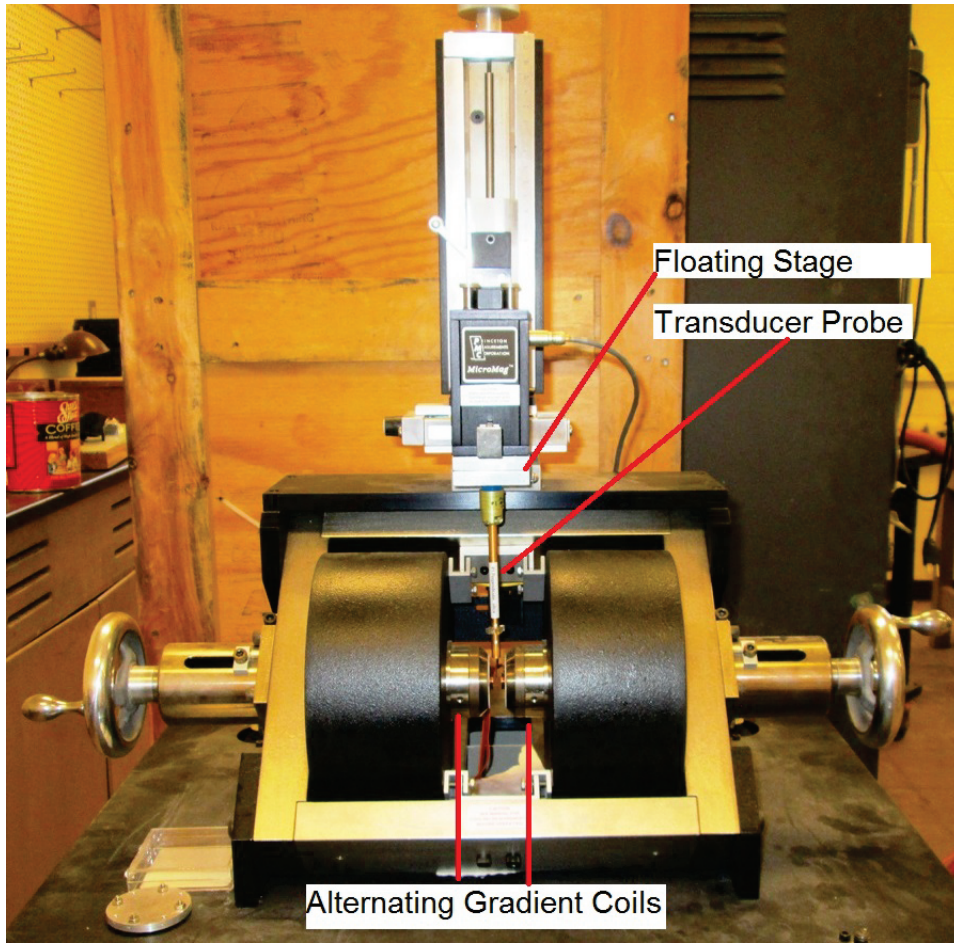


Figure 3.15: AGM

This Micromag 2900 alternating gradient magnetometer is made by Princeton Measurements (now part of LakeShore) and housed in the TTU Physics building.

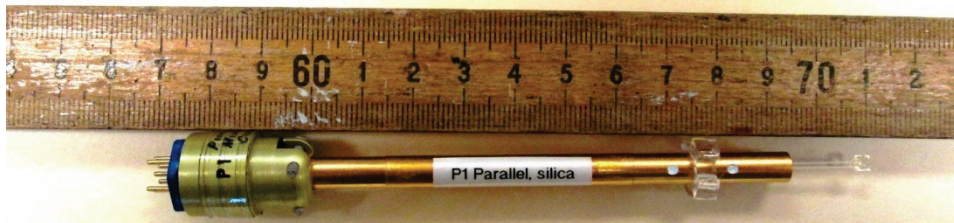


Figure 3.16: AGM Transducer probe

This probe is attached to the base of the floating stage on the AGM head. The sample is mounted on the clear glass square (under the 71cm mark) with a small dab of vacuum grease. Two sample orientations are possible where the glass plate is parallel or perpendicular to the applied magnetic field.

3.5. NEUTRON STUDIES

Research with thermal neutrons ($\gamma_n = 2\pi \times 29.16 \text{ MHz/T}$) involves passing a beam of these electrically neutral spin 1/2 particles through a sample and detecting their position (or momentum) after leaving the sample. Neutrons interact with nuclear moments (strong force interaction) and unpaired electrons (dipole–dipole) and therefore can reveal atomic or magnetic structure information of a material. *Hot* neutrons have energies on the order of $\sim 100 \text{ meV}$ to $\sim 500 \text{ meV}$ and wavelengths on the order of 0.4 \AA to 1 \AA opposed to *cold* neutrons that have energies on the order of $\sim 0.1 \text{ meV}$ to $\sim 10 \text{ meV}$ and wavelengths from 4 \AA to 30 \AA . There are a wide variety of scattering techniques, the primary difference between them are related to the energy (and wavelengths) of incident neutrons, what features they are capable of efficiently probing and whether or not energy is transferred to the sample (inelastic) or not (elastic). Small angle scattering techniques are used to probe features on lengths scales of 10 \AA to 100 \AA . Diffraction techniques, on the other hand, are used to probe static and structure on the order of nuclei spacing. Neutrons are produced by either spallation (H^+ collision with target) or fission (Reactor based). There are a plethora of sources on the neutron scattering techniques available and I will direct the reader to references such as [87,88,89] for the additional information as these measurements served only a supporting role in this project and one only needs a fundamental understanding of the technique to grasp the relevance of the measurements.

The high flux isotope reactor (HFIR) at Oak Ridge National Laboratory (ORNL, Oak Ridge, TN, USA) is an enriched U^{235} reactor based neutron source. Figure 3.17 shows the HFIR facility layout and location of the instruments.

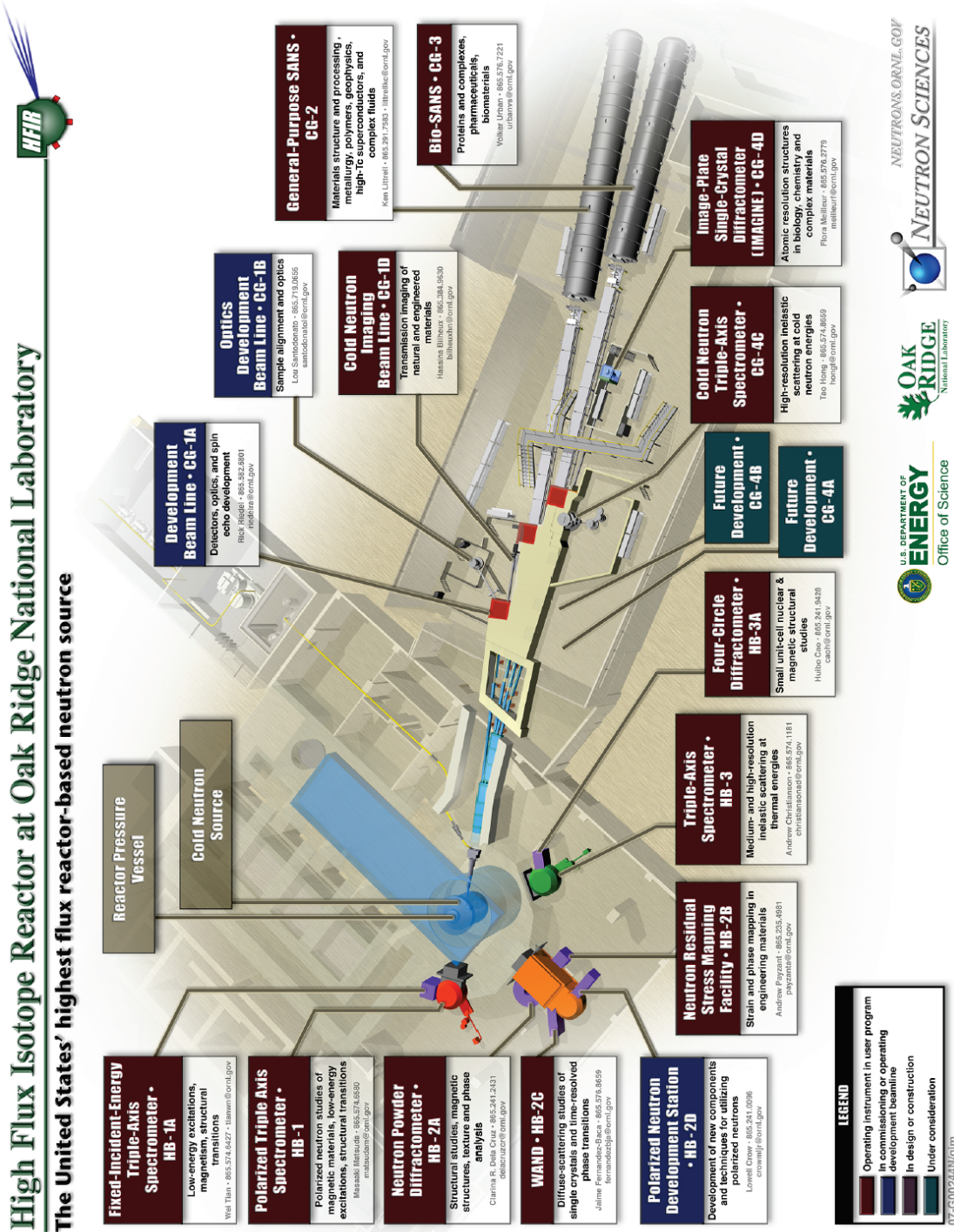


Figure 3.17: HFIR beamline and instrument layout [90]

3.5.1. Triple Axis Diffractometry (PTAX: HB-1)

The polarized triple axis spectrometer (PTAX) on the HB-1 beamline on HFIR at ORNL is configured to utilize thermal neutrons with an energy range from 5 meV to 120 meV. A schematic sketch of the instrument is shown in Figure 3.18. The available sample environments include $^4\text{He}/^3\text{He}$ dilution refrigerator, He flow cryostats and a cryofurnace providing an overall approximate range of 50 mK to well above 500 K. The sample can be rotated a full 360° on the mount while the scattering and analyzer angles can be varied from -90° to 120° and -40° to 140° , respectively. With the shorter wavelength probe, the PTAX system is well suited for investigating features such as spin waves in ordered magnets; excitations in low-dimensional itinerate magnets; excitations (spin and lattice) in high- T_c superconductors, colossal magnetoresistive compounds; spin density distributions in magnetic compounds and phonon dispersion curves in alloys. While specified as a polarized system, the polarized mode has yet to function as such. [91]

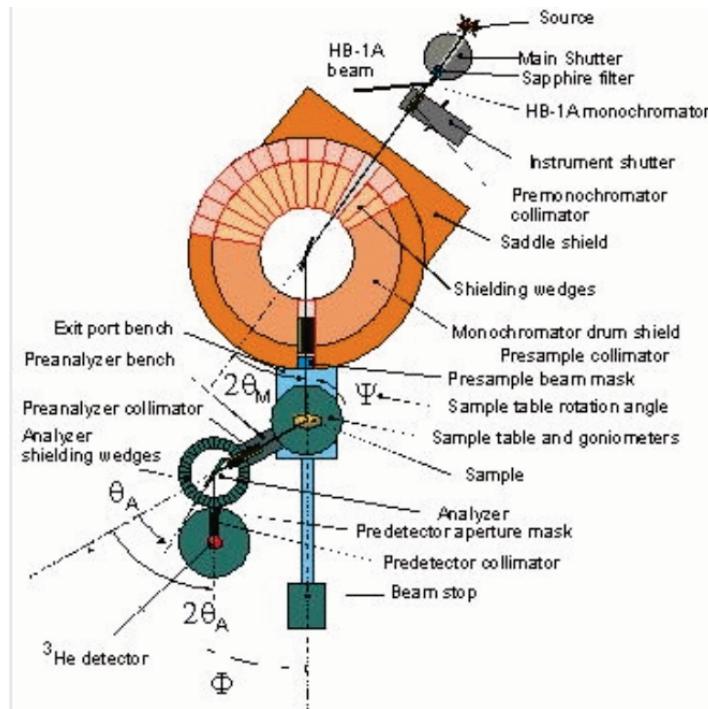


Figure 3.18: HB-1 diagram [90]

3.5.2. Magnetic Small Angle Neutron Scattering (GP-SANS: CG-2):

The general purpose small angle neutron diffractometer (GP-SANS) on the CG-2 beamline on HFIR at ORNL is configured to probe structural and magnetic features within the size range of 5 Å to 2000 Å as the available neutron wavelengths are between 5 Å and 30 Å and range of sample-to-detector distance of 1 m to 20 m. The sample environments range from cryomagnets, furnaces and mechanical load devices allowing for a variety of possible experiments. Some applications in soft condensed matter applications are molecular self assembly and interactions in complex fluids; order in glassy systems; polymer solutions and colloids. More closely related to this project are the applications in hard condensed matter and magnetic systems. Examples of these are phase separation, nanocomposites, orientation in metallurgical alloys, flux lattices in superconductors, ferrofluids and the relationship between structural and magnetic domains and ordering [92]. A schematic sketch of the CG-2 instrument is shown in Figure 3.19.

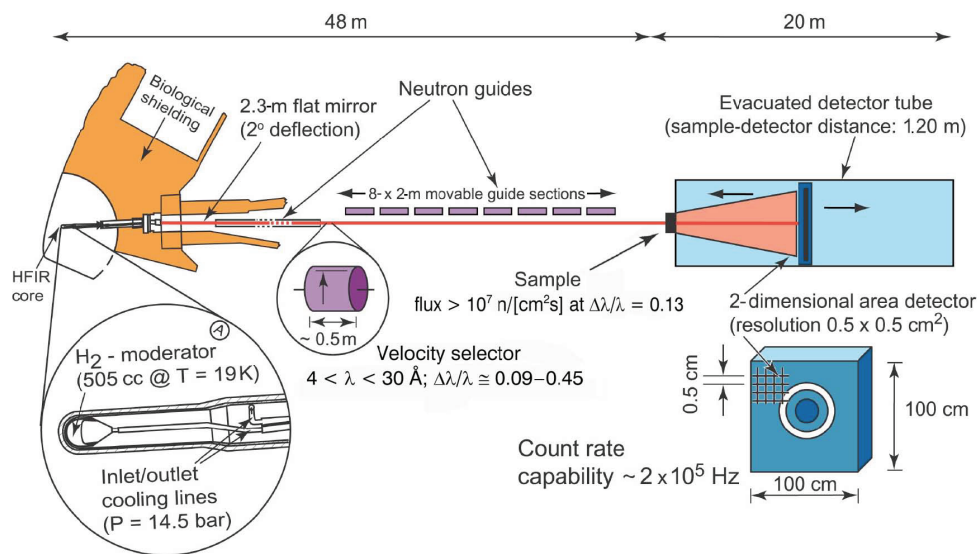


Figure 3.19: CG-2 diagram [90]

CHAPTER 4: EXPERIMENTAL DETAILS

4.1. SAMPLES

BAE Systems (Nashua, NH, USA) provided one *n*-type ZnGeP₂ single crystal (8 x 8 x 1 mm³) sample, an *n*-type CdGeAs₂ single crystal sample (8 x 8 x 1 mm³) and six Mn enriched *p*-type ZnGeP₂ samples, each with a different Mn content and cut from the same boule grown by the horizontal gradient freeze technique from a melt starting with 1.6 % Mn. Four are single crystalline and two are large grain samples which all measure nominally 9 x 15 (± 2) x 1.1 mm³. The Mn enriched samples are labeled by letters *A* through *F*, in order of increasing Mn content but all below ~5 %. Table 4.1 outlines the basic properties and labels associated with the relevant samples. Additional information on this class of materials is in Table 2.1. Figure 4. through Figure 4.4 show a few of the samples used in this project.

Table 4.1: Samples

<i>Compound</i>	<i>Label</i>	<i>Dimension</i> [mm ³]	<i>Orientation</i>	<i>Type</i>	<i>Dist from</i> <i>Seed</i> [mm]
ZnGeP ₂	253 A	7.1 x 8.5 x 1.1	[001]	<i>n</i>	<i>n/a</i>
ZnGeP ₂ :Mn < 0.01 at%	141 Z	8 x 18.7 x 1.1	[001]	~ <i>p</i>	<i>n/a</i>
CdGeAs ₂		~8 x ~8 x ~1	[001]	<i>p</i>	<i>n/a</i>
ZnGeP ₂ :Mn	146 AA	7.5 x 17 x 1.5	[001]	<i>p</i>	6
ZnGeP ₂ :Mn	146 BB	7.5 x 17 x 2.2	[001]	<i>p</i>	8
ZnGeP ₂ :Mn	146 CC	9 x 13 x 1	[001]	<i>p</i>	52
ZnGeP ₂ :Mn	146 DD	9 x 13 x 1	Random	<i>p</i>	75
ZnGeP ₂ :Mn	146 EE	9 x 13 x 1	Random	<i>p</i>	95
ZnGeP ₂ :Mn	146 FF	9 x 13 x 1	Random	<i>p</i>	120

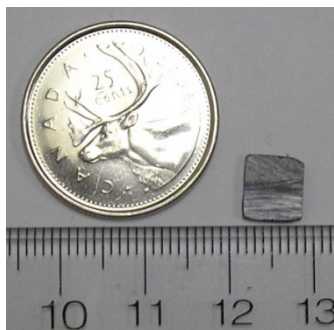


Figure 4.1: ZnGeP₂ – 253 A

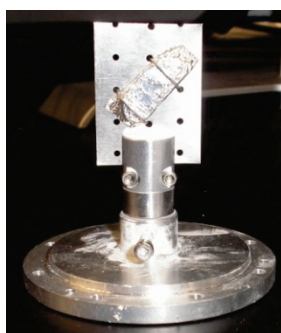


Figure 4.2: ZnGeP₂Mn – 146 BB

Left: Mounted on sample holder for HB-1 at ORNL (section 3.5.1); the sample is wrapped in aluminum foil (shown in *right* panel) and tied to an aluminum plate with aluminum wire to prevent movement and possible loss during measurement. The plate to which the sample is tied is approximately 25 mm x 34 mm.



Figure 4.3: ZnGeP₂:Mn – 146 CC

Sample is inserted into a standard sized drinking straw, placed at the end of the sample insert for use in the SQUID susceptometer (section 3.3).



Figure 4.4: $\text{ZnGeP}_2\text{:Mn}$ – 146 FF

Sample is mounted to the aluminum 'fly past' holder for *HiFi* and *EMU* at ISIS (section 3.2.2). Samples are typically affixed to the holder with a small dab of vacuum or grease (for thermal conductivity) wrapped with Al foil to hold the sample in place.

4.2. MUON SPIN ROTATION: TF–MUSR (HYPERFINE SPECTROSCOPY)

Transverse field muon spin rotation (TF–MuSR) measurements were performed with the *Belle*, *HiTime* and *Helios* spectrometers on the M15 and M20 surface muon channels at TRIUMF (described in section 3.2.1). A magnetic field is applied perpendicular to the initial spin polarization of the incoming 4 MeV 100 % spin polarized and positively charged muons. The main goals of these measurements include utilizing the similarities of μ^+ and Mu^0 to the proton (p^+) and hydrogen atom to explore the possible isolated hydrogen defect states in these materials. In addition to exploiting the large μ^+ magnetic moment to characterize the local magnetic fields (\mathbf{B}_{loc}). Recall that μ^+ precesses in the local environment at the Larmor frequency (equation (3.41): $\omega_{\mu} = -\gamma_{\mu} \mathbf{B}_{\text{loc}}$) which provides a *direct* measure for \mathbf{B}_{loc} at the site in which μ^+ resides. This type of measurement is not available by any other means.

Data were collected in fields ranging from 0.001 T to 7 T in temperatures ranging from 2 K to 564 K. The majority of TF measurements on the undoped ZnGeP_2 and CdGeAs_2 samples were completed at 4 T between 2 K and 310 K where on the doped samples fields of 0.01 T and 1.0 T in the same temperature range were utilized. For the Mn enriched samples, extra care was taken to use the same procedure for each sample. Specifically, all cooling was completed under zero applied field and when applying the magnetic field, all data were collected at the set field before increasing to the next higher desired field as to avoid unnecessary complications arising from hysteresis related effects. Data collected in *Belle* and *HiTime* were limited to 300 K and utilized the 4–counter arrangement (described in section 3.1.2) with and without the CaCO_2 reference counter for the Mn enriched and undoped samples, respectively. Additional data were collected via *Helios* configured in the TF mode in temperatures up to 564 K and comparable fields. Unfortunately, no reference sample arrangement is available in *Helios* and these measurements were geared towards a preliminary investigation of the line shapes and possible Mu^0 like species that may exist in $\text{ZnGeP}_2:\text{Mn}$.

4.3. MUON SPIN RELAXATION: LF– AND ZF– MUSR (DEPOLARIZATION)

Longitudinal field muon spin relaxation (LF–MuSR) data were collected with *Helios* on M20 at TRIUMF (3.2.1) as well as with the EMU and HiFi spectrometers on the muon beamline at the STFC ISIS facility (3.2.2). A magnetic field applied in a direction that is parallel to the initial spin polarization of the incoming 100% spin polarized μ^+ where the evolution of the time dependent muon polarization is sensitive to inhomogeneity in the local field, spin dynamics in the local environment, μ^+ (or Mu^0) diffusion throughout the system. In the case of Mu^0 diffusion, electron spin flips that occur with each subsequent hop, transfer back to the muon which cause dephasing due to the fluctuation in \mathbf{B}_{hyp} . The main goals for these measurements include further characterization of Mu^0 centers, μ^+ and Mu^0 mobility and characterize magnetic fluctuations and correlations throughout the system. Data were collected on the undoped *n*–type ZnGeP_2 sample in field and temperature ranges of 0 T to 0.45 T and 3 K to 600 K. Several magnetic field scans (Mu^0 decoupling curves) were completed, with EMU at ISIS, at a series of temperatures from 10 K to 250 K to study Mu^0 motion and further characterize the Mu^0 center. Zero applied field data on *p*–type CdGeAs_2 were collected over a temperature range of 8 K to 600 K on the EMU spectrometer at ISIS. A small subset of data were collected on the very weakly doped $\text{ZnGeP}_2:\text{Mn}$ sample on the *HiFi* spectrometer at ISIS with fields and temperatures ranging from ~ 0 to 1.9 T and ~ 3 K to 250 K. A series of preliminary field scans were completed to compare the weakly Mn doped ZnGeP_2 results with the undoped ZnGeP_2 results in order to determine the feasibility of utilizing μ^+ as a probe of the magnetic properties in the dilute $\text{ZnGeP}_2:\text{Mn}$ materials and to explore the properties of this very dilute material. Data collected on the *p*–type $\text{ZnGeP}_2:\text{Mn}$ samples were aimed at characterizing fluctuations and correlations in the local magnetic environment. Data were collected on four samples utilizing \mathbf{B}_{ext} from 0.01 to 4.0 T and a temperature range from 2 K to nearly 700 K. Detailed temperature scans were completed at $\mathbf{B}_{\text{ext}} = \{0.1, 0.375, 0.7 \text{ and } 1.5\}$ T. Detailed magnetic field scans were completed at various

temperatures below and above each transition ($T_{\text{AFM}} = 47 \text{ K}$; $T_{\text{FM}} \approx 320 \pm 10 \text{ K}$) and well into each phase.

4.4. BULK MAGNETIZATION

Initial room temperature and slightly cooled below room temperature Initial magnetization data were collected at room temperature ($T \approx 295 \pm 5 \text{ K}$) and slightly below room temperature ($T \approx 275 \pm 10 \text{ K}$) on $\text{ZnGeP}_2\text{:Mn}$, (146AA) utilizing a Princeton Instruments MicroMag 2900 Alternating Gradient Magnetometer (TTU Physics), to verify the room temperature FM phase. Multiple M vs H curves were produced with the maximum field range between $\pm 1.5 \text{ T}$. These data were collected to verify both the existence of a bulk magnetic phase in this sample and whether additional temperature dependence measurements would be warranted.

Detailed bulk magnetization data were collected from four $\text{ZnGeP}_2\text{:Mn}$ samples utilizing a Quantum Design SQUID DC Susceptometer at Michigan State University (Department of Physics and Astronomy, East Lansing, MI, USA). Detailed M vs T scans were completed at 0.01 T and 1.0 T with a temperature range of $\sim 5 \text{ K}$ to 400 K. Detailed M vs H scans were completed at $\{15, 80, 200, 280, 315, 350, 390\} \text{ K}$ with applied fields of -2.0 T to $+2.0 \text{ T}$.

4.5. TRIPLE AXIS NEUTRON SCATTERING

Triple axis neutron scattering measurements were performed with the polarized triple-axis spectrometer (PTAX), in the unpolarized mode, on the HB-1 beamline of the High Flux Isotope Reactor (HFIR) at Oak Ridge National Laboratory (ORNL, Oak Ridge, TN, USA) with the main goals of investigating the local magnetic structure and homogeneity of Mn substitution throughout the sample, specifically looking to identify phase separated complexes of MnP. These measurements were carried out in a temperature range of 10 K to 310 K and a large combination of sample and detector positional configurations.

4.6. MAGNETIC SMALL ANGLE NEUTRON SCATTERING

Magnetic small angle neutron scattering measurements were performed with the horizontal field cryomagnet and general purpose small angle neutron scattering diffractometer (GP-SANS) on the CG-2 beamline of the HFIR at ORNL with the goal of investigating these micro-scaled magnetic features by probing a different fluctuation and feature size regime than available via LF-MuSR measurements. Data were collected with a neutron wavelength of 6 ($\delta=0.15$) Å with detector distances of 1 m and 12 m from the 2.2mm thick ZnGeP₂:Mn sample (146BB). Data were collected in temperatures from 1.5 K to 300 K. zero applied field and 2.5 T applied perpendicular to the incident neutron beam were utilized.

CHAPTER 5: RESULTS AND DISCUSSION

5.1. MUON SPIN ROTATION: HYPERFINE SPECTROSCOPY (TF–MUSR)

5.1.1. $ZnGeP_2$

Fourier transforms of the time–domain TF spin precession data at $B_{\text{ext}} = 4$ T on the undoped single crystalline n –type $ZnGeP_2$ reveal three distinct frequencies at low temperatures. Temperature and magnetic field (B_{ext}) dependencies of these lines were followed with the *Belle* spectrometer (on M15 at TRIUMF) from 3 K to 300 K at 4 T and from 0.5 T to 7.0 T at 100 K, respectively. Similarly with the *HiTime* spectrometer (on M15 at TRIUMF) but with the temperature scan performed at 1.5 T and the accompanying field scan near 20 K. Figure 5. shows a sample Fast Fourier transform of the time–domain spectra (the observed signal from $ZnGeP_2$ at $T = 5$ K and $B_{\text{ext}} = 4.0$ T). Each spectra (at a particular temperature and field) were fit in the time–domain with a rotating reference frame set slightly below the μ^+ frequency. The spectra were fit best with a linear combination of three sinusoidal functions, each with a Lorentzian relaxing envelope function (c.f. equation (3.15))

$$P(t) = \sum_{n=1}^3 A_n \exp(-\lambda_n t) \cos(\omega_n t + \phi_n) \quad (5.1)$$

where the asymmetry (A_n), relaxation rate (λ_n), precession frequency (ω_n) and phase (ϕ_n) are fit as independent parameters. The line in the center of the frequency spectra shown (Figure 5.) is at the diamagnetic frequency (542.16 MHz; c.f. equation (3.41)) for μ^+ . In this 4–detector configuration, one can determine precession direction by reversing two of the counter’s position in the asymmetry calculation and look at the resulting asymmetry (i.e. forward direction is 1,3,4,2 opposed to the reverse direction of 1,3,2,4 c.f. Figure 3.9, Figure 3.10 and sections 3.1.2 or 3.2.1). The lower frequency line (ν_{12}), indeed, precesses in a negative direction (where positive is the direction in which the μ^+ precesses). Once properly accounting for the precession direction, it is

clear that frequencies of these satellite lines scale as a function of field and are symmetric about μ^+ , which is consistent with the hyperfine splitting of Mu^0 in an applied field [60,65] (c.f. equations (3.37)–(3.39) and surrounding discussion). The resulting temperature dependent hyperfine values ($A = \nu_{34} - \nu_{12}$) are shown in Figure 5.2 as extracted via the fits with equation (5.1). Identical results were obtained with the sample oriented with the [001] direction offset from the original [001] parallel alignment to the direction of the incoming μ^+ spin polarization, which indicates that the hyperfine interaction for this promptly formed Mu^0 state, visible via HTF measurements, is isotropic. Furthermore, the zero temperature hyperfine constant is found to be 1965.6 ± 1 MHz.

Two common models were used in the attempts to model the temperature dependence of the hyperfine interaction (shown in Figure 5.2). The Debye model, which assumes that Mu^0 couples with the long wavelength portion of the acoustic phonon spectrum [65] where the hyperfine parameter has a temperature variation of the form

$$A_{HF}(T) = A_{HF}(0) \left[1 - \left(\frac{T}{\theta_{DB}} \right)^4 C \int_0^{\theta_{DB}} \frac{x^3}{e^x - 1} dx \right] \quad (5.2)$$

where the zero temperature hyperfine value [$A_{HF}(0)$] and temperature dependent hyperfine value [$A_{HF}(T)$] are taken directly from the data and the Debye temperature (θ_{DB}) and coupling constant (C , which is a measure of orbit–lattice interaction) are the fit parameters. The result is a very poor fit to the data over the entire temperature range. An Einstein model that takes coupling to optical phonons or simply that local–mode vibrations of the Mu^0 dominate the temperature dependent variation in the hyperfine interaction, did a much nicer job fitting the data. Moreover, this model makes the bold assumption that all oscillations have the same frequency and that only the vibrational ground state is relevant. In this model, the vibrational amplitude increases as the sample is warmed. By taking a series on the mean square

displacement of the vibrating atom, as to describe the change in hyperfine interaction, the temperature dependence follows the form [93,94]

$$A(T) = A_0 + \frac{C_1}{\exp\left(\frac{h\nu}{k_B T}\right)} + \frac{C_2}{\left(\exp\left(\frac{h\nu}{k_B T}\right)\right)^2} \quad (5.3)$$

where the isotropic zero-temperature hyperfine parameter (A_0), the single vibrational frequency (ν) and the temperature independent coupling constants (C_1 and C_2) are fit to the data as independent parameters. From this data $h\nu$ is found to be 7.5 ± 0.3 meV ($\nu = 1.81 \times 10^{12}$ Hz). ZnSe is a zincblende II-VI compound that has a similar structure to the II-IV-V₂ chalcopyrite, ZnGeP₂. Mu⁰ also forms in ZnSe with a comparable energy when the hyperfine interaction is fit with a similar model [95].

Analysis in variations of the ν_{12} line shape (relaxation rate, λ) as a function of temperature reveal a dynamic character to the measured Mu⁰. Specifically the temperature dependence of the relaxation parameter for ν_{12} under an applied field of $B_{\text{ext}} = 4.0$ T is shown in Figure 5.3. The rapid increase in relaxation rate that begins around 200 K is characteristic of ionization and yields an energy of 208 ± 8 meV. Spectrometer resolution limitations prevented accurate detection of ν_{34} above 200 K so the analysis is limited to that of ν_{12} . Lastly, the decrease in measured asymmetry (above 200 K) of the ν_{12} and ν_{34} (at least the limited observable portion) lines correspond to the growth of the μ^+ line which confirm the assignment of Mu⁰ ionization above 200 K as this indicates the conversion of the Mu⁰ state to μ^+ . The lower temperature variations in the ν_{12} relaxation rate are discussed in conjunction with the LF- and ZF-MuSR data on this sample (section 5.2.1) as these measurements are necessary to confirm assignments and complete the picture as to what mechanism is causing these variations.

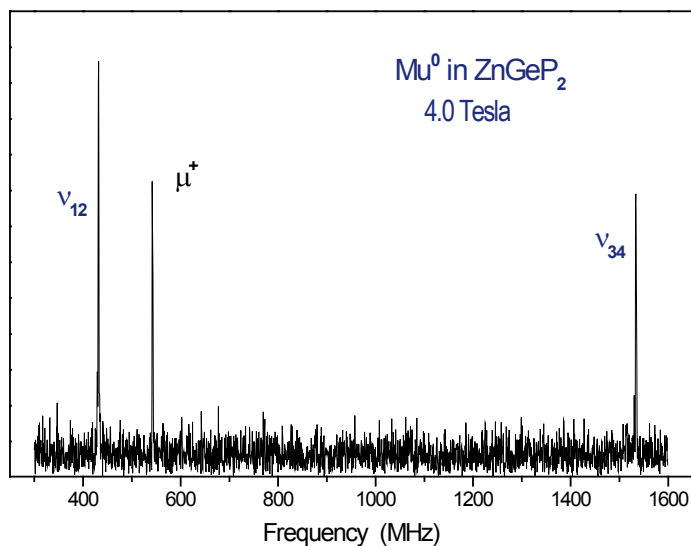


Figure 5.1: ZnGeP₂ HTF spectra at T=5 K and $B_{\text{ext}} = 4\text{ T}$

MuSR spectra showing the signals from the bare muon (μ^+), $\text{Mu}^0 \nu_{12}$ and $\text{Mu}^0 \nu_{34}$.

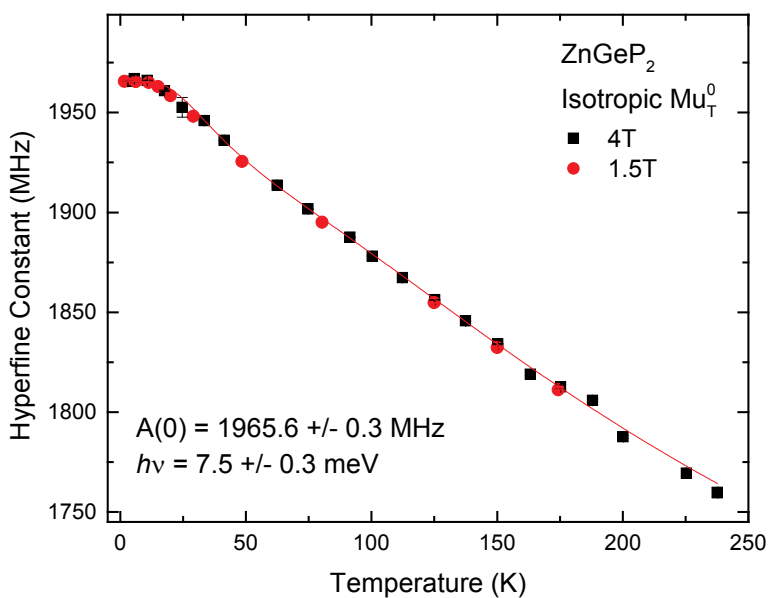


Figure 5.2: ZnGeP₂ Hyperfine constant variation with temperature

High TF–MuSR temperature dependence of the hyperfine parameter at B_{ext} of 1.5 T and 4 T determined from the difference it fit frequencies of ν_{12} and ν_{34} .

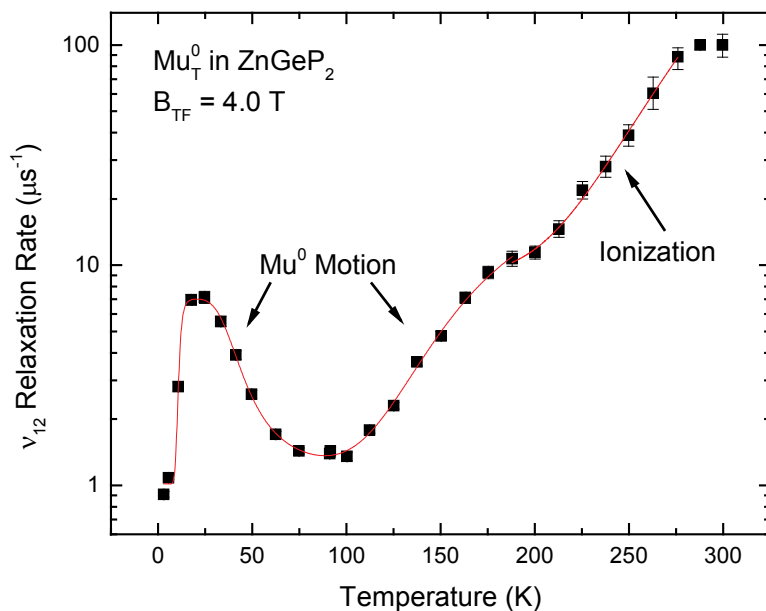


Figure 5.3: ZnGeP_2 Relaxation rate of $v_{12}(T)$

Temperature dependence of the relaxation rate associated with the v_{12} Mu^0 line. Fits to what is assigned to local Mu^0 motion (phonon assisted tunneling below 100 K) yields an energy barrier of $12 \pm 0.2 \text{ meV}$. Above 100 K, Mu^0 motion is assigned to thermally activated hopping with an activation energy of $E = 83 \pm 5 \text{ meV}$. Above 200 K is assigned to ionization with an energy of $E = 208 \pm 8 \text{ meV}$.

5.1.2. CdGeAs₂

As with the ZnGeP₂ (section 5.1.1) temperature dependence data at 4 T were collected on a closely related, single crystalline CdGeAs₂ sample. The results were strikingly different in that only the diamagnetic state (μ^+ or Mu^-) is present. That is the implanted μ^+ either does not capture an electron or it captures two electrons, hence forming the Mu^- state. Figure 5.4 shows that only a diamagnetic signal is visible within the low temperature data. To distinguish between μ^+ and Mu^- experimentally one really needs a system with large nuclear moments or significant dynamics. Additional remarks to describe how one concludes that μ^+ is the state observed in this TF spectra from diffusion measurements on CdGeAs₂ are found in section 5.2.2 where LF and ZF measurements are discussed.

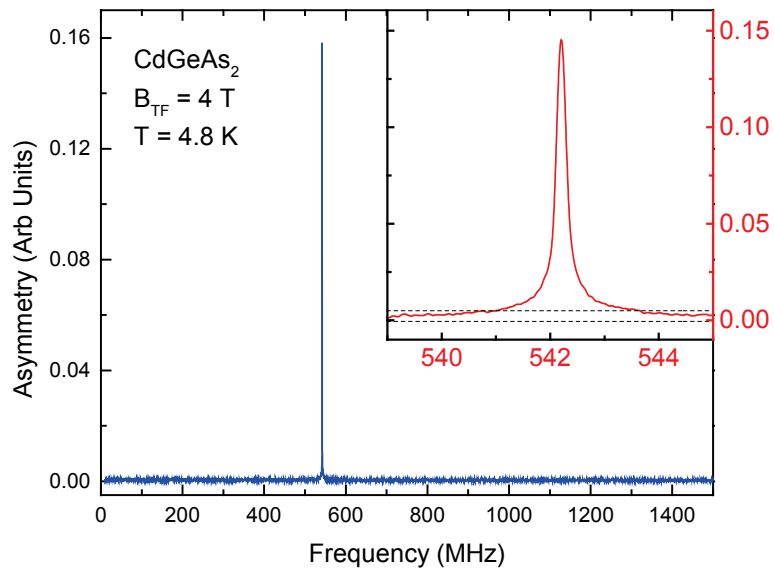


Figure 5.4: CdGeAs₂ FFT at 4.8 K and 4 T

5.1.3. $ZnGeP_2:Mn$

Analysis on four of the Mn enriched, p-type $ZnGeP_2$ samples (146 AA, CC, EE, FF) show features that are consistent across the sample range and show a clear trend as a function of Mn content (Figure 5.5). In general, a broad feature is present that when compared to a simultaneous reference sample measurement reveals that $B_{loc} - B_{ext}$ is between 0.2 ± 0.05 G to 5 ± 0.5 G *lower* than the measured field in the reference sample (which $B_{loc} = B_{ext}$) at high externally applied field ($B_{ext}^{TF} = 1$ T). At low applied field ($B_{ext}^{TF} = 10$ mT), an internal field of the same magnitude is measured but is *higher* than the field measured in the reference sample. Best fits to these data were obtained by utilizing a rotating reference frame and simultaneously fitting the time-domain spectra produced by muons decaying from within the sample and muons decaying within the reference sample to a sinusoidal muon spin polarization function with a Lorentzian relaxation envelope for the sample and a Gaussian relaxation envelope for the reference. By performing simultaneous fits on the sample and reference spectra, one is able to minimize the systematic uncertainty that may otherwise exist due to variations in particular aspects of the analysis routine such as frequency of the rotating reference frame, background removal, data binning and how far out in the time-domain one chooses to include. At low temperature, in the PM and AFM mixed state, this measured internal field is small. As the temperature increases the measured internal field also increases until near 200 K where the shift remains roughly constant to above 300 K. The corresponding asymmetry (normalized to maximum μ^+ fraction via Ag calibration, for discussion throughout this section) for measurements at both fields (10 mT and 1 T) are relatively flat at low temperature with values of 20.9 ± 0.5 %, 23.9 ± 0.5 % and 54.8 ± 0.6 % for AA, CC and FF (respectively) until above 40 K, where it begins to decrease nearly linearly to around 100 K, where AA and CC (lower Mn content) plateaus between 100 K and 175 K at 12.2 ± 0.5 % and 13.8 ± 0.4 %, respectively. For AA and CC, above 175 K the reduction in asymmetry continues nearly linearly with a smaller differential change to 4.7 ± 0.4 % and 6.1 ± 0.4 % at 300 K. In sample F (highest Mn content) the

differential change in asymmetry decreases slightly between 100 K and 150 K and then sharply increases until 225 K reducing the asymmetry from $41.0 \pm 0.7\%$ to $16.3 \pm 0.7\%$, where it remains up to 300 K. The asymmetry increases slightly up to 425 K, where it rapidly increases to recover nearly 100 % asymmetry above 565 K (normalized to the μ^+ asymmetry in a similarly sized piece of Ag at the same field, where Ag is well known to be nominally non-relaxing and give a full μ^+ fraction). The relaxation rate remains fairly constant through this temperature range. At 565 K, the μ^+ precession frequency (from the sample) matches the Larmor frequency expected for the applied field indicating that at 565 K, the local μ^+ environment is completely PM. The increase in relaxation rate is assigned to effects from rapid PM fluctuations and sufficiently short FM correlations contributing to broadening the field distribution at each μ^+ site. The high temperature ($T > 550$ K) regime relaxation rates fit best with a Lorentzian relaxation function, although when attempted with a Gaussian, the calculated uncertainties and reduced chi squared values are only marginally greater than the fits with a Lorentzian function. Below ~ 500 K, however, fits that utilize a Lorentzian relaxation function are better by a significant margin. One must consider that in a typical semiconductor, μ^+ diffusion results in the μ^+ sampling many sites (i.e. multiple local fields) and this change in environment reduces the spin polarization (via spin flip) with each subsequent hop. An effect referred to as *motional narrowing* may contribute to *reducing* the relaxation rate if the time between hops (inverse of the hop rate) is sufficiently shorter than the fluctuation rate of the local field and the local field distribution is sufficiently small. In these materials, μ^+ is mobile above 400 K (see sections 5.2.1 and 5.2.2) and yet the data show an *increase* in relaxation rate. From this, one concludes that there is clearly another mechanism affecting the μ^+ behavior.

These transverse field measurements verify local magnetic order at the μ^+ site (c.f. sample versus reference spectra) and a clear source of inhomogeneity (e.g. dynamics or a broad field distribution) in the local fields responsible for μ^+ dephasing at higher temperature that may be a related pre-cursor to the magnetic transitions. Unfortunately, these spectra were not defined well enough to extract more than the

overall shape of the relaxation function and a general measure of internal field strength.

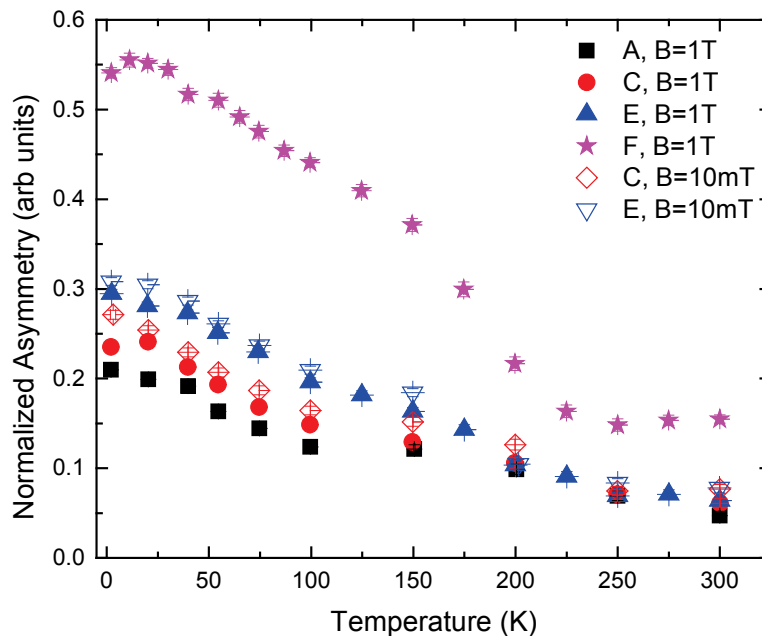


Figure 5.5: ZnGeP₂:Mn TF asymmetry trends with temperature and Mn content

These reported asymmetries are all from measurements on HiTime were the high temperature is limited to 300 K and normalized to the μ^+ asymmetry from silver, $\sim 22\%$.

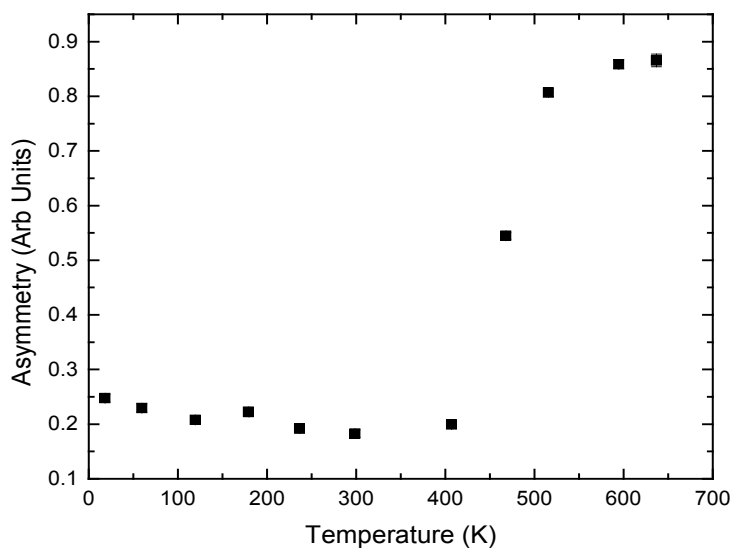


Figure 5.6: ZnGeP₂:Mn 146 AA asymmetry trend with temperature

These data are from fits to low transverse field ($B_{\text{ext}} = 10 \text{ mT}$) measurements on EMU and normalized to the μ^+ fraction present in silver at this field.

5.2. MUON SPIN RELAXATION: LF- AND ZF-MUSR

5.2.1. ZnGeP₂

Decoupling curves (asymmetry vs B_{ext}) [76] were used to further characterize the Mu^0 species found in ZnGeP_2 . These data were collected with *EMU* at ISIS at a series of temperatures and externally applied magnetic fields ($\mathbf{B}_{\text{ext}} \parallel \mathbf{S}_\mu$) in a range from 8 K to 300 K and 0 T to 0.45 T. The data were primarily fit to a linear combination of two Lorentzian relaxing components and a non-relaxing baseline component (A_3)

$$P(t) = \sum_{n=1}^2 A_n \exp(-\lambda_n t) + A_3 \quad (5.4)$$

where the asymmetry (A_n) and relaxation rate (λ_n) terms were fit as separate components in each time-domain spectra for a given temperature and applied magnetic field (B_{ext}). Initial analysis of the decoupling curves (A_n vs B_{ext} at a particular temperature) that assumed an isotropic Mu^0 with the parameters from the earlier TF hyperfine spectroscopy failed to fit the data, even as a rough approximation. A model accounting for axial symmetry in the Mu^0 hyperfine interaction [65,66,76] fit the experimental data quite well. This model has the form

$$Asy(B_{\text{ext}}) = \frac{N \left[\frac{1}{2} \frac{\cos(\phi)^2 + \frac{\gamma_-^* B_{\text{ext}}^2}{A_-^{xy}}}{1 + \frac{\gamma_-^* B_{\text{ext}}^2}{A_-^{xy}}} + \frac{\gamma_+^* B_{\text{ext}}^2}{A_+^{xy}} \right]}{1 + \frac{\gamma_+^* B_{\text{ext}}^2}{A_+^{xy}}} \quad (5.5)$$

where the angle (ϕ) is the angle between the symmetry axis and externally applied field and N is the paramagnetic fraction. For convenience, I have defined $\gamma_\pm^* \equiv 4(\gamma_e \mp \gamma_\mu)^2$ and $A_\pm^{xy} \equiv (A_x \pm A_y)^2$, where A_x and A_y are components of the hyperfine parameter that are mutually perpendicular. This results in $A_\perp = 2998 \pm \sim 300$ MHz and $A_\parallel = 3559 \pm \sim 350$ MHz. The perpendicular and parallel components refer to the hyperfine interaction direction with respect to bond orientation. In this case, deviations from the isotropic case are attributed to the dipolar coupling and can therefore be

written in terms of an anisotropic hyperfine term with a dipolar contribution (D), such as

$$\begin{aligned} A_{\parallel} &= A_2 + D \\ A_{\perp} &= A_2 - \frac{D}{2} \end{aligned} \quad (5.6)$$

which can then be solved to yield $A_2 = 3185$ MHz and $D = 374$ MHz ($\sim 10\%$ uncertainty).

This anisotropy can be accounted for if the Mu^0 resides in a pseudo T-site associated with the II–IV sublattice. In the case of a perfectly ordered ZnGeP_2 crystal, unequal charge transfer between Zn–P and Ge–P bonds give rise to an electric field oriented in the $[110]$ direction. These unequal charges for Zn ($+1.2q_e$) and Ge ($+1.8q_e$) lead to a distorted $1s$ Mu^0 electronic wavefunction, where the resulting anisotropy is along the axis of the electric field. Considering a perfectly ordered lattice with the nearest neighboring Zn and Ge ions as the only significant contributors to the electric field at this $\text{Mu}^0_{\text{T,II-IV}}$ site the resulting electric field ($\mathbf{E}_{\text{T,II-IV}}$) has the form

$$\mathbf{E}_{\text{T,II-IV}} = \mp \frac{1}{4\pi\epsilon_0} \frac{32\sqrt{3}}{9} (q_{\text{Zn}} - q_{\text{Ge}})[110] \quad (5.7)$$

where q_{Zn} and q_{Ge} are the effective charge of Zn and Ge, respectively (Figure 2.1). In a realistic system, there is considerable disorder so the electric field given by equation (5.8) represents one of several possible directions, although a maximum intensity as the ideal case is assumed.

Analysis of the relaxation rate as a function of field, for each temperature on this sample, yield dynamics related data. Specifically, by utilizing a single state model where one assumes that the depolarization is caused by fluctuations in the local field which is provided by the dipolar part of the hyperfine interaction [96]. Specifically, this model of the relaxation rate takes the form

$$\lambda \approx \left(1 - \frac{x}{\sqrt{1-x^2}}\right) \left(\frac{D^2\tau_c}{1 + \omega_{12}^2\tau_c^2}\right) \quad (5.8)$$

where the vacuum Mu^0 hyperfine parameter (A_0) is 4463.2 MHz and the magnetic field related parameter $x = B_{\text{LF,ext}}/B'$ normalizes the externally applied field ($B_{\text{LF,ext}}$)

to the decoupling field ($B' = 0.113$ T). The correlation time (τ_c), often expressed as a fluctuation or hop rate ($1/\tau_c$), is related to the time Mu^0 spends at each site. This model is based on the principle that the field from the nuclear hyperfine interaction (B_{hyp}) interacts with the unpaired electron spin and the Mu^0 diffusion direction is preferential to the direction in which this field fluctuates. This means that with each successive hop, an electron spin flip will occur and contribute to the depolarization of the muon via this variation in B_{hyp} . This model does not properly address the Mu^0 moving between two different sites or site anisotropy (unless the direction of the dipolar contribution varies randomly) and is therefore somewhat limited in its usefulness beyond an approximation of the Mu^0 behavior in this system. Temperature dependence of the hop rates, as extracted via equation (5.8), are shown in Figure 5.7. Here the increase in hop rate above 100 K is assigned to thermally activated hopping with Mu^0 ionization above 200 K. Below 100 K, the rapid increase in hop rate and ν_{12} relaxation rate (from section 5.1.1 and shown in Figure 5.3) with decreasing temperature is characteristic of quantum tunneling [97]. The decrease in hop rate with decreasing temperature below 25 K is behavior typically associated with interactions with defects or impurities.

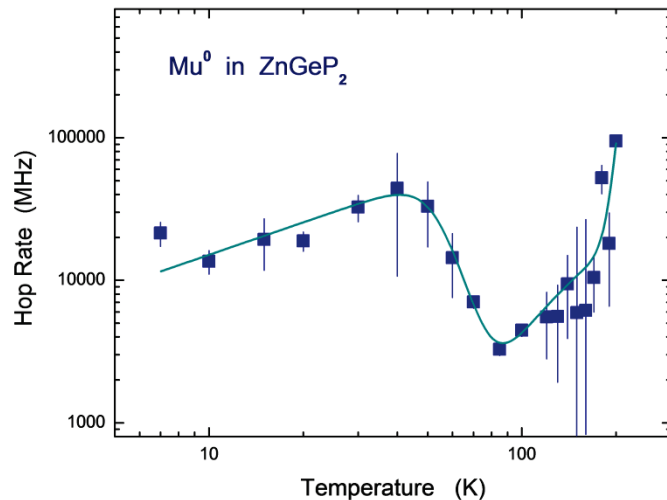


Figure 5.7: ZnGeP_2 Temperature dependent Mu^0 hop rates

5.2.2. *CdGeAs₂*

Since only diamagnetic Mu (either μ^+ or Mu^-) is present in CdGeAs_2 (as determined by TF measurements, discussed in section 5.1.2), applying a longitudinal field to investigate dynamics is not required (like it was for ZnGeP_2) since if Mu^- were to form, the net hyperfine field averages to zero and therefore does not affect the μ^+ frequency. Furthermore, one of the only ways to distinguish between μ^+ and Mu^- resides in analyzing the associated dynamics. Since this particular sample is specifically *p*-type, it is highly unlikely that Mu^- will actually form. These data were collected at ISIS on EMU under zero field and in a temperature range of 8 K to 600 K. Two data points were collected under a transverse field of 100 G in order to determine the appropriate value for the alpha correction parameter (by centering the oscillation about zero). These data fit equally well to a Gaussian Kubo Toyabe (equation (3.30)) and the LF Keren function (equation (3.31)) in a time range out to 22 μs as the Δ parameter is quite small. Parameters for these fits include asymmetry, second moment of the local field distribution (Δ^2) and the fluctuation rate (ν). As one can see from the form of the dynamic functions (either (3.30) or (3.31)), the Δ and ν parameter are highly correlated and hence will not normally yield a stable fit if allowed to simultaneously vary, unconstrained. These fits were performed first by assuming a completely static distribution of fields (force $\nu = 0$) and analyze the behavior of the Δ parameter. If Δ changes significantly it means that the field in which the muon is sampling is changing (e.g. via a change in local field distribution or from the onset of dynamics). In this case, Δ only slightly varies (7% reduction) from 9 K to ~ 280 K which compared to the 68% reduction (from 0.110 MHz to ~ 0.035 MHz) between 300 K and 425 K, the initial change is nearly negligible. Additionally, the static Kubo–Toyabe function does a very poor job of fitting the data above 300 K as the shape of the curve distinctly changes to a form that is clearly not a static Kubo–Toyabe function but instead takes the form of a dynamic Kubo–Toyabe (Figure 5.8). This rather clear change indicates that while the field properties (as sensed by the muon) are changing and the static Kubo–Toyabe function no longer provides a decent

fit, another process is affecting the local field – in this case, dynamics. The best fits to this range of data are achieved by setting $\Delta = 0.11369$ MHz chosen by averaging the fit Δ values over the few lowest temperature points where it changes very little (with $\alpha = 0.66599$), and allowing the Kubo–Toyabe or LF Keren function to be dynamic – that is, free the fluctuation rate (ν). This method makes the routine assumption that the RMS value of the field distribution (Δ) does not vary with temperature and that any observed variation is the result of dynamics of the sensed field. Starting from the lowest available temperature (Figure 5.9), the fluctuation rate increases only slightly from around 100 K until the first hint of significant motion, around 300 K. By around 466 K, ν increases by three orders of magnitude to near $\sim 2 \pm 0.5$ Mhz, where it plateaus. Here, the time–domain signal is nearly completely flat (Figure 5.8) and therefore insufficient variation in the observable time–dependent spin polarization function to fit these data with these functions reliably at any higher temperature indicating that there is no longer significant muon relaxation on the timescale that we are able to observe. These rates below 300 K are characteristic of local motion such as tunneling between nearby sites or between T–sites within a few unit cells. Above 300 K, the rates are still very low but a little more significant and we assign the dynamics in this range to thermally activated site–to–site motion that moves beyond the local range and whose diffusion rate is stifled by traps, above 400 K where the rates clearly plateau [77] (Figure 5.9).

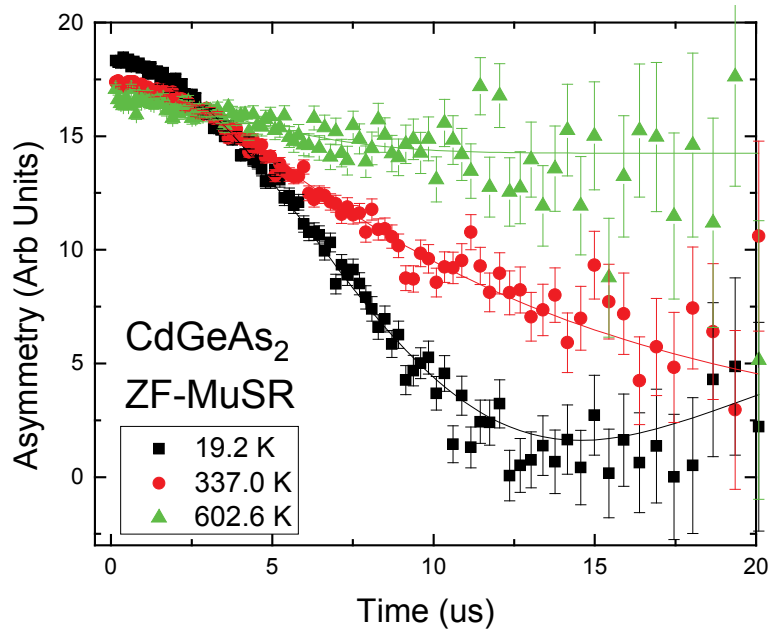


Figure 5.8: CdGeAs₂ raw data with dynamic KT fits at 3 temperatures

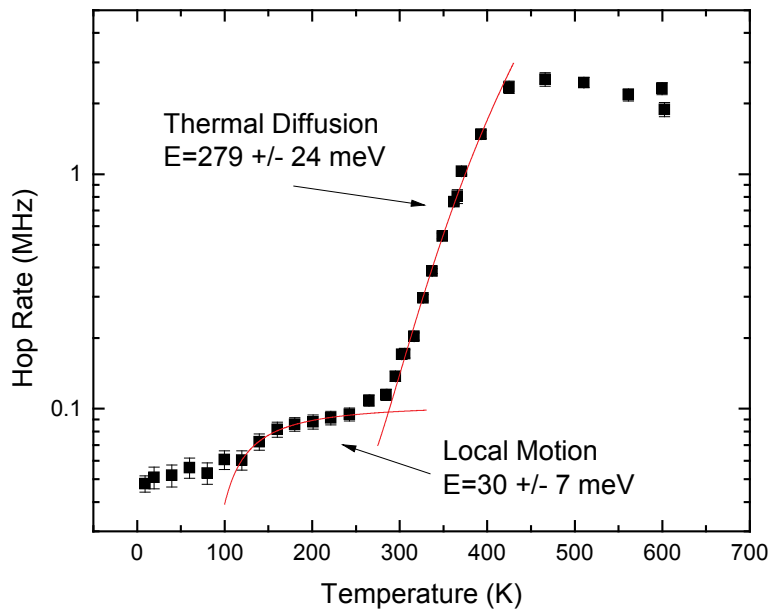


Figure 5.9: CdGeAs₂ Hop rate dependence on temperature

5.2.3. Dynamics in ZnGeP₂:Mn

Analysis of the LF data on four Mn doped ZnGeP₂ (146 AA, CC, EE, FF) reveal consistent behavior among each sample with clear trends as a function of Mn content. The best fits to time domain spectra were achieved by utilizing a spin polarization function composed of a linear combination of exponentials

$$P(t) = \sum_n A_n \exp(-\lambda_n t) \quad (5.9)$$

where the asymmetry (A_n) and relaxation rate (λ_n) for each separate component (n) are allowed to independently vary and fit simultaneously. Specifically, three distinct relaxing components are prevalent, each exhibiting similar trends but distinctly different parameters at any given temperature and field (i.e. Figure 5.10 and Figure 5.11). Not all of the components are completely resolved at every temperature and field. Figure 5.10 shows the fit relaxation rate data from the sample with the lowest Mn concentration (sample 146 AA), at applied fields of 0.1 T and 1.5 T. In addition to the three relaxing components, all fits were performed with a very slow relaxing component ($\lambda = 0.015 \mu\text{s}^{-1}$; Figure 5.11: *orange diamond* ♦) to resolve time dependent signals from the sample environment and not the sample. This rate is set based on calibration data collected using a comparably sized piece of silver, which is well known to be 100% diamagnetic and nearly non-relaxing. At the lowest applied field ($B_{\text{LF}} = 0.1 \text{ T}$), in sample AA, one relaxation feature is reliably fit from the lowest measured temperature, 2 K, up to nearly 400 K (Figure 5.10: *red circle*, ●) Between 400 K and 450 K, separation of this component from the other two relaxing components is not reliably achieved. The asymmetry corresponding to this portion of the first component (Figure 5.11: *red circle*, ●), decreases into the noise level and it is therefore unrealistic to expect stable and reliable extraction of the corresponding relaxation rate values. At a field of 1.5 T, the same qualitative behavior is observed below 100 K. Between 100 K and 300 K, the relaxation rate of this component appears to flatten (Figure 5.10: *red circle*, ●) around $0.2 \mu\text{s}^{-1}$ with extremely small asymmetry

values at low field (Figure 5.11a: *red circle*, ●) and at higher fields (Figure 5.11b: *red circle*, ●) the asymmetry of this component seems to increase but this is a result of the inability to reliably separate the competing components. Despite the very low relaxation rate and nominal asymmetry, it turns out that this component must be included with a non-zero asymmetry in order to produce reliable fits, which confirms that it is real. The second component (Figure 5.10 and Figure 5.11: *black square*, ■) has relaxation rates that fit reliably from $0.1 \mu\text{s}^{-1}$ up to $19.5 \mu\text{s}^{-1}$ and $0.1 \mu\text{s}^{-1}$ to $5.2 \mu\text{s}^{-1}$ between 300 K to 550 K and 275 K to 525 K, in fields of 0.1 T and 1.5 T, respectively. The third component (Figure 5.10 and Figure 5.11: *blue triangle*, ▲) has relaxation rates that fit reliably from $0.1 \mu\text{s}^{-1}$ up to $70 \mu\text{s}^{-1}$ and $0.1 \mu\text{s}^{-1}$ up to $8 \mu\text{s}^{-1}$ from about 350 K to the highest available 650 K, in applied fields of 0.1 T and 1.5 T, respectively. Temperature dependent LF data at applied fields of 0.375 T and 0.7 T were collected and the relaxation rates are completely consistent with the trends discussed here. The relaxation rates in these particular regions, in all three components, scale inversely with applied field and decreasing temperature, which is consistent with the expected behavior for weakly fluctuating moments [98,99,67]. Specifically, the relaxation rate associated with fluctuating spin, as sampled by μ^+ , is inversely proportional to the fluctuation rate and scaled by the root mean squared value of the fluctuating field (c.f. section 3.1.1). This relaxation rate behavior is consistent among all of the Mn enriched samples.

The relaxation rate of the second component at 0.1 T (Figure 5.10 left panel: *black square*, ■) appear to peak around 300 K. The fit asymmetry of that component (Figure 5.11 left panel: *black square*, ■) has a smooth rise from 400 K to 300 K, the subsequent fall in relaxation rate is accompanied by a slight decrease in asymmetry continuing down to an abrupt change at ~ 150 K. The very sharp dip in this relaxation rate, centered around 125 K, is complemented by very little change in asymmetry. This feature is in direct *contrast* with the 1.5 T data (Figure 5.11 right panel: *black square*, ■). This dip in the relaxation rate, while consistently present across the

samples at low field, does vanish as the field increases. That is, the relaxation rate *appears to increase* as the field increases.

At 1.5 T one finds a very smooth increase in relaxation rate (Figure 5.10b: *black square*, ■) from 550 K to ~220 K, below which the relaxation rate appears to flatten until ~100 K where it is no longer observable. The fractional asymmetry (Figure 5.11b: *black square*, ■) increases smoothly from 0 to 5 % between 550 K to about 425 K. There is a smooth but abrupt dip in asymmetry (Figure 5.11b: *black square*, ■), centered around 400 K, where the additional relaxing signal (Figure 5.10b and Figure 5.11: *blue triangle*, ▲) becomes much stronger. Specifically the dip near 400 K (Figure 5.11b: *black square*, ■) is complemented by a significant increase in fractional asymmetry (Figure 5.11: *blue triangle*, ▲), 5 % to 29 %, between 425 K and 325 K and then this additional component (*blue triangle*, ▲) is no longer visible below 300 K. From 300 K to 100 K the reduction to 10 % fractional asymmetry in the second component (Figure 5.11b: *black square*, ■) is very smooth. Below 100 K this component is no longer visible. This behavior below 200 K is consistent with what one expects for relaxation rates that are too fast for accurate measure (detection limits via spectrometer limitations). That is, these fits result in reduced asymmetry and relaxation rates due to not seeing enough of the signal to allow for an accurate fit for the particularly fast relaxing component. Therefore, this measured reduction in asymmetry and relaxation rate is likely not consistent with the actual μ^+ depolarization behavior. Alternatively, when a second process begins to dominate the μ^+ relaxation, clean separation of the individual components (from each process) where both processes are active, can become very difficult if not impossible. Consider a situation where the rate of local field fluctuation, from two different sources (processes), become comparable, two completely separate events that result in the same overall μ^+ response behavior can simply not be distinguished from each other based exclusively on that metric. Comparing the reliable portion of the first and second component's asymmetry and relaxation rates, one can see that the behaviors are qualitatively very similar. The first component Figure 5.10 and Figure 5.11, *red circle*, ●) has peaks in

asymmetry that correspond to a $\sim 1 \mu\text{s}^{-1}$ relaxation rate at all measured fields (including 3.75 kG and 7 kG, *not shown*). Likewise for the second component at 3.75 kG (*not shown*), 7 kG (*not shown*) and 1.5 T (Figure 5.10b and Figure 5.11b: *black square*, ■). A peak in the third relaxing component asymmetry (Figure 5.10 and Figure 5.11: *blue triangle*, ▲) is centered around 425 K and 390 K for 0.1 T and 1.5 T, respectively with an additional asymmetry peak near 550 K in the 1 kG data (Figure 5.10a and Figure 5.11a: *blue triangle*, ▲) corresponding to a $\sim 1 \mu\text{s}^{-1}$ relaxation rate. The qualitative consistencies between these features all suggest that a similar mechanism is responsible for the change in muon spin polarization. A peak in asymmetry specifically from weak fluctuations occur where the precession frequency of μ^+ matches the fluctuation rate of the local field and hence produce a smooth increase and decrease surrounding the peak if the fluctuation rate also varies smoothly (continually decreasing, in this case) with temperature [98,99].

These features are qualitatively consistent across the rest of the samples. Differences reside in where the asymmetry peaks occur and the actual measured relaxation rate – in general, the relaxation rates decrease with increasing Mn content.

The first relaxing component (*red circle*, ●) is assigned to be an interaction with AFM spin fluctuations detected from 350 K to the lowest measured temperature, 2 K. The second relaxing component (*black square*, ■) is assigned to fluctuations related to short-range FM correlations, detected from 550 K down to ~ 200 K. The third relaxing component (*blue triangle*, ▲) is detecting a precursor to the FM transition that may relate to small clusters with a net spin, aligning with the applied field, then weakly coupling via charge carrier mediated spin-exchange, hence contributing to field induced FM order.

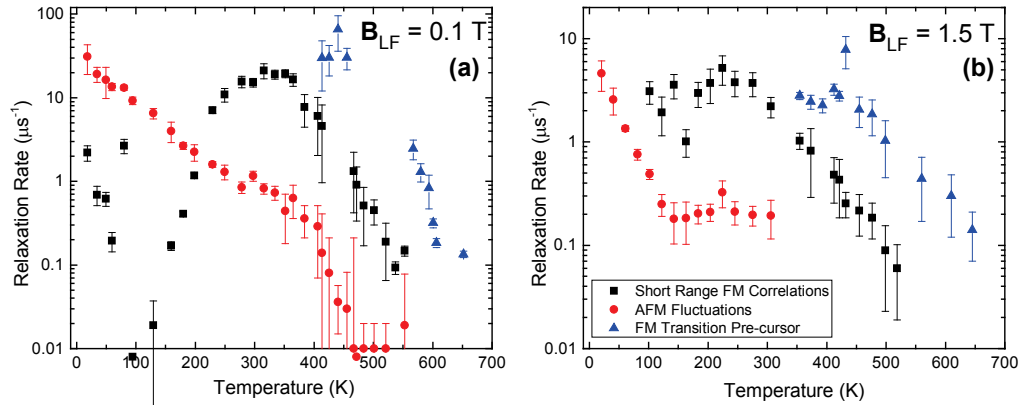


Figure 5.10: ZnGeP₂:Mn AA Temperature dependent LF relaxation rates

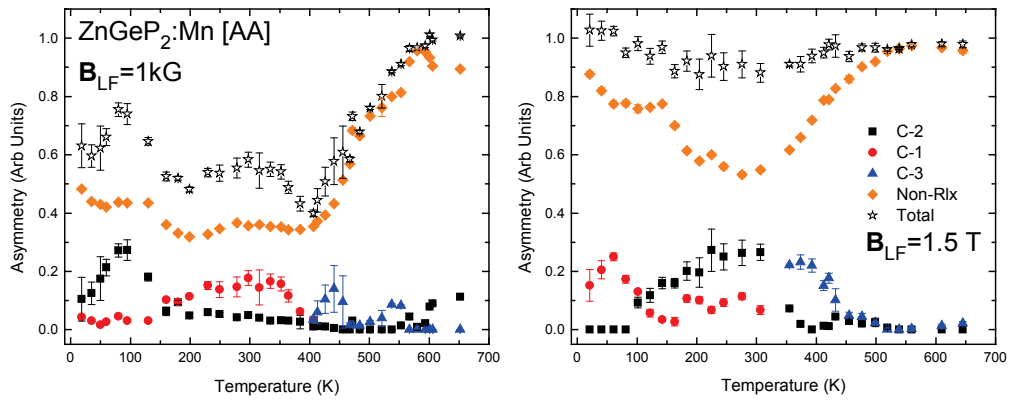


Figure 5.11: ZnGeP₂:Mn AA Temperature dependent LF asymmetry

5.3. BULK MAGNETIZATION MEASUREMENTS: AGM AND SQUID

The initial magnetization data, measured via the AGM at TTU (Department of Physics) showed a clear difference between the room temperature ($T \approx 295 \pm 5$ K) and cooled ($T \approx 275 \pm 10$ K) measurement, as shown in Figure 5.12. The kink in the lower temperature measurement shows hints of a slight hysteresis in addition to the obvious change in slope that indicates a clear, non-diamagnetic response between ± 1 kOe.

Much more detailed and complete measurements were performed via a DC SQUID Susceptometer at Michigan State University (Department of Physics and Astronomy). These data confirmed a mix of bulk PM and AFM below 47 K and a FM phase between 47 K and $\sim 320 \pm 15$ K in four Mn enriched samples (146 AA, CC, EE, FF). Measured bulk magnetic moment vs applied field curves (where the sample is held at a fixed temperature while the sample is measured at a series of applied magnetic fields) at 350 K revealed field induced FM order that collapses to zero in zero applied field, as shown in Figure 5.13. where the arrows indicate the chronological progression of collected data. Similar effects are observed above 320 K in the other $\text{ZnGeP}_2\text{:Mn}$ samples. This behavior is consistent with large cluster moments slowly aligning with the external field.

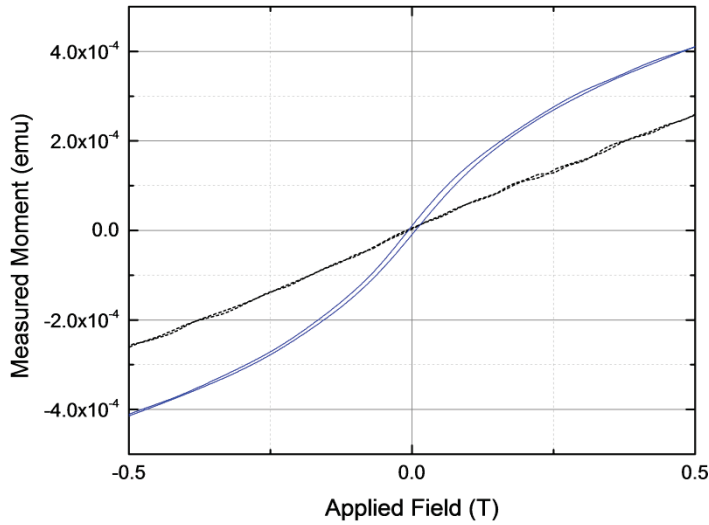


Figure 5.12: ZnGeP₂:Mn AGM magnetization curve

The ZnGeP₂:Mn AA sample was measured at two temperatures, first (black dotted line) at room temperature ($T \approx 295 \pm 5$ K) then cooled (solid blue line: $T \approx 275 \pm 10$ K) and measured again. Although slight, the coercively measures around 9 mT in the lower temperature measurement where there is clear non-diamagnetic behavior.

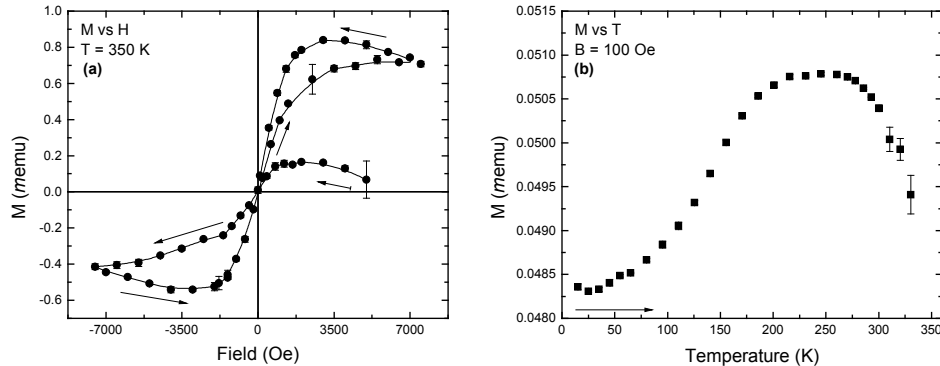


Figure 5.13: ZnGeP₂:Mn AA and CC SQUID Magnetization

- (a) Bulk magnetization versus applied magnetic field at $T = 350$ K, where the arrows indicate the chronological progression of the measurement and the solid line is a b-spline fit to the data points intended to be a guide for the eye. This measurement is well into the claimed PM phase (from low field M vs T measurements by other groups [30]).
- (b) Low applied field (10 mT) magnetization as a function of temperature measurements on a sample with higher Mn content [CC] sample indicating a clear FM phase between 50 K and 300 K. Extrapolating to the higher temperature, this curve suggests a 335 ± 5 K PM-FM transition temperature and qualitatively similar to the rest of the samples where the transition temperature scales with Mn content.

5.4. NEUTRON STUDIES

Triple axis unpolarized neutron scattering measurements revealed no convincing evidence of phase-separated complexes of MnP below 300 K. No apparent temperature dependence (over a range of ~ 2 K to the maximum available, 300 K) to the observed $\text{ZnGeP}_2\text{:Mn}$ (146 BB) features in the data indicate that if there is periodicity in the magnetic structure, it is beyond the detection limits of this measurement technique.

Magnetic small angle neutron scattering (SANS) data revealed no significant signs of magnetic clusters (i.e. large unpaired spin) below the maximum available 300 K, which suggests that if they exist below 300 K, they are below the detection limit. At the time of the experiment, the sample environment was not capable of exceeding 300 K thereby prohibiting the measurements in the PM region with and without an applied field, where the large clusters of unpaired spin were expected.

CHAPTER 6: CONCLUSION

This study has primarily utilized the unique properties of 100 % spin polarized muons to investigate the local electronic and magnetic environment of ZnGeP₂, CdGeAs₂ and a few samples of ZnGeP₂:Mn with varying Mn concentration. The similarities of μ^+ to H⁺ and Mu⁰ to the H atom provide the ability to utilize μ^+ and Mu⁰ as experimentally accessible analogs to hydrogen in a variety of materials. Additionally, the large magnetic moment allow the μ^+ to act as a local magnetometer and probe local fields on the scale of tenths of Gauss. This coupled with the probe itself (incoming μ^+) being 100 % spin polarized in their initial state give this technique a unique way of investigate material properties.

From this study we know that upon implantation in n-type ZnGeP₂, a neutral muonium (Mu⁰) is promptly formed in the tetrahedrally coordinated site associated with the group V neighbors and has an isotropic hyperfine parameter of ~1965 MHz. A second T-site is later occupied by Mu⁰, which is associated with the II-IV sublattice with an anisotropic hyperfine parameter of $A_2 = 3185$ MHz and $D = 374$ MHz. Mu⁰ dynamics in ZnGeP₂ are characterized by first (below 25 K) interacting with local impurities or defects. From 25 K to near 80 K, the dynamics are assigned to quantum (phonon assisted) tunneling as the hop rates decrease with increasing temperature ($E = 12 \pm 1$ meV). The dynamics between 100 K and 200 K are consistent with thermally activated hopping ($E = 83 \pm 5$ meV). Above 200 K, these dynamics also coincide with the Mu⁰ signal itself disappearing, which is assigned to Mu⁰ ionization with an energy close to 208 ± 8 meV, confirmed by both TF and LF measurements. Lastly, by modeling of the temperature variation in the hyperfine parameter, one determines a vibrational energy from an Einstein model of $h\nu = 7.50$ meV ($\nu = 1.81 \times 10^{12}$ Hz) which is rather comparable to the structurally similar zincblende ZnSe compound [95].

With respect to the specific isotropic T-site assignment, one ought to consider that rapid hopping between multiple anisotropic sites can show a single hyperfine term that is really an average of each visited site. The required hop rate must be much larger

than the hyperfine parameter ($\nu \gg 2\pi A_{\text{HF}}$) for this averaging to occur. In the opposite limit, where the hop rate is sufficiently slow ($2\pi A_{\text{HF}} \gg \nu$), the observed hyperfine signature has a much higher relaxation rate than a typical static Mu^0 as the field fluctuation in the hyperfine term (e.g. transitions ν_{12} and ν_{34}) are broadened by the sampling of multiple sites with significant dephasing occurring (via field dynamics) while in each site. Since the reported hop rates and hyperfine parameter are on the same order of magnitude we can safely conclude that the hyperfine frequency of ~ 1965 MHz for the T-site associated with the P neighbors, is isotropic.

In light of all of these considerations, the only reasonable model capable of describing all of the observed features in ZnGeP_2 including the two distinctly different hyperfine results, temperature variation of TF relaxation rates and LF derived hop rates is described here. That is, upon implantation, Mu^0 is promptly formed with an isotropic hyperfine constant which is in the T-site associated with the phosphorous neighbors. The Mu^0 then proceeds to hop the Mu^0_{T} associated with the II-IV sublattice with a different set of anisotropic hyperfine parameters. It is unclear as to whether this is a two-way process; however, there is no evidence to suggest that it is not.

From this study, we have determined that in *p*-type CdGeAs_2 , μ^+ remains bare (i.e. Mu^0 or Mu^- are not formed) and is very slow to diffuse through the bulk, even at temperatures in excess of 400 K where traps limit the diffusion rate. This relatively small hop rate in both CdGeAs_2 and ZnGeP_2 , at its fastest, demonstrate that complications due to motional averaging should not be an issue in these samples.

Experimental techniques that probe the bulk and local properties of $\text{ZnGeP}_2:\text{Mn}$ samples with less than 5 at % Mn content have been completed in an effort to expand the understanding of magnetic features and fundamental mechanisms that are active in this class of DMS systems.

Significant local, field induced, FM order from ~ 2 K to well above room temperature has been determined by TF-MuSR measurements. Three regimes of magnetic fluctuations have been revealed by LF-MuSR measurements. One related to

AFM fluctuations spanning both PM–FM and FM–AFM/PM transitions. Another related to short–range FM correlations, detected above and through the PM–FM transition and well into the bulk FM phase. A third regime, at high temperatures, is related to a precursor to the PM–FM transition. AGM and SQUID magnetization measurements clearly indicate a bulk response to an applied magnetic field that confirms the internal order. Additionally, SQUID measurements *above* T_{FM} clearly show a significant field induced bulk FM that collapses to zero at low applied field. The magnetic features were determined to be outside the detection capability of the two neutron scattering techniques utilized in this study. In the case of the above T_{FM} feature, in an experimentally inaccessible temperature range to the neutron instruments used.

Considering the ensemble of observed behavior above T_{FM} , most importantly:

- (1) In $\text{CdGeAs}_2\text{:Mn}$ the high applied field (and above T_{FM}) measurements showing a distinct shift in μ^+ precession frequency and broadened TF–MuSR spectral lines opposed to the rather sharp and single μ^+ feature in the pure CdGeAs_2 (e.g. Figure 2.2 and Figure 2.3)
- (2) In $\text{ZnGeP}_2\text{:Mn}$ the broadened and shifted TF–MuSR spectral line at high field and above the PM–FM transition until very high T ($T > \sim 600$ K), where the spectral line significantly narrows and distinctly shifts to the precise frequency expected for μ^+ in the provided B_{ext} (c.f. equation (3.41))
- (3) Slowing fluctuations (increasing relaxation rates), under applied longitudinal magnetic field from very high temperature ($T > \sim 600$ K) through the $\sim T_{\text{FM}}$ temperature region where the TF–MuSR “ μ^+ ” line ($\text{ZnGeP}_2\text{:Mn}$) both shifts and broadens (with decreasing temperature) and between 500 K and 400 K where the asymmetry of this fluctuation component peaks around 425 K (i.e. precession frequency of μ^+ match fluctuation rate of the field that it is probing)
- (4) Bulk magnetization measurements showing field induced FM collapsing at low applied field

The composite picture suggests that the mechanism leading to bulk FM order may be comprised of Mn moments that are aligned, preferentially with the applied field, and interact with neighboring moments through the semiconducting charge carrier (h^+ , in the case of these Mn enriched II–IV–V₂ chalcopyrites) whose wavefunctions are broadened by the applied field. That is, perhaps, the magnetic ion interacts, via spin–exchange, with a quasi–localized h^+ that has an expanded wavefunction encompassing multiple Mn ions where the gain in kinetic energy and change in entropy (ΔS_{ent}) from localization is offset by the exchange coupling and coulombic interactions between the h^+ and the Mn²⁺ local moment. Decreasing the temperature or increasing the applied field reduces the energy gained by h^+ localization, causing the wavefunction to expand and therefore increase the number of Mn ions involved in spin–exchange with this h^+ . This may increase the correlation length of the interactions within the reach of the h^+ and eventually develop significant wavefunction overlap of neighboring quasi–localized h^+ resulting in the long–range order that is present below T_{FM} , in the bulk FM state. The picture described here, is consistent with that of a *spin–polaron* [69,100,101]. To be clear, a spin polaron is an entity composed of a charge carrier (e^- or h^+) and reorientations of local spins that form its immediate FM environment that, as an ensemble, behave as a single quasiparticle with giant spin (S). The change in free energy (ΔF) is expressed in the form (e.g. [69,72,102] etc)

$$\Delta F = \frac{\hbar^2}{2m^*R^2} - J \left(\frac{a}{R}\right)^3 - \frac{q^2}{\epsilon R} + T\Delta S_{ent} \quad (6.1)$$

where R is the confinement radius for the charge carrier with effective mass (m^*) and charge (q), in a material with lattice constant (a) and dielectric constant (ϵ). J is the exchange interaction term. Spin polarons have been observed (by our collaboration [103]) in a wide variety of materials and seem to be a likely mechanism contributing to various phenomena such as magnetic order in a variety of systems [102,104,105]; large carrier mass enhancement; high T_c superconductivity [106]; various degrees of magnetoresistance or magnetostriction [71,107]; the coexistence of FM ordering, superconductivity and heavy fermion behavior [108]; a number of frustrated magnetic

systems and correlated metallic systems [72]. In nearly all of these other systems, evidence of SP were presented clearly enough to not only conclusively identify its signature but, in many cases, determine the carrier confinement radii and composite spin of the SP itself. Confinement radii were then compared to the expected μ^+ site and number of overlapping nuclei where the measured composite SP spin is consistent (within the experimental uncertainty) with the expected value. Data on these Mn enriched II–IV–V₂ Chalcopyrites are quite suggestive of the SP playing a key role in mediating the magnetism throughout the bulk, but admittedly, it would be much more convincing if more detail could be extracted. In addition to the data presented here, a picture that considers SP as a mediation mechanism would potentially resolve the issue of seemingly inconsistent variations of magnetic properties as a function of lattice parameter (as in double–exchange) and carrier concentration (as in Zener) for the transition metal enriched II–IV–V₂ chalcopyrite systems (e.g. [1,2,3,4], etc).

Dynamics (e.g. diffusion) of the μ^+ probe itself, as measured in these materials via ZF–MuSR, could potentially explain some of the TF spectral line narrowing above 500 K. That however, would not explain the distinct shift in the μ^+ line from the simultaneously measured μ^+ in the reference frequency – indicating the presence of a local magnetic field which is easily explained via a SP picture. Additionally, since below 400 K, μ^+ is very slow moving or nearly static (as is the case below 300 K) probe motional dynamics simply do not enter into the picture.

Interpreting the reduced amplitude, broad signal, and shift in μ^+ precession frequency (ω_{μ}) in ZnGeP₂:Mn (as compared to the simultaneously measured ω_{μ} from a reference sample) throughout the rest of the TF–MuSR data is rather unambiguous as it clearly shows that there is an internal field at the μ^+ stopping site. The width and shape of the TF spectral line directly relates to the relaxation rate, which is governed by field inhomogeneity or dynamics (c.f. 3.1.1). Field inhomogeneity, as sensed by a stationary probe, is simply the result of having a distribution of possible fields throughout the ensemble of sites within a material. Specifically for these dilute Mn enriched Chalcopyrites, sites that are closer to a Mn ion will have a stronger field than

one several sites away. Since several million muon decay events are collected at a set field and temperature, the ensemble samples a fair number of different sites throughout the bulk. The dynamics that may contribute to the broadening of a spectral line from a stationary probe refers to the dynamics of the field itself. In this case, the dynamics specifically relate to fluctuations of the Mn electronic moments that contribute to a non-zero (time dependent) δB_{loc} . The simple fact that the amplitude related to this shifted broad spectral peak that increases as a function of increasing Mn content, further supports the relation and μ^+ sensitivity to dynamics from the Mn moments.

The inability to resolve these features with greater detail reflects on the limitations of the current experimental configurations and the complexity (high disorder) of these dilute magnetic systems. While we do have some insight as to the local field strength, a rough picture of the microscopic field distribution and a possible mechanism that may be responsible for the magnetic phases. The development of a detailed model specifically for the II–IV–V₂ Chalcopyrites, is needed to further understand these materials. Since the models that are closest to describing the II–IV–V₂ Chalcopyrites in the dilute magnetic regime are for III–V or II–VI materials and are distinctly different when it comes to transition metal solubility – which is, arguably, one of the most important aspects that seem to be continually overlooked by the magnetic semiconductor community – they clearly fail to describe the magnetic interactions and their variations with respect to temperature and magnetic ion content. What may also help advance the understanding of the magnetism in these materials is to revisit the neutron studies with a sample environment that will allow for above T_{FM} investigation of large unpaired spin under an applied magnetic field, which ought to be within the resolution limits of SANS measurements. Analyzing the current data with an applicable SP based model, where one understands the variation in line shapes under different applied field conditions and fluctuation regimes (of moments internal and external to the confinement radius of the SP) may also be rather productive in exposing additional detail on the microscopic magnetic field structure.

Considering the generous lack of alternative explanations for these observed features, the SP picture seems to be consistent with all aspects of the data and as of now, a much more complete explanation than any other option.

This study provides the suggestion where SP mediate the magnetism in these dilute magnetic II–IV–V₂ chalcopyrite systems. Such a model would provide compromise between the vastly insufficient double–exchange and Zener models as the magnetic ion concentration nor the conductivity requirements, respectively, are not satisfactorily met for either.

As true with nearly any scientific project, idea or experiment, the effort to answer questions in reality merely addresses the original questions and, in the process, develops even more questions. In this case, the main and fundamental question at hand relates to how the magnetism in dilute magnetic semiconducting II–IV–V₂ chalcopyrites transfers from the local moments to the bulk. After this in depth study, we believe that a SP based mechanism is very likely to be at the root of mediating the magnetism in these materials. With this assignment, a plethora of questions relating to characterizing the SP or SP–like mechanism in these materials, comparing the SP in these materials to what is observed in a wide variety of other types of materials and how to really characterize the various properties of such a SP are introduced. While the data presented here may be primitive compared to many other well known and characterized phenomena and mechanisms, we believe that it is consistent with the observed properties and promising for continuing to develop an understanding of another class of dilute magnetic semiconductors that are very well suited for near future and practical applications such as in spin–electronic devices.

REFERENCES

1. K. Sato, L. Bergqvist, J. Kudrnovsky, P. H. Dederichs, O. Eriksson et al., *Rev Mod Phys* **82**, 1633–1690 (2010).
2. J. K. Furdyna, *J Appl Phys* **64**, R29–R64 (1988).
3. S. C. Erwin and I. Zutic, *Nat Mater* **3**, 410–414 (2004).
4. V. M. Novotortsev, A. V. Kochura and S. F. Marenkin, *Inorg Mater* **46**, 1421–1436 (2010).
5. V. G. Storchak, D. G. Eshchenko, H. Luetkens, E. Morenzoni, R. L. Lichti et al., *Physica B* **374–375**, 430–432 (2006).
6. R. L. Lichti and K. H. Chow, *TRIUMF: Experiment M1173*, unpublished data (2008–2010).
7. S. A. Wolf, D. D. Awschalom, R. A. Buhrman, J. M. Daughton, S. von Molnar et al., *Science* **294**, 1488 (2001).
8. I. Zutic, J. Fabian and S. Das Sarma, *Rev Mod Phys* **76**, 323–410 (2004).
9. J. R. Childress, M. J. Carey, S. Maat, N. Smith, R. E. Fontana et al., *IEEE Trans Magn* **44**, 90–94 (2008).
10. J. Daughton, J. Brown, E. Chen, R. Beech, A. Pohm et al., *IEEE Trans Magn* **30**, 4608 (1994).
11. S. Tumanski, in *Handbook of Magnetic Measurements* (CRC Press, 2011), pp. 159–256.
12. J. Wunderlich, B. Park, A. C. Irvine, L. P. Zarbo, E. Rozkotova et al., *Science* **330**, 1801–1804 (2010).
13. J. H. Yao, H. H. Lin, Y. L. Soo, T. S. Wu, J. L. Tsai et al., *Appl Phys Lett* **100**, 092404 (2012).
14. S. Datta and B. Das, *Appl Phys Lett* **56**, 665 (1990).
15. R. C. Myers, A. C. Gossard and D. D. Awschalom, *Phys Rev B* **69**, 161305 (2004).

16. E. Johnston–Halperin, D. Lofgreen, R. K. Kawakami, D. K. Young, L. Coldren et al., *Phys Rev B* **65**, 041306 (2002).
17. Y. Ohno, D. K. Young, B. Beschoten, F. Matsukura, H. Ohno et al., *Nature* **402**, 790–792 (1999).
18. R. Mattana, J. M. George, H. Jaffres, F. Nguyen Van Dau and A. Fert, *Phys Rev Lett* **90**, 166601 (2003).
19. S. H. Chun, S. J. Potashnik, K. C. Ku, P. Schiffer and N. Samarth, *Phys Rev B* **66**, 100408(R) (2002).
20. M. Tanaka and Y. Higo, *Phys Rev Lett* **87**, 026602 (2001).
21. I. Tsubokawa, *J Phys Soc Jpn* **15**, 1664–1668 (1960).
22. H. Munekata, H. Ohno, S. von Molnar, A. Segmuller, L. L. Chang et al., *Phys Rev Lett* **63**, 1849–1852 (1989).
23. H. Ohno, A. Shen, F. Matsukura, A. Oiwa, A. Endo et al., *Appl Phys Lett* **69**, 363–365 (1996).
24. H. Ohno, *J Magn Magn Mater* **200**, 110–129 (1999).
25. H. Ohno, D. Chiba, F. Matsukura, T. Omiya, E. Abe et al., *Nature* **408**, 944–946 (2000).
26. V. Novak, K. Olejnik, J. Wunderlich, M. Cukr, K. Vyborny et al., *Phys Rev Lett* **101**, 077201 (2008).
27. M. Wang, K. W. Edmonds, B. L. Gallagher, A. W. Rushforth, O. Makarovskiy et al., *Phys Rev B* **87**, 121301(R) (2013).
28. A. H. Macdonald, P. Schiffer and N. Samarth, *Nat Mater* **4**, 195–202 (2005).
29. F. W. Scholl and T. L. Tang, *Phys Rev B* **8**, 4607–4611 (1973).
30. S. Cho, S. Choi, G. Cha, S. C. Hong, Y. Kim et al., *Phys Rev Lett* **88**, 257203 (2002).
31. R. Demin, L. Koroleva, S. Marenkin, S. Mikhailov, T. Aminov et al., *J Magn Magn Mater* **290–291**, 1379–1382 (2005).
32. R. Demin, L. Koroleva, S. Marenkin, S. Mikhailov, R. Szymczak et al., *Phys Stat Sol c* **1**, 3525–3528 (2004).
33. R. V. Demin, L. I. Koroleva, S. F. Marenkin, S. G. Mikhailov, V. M. Novotortsev et al., *Tech Phys Lett* **30**, 924–926 (2004).

34. G. A. Medvedkin, T. Ishibashi, T. Nishi, K. Hayata, Y. Hasegawa et al., *Jpn J Appl Phys* **39**, L949–L951 (2000).
35. G. A. Medvedkin and V. G. Veovodin, *J Opt Soc Am B* **22**, 1884–1898 (2005).
36. G. A. Medvedkin, K. Hirose, T. Ishibashi, T. Nishi, V. G. Voevodin et al., *J Cryst Growth* **236**, 609–612 (2002).
37. K. Sato, G. A. Medvedkin, T. Nishi, Y. Hasegawa, R. Misawa et al., *J Appl Phys* **89**, 7027–7029 (2001).
38. S. Choi, G. B. Cha, S. C. Hong, S. Cho, Y. Kim et al., *Solid State Communications* **122**, 165–167 (2002).
39. P. Zapol, R. Pandey, M. Ohmer and J. Gale, *J Appl Phys* **79**, 671–675 (1996).
40. A. Sodeika, Z. Silevicius, Z. Januskevicius and A. Sakalas, *Phys Stat Sol A* **69**, 491–495 (1982).
41. G. K. Averkieva, V. S. Grigoreva, I. A. Maltseva, V. D. Prochukhan and Y. V. Rud, *Phys Stat Sol A* **39**, 453–457 (1977).
42. S. C. Abrahams and J. L. Bernstein, *J Chem Phys* **61**, 1140–1146 (1974).
43. H. Dittrich, N. Karl, S. Kuck and H. W. Schock, *Landolt–Bornstein: Numerical Data and Functional Relationships in Science and Technology* (Springer, 2000), Vol. 41E.
44. L. I. Koroleva, V. Y. Pavlov, D. M. Zashchirinskii, S. F. Marenkin, S. A. Varnavskii et al., *Phys Solid State* **49** (11), 2022–2026 (2007).
45. P. Mahadevan and A. Zunger, *Phys Rev Lett* **88**, 047205 (2002).
46. L. I. Koroleva, D. M. Zashchirinskii, T. M. Khapaeva, S. F. Marenkin, I. V. Fedorchenko et al., *Magnetism and Ferroelectricity* **51**, 286–291 (2009).
47. N. Y. Garces, L. E. Halliburton, P. G. Schunemann and S. D. Setzler, *Phys Rev B* **72**, 033202 (2005).
48. J. A. Aitken, G. M. Tsoi, L. E. Wenger and S. L. Brock, *Chem Mater* **19**, 5272–5278 (2007).
49. T. Hwang, J. H. Shim and S. Lee, *Appl Phys Lett* **9**, 1809–1811 (2003).
50. V. G. Storchak and J. H. Brewer, unpublished data (2002 – 2006, 2008–2009).
51. V. G. Storchak and J. H. Brewer, *TRIUMF: Experiment M 1044*, unpublished data (2005, 2006, 2009).

52. T. Dietl, *Nat Mater* **2**, 646–648 (2003).
53. T. Dietl, *Nat Mater* **9**, 965–974 (2010).
54. C. Zener, *Phys Rev* **81**, 440–444 (1951).
55. T. Dietl, H. Ohno, F. Matsukura, J. Cibert and D. Ferrand, *Science* **287**, 1019–1022 (2000).
56. C. Zener and R. R. Heikes, *Rev Mod Phys* **25**, 191–198 (1953).
57. J. H. Brewer, in *Encyclopedia of Applied Physics*, edited by G. L. Trigg, (VCH, New York, 1994), Vol. 11, pp. 23–53.
58. J. H. Brewer, D. G. Fleming, K. M. Crowe, R. F. Johnson, B. D. Patterson et al., *Physica Scripta* **11**, 144–148 (1974).
59. A. Yaouanc and P. D. de Reotier, *Muon Spin Rotation, Relaxation and Resonance Applications to Condensed Matter* (Oxford Press, New York, 2011).
60. A. Schenk, *Muon Spin Rotation Spectroscopy: Principles and Applications in Solid State Physics* (Adam Hilger, Bristol, 1985).
61. P. D. Group, *Eur Phys J C* **3**, 1–783 (1998).
62. R. S. Hayano, Y. J. Uemura, J. Imazato, N. Nishida, T. Yamazaki et al., *Phys Rev B* **20**, 850–859 (1979).
63. A. Keren, *Phys Rev B* **50**, 10039–10042 (1994).
64. Y. J. Uemura, T. Yamazaki, D. R. Harshman, M. Senba and E. J. Ansaldo, *Phys Rev B* **31**, 546–563 (1985).
65. B. D. Patterson, *Rev Mod Phys* **60**, 69–159 (1988).
66. M. Senba, *Phys Rev A* **62**, 042505 (2000).
67. S. J. Blundell, *Contemporary Physics* **40:3**, 175–192 (1999).
68. J. H. Brewer and V. G. Storchak, *TRIUMF Experiment 1044, Unpublished Data* (2005).
69. V. G. Storchak, O. E. Parfenov, J. H. Brewer, P. L. Russo, S. L. Stubbs et al., *Phys Rev B* **80**, 235203 (2009).
70. T. M. Riseman and J. H. Brewer, *Hyperfine Interactions* **65**, 1107–1112 (1990).
71. V. G. Storchak, J. H. Brewer, D. G. Eshchenko, P. W. Mengyan, H. Zhou et al., *J Phys Condens Matt* **25**, 115601 (2013).

72. V. G. Storchak, J. H. Brewer, S. L. Stubbs, O. E. Parfenov, R. L. Lichti et al., *Phys Rev Lett* **105**, 076402 (2010).
73. B. R. Carroll, R. L. Lichti, K. P.J. C, Y. G. Celebi, I. Yonenaga et al., *Phys Rev B* **82**, 205205 (2010).
74. J. E. Sonier, J. H. Brewer and R. F. Kiefl, *Rev Mod Phys* **72**, 769–811 (2000).
75. V. G. Storchak and N. V. Prokofev, *Rev Mod Phys* **70**, 929–978 (1998).
76. F. L. Pratt, *Philos Mag Lett* **75**, 371–379 (1997).
77. R. L. Lichti, in *Hydrogen in Semiconductors II*, edited by N. H. Nickel, (Academic Press, San Diego, 1999), Vol. 61, pp. 331–371.
78. P. W. Mengyan, R. L. Lichti, Y. G. Celebi, B. R. Carroll, B. B. Baker et al., *Phys B Condens Matt* **407**, 2829–2832 (2012).
79. R. L. Lichti, S. F.J. Cox, K. H. Chow, E. A. Davis, T. L. Estle et al., *Phys Rev B* **60**, 1734–1745 (1999).
80. A. Seeger and P. Monachesi, *Philos Mag B* **46**, 283–312 (1982).
81. J. H. Brewer, Available at <http://musr.ca>.
82. P. J.C. King, R. de Renzi, S. P. Cottrell, A. D. Hillier and S. F.J. Cox, *Physica Scripta* **88**, 068502 (2013).
83. Available at <http://www.isis.stfc.ac.uk/instruments/hifi/> (2014).
84. R. C. Jaklevic, J. Lambe, A. H. Silver and J. E. Mercereau, *Phys Rev Lett* **12**, 159–160 (1964).
85. H. Zijlstra, *Rev Sci Instru* **41**, 1241– (1970).
86. P. J. Flanders, *J Appl Phys* **63**, 3940–3945 (1988).
87. T. Vogt, in *Encyclopedia of Applied Physics*, edited by G. L. Trigg, (VCH, New York, 1994), Vol. 11, pp. 339–352.
88. H. G. Smith, in *Encyclopedia of Applied Physics*, edited by G. L. Trigg, (VCH, New York, 1994), Vol. 11, pp. 353–377.
89. A. Furrer, J. Mesot and T. Strassle, *Neutron Scattering in Condensed Matter Physics* (World Scientific, 2009).
90. Available at <http://neutrons.ornl.gov/instruments/HFIR/> (2014).
91. Available at neutrons.ornl.gov/hb1.

92. Available at neutrons.ornl.gov/gpsans.
93. E. Roduner, P. W. Percival, P. Han and D. M. Bartels, *J Chem Phys* **102**, 5989–5997 (1995).
94. J. R. Morton, F. Negri and K. F. Preston, *Phys Rev B* **49**, 12446–12450 (1994).
95. R. C. Vilao, H. V. Alberto, J. Piroto Duarte, J. M. Gil, A. Weidinger et al., *Phys Rev B* **72**, 235203 (2005).
96. R. Kadono, R. F. Kiefl, E. J. Ansaldo, J. H. Brewer, M. Celio et al., *Phys Rev Lett* **64**, 665–668 (1990).
97. H. N. Bani-Salameh, R. L. Lichti, Y. G. Celebi and C. S.F. J, *Phys Rev B* **74**, 245203 (2006).
98. A. Keren, *J Phys Condens Matt* **16**, S4603–S4618 (2004).
99. P. Dalmas de Reotier, P. C.M. Gubbens and A. Yaouanc, *J Phys Condens Matt* **16**, S4687–S4705 (2004).
100. E. L. Nagaev, *Journal of Magnetism and Magnetic Materials* **110**, 39–60 (1992).
101. E. L. Nagaev, *Colossal Magnetoresistance and Phase Separation in Magnetic Semiconductors* (Imperial College, London, 2002).
102. V. G. Storchak, J. H. Brewer, R. L. Lichti, T. A. Lograsso and S. D, *Phys Rev B* **83**, 140404(R) (2011).
103. J. H. Brewer, V. G. Storchak, P. W. Mengyan and R. L.E.D.G. Lichti, *TRIUMF: Experiment M* 938, 1044, 1088, 1199, 1221, 1222, 1253, 1254, 1270, 1304, 1342, 1343.
104. V. G. Storchak, J. H. Brewer, D. J. Arseneau, S. L. Stubbs, O. E. Parfenov et al., *Phys Rev B* **79**, 220406(R) (2009).
105. V. G. Storchak, J. H. Brewer, D. J. Arseneau, S. L. Stubbs, O. E. Parfenov et al., *Phys Rev B* **79**, 193205 (2009).
106. V. G. Storchak and J. H. Brewer, *TRIUMF: Experiment M* 1044, 1088, 1199, etc., 2008–2012.
107. V. G. Storchak, J. H. Brewer, D. G. Eshchenko, P. W. Mengyan, O. E. Parfenov et al., *Spin Gap in Heavy Fermion UBe13*, Submitted to: Nat Phys (2014).
108. V. G. Storchak, J. H. Brewer, D. G. Eshchenko, P. W. Mengyan, O. E. Parfenov et al., *Spin-polaron band of heavy carriers in the heavy-fermion ferromagnetic superconductor UGe2*, Submitted to: Nat Phys (2014).

APPENDIX A: AUTHOR RESEARCH ACTIVITY

A.1. PUBLICATION LIST

1. Hyperfine spectroscopy and characterization of muonium in ZnGeP₂.
P.W. Mengyan, B.B. Baker, R.L. Lichti, K.H. Chow, Y.G. Celebi, K.T. Zawilski, P.G. Schunemann.
Physica B. **404** (2009) 5121–5124. doi: 10.1016/j.physb.2009.08.212
2. Spin Polarons in Correlated Metallic Pyrochlore Cd₂Re₂O₇.
V.G. Storchak, J. H. Brewer, S. L. Stubbs, O. E. Parfenov, R. L. Lichti, P. W. Mengyan, J. He, I. Bredeson, D. Hitchcock, D. Mandrus.
Phys. Rev. Lett. **105** (2010) 076402.
3. Longitudinal Muon Spin Depolarization in Ge–Rich SiGe Alloys.
P.W. Mengyan, Y.G. Celebi, R.L. Lichti, B.R. Carroll, B.B. Baker, H.N. Bani–Salameh, I. Yonenaga.
Physics Procedia. **30** (2012) 214–218.
4. Motion of Mu⁺ in Transparent Conducting Oxides.
Y.G. Celebi, R. L. Lichti, B.B. Baker, P.W. Mengyan, H.N. Bani–Salameh.
Physics Procedia. **30** (2012) 206–209.
5. Initial Study of Positively Charged Muonium Motion in ZnO, CdO, TiO₂ and SnO₂.
B.B. Baker, Y.G. Celebi, R.L. Lichti, H.N. Bani–Salameh, P.W. Mengyan, B.R. Carroll.
Physics Procedia. **30** (2012) 101–104.
6. Spin Polarons in Strongly Correlated Electron Materials
V.G. Storchak, O.E. Parfenov, J.H. Brewer, D.G. Eshchenko, R.L. Lichti, P.W. Mengyan, D.J. Arseneau, and B.Hitti.
Physics Procedia. **30** (2012) 178–181.
7. Muonium Transitions in Ge–rich SiGe Alloys.
P.W. Mengyan, R.L. Lichti, Y.G. Celebi, B.R. Carroll, B.B. Baker, H.N. Bani–Salameh, I. Yonenaga.
Physica B. **407** (2012) 2829–2832.

8. Motion of Positively Charged Muonium in ZnO.
B.B. Baker, Y.G. Celebi, R.L. Lichti, P.W. Mengyan, H.N. Bani-Salameh and B.R. Carroll.
Physica B. **407** (2012) 2864–2866.
9. Muonium Dynamics in Transparent Conducting Oxides.
Y.G. Celebi, R.L. Lichti, B.B. Baker, P.W. Mengyan and H.N. Bani-Salameh.
Physica B. **407** (2012) 2879–2882.
10. Antiferromagnetism in the spin-gap system NaV₂O₅: Muon spin rotation measurements.
V.G. Storchak, O.E. Parfenov, D.G. Eshchenko, R.L. Lichti, P.W. Mengyan, M. Isobe and Y. Ueda.
Phys Rev B. **85** (2012) 094406.
11. Observation of magnetic polarons in the magnetoresistive pyrochlore Lu₂V₂O₇.
V.G. Storchak, J.H. Brewer, D.G. Eshchenko, P.W. Mengyan, H.D. Zhou and C.R. Wiebe.
Journal of Physics: Condensed Matter **25** (2013) 115601.
12. Magnetic fluctuations and fields in weakly Mn doped ZnGeP₂.
P.W. Mengyan, R.L. Lichti, Y.G. Celebi, B.B. Baker, B.R. Carroll, E. Catak, K.T. Zawilski and P.G. Schunemann.
AIP Conference Proceedings. **1583** (2014) 190.
13. Transition Dynamics for Mu Acceptor States in Si_{1-x}Ge_x Alloys.
G. Jayarathna, P.W. Mengyan, R.L. Lichti, B.B. Baker, Y.G. Celebi, B.R. Carroll and I. Yonenaga.
AIP Conference Proceedings. **1583** (2014) 56.
14. Motional Characteristics of Positively Charged Muonium Defects in In₂O₃.
B.B. Baker, Y.G. Celebi, R.L. Lichti and P.W. Mengyan.
AIP Conference Proceedings. **1583** (2014) 323.
15. Spin Gap in Heavy Fermion UBe₁₃.
V.G. Storchak, J.H. Brewer, D.G. Eshchenko, P.W. Mengyan, O.E. Parfenov, P. Dosanjh, Z. Fisk and J. L. Smith.
Nat Phys **Submitted** Feb 2014.
16. Spin-polaron band of heavy carriers in the heavy-fermion ferromagnetic superconductor UGe₂.
V.G. Storchak, J.H. Brewer, D.G. Eshchenko, P.W. Mengyan, O.E. Parfenov and D. Sokolov.
Nat Phys **Submitted** Mar 2014.

A.2. EXPERIMENT PROPOSALS

This section is a list of experiment proposals accepted by the experimental evaluation committees at the respective institutions that I have either authored or advised on (as noted).

1. Magnetic Features in Mn–Doped II–VI Compounds.
TRIUMF: M1275 – Accepted *Nov 2010*; Scheduled *Nov 2012* and *Jun 2013*
2. Magnetic Field Distribution in Mn–Doped Chalcopyrites.
TRIUMF: M1310 – Accepted *Nov 2010*; Scheduled *Nov 2012* and *Jun 2013*
3. Investigation of Magnetic Fields in ZnGeP₂:Mn.
ISIS: RB 1120240 – Accepted *Apr 2011*, Scheduled *Dec 2011*
4. Magnetic Ordering in Manganese–doped ZnGeP₂.
Oak Ridge National Laboratory: IPTS 4537–Accepted; Scheduled Feb 2011
Primarily written by B.R. Carroll, I am CoPI
5. Secondary Chemical Phase in Manganese–doped Zinc Germanium Diphosphide (ZnGeP₂).
Oak Ridge National Laboratory: IPTS 4747 – Accepted; Scheduled *Aug 2011*
Primarily written by B.R. Carroll, I am CoPI
6. Compositional trends of magnetic SANS features in ZnGeP₂ alloyed with Mn.
Oak Ridge National Laboratory: IPTS 6407 – Accepted
Primarily written by B.R. Carroll, I am CoPI
7. Study of Magnetic Features in Weakly Mn–Doped ZnGeP₂.
ISIS: RB 1220205 – Accepted *July 2012*; Scheduled *3–17 Oct 2012*
8. Cyclic Processes in Mid–Range SiGe Alloys.
ISIS: 1220201 – Accepted *July 2012*; Scheduled *3–17 Oct 2012*
9. Cyclic Muonium Dynamics in Mid–Range SiGe Alloys.
ISIS: 1310432 – Accepted *Dec 2012*; Scheduled *11–14 Jul 2013*
10. Investigation of muonium diffusion, states and charge cycles in vanadium dioxide
ISIS: 1320350 – Accepted *June 2013*; Scheduled *4–10 Oct 2013*
11. Properties of Hydrogen in Vanadium Dioxide Studied via Muonium
TRIUMF: M1416 – Accepted *July 2013*; partially scheduled *22–30 Oct 2013*

12. Investigation of low temperature magnetism in vanadium dioxide compounds
ISIS: RB 1410438 – Accepted *Fall 2013*; Scheduled *22–26 Feb 2014*)

A.3. CONFERENCE PRESENTATIONS (PRIMARY AUTHOR OR PRESENTER)

1. Hyperfine Spectroscopy and Characterization of Muonium Centers in ZnGeP₂.
P.W. Mengyan, B.B. Baker, R.L. Lichti, K.H. Chow, Y.G. Celebi, K.T. Zawilski,
and P.G. Schunemann.
International Conference on Defects in Semiconductors (ICDS–25). St. Petersburg, Russia. 20–24/July/2009. [Presented on my behalf by R.L. Lichti].
2. Hyperfine Spectroscopy and Characterization of Muonium Centers in ZnGeP₂.
P.W. Mengyan, B.B. Baker, R.L. Lichti, K.H. Chow, Y.G. Celebi, K.T. Zawilski,
and P.G. Schunemann.
Texas Section APS Fall Meeting. San Marcos, TX (22–24/Oct/2009).
3. Observing Spin Polarons in Magnetic Semiconducting and Various Other Materials via μ^+ SR.
P.W. Mengyan, R.L. Lichti, V.G. Storchak, D.G. Eshchenko and J.H. Brewer.
Gordon Research Conference: Defects in Semiconductors. New London, NH (8–13/Aug/2010).
4. Longitudinal Muon Spin Depolarization in Ge-rich SiGe Alloys.
P.W. Mengyan, B.R. Carroll, R. L. Lichti, Y.G. Celebi, B.B. Baker, H.N. Bani-Salameh and I. Yonenaga.
12th International conference on Muon Spin Rotation, Relaxation and Resonance. Cancun, Mexico (16–20/May/2011).
5. Muonium Transitions in Ge-rich SiGe Alloys.
P.W. Mengyan, Y.G. Celebi, B.R. Carroll, R.L. Lichti, H.N. Bani-Salameh, B.B. Baker and I. Yonenaga.
26th International Conference on Defects in Semiconductors. Nelson, New Zealand (17–22/July/2011).
6. Probing the internal magnetic field features of the II–IV–V₂:Mn Dilute Magnetic Semiconducting systems via μ SR.
P.W. Mengyan, R.L. Lichti, Y.G. Celebi, B.B. Baker, L.J. Hudy, E. Catek, K.T. Zawilski and P.G. Schunemann.
Joint Spring 2012 Meeting of the Texas Sections of the APS, AAPT and Zone 13 of the SPS. San Angelo, TX (22–24/Mar/2012).
7. Probing Local Features in Dilute Magnetic Semiconducting ZnGeP₂:Mn via μ^+ SR.

P.W. Mengyan, R.L. Lichti, Y.G. Celebi, B.B. Baker, E. Catek, K.T. Zawilski and P.G. Schunemann.

Gordon Research Conference: Defects in Semiconductors. Biddeford, ME (12–17/Aug/2012).

8. Probing Local Features in Dilute Magnetic Semiconducting ZnGeP₂:Mn via μ^+ SR.
P.W. Mengyan, R.L. Lichti, Y.G. Celebi, B.B. Baker, E. Catek, K.T. Zawilski and P.G. Schunemann.
2012 Joint Fall Meeting Texas Section of APS, AAPT & Zone 13 SPS. Lubbock, TX (25–27/Oct/2012).
9. Positive Muonium in In₂O₃.
B.B. Baker, P.W. Mengyan, R.L. Lichti and Y.G. Celebi.
2012 Joint Fall Meeting Texas Section of APS, AAPT & Zone 13 SPS. Lubbock, TX (25–27/Oct/2012).
10. Magnetic Fields and Fluctuations in Weakly Mn Doped ZnGeP₂.
P.W. Mengyan, R.L. Lichti, Y.G. Celebi, B.B. Baker, B.R. Carroll, E. Catak, K. T. Zawilski and P.G. Schunemann
27th International Conference on Defects in Semiconductors. Bologna, Italy (21–26/July/2013).

A.4. CONFERENCE PRESENTATIONS (CO-AUTHOR)

1. Characterization of the Motion of Muonium Centers in II–IV–V₂ Semiconductors.
B.B. Baker, P.W. Mengyan R.L. Lichti, K.H. Chow, Y.G. Celebi, K.T. Zawilski, and P.G. Schunemann.
Texas Section APS Fall Meeting, San Marcos, TX (22–24/Oct/2009).
2. Motion of Mu^+ in Transparent Conducting Oxides.
Y.G. Celebi, B.B. Baker, R.L. Lichti, P.W. Mengyan, B.R. Carroll.
Gordon Research Conference: Defects in Semiconductors (8–13/Aug/2010).
3. Motion of Diamagnetic Muonium in ZnO.
B.B. Baker, Y.G. Celebi, R.L. Lichti, P.W. Mengyan.
Gordon Research Conference: Defects in Semiconductors (8–13/Aug/2010).
4. Shallow Muonium Acceptors in Si_{0.06}Ge_{0.94}.
B.R. Carroll, R.L. Lichti, Y.G. Celebi, P.W. Mengyan, B.B. Baker.
Gordon Research Conference: Defects in Semiconductors (8–13/Aug/2010).
5. Initial Study of Diamagnetic Muonium Motion in ZnO, CdO, TiO₂ and SnO₂.
B.B. Baker, Y.G. Celebi, R.L. Lichti, H.N. Bani–Salameh, P.W. Mengyan, B.R.

- Carroll.
International conference on Muon Spin Rotation, Relaxation and Resonance.
Cancun, Mexico (16–20/May/2011).
6. Motion of Mu^+ in Transparent Conducting Oxides.
Y.G. Celebi, R.L. Lichti, B.B. Baker and P.W. Mengyan.
International conference on Muon Spin Rotation, Relaxation and Resonance.
Cancun, Mexico (16–20/May/2011).
 7. Spin Polarons in Strongly Correlated Electron Materials.
V. G. Storchak, O. E. Parfenov, J. H. Brewer, D. G. Eshchenko, R. L. Lichti, P. W. Mengyan, D. J. Arseneau and B. Hitti.
International conference on Muon Spin Rotation, Relaxation and Resonance.
Cancun, Mexico (16–20/May/2011).
 8. MuSR Study of Positive Muonium Motion in ZnO.
B.B. Baker, Y.G. Celebi, R.L. Lichti, P.W. Mengyan, H.N. Bani–Salameh and B.R. Carroll.
26th International Conference on Defects in Semiconductors. Nelson, New Zealand
(17–22/July/2011).
 9. Muonium Dynamics in Transparent Conducting Oxides.
Y.G. Celebi, R.L. Lichti, B.B. Baker, P.W. Mengyan and H.N. Bani–Salameh.
26th International Conference on Defects in Semiconductors. Nelson, New Zealand
(17–22/July/2011).
 10. Magnetic polarons in frustrated magnetic systems.
V.G. Storchak, J.H. Brewer, R.L. Lichti and P.W. Mengyan.
2012 The International Conference on Highly Frustrated Magnetism. Ontario, CA
(4–8/June/2012).
 11. Motion of Positively Charged Muonium Centers in Transparent Conducting Oxides.
B. B. Baker, Y.G. Celebi, R.L. Lichti, E. Catak, P.W. Mengyan
Gordon Research Conference: Defects in Semiconductors. Biddeford, ME
(12–17/Aug/2012).
 12. Cyclic Transition Processes for Muonium in Silicon Germanium Alloys.
G. Jayarathna, P.W. Mengyan, B.B. Baker, B.R. Carroll, Y.G. Celebi and R.L. Lichti.
Gordon Research Conference: Defects in Semiconductors. Biddeford, ME
(12–17/Aug/2012).

13. Cyclic Transition Processes for Muonium in Silicon Germanium Alloys.
G. Jayarathna, P.W. Mengyan, B.B. Baker, B.R. Carroll, Y.G. Celebi and R.L. Lichti.
2012 Joint Fall Meeting Texas Section of APS, AAPT & Zone 13 SPS. Lubbock, TX (25–27/Oct/2012).
14. Transition Dynamics for Mu Acceptor States in $\text{Si}_{1-x}\text{Ge}_x$ Alloys.
G. Jayarathna, P.W. Mengyan, R.L. Lichti, B.B. Baker, Y.G. Celebi, B.R. Carroll and I. Yonenaga.
27th International Conference on Defects in Semiconductors. Bologna, Italy (21–26/Jul/2013).
15. Motional Characteristics of Positively Charged Muonium Defects in In_2O_3 .
B.B. Baker, Y.G. Celebi, R.L. Lichti, P.W. Mengyan and E. Catak
27th International Conference on Defects in Semiconductors. Bologna, Italy (21–26/Jul/2013).

APPENDIX B: SELECT PAPERS

B.1. SPIN–POLARON BAND OF HEAVY CARRIERS IN THE HEAVY–FERMION FERROMAGNETIC SUPERCONDUCTOR UGe_2

This paper was submitted to *Nature Physics* in March of 2014 and the text included here is in the exact form in which it was submitted with the only exception being the equation, figure and citation numbers have been modified as to minimize confusion with the rest of this document.

B.1.1. UGe_2 : Author Information and Associations

Vyacheslav G. Storchak¹, Jess H. Brewer², Dmitry G. Eshchenko³,
Patrick W. Mengyan⁴, Oleg E. Parfenov¹ & Dmitry Sokolov⁵

¹*Russian Research Centre “Kurchatov Institute”, Kurchatov Sq. 1, Moscow 123182, Russia*

²*Department of Physics and Astronomy, University of British Columbia, Vancouver, BC, Canada V6T 1Z1*

³*Bruker BioSpin AG, Industriestrasse 26, 8117 Fallanden, Switzerland*

⁴*Department of Physics, Texas Tech University, Lubbock, Texas 79409–1051, USA*

⁵*School of Physics and CSEC, The University of Edinburgh, Mayfield Road, Edinburgh EH9 3JZ, UK*

B.1.2. UGe_2 : Text

In strongly correlated materials, cooperative behaviour of the electrons causes a variety of quantum ordered states that may, in some cases, coexist [B1.1–B1.3]. It has long been believed, however, that such coexistence among ferromagnetic ordering, superconductivity and heavy–fermion behaviour is impossible, as the first supports parallel spin alignment while the conventional understanding of the latter two phenomena assumes spin–singlet or antiparallel spins. This understanding has recently been challenged by an increasing number of observations in uranium intermetallic systems (UGe_2 , URhGe, UIr and UCoGe) [B1.4–B1.7] in which superconductivity is found within a ferromagnetic state and, more fundamentally, both ordering phenomena are exhibited by the same set of comparatively heavy $5f$ electrons. Since

the coexistence of superconductivity and ferromagnetism is at odds with the standard theory of phonon-mediated spin-singlet superconductivity, it requires an alternative pairing mechanism, in which electrons are bound into spin-triplet pairs by spin fluctuations [B1.8, B1.9]. Within the heavy-fermion scenario, this alternative mechanism necessarily assumes that the magnetism has a band character and that said band forms from heavy quasiparticles composed of f electrons. This band is expected to be responsible for all three remarkable phenomena — heavy-fermion behaviour, ferromagnetism and superconductivity — although its nature and the nature of those heavy quasiparticles still remains unclear.

Here we report spectroscopic evidence (from high-field muon spin rotation measurements) for the formation in UGe_2 of subnanometer-sized spin polarons whose dynamics we follow into the paramagnetic and ferromagnetic phases. These spin polarons behave as heavy carriers and thus may serve as heavy quasiparticles made of $5f$ electrons; once coherence is established, they form a narrow spin-polaron band which thus provides a natural reconciliation of itinerant ferromagnetism with spin-triplet superconductivity and heavy-fermion behaviour.

Within the BCS theory of superconductivity (SC), it became clear long ago [B1.10] that pairing of electrons in the spin-singlet state is effectively destroyed by an exchange mechanism arising from strong Coulomb interactions between the valence electrons. In a ferromagnetically (FM) ordered state, this exchange interaction tends to align the spins of electrons within a Cooper pair in parallel, thereby effectively preventing the pairing. Likewise, within the standard heavy-fermion (HF) approach, the Kondo effect quenches the on-site magnetic moment below the Kondo temperature (T_K) by spin fluctuations (flips caused by interactions between the conduction electrons and localized f -electrons of the magnetic ions), thereby destroying pairs. However, such antagonism can be effectively avoided if the HF behaviour does not involve Kondo scattering [B1.11, B1.12].

Although these three phenomena — magnetism, superconductivity and heavy-fermion behaviour — have been considered in the past to be mutually

antagonistic, the following findings clearly establish their possible coexistence (for a recent review, see Reference B1.3). A distinctive class of f -electron Ce- or U-based systems [B1.2, B1.3, B1.13, B1.14] convincingly shows that HF behaviour may coexist with SC. Most importantly, the SC pairing occurs among the heavy quasiparticles rather than within a band of light electrons, as was first demonstrated in CeCu_2Si_2 [B1.15] and uranium HF compounds [B1.16, B1.17]. In these materials, the scale of the specific-heat anomaly at the superconducting transition temperature T_{SC} clearly demonstrates not only a large density of states associated with itinerant quasiparticles but, more fundamentally, that the SC energy gap opens up within the band of heavy quasiparticles. Since the strong mass enhancement in HF systems goes hand-in-hand with a dramatic renormalization of the heavy quasiparticle bandwidth, the characteristic quasiparticle velocity (Fermi velocity) is reduced by several orders of magnitude. This circumstance violates the fundamental requirement for phonon-mediated pairing, specifically that the sound (phonon subsystem) velocity is much lower than the quasiparticle velocity — the so-called time-delayed charge-charge interaction [B1.3, B1.18] — which then fails to suppress the direct Coulomb repulsion, making the phonon coupling mechanism ineffective. This fact alone indicates that the attractive interaction between the quasiparticles is probably not provided by the electron-phonon interaction as in ordinary BCS superconductors, but rather calls for an alternative mechanism which is offered by various spin-fluctuation models [B1.1, B1.2, B1.8, B1.18 B1.19] of magnetically mediated SC.

Furthermore, in these HF materials SC may coexist and couple with magnetism. In fact, many f -electron HF systems exhibit SC deep within magnetically ordered states, suggesting that magnetism may promote rather than destroy the superconductivity [B1.3]. It is remarkable that in this class of materials the same set of heavy quasiparticles apparently supports both the magnetism and superconductivity [B1.13, B1.14]. In particular, both SC and HF behaviour are suppressed in CeCu_2Si_2 when magnetic Ce^{3+} ($4f^1$) ions are replaced by nonmagnetic La^{3+} ($4f^0$) ions [B1.15]. Coexistence of superconductivity and magnetism thus constitutes a clear distinction

from other classes of SC magnetic materials [B1.20–B1.23] where fundamentally different electron subsystems are responsible for the two phenomena.

Although there is a growing consensus that HF f -electron materials do exhibit unconventional forms of magnetically mediated SC, the majority of systems studied so far support unconventional spin–singlet pairing mediated by antiferromagnetic (AFM) fluctuations [B1.3, B1.13–B1.19], as opposed to ferromagnetic coupling, which is expected to adopt a spin–triplet configuration. However, an increasing number of observations in uranium HF compounds clearly demonstrate coexistence of SC and ferromagnetism. So far, this list includes UGe₂ [B1.4], URhGe [B1.5], UIr [B1.6] and UCoGe [B1.7]. In all of these materials, the SC state is detected within the FM ordered state, at either ambient or elevated pressures.

In the theory of magnetically mediated superconductivity, it is important that the ferromagnetism itself is of itinerant character, similar to that in the canonical d -electron ferromagnets Fe, Co or Ni. In the majority of the HF compounds, the $5f$ orbitals are more localized, due to dominance of the strong intra–atomic Coulomb repulsion energy over corresponding bandwidths. However, in this group of compounds the $5f$ electrons seem to exhibit rather itinerant behaviour as a result of hybridization (mixing) with conduction band states [B1.4, B1.24, B1.25]. This point requires somewhat deeper consideration.

Conventionally, electrons in solids are classified as either itinerant or localized. In strongly correlated electron systems, specifically HF systems, such a clear distinction is often obscured, since signatures of both pictures appear [B1.13, B1.14]. Here the strong Coulomb repulsion suppresses charge fluctuations at each site, leaving only spin and orbital degrees of freedom of localized states. These localized states interact with conduction electrons, and thereby affect one another. Heavy fermions are typically described by the Anderson–Kondo lattice models of coupled itinerant and localized electrons originating from different orbitals, in particular using a two–fluid description [B1.26]. The possibility that the same electrons might simultaneously exhibit both localized and itinerant characteristics due to strong Coulomb interactions

has developed into a duality problem [B1.27] which, in fact, speaks to the heart of the debate concerning the nature of f electrons in condensed matter systems — are they localized, itinerant or of a dual nature (partially localized and partially itinerant)? In U- and Pu-based HF materials, a segregation has been proposed in which some of the $5f$ electrons are localized while the rest are itinerant. It has been suggested that two of uranium's three $5f$ electrons are localized close to the ionic core to produce AFM order, while the remaining f electron is delocalized to ensure SC in UPt_3 [B1.28] and UPd_2Al_3 [B1.29, B1.30]. Similarly, four of the five plutonium f electrons are suggested to be localized and one to be itinerant in order to account for both magnetism and SC in PuCoGa_5 [B1.31]. Although such a duality model offers a transparent mechanism for producing quasiparticle mass enhancement — the exchange interaction between the itinerant and localized f electrons — it fails to receive support from de Haas van Alphen (dHvA) experiments [B1.32]. Moreover, the huge amount of condensation entropy (on the order of the spin entropy) released at the SC transition clearly indicates that spins of *all* local moments participate in the formation of the SC order parameter [B1.16]. In general, it is hard to find an explanation within the existing duality models of how competition between intra-atomic Coulomb interactions and anisotropic hybridization of f electrons (both on the order of eV) can differentiate between indistinguishable intra-atomic electrons and result in a ground state of coexisting magnetism and SC which is controlled by f electrons on an energy scale of 1 meV [B1.33]. The situation is even more confusing if a *single* f electron, such as in cerium, were to display localized and itinerant character *simultaneously*, as is required within the duality model(s) in, for instance, CeCu_2Si_2 [B1.15], CeIrIn_5 [B1.33] and other Ce-based HF superconductors, to account for coexisting magnetism and SC. The electronic duality proposed for many different HF systems exhibiting simultaneous SC and magnetism would require *the same* f -electron to display both localized and itinerant nature *simultaneously*. This fundamental problem requires a new conceptual framework in which an appropriate description of strong electronic correlations with theoretical access to low energy scales must be a key ingredient [B1.33].

Here we propose a specific concept that may supply the necessary requirement of simultaneously itinerant and localized electrons: formation of a spin–polaron band in which quasiparticle excitations of a low energy scale (several meV) around the Fermi energy (E_F) are responsible for HF behaviour, SC and magnetism.

The $5f$ electron duality problem is still debated in UGe_2 , which is proposed to be viewed as a two–subset electronic system, where some of the $5f$ electrons are localized and responsible for the ferromagnetic moment and huge magnetocrystalline anisotropy, while the remaining $5f$ electrons are itinerant and responsible for unconventional SC [B1.34]. The nearest distance between U atoms in UGe_2 , 0.39 nm, far exceeds the Hill limit, so without hybridizing with conduction electrons, the $5f$ electrons will be localized [B1.3, B1.35]. The Curie–Weiss–like temperature dependence of the susceptibility, the strong anisotropy, the large orbital moment of the U atom, the lack of induced magnetization at Ge sites and several other features [B1.3, B1.35, B1.36] all indicate a local character of $5f$ electrons in UGe_2 . On the other hand, there is strong experimental evidence for their itinerant nature. In particular, UGe_2 exhibits rather good agreement between specific heat [B1.35, B1.37] and de Haas van Alphen [B1.38–B1.40] results, which both attest to the itinerant character of the heavy quasiparticles; these data yield an effective mass $m^* \sim 10\text{--}25m_0$ at ambient pressure (m_0 is the free electron mass), similar to m^* in the itinerant–electron $3d$ ferromagnet MnSi. Furthermore, itinerant behaviour of the $5f$ electrons in UGe_2 is suggested by Hall–effect [B1.41] and muon spin relaxation [B1.42] measurements and is also frequently discussed for other uranium HF compounds [B1.28, B1.43]. The band picture is also consistent with spontaneous magnetization with non–integer Bohr magneton (μ_B) values per atom — $1.48\mu_B$ in UGe_2 [B1.4, B1.35], $0.42\mu_B$ in URhGe [B1.5], $0.5\mu_B$ in UIr [B1.6] and $0.03\mu_B$ in UCoGe [B1.7] — which is significantly smaller than the Curie–Weiss moment ($2.7 \mu_B/\text{ion}$ in UGe_2 [B1.35]) detected in the paramagnetic state above T_{Curie} — again similar to $3d$ band magnetism in MnSi [B1.44].

The magnetism in itinerant FM systems originates from exchange splitting of the band states rather than from strongly localized electrons. The mass enhancement comes from an extreme renormalization of band widths (Δ) — from $\Delta_0 \sim 1\text{--}10$ eV, typical of conventional metals, to renormalized $\Delta \sim 0.001\text{--}0.01$ eV in the canonical HF systems in which the f -electron degrees of freedom are typically modeled as hybridized with conduction band states to yield heavy itinerant quasiparticles that form extremely narrow spin-split bands in the vicinity of the Fermi surface [B1.24]. In the FM state, within such a spin-polarized band the heavy quasiparticles would have difficulty forming ordinary spin-singlet Cooper pairs but may instead select unconventional configurations [B1.4, B1.35] that involve non-zero spin and angular momentum states analogous to those in ^3He , in which a spin-fluctuation mechanism is responsible for the formation of spin-triplet pairs [B1.1]. Thus we arrive at a familiar picture of a band of delocalized states, albeit rather heavy, that would be responsible for FM and SC. However, the nature of this band and the nature of said delocalized states (heavy quasiparticles) both have yet to be determined.

The standard theory for the formation of the extremely narrow high mass bands characteristic of heavy fermion metals, such as UGe_2 , starts from a set of strongly localized f -electrons. The appearance of a new (low) energy scale in this approach results from hybridization with the delocalized conduction states and strong correlations within the f -shells. A different approach, that we wish to develop here, starts with a delocalized band carrier whose transport depends upon the strength of its coupling with excitations of the medium. This is similar to the case of a lattice polaron [B1.45] (LP), where in the limit of strong coupling an electron accompanied by lattice modes (displacements of ions) forms a quasiparticle in which a local distortion of the crystal structure follows the charge carrier adiabatically and whose bandwidth Δ_{LP} is reduced by up to 4 orders of magnitude relative to that of ordinary electrons in conventional metals [B1.46]. At low temperature, as long as the polaron is still much lighter than the atoms composing the medium, the charge is then delocalized within the LP band [B1.47, B1.48]. A remarkable collapse of Δ_{LP} at higher temperature marks

a crossover from coherent band dynamics to incoherent hopping of localized states, analogous to the so-called “dynamic destruction of the band” [B1.49, B1.50] for the tunneling dynamics of heavy particles, such as protons, isotopic defects, or muons and muonium [B1.51]. In close analogy, the exchange interaction (J) between a free carrier and local spins can cause electron localization into a FM “droplet” on the scale of the lattice spacing in a paramagnetic (PM) or AFM “sea” [B1.47]. This charge carrier, accompanied by reorientations of local spins, forms a *spin polaron* [B1.46, B1.47, B1.52] (SP) — a “giant spin molecule” [B1.53] — with a large composite spin (S). As in the case of the LP, formation of a SP profoundly renormalizes the “bare electron” band into an extremely narrow ($\Delta_{SP} \sim 0.001\text{--}0.1\text{eV}$) spin-polaron band, which will favour coherent SP band dynamics at low temperature as long as spin fluctuations are suppressed [B1.46, B1.47].

Within this conceptual framework the *composite quasiparticle* (spin polaron) consists of the light, initially delocalized bare carrier (say, an s - or p -electron) from the initially non-renormalized band (Δ_0) which undergoes localization within the SP, and a set of local f -spins confined within the scale of the electron’s wavefunction. Such a composite quasiparticle is free to propagate within the renormalized, though coherent, SP band (Δ_{SP}) *via* coherent reorientations of local f -spins [B1.47] in essentially the same way as another composite quasiparticle — the famous Landau lattice polaron [B1.45] (a bare electron plus lattice displacements or phonons). Once coherence among such spin polarons is established within the SP band, a remarkable result is that heavy f -like quasiparticles (SP) become part of the Fermi surface. We specifically note that within this framework the heavy quasiparticle is not an f -electron but the composite quasiparticle, a SP, formed as a result of $s(p)\text{--}f$ interaction.

Regardless of these heavy quasiparticles’ origin, an issue of a fundamental importance is that, being part of the Fermi surface, they should obey the principles of the Landau Fermi liquid — in particular, the counting rule or Luttinger’s theorem [B1.54], which states that, in non-interacting electron band theory, the volume of the

Fermi surface (V_{FS}) counts the number of conduction electrons (n_e). For interacting systems, this rule changes [B1.55–B1.57] to manifest a remarkable result that the local spin states (n_{spins}) are also included into the sum: $2V_{\text{FS}}/(2\pi)^3 = n_e + n_{\text{spins}}$. Therefore, even though f -electrons are localized as magnetic moments at high temperature, they contribute to the Fermi surface volume in the heavy Fermi liquid [B1.57]. This fundamental point of the heavy fermion physics is often discussed in terms of the transformation from a “small” Fermi surface containing only conduction electrons to a “large” Fermi surface which includes both conduction electrons and local spins [B1.56, B1.57]. Related issues arise in the context of a quantum critical point separating the heavy-fermion paramagnet from the local moment magnet, at which point the Fermi surface contracts from a large to a small volume [B1.56, B1.57]. We argue that formation of a spin-polaron band may not only give a natural description of how f -spins, being local moments, nevertheless acquire itinerancy (the duality problem), but may also pave a way to understanding of how Luttinger’s theorem works in strongly correlated materials. Such an approach finds its experimental confirmation in quantum oscillatory studies, Hall measurements or optical experiments, all of which indicate that the Fermi surface reconstructs to include f -spins at low temperature or contracts when composite quasiparticles disintegrate at a quantum critical point [B1.57].

In $5f\text{UGe}_2$, formation of an extremely narrow spin-polaron band might be expected to occur in a manner very similar to the SP band formation in $4f$ systems [B1.46], since the $p(d)$ - f exchange constant in UGe_2 is rather large ($J = 0.44$ eV) [B1.25], comparable to that found in the $4f\text{Eu}$ and Sm chalcogenides [B1.46] where $J \approx 0.5$ eV. Dramatic renormalization of such a SP band is expected to be associated with a change in the coherence properties and will go hand-in-hand with a significant increase of the electron effective mass, which might allow for the application of general concepts developed for the coherent-to-incoherent crossover of the heavy particle tunnelling dynamics [B1.49, B1.51]. For such particles, one encounters different behaviour in metals and insulators due to the essentially different spectral

properties of the environments: incoherent dynamics take over at high temperature ($k_B T \gg \Delta_{SP}$) in insulators while suppression of the coherence in a metal is expected at temperatures as low as $k_B T \sim \Delta_{SP}$ [B1.49, B1.51]. Thus at high temperature, the SP dynamics are characterized by incoherent hopping (diffusive) transport and the band picture, with its Bloch states, breaks down. However, in the low-temperature limit, the band picture manifests itself in coherent transport of heavy quasiparticles — the spin polarons. Such thermal destruction of spin-polaron bands has recently been reported in correlated $3d$ -electron semiconductors [B1.58] and $5d$ -electron metallic host [B1.59]. Thus, a description involving SP allows one to arrive at results qualitatively similar to those produced by the standard approach to heavy fermion systems, albeit without the involvement of Kondo screening.

Here we present spectroscopic evidence, obtained by positive muon spin rotation (μ^+SR), for spin polarons in UGe_2 , confined within $R = 0.25(1)$ nm, with a high spin of $S = 4.3 \pm 0.3$. At low temperature, SP tend to form a narrow spin-polaron band in the vicinity of E_F , profoundly modifying the magnetic, transport, optical and thermodynamic properties of the host.

To develop a physical picture we consider a charge carrier (electron which has a strong exchange interaction (J) with surrounding magnetic ions [B1.52, B1.53]. In a magnetic system, the electron's energy depends strongly on the magnetization, with the minimum energy achieved by FM ordering [B1.46]. As long as the direct coupling between ions is comparatively weak, the indirect coupling of magnetic ions mediated by this shared electron can cause local FM ordering accompanied by strong electron localization [B1.46, B1.47, B1.52, B1.53, B1.60]. Such localization inevitably involves a significant increase of the electron's kinetic energy — which can, however, be compensated by the corresponding energy reduction associated with the local FM ordering of the ions mediated by the aforementioned electron. Thus, the increase of electron kinetic energy, due to confinement, may be compensated by the difference in exchange energy between the final locally saturated FM region and the initial paramagnetic, AFM or even non-saturated FM state. Therefore, the electron tends to

establish and support this local ordering, thereby forming a FM “droplet” over the extent of its wave function (typically on the order of the lattice spacing, a) [B1.46, B1.47, B1.52 B1.53]. This charge carrier, accompanied by reorientations of local spins to form its immediate FM environment, together behave as a single quasiparticle — a spin polaron — with a composite spin (S) [B1.46, B1.47, B1.60]. In magnetic semiconductors (MS), in the process of electron localization at a donor impurity (an implanted muon in our case), the discussed increase in the kinetic energy, assisted by the entropy change (ΔS) due to ordering within the SP, is compensated by the combined efforts of the exchange interaction and the Coulomb interaction with the corresponding donor. The net change in the free energy

$$\Delta F = \frac{\hbar^2}{2m^*R^2} - \frac{Ja^3}{R^3} - \frac{e^2}{\epsilon R} + T\Delta S \quad (\mathbf{B1.1})$$

has a minimum as a function of R , which represents the radius of electron confinement (or equivalently, the extent of its wavefunction). ΔF decreases with decreasing R until $R \ll a$, at which point the electron wavefunction no longer overlaps even the nearest ions, and the exchange term vanishes [B1.46]. The exchange energy [second term in equation (B1.1)] is optimized by maximizing the SP electron’s net overlap with the f -shells of nearby ions. The Coulomb interaction [third term in equation (B1.1)], important in MS [B1.58, B1.60–B1.65], is effectively screened in metals [B1.59, B1.66]. Once the Coulomb interaction can be neglected, one immediately arrives at the initial idea of de Gennes on carrier confinement within free delocalized SP [B1.52]. In UGe_2 , the high electron concentration ($\sim 10^{22} \text{cm}^{-3}$) [B1.41] ensures that the screening length of the Coulomb term is much smaller than R . At low temperature, the entropy term $T\Delta S$ is also small. Each of the remaining two terms in equation (B1.1), namely the electron’s kinetic energy and the exchange energy, is on the order of an eV and not only far exceeds any other energy scale in the problem but also reduces the length scale for electron confinement to within less than one unit cell [B1.59, B1.66].

Thus far, extensive studies of the formation and dynamics of spin polarons in magnetic semiconductors, magnetoresistive perovskites and related compounds [B1.46, B1.61 B1.67] have been restricted to a quite narrow temperature range close to

a magnetic phase transition (large polaron region). Different macroscopic techniques (*e.g.*, SQUID magnetometry or magnetotransport) are spatially averaged, providing little information on possible spatial inhomogeneities. The spatial resolution of magneto–optical measurements [B1.68], photoluminescence [B1.69] or soft X–ray magnetic circular dichroism [B1.70] is severely restricted by wavelengths on the order of 10 nm. Studies of spin polarons in MS by microscopic techniques like NMR [B1.71] or Raman scattering [B1.72] are restricted to the close vicinity of a transition by limitations in their sensitivity that makes it essentially impossible to detect a spin polaron as it shrinks towards the sub–nm scale. Although the significantly better spatial resolution of the small–angle neutron scattering technique made it possible to detect spin polarons of about 1.2 nm size in magnetoresistive perovskites just above the transition temperature, this technique is still limited to a narrow temperature range by the neutron wavelength of about 0.5 nm, which made it impossible to detect smaller spin polarons [B1.73]. In general, the limited sensitivity and/or spatial resolution of many different techniques precludes detection of a SP of subnanometer size.

Here the unique sensitivity of polarized positive muons as a local magnetic probe makes muon spin rotation and relaxation (μ^+ SR) [B1.74–B1.76] ideally suited for mapping the magnetic state on the atomic (sub–nm) scale. As the spin polaron expands toward a 10 nm scale, this sensitivity advantage is lost, making μ^+ SR complementary to a variety of other techniques mentioned above. This approach has already been applied to studies of SP in different materials ranging from insulators (including AFM [B1.77]) to itinerant ferromagnets [B1.66] analogous to earlier studies of nonmagnetic semiconductors [B1.78], which revealed the details of electron capture to form the muonium ($\text{Mu} \equiv \mu^+ e^-$) atom (a light analogue of the H atom) [B1.79–B1.82]. Assorted SP have recently been detected in *4f* and *3d* magnetic semiconductors [B1.58, B1.60, B1.62–B1.65, B1.83], in the *5d* and *3d* correlated metals [B1.59, B1.66] and in a quasi–1D AFM insulator [B1.77] *via* μ^+ SR spectroscopy.

Single crystals of UGe_2 for the current studies were grown by the Czochralski technique under purified Ar atmosphere with a water-cooled crucible and radio-frequency heating. Single crystals were oriented using a white beam X-ray backscattering Laue method, sparkcut and etched to remove the oxidised surface. The electrical resistivity was measured by the conventional four-probe method between 1.8 and 300 K in zero magnetic field. Small crystals cut off the single crystals used in μ^+ SR experiments showed a residual resistivity ratio $\text{RRR}=62$ and $T_{\text{curie}}=52.6$ K.

Time-differential μ^+ SR experiments, using 100% spin-polarized positive muons implanted into these samples, were carried out on the M15 surface muon channel at TRIUMF using the *HiTime* spectrometer. At high temperature, Fourier transforms of the μ^+ SR time spectra in a magnetic field (\mathbf{B}) transverse to the initial muon spin polarization direction and parallel to the easy magnetization direction (\mathbf{a} axis) of the single crystal of UGe_2 exhibit a single peak at the muon frequency $\nu_\mu = \gamma_\mu B / 2\pi$ (where $\gamma_\mu / 2\pi = 135.53879$ MHz/T is the muon gyromagnetic ratio). However, below $T \approx 100$ K the μ^+ SR spectra change abruptly to reveal two peaks (Figure B1.1) — a characteristic SP doublet similar to that in another itinerant FM system, MnSi [B1.66]. The evolution of SP signals with temperature is presented in Figure B1.2. These two peaks are also shifted to lower frequencies (although to a lesser amount than in MnSi) relative to the single peak (not shown in Figure B1.1) detected in a reference sample (CaCO_3), which occurs at the bare muon frequency. The smaller shift detected in UGe_2 is consistent with its lower magnetization compared to that in MnSi, and similar to the corresponding shifts in magnetic semiconductors, which empirically scale with the magnetization [B1.60, B1.62]. Utilizing the same experimental setup as used for measurements with MnSi [B1.66] ensured that there is essentially no background in our UGe_2 signals — the muons that miss the sample and stop in CaCO_3 are detected in a different combination of counters and routed to independent histograms which form the reference signal. This reference frequency does not depend on temperature, since CaCO_3 is nonmagnetic, and therefore provides an independent monitor of the applied magnetic field.

There are, however, several important differences in the Fourier spectra observed in MnSi and UGe₂. First, in MnSi the characteristic two-frequency spectra persist up to room temperature, whereas the doublet pattern is detected only below about 100 K in UGe₂. Second, the amplitudes of the two lines are temperature independent and almost equal in MnSi over the entire temperature range, whereas in UGe₂ they exhibit a remarkable temperature dependence: they are temperature independent below about 80 K, but between 80 K and 100 K the μ^+ SR doublet spectra exhibit a strong temperature dependence with increasingly different amplitudes of the two lines (Figure B1.3). We discuss these two essential points below.

Observation of two peaks in the Fourier spectra prompted the authors of Ref. B1.84 to suggest two magnetically inequivalent sites occupied by the positive muon in UGe₂. Although such an approach constitutes the conventional assignment of multiple signals in a magnetically ordered state, fast spin fluctuations make this interpretation irrelevant in the paramagnetic phase [B1.59, B1.60, B1.62–B1.66], while possible Knight shifts from the conduction electrons are typically at least 2–3 orders of magnitude smaller than the characteristic splittings detected in this experiment [B1.74]. Moreover, the two peaks do not follow the temperature dependence of the magnetization, which clearly indicates that the muon does not stay “bare” and act as local magnetometer. Instead, while one peak goes up in frequency the other goes down as temperature varies (Figure B1.4) — the fingerprint of a muon–electron bound state [B1.75]. Furthermore, a qualitative change in the amplitude ratios within the doublet (Figure B1.2 and Figure B1.3) is obviously incompatible with the two-site interpretation, which assumes a constant muon site occupation ratio. Finally, in the PM state the Knight shifts are expected to be linear with magnetic field, which contradicts the experiment (Figure B1.5). This line of argumentation is similar to that presented for another HF superconductor, UBe₁₃, which also exhibits SP [B1.85].

Instead, we argue that the two lines shown in Figure B1.1 and Figure B1.2 constitute the characteristic signature of a coupled muon–electron spin system in high magnetic field [B1.59, B1.60, B1.62–B1.66, B1.74, B1.75, B1.78, B1.86]. The

solution of the Breit–Rabi Hamiltonian which governs a muon–electron spin system yields 4 eigenvalues (due to 4 possible combinations of spins) corresponding to 4 energy levels with different allowed transitions [B1.78]. In high magnetic field, the two allowed transitions correspond to the two allowed muon spin–flip transitions between states with fixed electron spin orientation; the frequency splitting between these two transitions is determined by the muon–electron hyperfine interaction A [B1.74, B1.75, B1.78]. Moreover, we argue that the observed bound state is a spin polaron. In a PM or metallic (or both) environment, the strong pair exchange interaction of the bound electron with itinerant spins (spin exchange [B1.74, B1.78]) would result in rapid spin fluctuations of this electron, averaging the hyperfine interaction to zero — which, in turn, would result in a collapse of the doublet into a single line at ν_μ (see Ref. B1.86 for details), if the local FM ordering mediated by this electron did not hold the electron's spin orientation “locked” [B1.59, B1.60, B1.62–B1.66, B1.85, B1.86]. In metals, however, even the protective local FM environment of a SP does not ensure observation of the doublet unless the SP spin (S) is decoupled from its magnetic environment [B1.59, B1.66, B1.86]. Such decoupling is possible in high B when the Zeeman energy of S exceeds an exchange interaction (I) between local spins [B1.60, B1.85]. This is the case in magnetic insulators where the SP doublet is detected up to very high temperature [B1.60, B1.62–B1.65]. In metals, RKKY interactions make I much stronger, so that decoupling would require a very high magnetic field [B1.85] that is inaccessible in the current experiment. In UGe_2 , above about 100 K, spin exchange with the magnetic environment effectively averages the muon–electron hyperfine interaction, causing the collapse of the doublet into a single peak, as observed, discussed and presented here in Figure B1.2 and Figure B1.4.

Such a collapse by no means signifies that the SP does not form in UGe_2 above 100 K; we just do not see its fingerprint, which is a characteristic doublet [B1.85, B1.86]. The abrupt appearance of a SP doublet below about 100 K is possible due to another effective decoupling mechanism — the opening of a spin gap due to crystal

field splitting of the U ion's spin excitation, characteristic of U compounds [B1.34]. Crystal field splitting eliminates low-lying spin excitation from the spectrum, making spin exchange of the SP spin (S) with its magnetic environment rather ineffective. A detailed evaluation of the crystal field splitting shows a spin gap of about 120 K between the almost degenerate ground state and the first excited state [B1.34]. This circumstance makes it possible to detect the characteristic SP doublet below about 100 K in UGe_2 , much like that in another heavy-fermion compound, UBe_{13} , that exhibits a spin gap of about 180 K [B1.85]. Likewise, optical conductivity exhibits a dramatic reduction of the spin scattering rate below the characteristic energy of about 120 K [B1.87]. By contrast, very strong crystal field splitting, characteristic of $3d$ systems, effectively prevents spin exchange in MnSi , enabling detection of the SP doublet all the way up to room temperature [B1.66] in that $3d$ -electron counterpart of UGe_2 . A spin gap opening in the U ion spin excitation spectrum, although a necessary condition, does not prevent spin exchange between SP and conduction electrons, which would cause the doublet to collapse. However, the dominance of the orbital moment of U ions in UGe_2 [B1.88] makes spin exchange with conduction electrons (which have zero orbital moment) again rather ineffective due to the orbital moment conservation law. Thus, the conditions for observation of SP in a metallic or PM (or both) environment are rather specific: one must eliminate any possible spin exchange mechanism in order to prevent the muon-electron hyperfine coupling from averaging to zero. However, the mere observation of the characteristic doublet in the μ^+ SR spectra of a metal constitutes strong evidence for SP formation [B1.59, B1.66, B1.86]. The evolution of the two signals within the doublet as a function of temperature (Figure B1.2 and Figure B1.4) and magnetic field (Figure B1.5) is consistent with that of the muon-electron bound state when the electron spin is locked to the SP spin, providing strong support for this picture.

Temperature and magnetic field dependencies of the SP signal frequency splitting (within the doublet), $\Delta\nu$, provide information on the characteristic size (the localization radius, R , for the electron confinement) through the hyperfine coupling

(A) and determine the composite spin (S) of the SP [B1.60, B1.86]. Within a mean field approximation [B1.89], $\Delta\nu$ is proportional to a Brillouin function. For $g \mu_B B \ll k_B T$, $\Delta\nu$ is a linear function of both B and $1/(T-T_c)$ [B1.60, B1.86]

$$\Delta\nu = A \left[\frac{g \mu_B B}{3k_B(T - T_c)} \right] (S + 1) \quad (\text{B1.2})$$

where k_B is Boltzmann's constant and T_c is the Curie temperature of UGe₂. At low T and high B , however, equation (B1.2) is no longer valid, as the composite spin (S) is fully polarized. Therefore, in a magnetic field high enough that the muon Zeeman energy exceeds the hyperfine coupling, $\Delta\nu$ saturates at the value of A [B1.60, B1.74, B1.75, B1.78]. In UGe₂, the splitting ($\Delta\nu$) saturates as a function of both inverse temperature (in a magnetic field $H = 1$ T) and H (at $T = 5$ K) at the same value, $A = 41 \pm 2$ MHz (see Figure B1.5).

For our model of a SP captured by a muon, the SP electronic wave function is an extended hydrogen or muonium (Mu) atom $1s$ function, for which the value of A scales as $A_{\text{vac}} (a_0/R)^3$, where R is the characteristic Bohr radius (radius of the electron confinement) and $A_{\text{vac}} = 4463$ MHz is the hyperfine frequency of Mu in vacuum (for which $R = a_0 = 0.0531$ nm — the Bohr radius of Mu in vacuum) [B1.75]. In UGe₂ at low temperature, the hyperfine coupling in the SP is about 100 times less than that for Mu in vacuum, implying that the radius of the electron confinement is $R \approx 0.25(1)$ nm. This is consistent with the muon being centred between two U atoms ($x=0.5, y=0.5, z=0.5$) giving a muon–U distance of 0.214 nm. As the f -orbital radius is 0.0527 nm, this muon position ensures the maximum overlap of the SP electron with U f -wavefunctions, resulting in a SP composed of one SP electron and the two nearest U ions. We can estimate the composite spin (S) for this SP. The magnetic moment for such a SP is determined by 2 fully polarized U ions, each having $\mu_U = 2.7\mu_B$ [B1.4], minus the SP electron's $1\mu_B$, since the SP electron spin is antiparallel to the composite SP spin at high temperature (see below). Meanwhile, $\mu_{\text{SP}} = 2\mu_U - 1\mu_B = g \cdot \mu_B \cdot [S(S+1)]^{0.5}$. From this relation, and accounting for the dominance of the orbital moment in UGe₂ (which causes $g = 0.8$) [B1.88], we find $S \approx 5$. On the other hand, fitting equation

(B1.2) to the μ^+ SR data in Figure B1.5 using $A = 41 \pm 2$ MHz and $g = 0.8$ yields $S = 4.3(3)$ and $T_c = 52(1)$ K, consistent with our estimate of S from the SP radius and T_{Curie} of our sample, respectively. At low temperature, the SP electron's spin flips to be parallel to the composite SP spin, causing the SP spin to increase to $S \approx 6$. For comparison, the SP detected in MnSi gives $A = 12 \pm 1$ MHz and $R \approx 0.4$ nm, corresponding to a rather large SP confinement radius within one unit cell of MnSi [B1.66]. On the other hand, the size of the SP found in UGe₂ is, in fact, the same as that in UBe₁₃ [B1.86], while in the *5d* correlated metal Cd₂Re₂O₇ at low temperature the SP contracts to a rather compact 0.15 nm [B1.59]. Apparently, in the orthorhombic structure of UGe₂ the SP prefers to localize within a uranium pair in order to maximize the gain in the exchange energy, which is necessary to ensure its localization.

Although the possibility of SP formation in AFM and PM states has long been anticipated [B1.46– B1.48, B1.52, B1.53] and experimentally established [B1.58– B1.73, B1.77, B1.85, B1.86] in a great variety of materials by many different techniques, its existence would seem to be incompatible with the FM state. The exchange contribution to SP stabilization amounts to the *difference* between the PM disorder (or AFM order) of the host and the FM order within the SP; in a fully saturated FM state the exchange contribution to the localization would be negligible, as the lattice spins are already aligned. Such an increased alignment prevents SP formation in the FM state, as well as when a sufficiently high magnetic field is applied in the PM state in Heisenberg ferromagnets [B1.60, B1.62, B1.63], where FM originates from localized electrons. In itinerant–electron ferromagnets, however, local spins are far from being saturated in the FM state, as evidenced by the rather low effective magnetic moments in UGe₂ [B1.4, B1.35], URhGe [B1.5], UIr [B1.6] and UCoGe [B1.7], as well as that in MnSi [B1.66]. Therefore, electron localization into a SP that completes the spin alignment within the fully saturated SP core region is clearly possible within an itinerant–electron FM ordered phase [B1.66]. Specifically, in UGe₂ the U atom spin saturation increases from its low temperature value

$\mu_U = 1.5\mu_B$ to the fully polarized value $\mu_U = 2.7\mu_B$, making a huge difference in the exchange energy and ensuring electron localization *via* SP formation.

The exchange interaction governs spin polaron formation and dynamics in UGe_2 , since the Coulomb interaction is effectively screened [see Equation (B1.1)]. Therefore the role of the muon, which may be important for SP formation in MS [B1.60, B1.62– B1.65] and insulators [B1.77], is reduced to that of an “innocent bystander” microscopic magnetic probe in metals. We argue that once the host lattice is populated by free SP, one of them is captured by the muon, as in $\text{Cd}_2\text{Re}_2\text{O}_7$ [B1.59], MnSi [B1.66] and UBe_{13} [B1.85], to reveal the fingerprint of a bound muon–electron state — the characteristic SP doublet.

In UGe_2 , the dynamics of such SP clearly shows a qualitative change around 80 K. At high temperature, the asymmetric doublet shape (Figure B1.2, right panel) indicates the nearly static character of the SP. The spectral weights (populations) of the spin–up and spin–down states, being determined by a thermal (Boltzmann) distribution, should be almost equal as the Zeeman splitting $\mu_{SP}H \ll k_B T$, which is apparently not the case (Figure B1.3). The temperature fails to equilibrate the amplitudes (populations) of the spin–up and spin–down states because the composite SP spin (S) is strongly decoupled from the magnetic environment. This decoupling occurs because spin exchange with both local spins and conduction electrons is rather ineffective, making it possible to detect the characteristic SP doublet in the first place (see discussion above). The difference in population of the two spin states is due to one of them being parallel to the magnetic field, resulting in a long–lived eigenstate, while the other state (antiparallel to the field) is short–lived or unpopulated [B1.59]. The temperature dependence of the corresponding line widths (relaxation rates) clearly reflects this difference: at high temperature the line width of the stable eigenstate (higher frequency line) is much less than that of the other state (Figure B1.2 and Figure B1.6). Similar asymmetric distributions of the spectral weight between the two lines of the SP doublet are detected in magnetic semiconductors and insulators where the SP is found to be static [B1.60, B1.62– B1.64, B1.77].

A remarkable crossover occurs at about 80 K, where not only do the line widths become equal (Figure B1.6), but also the spectral weights (corresponding state populations) of the two lines within the doublet effectively equilibrate (Figure B1.3), clearly indicating the onset of the effective spin–exchange mechanism *within the SP system*, as other spin–exchange channels are rather ineffective (see above). This marks a crossover from the static SP to itinerant spin polaron behaviour. At high temperature, the characteristic length (in Angstroms) of the ferromagnetic fluctuations determined from neutron measurements [B1.90], $\xi_{\text{FM}} = 3.45/(T/T_C - 1)^{1/2}$, is much less than the SP size, $2R$, which causes strong SP localization due to the significant energy shift of the nearest equivalent SP positions within the lattice (so-called “static destruction of the band” [B1.49, B1.51]). At lower temperature, once ξ_{FM} exceeds the SP size, energy levels equilibrate within the length scale of ξ_{FM} , which causes SP delocalization. A simple estimate shows that ξ_{FM} becomes equal to $2R$ at 77 K, which agrees well with the experiment. Thus, a crossover at about 80 K (Figure B1.2, Figure B1.3 and Figure B1.6) marks a fundamental change from localized to itinerant SP behaviour in UGe_2 . A similar crossover in SP dynamics is found in correlated metallic $\text{Cd}_2\text{Re}_2\text{O}_7$, in which the classical Boltzmann distribution of the spectral weights breaks down to leave a uniform distribution within a narrow SP band [B1.59]. In UGe_2 , the small difference in amplitudes below 80 K (Figure B1.3, also found in Ref. B1.84) is due to the difference in Zeeman energy between the spin–up and spin–down states in the ferromagnetic environment. What is more fundamental is that the amplitudes or spectral weights of both lines are *temperature independent* below about 80 K (Figure B1.3), which clearly indicates temperature independent populations of the spin–up and spin–down states — which in turn is inconsistent with a localized SP but rather signifies its itinerant nature. Thus, our model suggests that the SP, captured by the muon, stays localized and is protected from spin exchange above 80 K; however, below 80 K it remains localized but undergoes active spin exchange with free itinerant SP. The increased length scale of the FM fluctuations ensures the remarkable itinerancy of the SP.

Another remarkable feature which accompanies the onset of the SP itinerancy at 80 K is that the majority of the spin states at high temperature (red circles in Figure B1.3) becomes a minority of spin states at low temperature (with the corresponding changeover of the black squares, Figure B1.3). The distribution of the spin states is controlled by the Hund's rule, which ensures that the SP electron's spin (s) in UGe_2 will be parallel to electron spins of the unfilled $5f$ orbital, similar to that in unfilled $3d$ orbital in MnSi [B1.66] or CdCr_2Se_4 [B1.64] and in marked contrast to completely filled $4f$ orbital in Eu-based materials [B1.60, B1.63] (see Ref. B1.64 for a discussion on the Hund's rule control of the spin states within the SP). In UGe_2 , the orbital magnetic moment of the U ion is twice as large as, and antiparallel to, that of the U ion spin [B1.88], so that the SP electron spin (s) in the majority spin state finds itself to be opposite to the aggregate spin (S) of the SP at high temperature. The remarkable crossover at 80 K indicates that the majority of spin states prefer the orientation of the SP electron spin (s) to be parallel to S at low temperature. As the SP electron spin (s) couples to spin moments of U ions, and not to their orbital moments, this parallel orientation reveals the departure from Hund's rule, with a corresponding increase of the Hund energy. Such an increase is very unlikely unless it is compensated by a decrease of some other energy by at least as much. The compensation comes from the significant decrease in the kinetic energy of the SP in the process of its delocalization, which presents another indication of the SP itinerancy below 80 K. A crossover from the antiparallel orientation of s (with respect to S) to a parallel orientation within the SP, occurs for the fundamental reason of greatly reducing spin scattering, allowing for much higher SP mobility within the local FM environment and hence, within the FM fluctuations — which occurs once the size of the fluctuations exceed the SP size at lower temperature.

Thus, at high temperature the majority of the localized SP states have their electron spin (s) antiparallel to their aggregate spin (S) which is dominated by the orbital moments of U ions. Quite in contrast, at low temperature the majority of SP states are itinerant SP with their spin S still dominated by the orbital moments of U

ions but their electron spin (s) parallel to \mathcal{S} . A significant consequence of the crossover at 80 K is that at low temperature, magnetic moments of itinerant SP are parallel to those of U ions, once the latter order along the \mathbf{a} -axis below T_c , which suppresses spin-flip scattering events, providing greater SP mobility.

However, the remarkable itinerancy acquired by SP below 80 K does not mean they form a band at 80 K. Instead, spin polaron transport in UGe_2 just below 80 K is determined by hopping (diffusive) dynamics similar to the hopping dynamics of muon or Mu states in the regime dominated by “static destruction of the band” when dynamic fluctuations of the environment (phonons in the case of Mu) makes such hopping dynamics possible [B1.49, B1.51, B1.91, B1.92]. The latter regime is characterized by spatially inhomogeneous tunneling dynamics when the small size of the particle bandwidth compared to all other energy parameters of the crystal (specifically, the typical difference between energy levels at adjacent tunneling sites) restricts particle tunneling dynamics to undisturbed regions and causes strong localization outside such regions. Likewise below 80 K, spin polarons in UGe_2 acquire itinerancy in a *restricted space* within the size of the FM fluctuation (ξ_{FM}) once $\xi_{\text{FM}} > 2R$ (see above). At lower temperature, where ξ_{FM} exceeds the average distance between SP, polarons are no longer isolated but rather experience strong inelastic mutual spin-flip scattering, which again disables their coherent dynamics.

Evidence for the appearance at low temperature of spin-polarized itinerant carriers with magnetic moments of about $0.02\mu_B$ per U atom is present in several experiments on UGe_2 , including measurements of magnetic entropy [B1.34], muon spin relaxation in zero magnetic field [B1.42], neutron measurements and magnetic susceptibility [B1.93]. Optical studies [B1.87] indicate a suppression of spin-flip scattering below T_c with a significant increase of itinerant carrier effective mass to about $25m_0$. All of these facts indicate the formation of a spin-polarized band composed of heavy carriers at low temperature in UGe_2 . We argue that this band is a SP band. Such a SP band will form near T_c when FM fluctuations extend over the entire crystal and SP become completely delocalized. However, mutual spin-flip

scattering between SP, depending on the SP size and aggregate spin, makes their dynamics incoherent.

In fact, coherent SP transport is only possible in a spin-polarized band where spin-flip scattering is suppressed due to the absence of SP with the opposite spin state. In a FM state, such coherent transport of SP becomes possible due to splitting of the majority and minority spin subbands. This splitting may be viewed as Zeeman splitting due to spontaneous magnetization. As a result, a characteristic sharp double peak structure is formed in the density of states (DOS) at the Fermi level. In UGe₂, such splitting (Δ) is not large enough to leave the minority spin band empty [B1.4, B1.94]. The crucial point here is that $\Delta \ll W_{SP}$, where W_{SP} is the SP bandwidth. Therefore, the Fermi surface contains both majority and minority spin sheets. Position of the Fermi level determines the spin polarization, $P = (n_{\downarrow} - n_{\uparrow}) / (n_{\downarrow} + n_{\uparrow})$, which is essentially nonzero at low temperature [B1.95]. This remarkable feature not only ensures coherent band dynamics of SP, but is also of a fundamental importance to the superconducting state: NQR measurements have revealed that the spin-up band is gapped but the spin-down band remains gapless, thereby indicating the unconventional nature of SC in UGe₂ [B1.95].

The primary condition for the coherent band dynamics of SP is suppression of spin-flip scattering on the Fermi level when $\Delta(T) > 2k_B T$, where $2k_B T$ is the thermal broadening of the Fermi function. We find the characteristic temperature of coherent SP band formation from

$$2k_B T_{SPB} \cong \Delta(T) \quad (\text{B1.3})$$

In FM metals, spin splitting follows the bulk magnetization [B1.96]. According to neutron studies of the temperature dependence of the magnetic moment in UGe₂ [B1.35],

$$\Delta(T) \cong \Delta_0 \left(1 - \frac{T}{T_c}\right)^{0.3}, \quad (\text{B1.4})$$

where Δ_0 is the spin splitting at $T = 0$. On the other hand, following [B1.96]

$$\Delta_0 = P W_{SP} \quad (\text{B1.5})$$

according to our data (Figure B1.3), the difference between majority and minority spin SP states, $P = 0.12$, which is close to the spin polarization of charge carriers found by NQR [B1.95] at elevated pressures (1.17 and 1.2 Gpa): $P = 0.14$.

We determine the SP bandwidth from [B1.47]

$$W_{SP} = \frac{z\hbar^2}{m_{SP}a^2} \quad (\text{B1.6})$$

where z is a coordination number, m_{SP} is the SP mass and a is the lattice constant. For a crude estimate we use UGe₂ values $z = 4$, $m_{SP} = 25$ and $a = 0.4$ nm to get $W_{SP} \approx 70$ meV, $\Delta_0 \approx 8$ meV and to confirm that $\Delta \ll W_{SP}$. Then using (3) and (4) we arrive at the relation $T_{SPB} = 46 (1 - T_{SPB}/T_C)^{0.3}$ which, solved numerically, yields $T_{SPB} = 34$ K, in close agreement with a characteristic crossover temperature $T^* = 30$ K [B1.34, B1.35].

In UGe₂, this weak first-order transition (the crossover at ambient pressure) at T^* separates the high-temperature (high pressure) weakly polarized phase (FM1) from the low-temperature (low pressure) strongly polarized phase (FM2) [B1.35] (see Figure B1.7) and shows up as anomalies in resistivity [B1.4, B1.37], heat capacity [B1.34, B1.37], magnetization [B1.97] and magnetoresistivity [B1.34]. What is more fundamental is that this transition shows up as a distinct change in the Fermi surface as revealed by dHvA measurements [B1.38– B1.40]. The nature of the transition at T^* is not clear at the moment, but experimental results indicate it to be closely related to superconductivity in UGe₂ [B1.3, B1.4, B1.35]. It has been suggested that this transition is due to charge or spin density wave(s) or both. However, neutron studies do not detect any such phases [B1.35]. An alternative suggestion, which is also supported by our data, is that there is a first-order Stoner-type phase transition in the spin magnetization due to a sharp double peak in the density of states near E_F [B1.94]. In the latter scenario, both the FM1–FM2 and SC transitions are driven in the FM phase by tuning the majority spin Fermi level through one of two peaks in the density of states. The tuning parameter is the magnetization, which changes the topology of the Fermi surface for different spin species [B1.94]. Magnetization measurements

[B1.97] do indicate that the FM1–FM2 transition occurs at a particular spin splitting between the majority and minority spin bands, since the Fermi level passes through a sharp peak in the DOS for one spin species. A qualitative change in DOS at the FM1–FM2 transition is also supported by dHvA [B1.38– B1.40] and Hall [B1.41] measurements, although the nature of the spin bands and spin species is not discussed. We suggest that such a band is made of SP and the double–peak DOS is due to spin splitting of SP band, as discussed above. We argue that the FM1–FM2 transition may be a Stoner–type transition where coherent SP band dynamics sets in at $T^* = T_{\text{SPB}}$. This is consistent with an increase of the easy axis magnetic moment per U ion at T^* in the low temperature FM2 phase, with respect to that in FM1 [B1.97].

Further support for coherent SP band formation at T^* comes from the measurements of the local magnetic field shift on the muon (ΔB) with respect to external magnetic field B_0 (Figure B1.8). The local magnetic field on the muon (B) includes all contributions from the magnetic environment (from both local moments and itinerant species) but excludes a contribution from the hyperfine field of the electron that belongs to the SP captured by the muon. In other words, ΔB presents the magnetic field shift on the muon as if this muon stays bare and does not capture a SP, similar to the shift measured in EuS [B1.60]. It is determined as $\Delta B = B_0 - 2\pi(v_1+v_2)/2\gamma_\mu$, where v_1 and v_2 are the two frequencies presented in Figure B1.4, as they appear symmetrically split by $\pm A/2$ about the hypothetical bare muon frequency: $v_{1,2} = \pm A/2 + 2\pi(B+B_0)/\gamma_\mu$ [B1.60, B1.75, B1.78]. At high temperature, ΔB follows the bulk magnetization (measured in the same sample using a SQUID magnetometer). In this case, the itinerant species' contribution to the local field is small enough that both techniques result in similar measurements, mainly contributions from the local magnetic moments of U ions. However, below T_c where FM fluctuations extend over the entire crystal, spin polarons become completely delocalized and tend to screen the magnetic moment of a single localized SP captured by the muon, thereby reducing the magnetic field on the muon, which causes the deviation of ΔB from the bulk magnetization (Figure B1.8). This effect is analogous to Kondo screening in the single

magnetic impurity Kondo problem [B1.98]. The difference is that the canonical Kondo effect involves free electrons, while in our case the screening cloud consists entirely of itinerant spin polarons. In fact, deviation of ΔB from the bulk magnetization starts below T_c , which sets up a nonzero spontaneous internal magnetic field that determines the nonzero Zeeman splitting (Δ) between SP spin-up and spin-down species. However, this contribution stays small (although significant) above T^* once $\Delta(T) < k_B T^*$. A qualitative change sets in below $T^* = 30$ K (Figure B1.8) once $\Delta(T)$ exceeds this temperature (see above discussion). Formation of a coherent SP band causes effective Kondo-like screening of the muon-captured SP by itinerant spin polarons, which determines a strong reduction of ΔB below T^* , while the bulk magnetization (performed *via* SQUID measurements) continue to increase below T^* . We note that this Kondo-like screening of the muon-captured SP is only possible within the SP system.

Thus, a non-monotonic behaviour of the magnetic field shift on the muon with its maximum at T^* (displayed in Figure B1.8) might be explained by formation of a Kondo screening cloud made of SP within the spin-polaron band. The characteristic screening length scale of such a Kondo cloud can be estimated [B1.99] as $\xi = \hbar v_F / k_B T_K$, where v_F is the Fermi velocity of a SP within the SP band. Setting $T_K = T_{SPB} = T^*$ and getting $v_F \approx 3 \times 10^6$ cm/s (which is about 100 times less than that for electrons in a metal being renormalized by the effective mass) from the SP band width, $W_{SP} \approx 70$ meV, with the SP mass, $m_{SP} = 25m_0$, we arrive at $\xi \approx 0.7 \times 10^{-6}$ cm. For comparison, depending on the Kondo temperature, the Kondo cloud in a canonical system of a single magnetic impurity in a simple metal may have a significant extension of $\sim 10^{-4}$ cm [B1.100]. Although the characteristic size of a Kondo cloud made of spin polarons is about 100 times smaller than that in a canonical system, it is much larger than the SP size, which ensures effective screening within the spin polaron band.

Formation of such a narrow SP band should be directly relevant to a large electron mass enhancement and critical spin fluctuations as are inferred from optical

conductivity measurements in UGe_2 [B1.87] and several other strongly correlated materials including UPd_2Al_3 [B1.101], UPt_3 [B1.101], $\text{Cd}_2\text{Re}_2\text{O}_7$ [B1.102], MnSi [B1.103] and UBe_{13} [B1.104]. At low temperature, all of these materials exhibit a narrow peak separated by a hybridization gap from a broad mid-infrared excitation feature in the frequency-dependent optical conductivity, which are associated with a low-spectral-weight, low-energy “heavy fermion” Drude peak and a high-spectral-weight, high-energy interband transition, respectively. In the latter three materials, observation of itinerant spin polarons [B1.59, B1.66, B1.85] appears to be associated with the low-energy and mid-infrared features detected by optical conductivity [B1.102– B1.104]. Furthermore, in all of these materials enhancement of the effective mass (to several dozens of m_0 at low T) and suppression of the scattering rate mainly occur below a characteristic energy, consistent with the formation of a SP band.

Formation of a spin polaron band offers a straightforward explanation of the remarkable magnetoresistance (MR) in UGe_2 [B1.34]. Both MR and magnetostriction [B1.105] indicate that the carrier number is a strong function of magnetic field. The remarkable sensitivity of the electron transport to the magnetization (an order of magnitude stronger than in hole-doped manganites) shows that carrier localization into SP and its release by a magnetic field may be a missing key ingredient of HF models. A SP model [B1.106, B1.107] predicts the MR to be dependent on the carrier density through formation of SP and carrier release from SP. The recent observation of SP in magnetoresistive $\text{Lu}_2\text{V}_2\text{O}_7$ [B1.83] supports this model. High magnetic field destroys the SP because in high B the spins are already polarized, so that the exchange coupling of the carrier with these spins offers no energy advantage to compensate the increase in kinetic energy that occurs due to localization. Application of a magnetic field releases the carrier from SP into the conduction band — a process that not only explains the huge negative MR and its strong anisotropy, but also reveals the reason why carrier number is a strong function of magnetic field in UGe_2 [B1.41]. This effect

may be relevant to earlier studies on suppression of heavy fermions by high magnetic field [B1.108– B1.110].

Formation of the spin polaron band may provide an explanation for a list of mysteries of UGe_2 as well as other HF and strongly correlated materials, such as itinerant versus localized carriers in a duality problem when local moments acquire itinerancy, “small” Fermi surface versus “large” Fermi surface including both conduction electrons and local spins, huge anisotropic magnetoresistance, Fermi surface reconstruction at T^* and the nature of the mysterious FM transition within the FM phase. Emergence of such SP bands might be a general phenomenon in HF systems [B1.85, B1.111]. Furthermore, formation of spin bipolarons [B1.59, B1.112] — a pairing within the SP band — may be a missing ingredient for magnetically mediated spin–triplet SC models, including those in HF materials, FM materials or both. Finally, a spin polaron may serve as a *composite quasiparticle* — a heavy fermion — in HF materials.

This work was supported by the Natural Sciences and Engineering Research Council of Canada and the U.S. Department of Energy, Basic Energy Sciences, Division of Materials Science and Engineering (Award # DE–SC0001769).

B.1.3. Figures for Appendix C.1

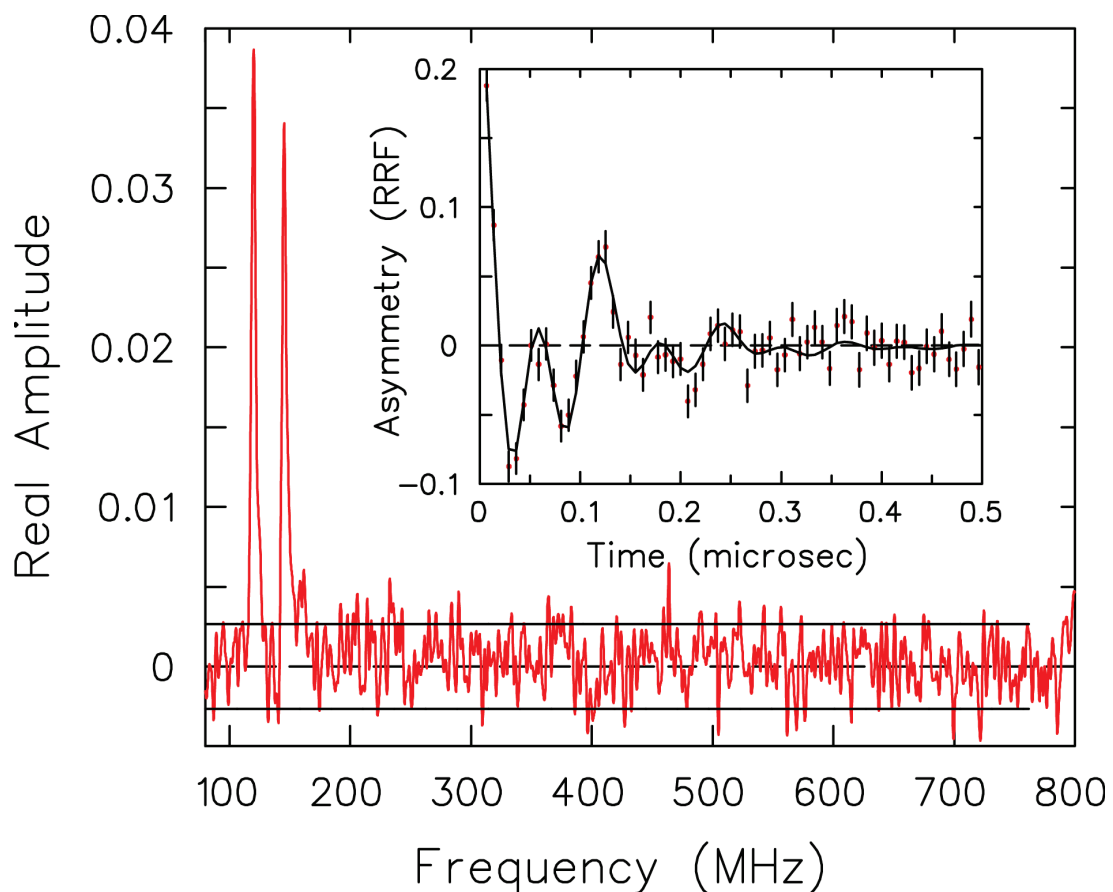


Figure B1.1: Frequency spectrum of muon spin precession in UGe2

Frequency spectrum of muon spin precession in UGe2 in a transverse magnetic field of $H = 1$ T at $T = 40$ K. Only the real part is shown, as including the imaginary part artificially broadens the overall lineshape⁷⁵. Inset: same spectrum in the time domain transformed into a rotating reference frame [B1.75] at 135.53333 MHz. The two-frequency precession pattern characteristic of a localized electron hyperfine-coupled to a muon is clearly apparent in both domains.

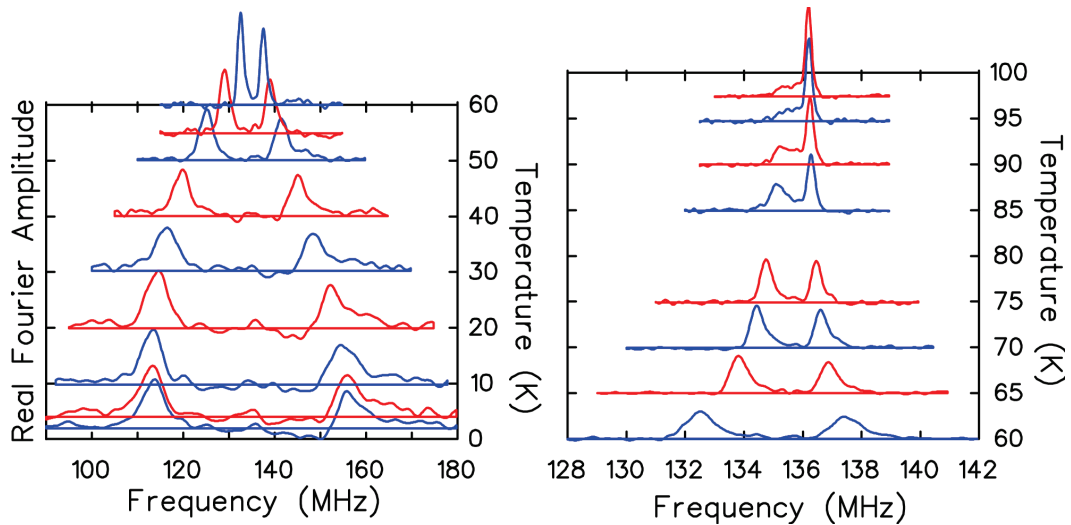


Figure B1.2: FFTs of TF-MuSR signal at various temperatures in UGe₂

Fourier transforms of the muon spin precession signal in UGe₂ in a transverse external magnetic field of 1 T at different temperatures. The characteristic SP lines appear below about 100 K and persist through the FM transition ($T_c = 52.6$ K) down to the lowest measured temperature. Note that the frequency scale changes by a factor of 0.156 between low and high T , reflecting the dramatic reduction of the splitting at high T . Also note the qualitative change in the line shapes around 80 K.

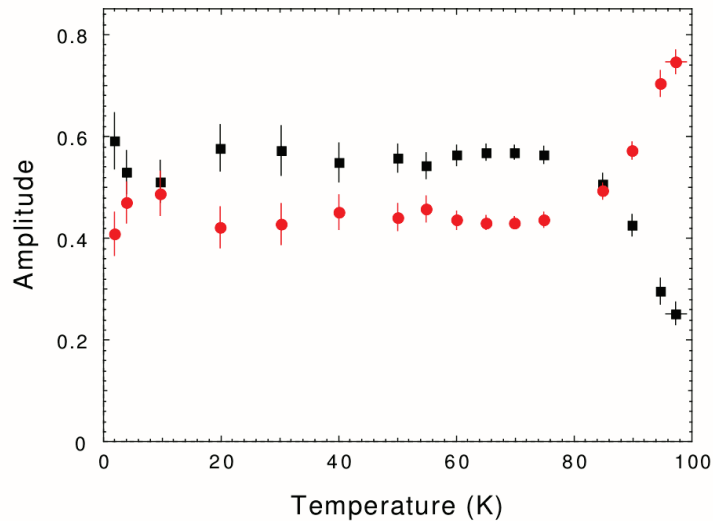


Figure B1.3: Temperature dependent asymmetries in UGe₂

Temperature dependence of the amplitudes of muon spin precession signals (spectral weight or population) in UGe₂ in a transverse external magnetic field of 1 T. Red circles (●) and black squares (■) show the evolution of the signal with the higher and lower frequency, respectively, around 100 K. Note the qualitative change around 80 K.

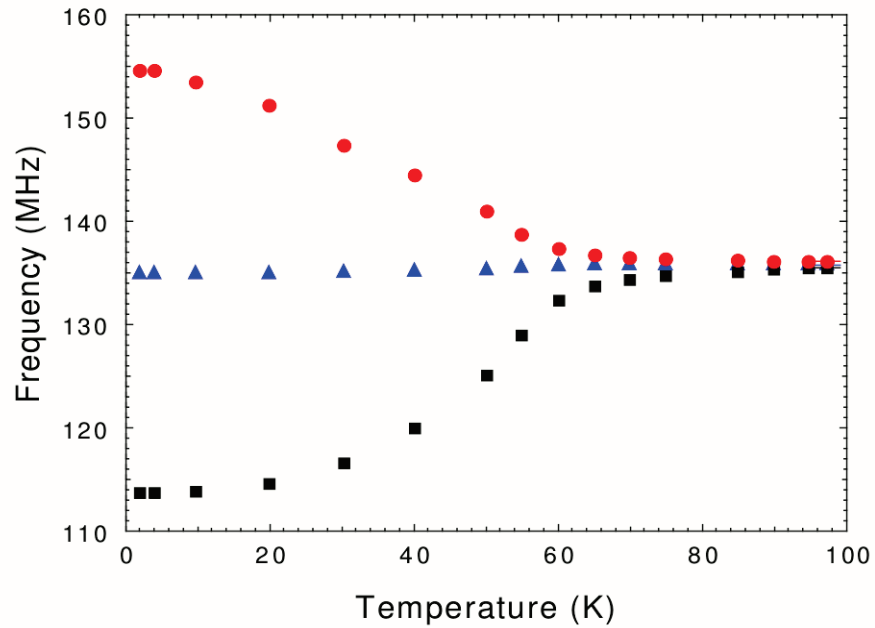


Figure B1.4: Temperature dependences of frequencies in UGe_2

Temperature dependences of muon spin precession signals frequencies in UGe_2 in a transverse external magnetic field of 1 T. The SP lines appear below about 100 K where the doublet is composed of a higher (red circles ●) and lower (black squares ■) frequency signal. The signal (blue triangles ▲) from [nonmagnetic] $CaCO_2$, mounted directly behind the sample, provides a direct measure of the magnetic field at the sample *via* the measured frequency.

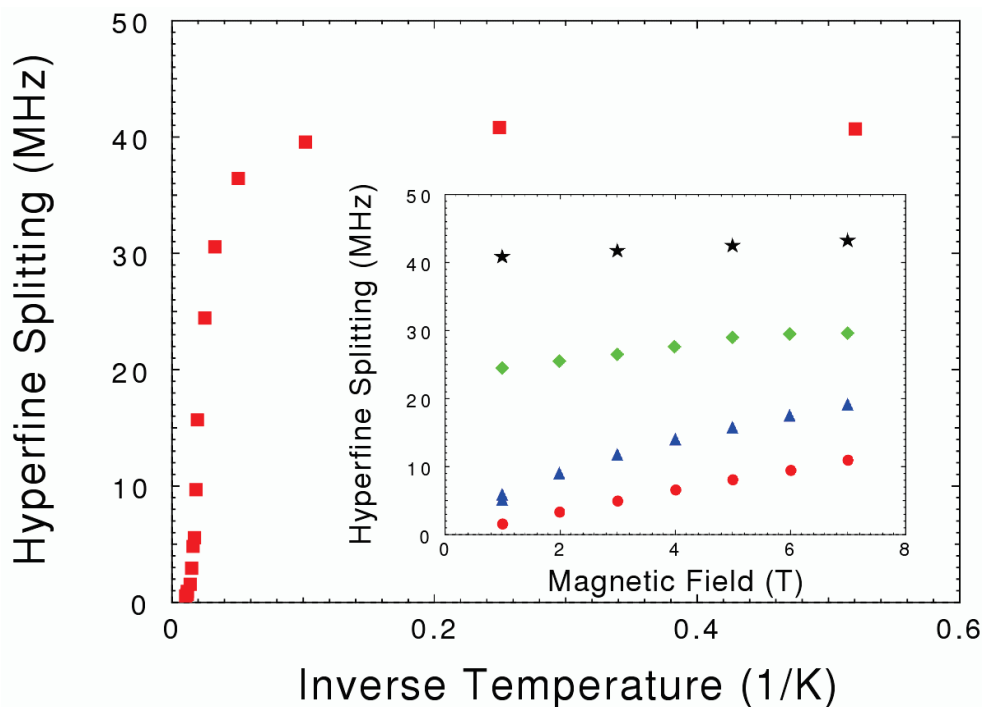


Figure B1.5: SP frequency splitting in UGe₂

Temperature dependence of the SP frequency splitting ($\Delta\nu$) in UGe₂ in a magnetic field of $H = 1$ T. At low temperature, the SP is fully polarized and the splitting saturates at the full strength of the μ^+e^- hyperfine coupling (A). *Inset*: magnetic field dependence of $\Delta\nu$ at $T = 75$ K (red circles, \bullet), $T = 60$ K (blue triangles, \blacktriangle), $T = 40$ K (green diamonds, \blacklozenge) and $T = 5$ K (black stars, \star). The saturation of both temperature and magnetic field dependences of $\Delta\nu$ are characteristic of hyperfine-coupled μ^+e^- spin systems. Both curves saturate at the same value of $A = 41 \pm 2$ MHz.

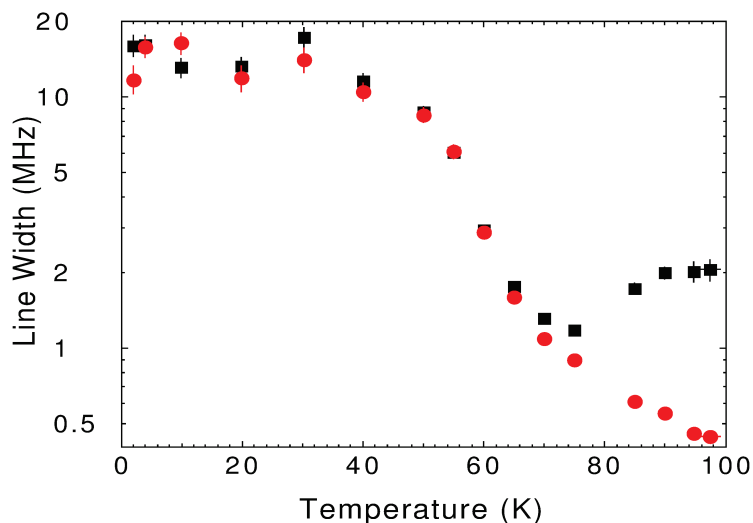


Figure B1.6: Temperature dependences of SP line width in UGe_2

Temperature dependences of the SP line widths of the signals with higher (*red circles*, \bullet) and lower (*black squares*, \blacksquare) frequencies in UGe_2 at 100 K in a magnetic field of $H = 1$ T. Note the qualitative change around 80 K.

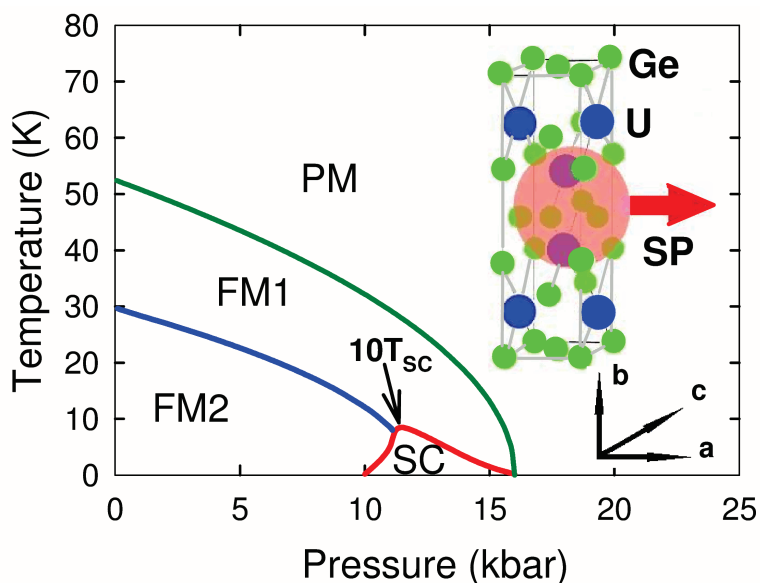


Figure B1.7: Temperature–pressure phase diagram of UGe_2

The temperature–pressure phase diagram of UGe_2 . The blue line (T^*) separates the weakly polarized magnetic phase (FM1) from the strongly polarized magnetic phase (FM2). The superconducting phase (SC) is confined within the red line (note that the T_{SC} values are scaled by a factor of 10). The green line separates the paramagnetic (PM) phase from the ferromagnetic phase (FM1). The upper right inset shows the orthorhombic unit cell of UGe_2 ,

composed of the U atoms (*blue circles*), Ge atoms (*green circles*) and a spin polaron (SP, large *pink circle*) that confines two U atoms. The lower right inset shows the a,b,c axes of the UGe₂ unit cell. The SP propagates along easy axis a, which is also its spin direction (see text).

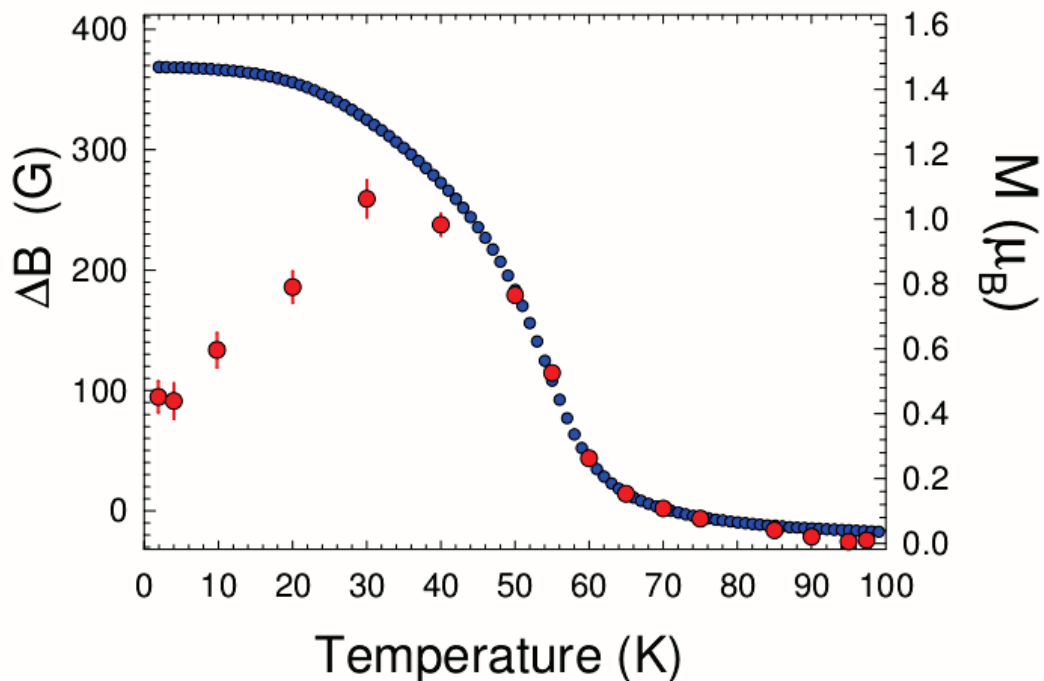


Figure B1.8: Temperature dependence of B_{loc} and bulk magnetization in UGe₂

Temperature dependence of the magnetic field shift detected by the muon (*red circles*, ●) and bulk magnetization measurements (blue circles, ●, presented as magnetic moment per U ion). In UGe₂. All data were collected with a magnetic field of $H = 1$ T externally applied parallel to the easy axis, *a*.

B.1.4. References for Appendix B.1

- [B1.1] Leggett, A. G. A theoretical description of the new phases of liquid ³He. *Rev. Mod. Phys.* **47**, 331–414 (1975).
- [B1.2] Sigrist, M. & Ueda, K. Phenomenological theory of unconventional superconductivity. *Rev. Mod. Phys.* **63**, 239–311 (1991).
- [B1.3] Pfleiderer, C. Superconducting phases of *f*-electron compounds. *Rev. Mod. Phys.* **81**, 1551–1624 (2009).

- [B1.4] Saxena, S. S. *et al.* Superconductivity on the border of itinerant–electron ferromagnetism in UGe₂. *Nature* **406**, 587–592 (2000).
- [B1.5] Aoki, D. *et al.* Coexistence of superconductivity and ferromagnetism in URhGe. *Nature* **413**, 613–616 (2001).
- [B1.6] Akazawa, T. *et al.* Pressure–induced superconductivity in ferromagnetic UIr without inversion symmetry. *J. Phys.: Condens. Matter* **16**, L29–L32 (2004).
- [B1.7] Huy, N. T. *et al.* Superconductivity on the border of weak itinerant ferromagnetism in UCoGe. *Phys. Rev. Lett.* **99**, 067006–067009 (2007).
- [B1.8] Fay, D. & Appel, J. Coexistence of p–state superconductivity and itinerant ferromagnetism. *Phys. Rev. B* **22**, 3173–3182 (1980).
- [B1.9] Lonzarich, D. D. in *Electron: A Centenary Volume*, ed. Springford, M. (Cambridge Univ, Cambridge, 1997), Ch. 6.
- [B1.10] Berk, N. F. & Schrieffer, J. R. Effect of Ferromagnetic Spin Correlations on Superconductivity. *Phys. Rev. Lett.* **17**, 433–435 (1966).
- [B1.11] Fulde, P. Quasiparticles in heavy–fermion systems. *J. Low Temp. Phys.* **95**, 45–57 (1994).
- [B1.12] Fulde, P. & Zwicknagl, G. Different routes to heavy fermion behaviour. *Physica B* **206 & 207**, 125–128 (1995).
- [B1.13] Fisk, Z., Ott H. R., Rice, T. M. & Smith, J. L. Heavy–electron metals. *Nature* **320**, 124–129 (1986).
- [B1.14] Fisk, Z. *et al.* Heavy–Electron Metals: New Highly Correlated States of Matter. *Science* **239**, 33–42 (1988).
- [B1.15] Steglich, F. *et al.* Superconductivity in the Presence of Strong Pauli Paramagnetism: CeCu₂Si₂. *Phys. Rev. Lett.* **43**, 1892–1896 (1979).
- [B1.16] Ott, H. R., Rudigier, H., Fisk, Z. & Smith, L. UBe₁₃: An Unconventional Actinide Superconductor. *Phys. Rev. Lett.* **50**, 1595–1598 (1983).
- [B1.17] Stewart, G. R., Fisk, Z., Willis, J. O. & Smith, J. L. Possibility of Coexistence of Bulk Superconductivity and Spin Fluctuations in UPt₃. *Phys. Rev. Lett.* **52**, 679–682 (1984).
- [B1.18] Mathur, N. D. *et al.* Magnetically mediated superconductivity in heavy fermion compounds. *Nature* **394**, 39–43 (1998).
- [B1.19] Monthoux, P., Pines, D. & Lonzarich, G. G. Superconductivity without phonons. *Nature* **450**, 1177–1183 (2007).

- [B1.20] Fertig, W. A. *et al.* Destruction of Superconductivity at the Onset of Long-Range Magnetic Order in the Compound ErEh_4B_4 . *Phys. Rev. Lett.* **38**, 987–990 (1977).
- [B1.21] Fischer, Ø. Chevrel Phases: Superconducting and Normal State Properties. *Applied Physics* **16**, 1–28 (1978).
- [B1.22] Cava, R. J. *et al.* Superconductivity in the quaternary intermetallic compound $\text{LnNi}_2\text{B}_2\text{C}$. *Nature* **367**, 252–253 (1994).
- [B1.23] Canfield, P. C., Bud'ko, S. L. & Cho, B. K. Possible co-existence of superconductivity and weak ferromagnetism in $\text{ErNi}_2\text{B}_2\text{C}$. *Physica C* **262**, 249–254 (1996).
- [B1.24] Zwicknagl, G. Quasiparticles in heavy fermion systems. *Physica Scripta* **T49**, 34–41 (1993).
- [B1.25] Shick, A. B. & Pickett, W. E. Magnetism, Spin-Orbit Coupling, and Superconducting Pairing in UGe_2 . *Phys. Rev. Lett.* **86**, 300–303 (2001).
- [B1.26] Nakatsuji, S., Pines, D. & Fisk, Z. Two Fluid Description of Kondo Lattice. *Phys. Rev. Lett.* **92**, 016401 (2004).
- [B1.27] Kuramoto, Y. & Miyake, K. Quantum Phenomenology for Heavy-Fermion Systems. 1. Formulation of the Duality Model. *J. Phys. Soc. Jap.* **59**, 2831–2840 (1990).
- [B1.28] Zwicknagl, G., Yaresko, A. & Fulde, P. Microscopic description of origin of heavy quasiparticles in UPt_3 . *Phys. Rev. B* **65**, 081103 (2002).
- [B1.29] Caspary, R. *et al.* Unusual ground-state properties of UPd_2Al_3 : Implications for the coexistence of heavy-fermion superconductivity and local-moment antiferromagnetism. *Phys. Rev. Lett.* **71**, 2146–2149 (1993).
- [B1.30] Sato, N. K. *et al.* Strong coupling between local moments and superconducting ‘heavy’ electrons in UPd_2Al_3 . *Nature* **410**, 340–343 (2001).
- [B1.31] Joyce, J. J. *et al.* Photoemission and the Electronic Structure of PuCoGa_5 . *Phys. Rev. Lett.* **91**, 176401 (2003).
- [B1.32] McMullan, G. J. *et al.* The Fermi surface and f -valence electron count in UPt_3 . *New J. Phys.* **10**, 053029 (2008).
- [B1.33] Park, T. Graf, M. J., Boulaevskii, L., Sarrao, J. L. & Thompson, J. D. Electronic duality in strongly correlated matter. *Proceedings of the National Academy of Sciences of the USA* **105**, 6825–6828 (2008).
- [B1.34] Troć, R., Gajek, Z. & Pikul, A. Dualism of the $5f$ electrons of the ferromagnetic superconductor UGe_2 as seen in magnetic, transport and specific-heat data. *Phys. Rev. B* **86**, 224403 (2012).

- [B1.35] Huxley, A. D. *et al.* UGe₂: A ferromagnetic spin–triplet superconductor. *Phys. Rev. B* **63**, 144519 (2001).
- [B1.36] Biasini, M. & Troc, R. Fermi surface of UGe₂ in the paramagnetic phase. *Phys. Rev. B* **68**, 245118 (2003).
- [B1.37] Tateiwa, N. *et al.* Pressure–induced superconductivity in a ferromagnet UGe₂. *J. Phys.: Condens. Matter* **13**, L17–L23 (2001).
- [B1.38] Terashima, T. *et al.* Evolution of Quasiparticle Properties in UGe₂ with Hydrostatic Pressure Studied via the de Haas–van Alphen Effect. *Phys. Rev. Lett.* **87**, 166401 (2001).
- [B1.39] Settai, R. *et al.* A change of the Fermi surface in UGe₂ across the critical pressure. *J. Phys.: Condens. Matter* **14**, L29–L36 (2002).
- [B1.40] Haga, Y. *et al.* A change of the Fermi surface across the metamagnetic transition under pressure in UGe₂. *J. Phys.: Condens. Matter* **14**, L125–L135 (2002).
- [B1.41] Tran, V. H., Paschen, S., Troc, R., Baenitz, M. & Steglich, F. Hall effect in ferromagnet UGe₂. *Phys. Rev. B* **69**, 195314 (2004).
- [B1.42] Yaouanc, A. *et al.* Evidence for Weak Itinerant Long–Range Magnetic Correlations in UGe₂. *Phys. Rev. Lett.* **89**, 147001 (2002).
- [B1.43] Zwicknagl, G., Yaresko, A. & Fulde, P. Fermi surface and heavy masses for UPd₂Al₃. *Phys. Rev. B* **68**, 052508 (2003).
- [B1.44] Taillefer, L., Lonzarich, G. G. & Strange, P. The band magnetism of MnSi. *J. Magn. Magn. Mater.* **54–57**, 957–958 (1986).
- [B1.45] Landau, L. D. Electron motion in crystal lattices. *Phys. Z. Sowjet.* **3**, 664–665 (1933).
- [B1.46] Nagaev, E. L. *Colossal Magnetoresistance and Phase Separation*. (Imperial College, London, 2002).
- [B1.47] Mott, N. F. *Metal–insulator transitions*. (Taylor & Francis, Bristol, 1990).
- [B1.48] Emin, D. Optical properties of large and small polarons and bipolarons. *Phys. Rev. B* **48**, 13691–13702 (1993).
- [B1.49] Kagan, Yu.M. and Prokofev N.V. Quantum tunneling diffusion in solids. In *Quantum Tunneling in Condensed Media*, editors Leggett, A. J. & Kagan Y. (North–Holland, 1992).
- [B1.50] Holstein, T. Studies of polaron motion: Part II. The ‘small’ polaron.” *Ann. Phys.* **8**, 343–389 (1959).
- [B1.51] Storchak, V. G. & Prokofev, N. V. Quantum diffusion of muons and muonium atoms in solids. *Rev. Mod. Phys.* **70**, 929–978 (1998).

- [B1.52] de Gennes, P. –G. Effects of Double Exchange in Magnetic Crystals. *Phys. Rev.* **118**, 141–154 (1960).
- [B1.53] Kasuya, T. and Yanase, A. Anomalous Transport Phenomena in Eu–Chalcogenide Alloys. *Rev. Mod. Phys.* **40**, 684–698 (1968).
- [B1.54] Luttinger, J. M. Fermi Surface and Some Simple Equilibrium Properties of a System of Interacting Fermions. *Phys. Rev.* **119**, 1153–1163 (1960).
- [B1.55] Martin, R. M. Fermi–Surface Sum Rule and its Consequences for Periodic Kondo and Mixed–Valence Systems. *Phys. Rev. Lett.* **48**, 362–365 (1982).
- [B1.56] Coleman, P., Paul, I. & Rech, J. Sum rules and Ward identities in the Kondo lattice. *Phys. Rev. B* **72**, 094430 (2005).
- [B1.57] Coleman, P. “Heavy fermions: electrons at the edge of magnetism” in *Handbook of Magnetism and Advanced Magnetic Materials*, eds. Kronmüller, H. & Parkin, S. (Wiley, 2007)
- [B1.58] Storchak, V. G., Brewer, J. H., Lichti, R. L., Hu, R. & Petrovic, C. Thermal destruction of spin–polaron bands in the narrow–gap correlated semiconductors FeGa₃ and FeSb₂. *J. Phys.: Condens. Matter* **24**, 185601 (2012).
- [B1.59] Storchak, V. G. *et al.* Spin Polarons in Correlated Metallic Pyrochlore Cd₂Re₂O₇. *Phys. Rev. Lett.* **105**, 076402 (2010).
- [B1.60] Storchak, V. G. *et al.* Direct observation of the magnetic polaron. *Phys. Rev. B* **80**, 235203 (2009).
- [B1.61] von Molnar, S. & Stampe, P.A. “Magnetic Polarons” in *Handbook of Magnetism and Advanced Magnetic Materials*, eds. Kronmüller, H. & Parkin, S. **v.5**: Spintronics and Magnetoelectronics (Wiley, 2007)
- [B1.62] Storchak, V. G. *et al.* Magnetic polaron bound to the positive muon in SmS: Exchange–driven formation of a mixed–valence state. *Phys. Rev. B* **79**, 193205 (2009).
- [B1.63] Storchak, V. G. *et al.* Novel muonium centers — magnetic polarons — in magnetic semiconductors. *Physica B* **404**, 899–902 (2009).
- [B1.64] Storchak, V. G. *et al.* Bound Magnetic Polarons in the 3*d*–electron Ferromagnetic Spinel Semiconductor CdCr₂Se₄. *J. Phys.: Condens. Matter* **22**, 495601 (2010).
- [B1.65] Storchak, V. G. *et al.* Magnetic polaron in Eu–based films of magnetic semiconductors. *Phys. Rev. B* **81**, 153201 (2010).
- [B1.66] Storchak, V. G. *et al.* Electron localization into spin–polaron state in MnSi. *Phys. Rev. B* **83**, 140404(R) (2011).

- [B1.67] Coey, J. M. D., Viret, M. & von Molnár, S. Mixed–valence manganites. *Adv. Phys.* **48**, 167–293 (1999).
- [B1.68] Kimura, S. *et al.* Electronic inhomogeneity of EuO: Possibility of magnetic polaron states. *Phys. Rev. B* **78**, 052409 (2008).
- [B1.69] Heiss, W., Prechtel, G. & Springholz, G. Giant tunability of exciton photoluminescence emission in antiferromagnetic EuTe. *Phys. Rev. B* **63**, 165323 (2001).
- [B1.70] Ott, H. *et al.* Soft x–ray magnetic circular dichroism study on Gd–doped EuO films. *Phys. Rev. B* **73**, 094407 (2006).
- [B1.71] Comment, A. *et al.* Magnetic properties of pure and Gd–doped EuO probed by NMR. *Phys. Rev. B* **72**, 014428 (2005).
- [B1.72] Snow, C. S. *et al.* Magnetic polarons and the metal–semiconductor transitions in (Eu,La)B₆ and EuO: Raman scattering studies. *Phys. Rev. B* **64**, 174412 (2001).
- [B1.73] De Teresa, J. M. *et al.* Evidence for magnetic polarons in the magnetoresistive perovskites. *Nature* **386**, 256–259 (1997).
- [B1.74] Schenck, A. *Muon Spin Rotation: Principles and Applications in Solid State Physics*. (Hilger, Bristol, 1986).
- [B1.75] Brewer, J. H. Muon Spin Rotation/Relaxation/Resonance. *Encyclopedia of Applied Physics*. **11**, 23–53 (VCH, New York, 1994).
- [B1.76] Yaouanc, A. & Dalmas de Reotier, P. *Muon Spin Rotation, Relaxation, and Resonance: Applications to Condensed Matter* (Oxford Univ, New York, 2011).
- [B1.77] Storchak, V. G. *et al.* Electron localization into a bound spin polaron in the quasi–one–dimensional $S = 1/2$ antiferromagnet LiCu₂O₂. *Phys. Rev. B* **79**, 220406–220409(R) (2009).
- [B1.78] Patterson, B. D. Muonium states in semiconductors. *Rev. Mod. Phys.* **60**, 69–159 (1988).
- [B1.79] Storchak, V. G. *et al.* Muonium Formation via Electron Transport in Silicon. *Phys. Rev. Lett.* **78**, 2835–2838 (1997).
- [B1.80] Storchak, V. G., Eshchenko, D. G., Lichti, R. L. & Brewer, J. H. Weakly bound muonium state in GaP. *Phys. Rev. B* **67**, 121201–121204 (2003).
- [B1.81] Storchak, V. G., Eshchenko, D. G. & Brewer, J. H. Formation and dynamics of muonium centres in semiconductors — a new approach. *J.Phys.: Condens. Matter* **16**, S4761–S4778 (2004).

- [B1.82] Eshchenko, D. G., Storchak, V. G., Cottrell, S. P. & Morenzoni, E. Electric-Field-Enhanced Neutralization of Deep Centers in GaAs. *Phys. Rev. Lett.* **103**, 216601 (2009).
- [B1.83] Storchak, V. G. *et al.* Observation of magnetic polarons in the magnetoresistive pyrochlore $\text{Lu}_2\text{V}_2\text{O}_7$. *J. Phys.: Condens. Matter* **25**, 115601 (2013).
- [B1.84] Sakarya, S. *et al.* Positive muon spin rotation and relaxation measurements on the ferromagnetic superconductor UGe_2 at ambient and high pressure. *Phys. Rev. B* **81**, 024429 (2010).
- [B1.85] Storchak, V. G. *et al.* Spin gap in heavy fermion UBe_{13} . ArXiv: 1309.6407 (2013).
- [B1.86] Storchak, V. G. *et al.* Reply to “Comment on ‘Direct observation of the magnetic polaron’ ”. *Phys. Rev. B* **83**, 077202 (2011).
- [B1.87] Guritanu, V. *et al.* Optical spectra of the heavy fermion uniaxial ferromagnet UGe_2 . *Phys. Rev. B* **78**, 172406 (2008).
- [B1.88] Sakurai, Y., Itou, M., Yamamoto, E., Haga, Y. & Onuki, Y. Orbital-Wise Decomposition of Magnetic Compton Profiles in Ferromagnetic Uranium Compound. *J. Phys. Soc. Jpn. Suppl.* **75**, 96–98 (2006).
- [B1.89] Smart, J. S. *Effective Field Theories of Magnetism*. (Sounders, Philadelphia, 1966).
- [B1.90] Huxley, A.D., Raymond, S. & Ressouche, E. Magnetic Excitations in the Ferromagnetic Superconductor UGe_2 . *Phys. Rev. Lett.* **91**, 207201 (2003).
- [B1.91] Storchak, V., Brewer, J. H., Hardy, W. N., Kreitzman, S. R. & Morris, G. D. Two-phonon quantum diffusion of muonium in solid nitrogen. *Phys. Rev. Lett.* **72**, 3056–3059 (1994).
- [B1.92] Storchak, V., Brewer, J. H. & Morris, G. D. Inhomogeneous quantum diffusion. *Phys. Rev. B* **53**, 11300–11303 (1996).
- [B1.93] Kernavanois, N. *et al.* Neutron scattering study of the ferromagnetic superconductor UGe_2 . *Phys. Rev. B* **64**, 174509 (2001).
- [B1.94] Sandeman, K. G., Lonzarich, G. G. & Schofield, A. J. Ferromagnetic Superconductivity Driven by Changing Fermi Surface Topology. *Phys. Rev. Lett.* **90**, 167005 (2003).
- [B1.95] Harada, A. *et al.* Experimental evidence for ferromagnetic spin-pairing superconductivity emerging in UGe_2 : A ^{73}Ge -nuclear-quadrupole-resonance study under pressure. *Phys. Rev. B* **75**, 140502 (2007).
- [B1.96] Mott, N. F. Electrons in transition metals. *Adv. Phys.* **13**, 325–422 (1964).

- [B1.97] Pfleiderer, C. and Huxley, A. D. Pressure dependence of the magnetization in the ferromagnetic superconductor UGe₂. *Phys. Rev. Lett.* **89**, 147005 (2002).
- [B1.98] Hewson, A. C. *The Kondo Problem to Heavy Fermions*. (Cambridge Univ., Cambridge, 1993).
- [B1.99] Nozières, P. A “Fermi–liquid” description of the Kondo problem at low temperatures. *J. Low Temp. Phys.* **17**, 31–42 (1974).
- [B1.100] Borda, L. Kondo screening cloud in a one–dimensional wire: Numerical renormalization group study. *Phys. Rev. B* **75**, 041307(R) (2007).
- [B1.101] Dressel, M. *et al.* Nature of Heavy Quasiparticles in Magnetically Ordered Heavy Fermions UPd₂Al₃ and UPt₃. *Phys. Rev. Lett.* **88**, 186404 (2002).
- [B1.102] Wang, N. L. *et al.* Optical evidence for mass enhancement of quasiparticles in pyrochlore Cd₂Re₂O₇. *Phys. Rev. B* **66**, 014534 (2002).
- [B1.103] Mena, F.P. *et al.* Heavy carriers and non–Drude optical conductivity in MnSi. *Phys. Rev. B* **67**, 241101 (2003).
- [B1.104] Brown Holden, A. A., Wardlaw, G. M., Reedyk, M. & Smith, J. L. Emergence of Coherent Transport in UBe₁₃: An Optical Investigation in Both the Normal and Superconducting States. *Phys. Rev. Lett.* **91**, 136401 (2003).
- [B1.105] Kabeya, N. *et al.* First–order transition switch–off of superconductivity in UGe₂. *Physica B: Condens.Matter* **404**, 3238–3241 (2009).
- [B1.106] Majumdar, P. & Littlewood, P. Magnetoresistance in Mn Pyrochlore: Electrical Transport in a Low Carrier Density Ferromagnet, *Phys. Rev. Lett.* **81**, 1314–1317 (1998).
- [B1.107] Majumdar, P. & Littlewood, P. B., Dependence of magnetoresistivity on charge–carrier density in metallic ferromagnets and doped magnetic semiconductors. *Nature* **395**, 479–481 (1998).
- [B1.108] Joss, W. *et al.* Observation of the magnetic field dependence of the cyclotron mass in the Kondo lattice CeB₆. *Phys. Rev. Lett.* **59**, 1609–1612 (1987).
- [B1.109] Stewart, G. R. *et al.* Suppression of heavy fermions by high fields in CeCu₆. *Phys. Rev. B* **37**, 3344–3348 (1988).
- [B1.110] van der Meulen, H. P. *et al.* Field suppression of the heavy–fermion state in CeRu₂Si₂. *Phys. Rev. B* **44**, 814–818 (1991).
- [B1.111] Recently, by using MuSR technique we found SP in several HF systems: CeCu₆, CeCoIn₅, Ce₂RhIn₈ etc.

[B1.112] Mott, N. F. Polaron models in high-temperature superconductors.
J.Phys.: Condens. Matter **5**, 3487–3506 (1993).

B.2. SPIN GAP IN HEAVY FERMION UBe_{13}

This paper was submitted to *Nature Physics* in February of 2014 and is currently under review. Additionally, the text included here is in the exact form in which it was submitted with the only exception being the equation, figure and citation numbers have been modified as to minimize confusion with the rest of this document.

B.2.1. UBe_{13} : Author Information and Associations

V. G. Storchak^{1*}, J. H. Brewer², D. G. Eshchenko³, P. W. Mengyan⁴,
O. E. Parfenov¹, P. Dosanjh², Z. Fisk⁵ & J. L. Smith⁶

¹*National Research Centre ‘Kurchatov Institute’, Kurchatov Sq. 1, Moscow 123182, Russia*

²*Department of Physics and Astronomy, University of British Columbia, Vancouver, BC, Canada V6T 1Z1*

³*Bruker BioSpin AG, Industriestrasse 26, 8117 Fällanden, Switzerland*

⁴*Department of Physics, Texas Tech University, Lubbock, Texas 79409–1051, USA*

⁵*Department of Physics and Astronomy, University of California, Irvine, CA 92697, USA*

⁶*Materials Science and Technology Division, Los Alamos National Laboratory, Los Alamos, NM 87545, USA*

B.2.2. UBe_{13} : Text

Heavy fermion compounds are well known for their unique properties such as narrowness of bandwidths, loss of coherence in a metal, non–Fermi–liquid behaviour, unconventional superconductivity, huge magnetoresistance etc. While these materials have been known since the 70s, there is still considerable uncertainty regarding the fundamental mechanisms responsible for some of these features. Here we discuss the direct observation of spin polarons in the heavy fermion compound, UBe_{13} , that detect a spin gap in the spin excitation spectrum of f –electrons, opening near 180 K which is consistent with anomalies observed in resistivity, heat capacity, NMR or optical conductivity measurements. Together, the observation of spin polarons and detection of a spin gap contribute to a robust picture of the mechanisms responsible for many of

these characteristics including identification of the spin polaron as a heavy fermion. We find similar behaviour in several other heavy fermion systems.

In strongly correlated metallic materials, the interplay between local spins and itinerant electrons determines the spin fluctuation spectrum. In a 3d–electron system, such a spectrum emerges as a result of a strong dominance of the Fermi energy over magnetic energy [B2.1]. By contrast, in *f*–electron itinerant systems the Fermi energy is heavily renormalized down to the scale of the magnetic energy [B2.2], resulting in a strong influence of the spin dynamics and spectral weight of spin fluctuations on transport, magnetic and thermodynamic properties of a system. A depletion of spectral weight upon cooling may indicate the opening of a gap (or pseudogap) in the spectrum of spin fluctuations.

The concept of a pseudogap has recently become essential for understanding strongly correlated electron systems [B2.3]. Particularly interesting is the opening of a gap in a system of *f*–electron spin excitations [B2.4]. At low temperature, such systems display a continuous transition from an array of uncorrelated local magnetic moments to a Fermi-liquid (FL) phase in which *f* electrons are strongly hybridized with conduction band electrons [B2.5]. As a result, *f* electrons not only create a sharp resonance on the Fermi level, giving rise to a large effective mass, m^* , of quasiparticles, but also transfer their magnetic entropy to the Fermi surface. In this case, a gap may open up as in URu₂Si₂ at T=17.5 K [B2.4]. In this article, we present data that are explained by a spin gap opening in UBe₁₃ at T=180 K.

UBe₁₃ crystallizes in the cubic NaZn₁₃ structure with lattice constant $a=1.025$ nm. The U atoms form a simple cubic sublattice with a rather large U–U spacing, suggesting strong hybridization with the itinerant carriers [B2.6]. Unlike in other uranium–based HF compounds, there is no evidence for static magnetic order in UBe₁₃ though short–range magnetic correlations have been reported [B2.7]. In UBe₁₃, superconductivity (SC) arises from a paramagnetic (PM) metallic phase as a cooperative phenomenon involving heavy quasiparticles that form pairs [B2.6, B2.8]. The susceptibility, χ , exhibits typical Curie–Weiss behaviour at high temperature with

$\mu_{\text{eff}} \approx 3.36 \mu_{\text{B}}$ but deviates from this law below 200 K and then levels off at 20 K [B2.9].

Interest in UBe_{13} is reinforced by various observations of non-Fermi-liquid (NFL) behaviour [B2.6, B2.9, B2.10–B2.12], often explained by the proximity to the quantum critical point [B2.10, B2.11, B2.13], which challenges the validity of the quasiparticle concept. However, various experiments indicate a dominant role of quasiparticles, although the specific quantum states that might replace the Fermi liquid remains unclear [B2.13].

Quite remarkably, FL behaviour in UBe_{13} (as in some other HF systems) is restored by application of a strong magnetic field [B2.11]. Another remarkable feature which requires explanation is that UBe_{13} displays coherent quasiparticle behaviour at low temperature, however, at higher temperature an incoherent metallic state dominated by spin-flip scattering is present [B2.11, B2.14]. Both NFL and loss of coherence phenomena cannot be explained by quadrupolar Kondo effect [B2.10]. Furthermore, energy band calculations produce an m^* value that is at least an order of magnitude too low [B2.15]. Moreover, the band theory fails to explain the loss of coherence.

In order to identify a fundamental electronic state that is consistent with all of the crucial experimental results, different polaron models have been proposed [B2.15, B2.16]. Although both electronic and magnetic polaron models may account for NFL behaviour, loss of coherence and produce a correct m^* [B2.15], the former fails to explain the strong influence of a magnetic field. By contrast, a spin polaron (SP) model [B2.16] claims to establish an electronic state which may help to reconcile theoretical treatment with the experiment. In particular, the SP model [B2.17, B2.18] offers a straightforward explanation of a major puzzle of UBe_{13} — a remarkable magnetoresistivity (MR) [B2.9] — which can hardly find explanation within any other model. Both MR and magnetostriction indicate that the carrier number is a strong function of magnetic field as if ‘the carrier is released by B’ [B2.12]. The remarkable sensitivity of the electron transport to the magnetization (an order of magnitude

stronger than in hole-doped manganites) shows that carrier localization into SP, and its release by a magnetic field, may be a missing key ingredient of HF models. A SP model [B2.17,B2.18] predicts that narrowness of the conduction band may cause the carriers to self-trap as SP. Recent observation of SP in magnetoresistive $\text{Lu}_2\text{V}_2\text{O}_7$ [B2.19] supports this model. Here, we present observation of SP in UBe_{13} . It is this observation which allows detection of a spin gap.

Standard measurements to characterize lattice constants, resistivity behaviour, T_c and effective magnetic moments were completed and show that properties of our single crystal samples are consistent with literature data. Time-differential μ^+ SR experiments [B2.20, B2.21] using 100% spin-polarized positive muons implanted into these samples within a temperature range of 0.025 K to 300 K and magnetic fields, \mathbf{B}_{ext} , applied perpendicular to the initial muon polarization direction, up to 7 T, were carried out on the M15 surface muon channel at TRIUMF using the HiTime and DR spectrometers. Another set of these measurements were carried out with a mosaic of crystals oriented randomly with respect to the direction of the external magnetic field. At high temperature Fourier transforms of the μ^+ SR time spectra exhibit a single line at the muon frequency, $\nu_\mu = \gamma_\mu B / 2\pi$ (where $\gamma_\mu = 2\pi \times 135.53879$ MHz/T is the muon magnetogyric ratio), which coincides with that detected in a CaCO_3 reference sample used for independent measurements of B. However, below $T^* \approx 180$ K such simple spectra change abruptly to reveal a characteristic doublet (Figure B2.1) which persists down to the lowest temperature (Figure B2.2).

Previous observations of such two-line spectra [B2.22,B2.23] prompted a suggestion of two inequivalent sites occupied by positive muons in UBe_{13} . However, a two-site assignment suggests a temperature independent strict 1:2 muon site occupation ratio [B2.22,B2.23] while experiment shows a temperature dependent amplitude ratio well below 0.5 (Figure B2.3). Furthermore, the two lines do not follow the temperature dependence of the magnetization (Figure B2.4), which indicates that the muon does not stay bare and does not act as a local magnetometer. Instead, one line goes up in frequency while the other goes down as temperature decreases —

which is a signature of a muon–electron bound state [B2.20,B2.21]. Moreover, in the bare muon scenario one expects strong anisotropy in the position and splitting of the two lines when the magnetic field is applied along different crystalline axes, whereas our measurements with randomly aligned crystals matched results produced from an oriented single crystal(s), thereby indicating very isotropic signals. Finally, the departure from linear magnetic field dependences of the two frequencies allows one to rule out possible Knight shifts within the bare muon scenario.

Instead, the doublet in Figure B2.1 and Figure B2.2 is a fingerprint of a coupled μ^+e^- spin system in high transverse field [B2.19–B2.21,B2.24–B2.29]: the two lines correspond to two muon spin–flip transitions between states with electron spin orientation fixed, the splitting between them being determined by the muon–electron hyperfine interaction, A [B2.24, B2.25]. In a magnetic system, an electron’s energy depends strongly on the magnetization, with the minimum energy being achieved by ferromagnetic (FM) ordering [B2.30]. Then the strong exchange interaction, J , between a carrier and local $f(d)$ moments can cause electron localization into a FM ‘droplet’ over the extent of its wavefunction (typically, the first coordination sphere) in a PM (or AF) sea [B2.30, B2.31]. This charge carrier, accompanied by reorientations of local spins to form its immediate FM environment, together behave as a single quasiparticle with a giant spin S — a spin polaron [B2.30,B2.31]. In the process of electron localization into a SP, in a metal, the exchange energy gain upon transition from the PM to the FM state is opposed by the increase of the electron kinetic energy (the entropy term due to ordering within the SP becomes significant only at very high T) [B2.24,B2.25,B2.27,B2.28].

High magnetic field destroys the SP because in high B the spins are already polarized so that the exchange coupling of the carrier with these spins offers no energy advantage to compensate the increase in kinetic energy due to localization. Application of a magnetic field thus releases the carrier from SP into the conduction band — a process which offers not only an explanation of the huge negative MR but

also reveals the reason why the carrier number is a strong function of magnetic field in UBe_{13} .

Such SP states with the electron confined in a $R \approx 0.2\text{--}0.5$ nm FM ‘droplet’ attached to a positive muon are found in strongly correlated insulators [B2.26,B2.32], semiconductors [B2.24,B2.25,B2.29] and metals [B2.27,B2.28]. In metals, an itinerant SP is captured by the muon to exhibit the characteristic μ^+e^- hyperfine splitting [B2.27,B2.28] through the frequency splitting $\Delta\nu$ between two SP lines (Figure B2.5). Within a mean field approximation, $\Delta\nu$ follows a Brillouin function [B2.24,B2.25,B2.27,B2.28]. For $g\mu_B B \ll k_B T$,

$$\Delta\nu = A \left[\frac{g\mu_B B}{3k_B(T - \tau)} \right] (S + 1) \quad (\text{B2.1})$$

A strong deviation from the Curie–Weiss law, which lies in the heart of HF behaviour, restricts UBe_{13} to the small B/T limit so that equation (B2.1) stays valid in the entire measured B range, in contrast to other systems which support SP [B2.24, B2.25, B2.27, B2.28]. Fitting $\Delta\nu(B)$ for T between 15 K and 150 K, with τ determined from magnetization measurements (see inset in Figure B2.6), and taking into account the dominance of the orbital magnetic moment, which causes $g=0.8$ [B2.33], gives $A=45(5)$ MHz and $S=8.5(0.5)$. From the value of $A\alpha R^{-3}$ we get $R=0.25(1)$ nm, which rather remarkably indicates a maximum overlap of corresponding s and f wavefunctions within the SP [B2.24, B2.25, B2.27, B2.28], as the U–U distance is 0.5124 nm and the radius of the f -orbital is 0.0527 nm. This is consistent with the muon sitting in between the two U ions [B2.22, B2.23] that capture a SP consisting of an electron whose wavefunction overlaps f -orbitals of said U ions; each having a magnetic moment $\mu_U = g\mu_B(S + 1/2)/2 = 3.6\mu_B$, which is close to the μ_{eff} found from susceptibility measurements.

In a PM, strong spin exchange with the environment [B2.20, B2.21] would result in rapid spin fluctuations of the SP electron, averaging the hyperfine interaction to zero, which in turn would result in a collapse of the doublet into a single line at ν_μ (see [B2.24, B2.34] for details) unless the SP spin, S , is decoupled from the local spins

[B2.24, B2.25, B2.27, B2.34]. Such decoupling is possible in high B when the Zeeman energy of S exceeds an exchange interaction, J , between local spins — this is the case in magnetic insulators where the SP doublet is detected up to very high temperature [B2.19, B2.24–B2.26]. In metals, RKKY interactions make J much stronger, so that decoupling requires B strengths that are inaccessible in the current experiment. That is why we see a single line above 180 K, which by no means indicates the absence of the SP above 180 K — just active spin exchange with the environment [B2.24, B2.25, B2.27, B2.34]. We interpret the abrupt appearance of a SP doublet at 180 K (Figure B2.4 and Figure B2.5) as a result of opening a spin gap that eliminates low-lying spin excitations, thereby making spin exchange of S with its environment ineffective. This explanation is consistent with anomalies in specific heat [B2.35], NMR [B2.36] and optical conductivity [B2.14], which are discussed in terms of crystal field splitting of the $5f^3$ U ion by a characteristic energy of ~ 180 K.

Our electric resistivity, ρ , measurements in the same single crystals (Figure B2.6) confirm a spin gap opening in UBe_{13} near 180 K. A basic behaviour of resistivity lies in the context of carrier scattering in metals with local spins [B2.37–B2.39]; as in UBe_{13} below 300 K, ρ is dominated by carrier scattering on spins [B2.40]. At high temperature, it consists of a temperature-independent local scattering term and a $1/T$ term due to scattering on paramagnons [B2.37–B2.39]. At lower temperature down to τ , Kondo scattering takes over. A crossover from $\rho(T)=A/T+C$ to $\rho(T)=D\ln(E/T)$ at about 180 K signifies a characteristic change in the spin fluctuation spectrum of the system. Fits to the data yield the following values:

$A=8.5\times 10^{-3}$ Ohm·cm·K, $C=94\times 10^{-6}$ Ohm·cm, $D=47.4\times 10^{-6}$ Ohm·cm and

$E=3500$ K. At high temperature, the largest contribution to ρ comes from carriers with small momentum $q\sim 0$ [B2.37–B2.39] scattered by low-lying excitations dwarfing both $1/T$ and C as the spin gap opens up, eliminating such excitations. On the other hand, an opening of the spin gap promotes resonant Kondo scattering effective at a significant q and energy [B2.41]. Moreover, disappearance of the low-lying spin excitations causes strong suppression of long-wavelength magnetic fluctuations

accompanied by deviation of χ from the Curie–Weiss law at 180 K observed in $\tau(T)$ dependence (inset in Figure B2.6). An opening of the spin gap might be explained by the position of an f -level lying 180 K below the Fermi surface.

A standard approach to HF systems considers, as a starting point, a set of strongly localized f -electrons; the appearance of a new energy scale results from hybridization of conduction electrons with local f moments so that heavy quasiparticles appear on the Fermi surface. An alternative approach [B2.42] starts from a delocalized band carrier whose transport depends upon the strength of its coupling with excitations of the medium: in the limit of strong coupling an electron accompanied by lattice or spin excitations forms a quasiparticle — a polaron. As is the case for the well-known lattice polaron, formation of a spin polaron may profoundly renormalize the bare electron band (bandwidth $\Delta_0 \sim 1$ eV) into an extremely narrow ($\Delta_{\text{SP}} \sim 10^{-4} - 10^{-3}$ eV) SP band [B2.30]. At low temperature, such a SP band supports coherent SP dynamics [B2.29]. As SP have spin higher than 1/2, they do not need to follow a FL state — hence NFL behaviour is possible. At still lower temperature, formation of spin bipolarons might cause SC [B2.27, B2.43]. Here, the opening of a spin gap is a ‘must have’ ingredient, as it protects paired electrons from spin exchange with the environment, which destroys pairs. At higher T , however, the SP dynamics occur on a background of strong coupling to spin fluctuations, which destroys coherence. A dramatic renormalization of the SP band is expected to go hand-in-hand with a significant increase of the electron effective mass, which may allow application of general concepts developed for coherent-to-incoherent crossover of the tunneling dynamics of heavy particles: suppression of coherence in a metal is expected at $T \sim \Delta_{\text{SP}}$ [B2.44]. As a result, at high temperature SP are characterized by incoherent hopping transport and the band picture breaks down. However, at low temperature the band picture manifests itself in a coherent transport of heavy quasiparticles — SP. Thus, such SP description allows to arrive to a qualitatively similar results as the standard approach to HF, albeit without involvement of the Kondo screening. A remarkable

advantage of such an approach is that it naturally accounts for the loss of coherence at higher temperature.

In summary, a spin gap opens up in UBe_{13} at 180 K, detected by spin polarons. Formation of the SP band may explain several long-standing mysteries of UBe_{13} : NFL behaviour, loss of coherence in a metal, and huge magnetoresistance. Emergence of such SP bands might be a general phenomenon in HF systems as we have recently found SP in several HF systems, such as CeCu_6 , CeCoIn_5 and Ce_2RhIn_8 utilizing the same $\mu^+\text{SR}$ measurement technique as with UBe_{13} . Within this picture, the SP is itself the celebrated heavy fermion.

This work was supported by the Kurchatov Institute, NSERC of Canada and the U.S. DOE, Basic Energy Sciences (Grant DE-SC0001769).

B.2.3. Figures for Appendix B.2

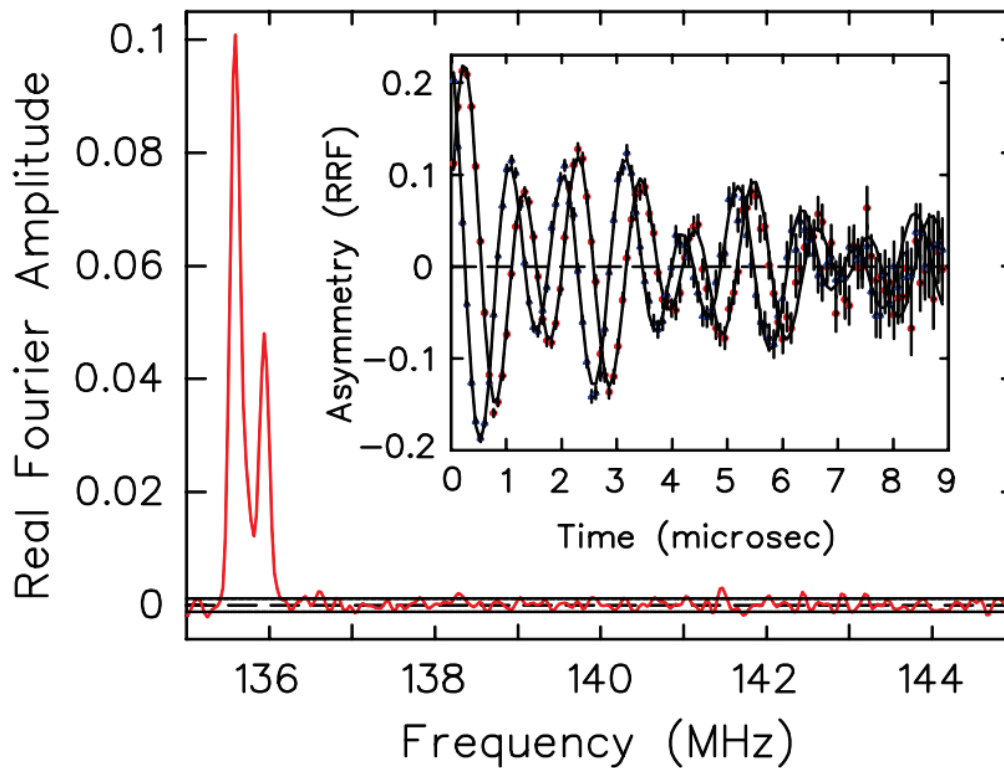


Figure B2.1: Frequency spectrum of muon spin precession in UBe_{13}

Frequency spectrum of muon precession in UBe_{13} in a transverse magnetic field $B = 1$ T at $T = 150$ K. *Inset:* same spectrum in the time domain in a rotating reference frame. The two-frequency precession characteristic of a muon–electron hyperfine coupled state is evident in both domains.

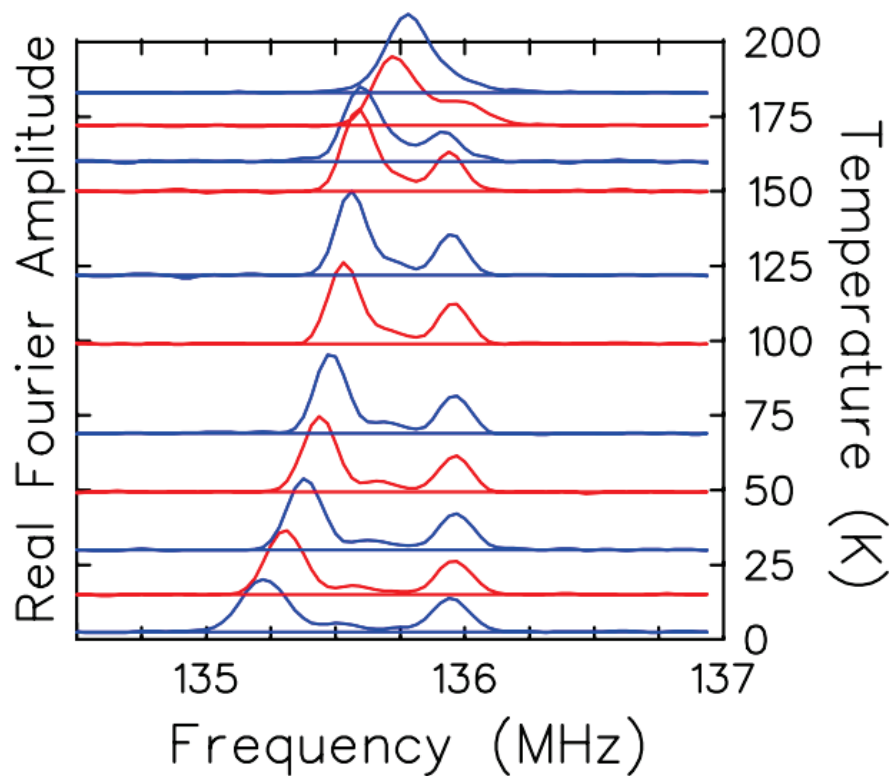


Figure B2.2: FFTs of TF-MuSR signal at various temperatures in UBe_{13}

Fourier transforms of the muon spin precession signal in UBe_{13} in a transverse magnetic field of 1 T at different temperatures. The characteristic SP doublet persists down to the lowest measured temperature, $T = 0.025$ K. A very small line in between the 2 main lines comes from a small fraction of muons which fail to capture a SP. Inclusion of the third signal in the fits has no effect on the results for the two main signals.

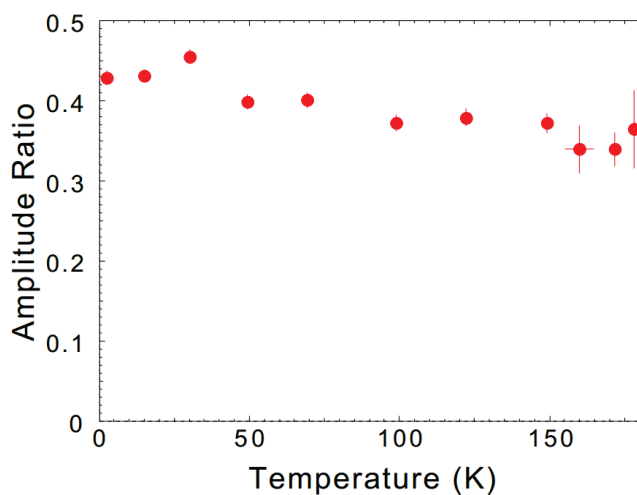


Figure B2.3: UBe_{13} ratio of asymmetry within doublet

Temperature dependences of the ratio of the amplitudes of the two lines within the SP doublet. Note that this ratio is significantly lower than 0.5 and is significantly temperature dependent.

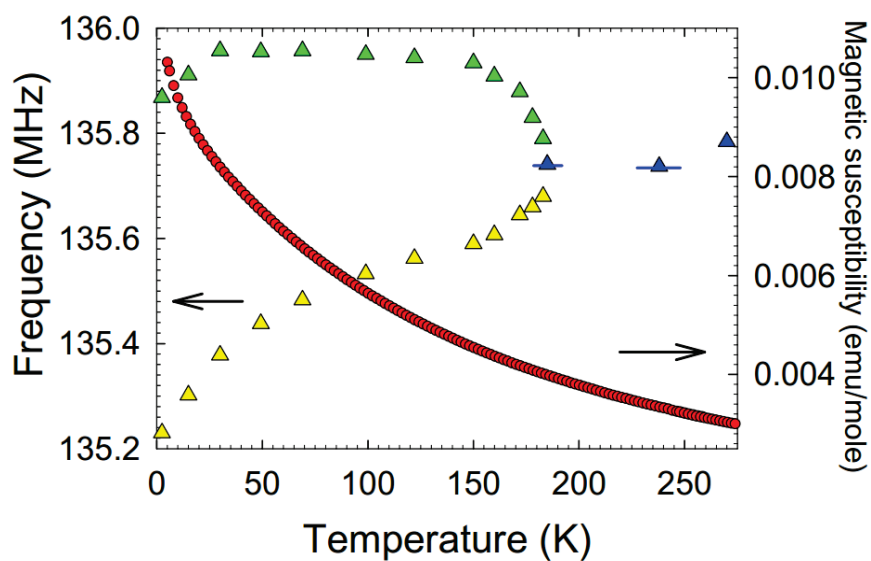


Figure B2.4: UBe_{13} temperature dependence of frequency splitting and magnetic susceptibility

Temperature dependences of the magnetic susceptibility (red circles) and muon spin precession frequencies at $H=1$ T (triangles: blue (online) — a single line above 180 K; yellow (online) — a spin majority line; green (online) — a spin minority line). Neither SP doublet frequencies follow the susceptibility, which rules out any possible bare muon scenario.

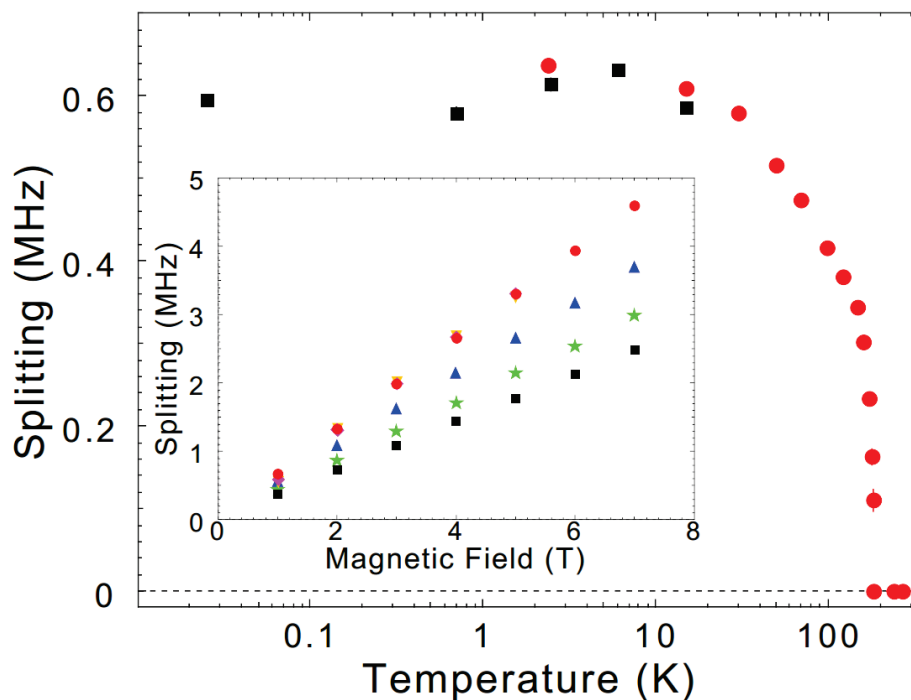


Figure B2.5: UBe₁₃ Temperature dependence of SP frequency splitting

Temperature dependence of the SP frequency splitting $\Delta\nu$ in UBe_{13} in a magnetic field of $B = 1$ T measured using *HiTime* (circles) and *DR* (squares) spectrometers. *Inset*: Magnetic field dependences of $\Delta\nu$ at $T = 150$ K (squares), $T = 99$ K (stars), $T = 50$ K (triangles), $T = 15$ K (circles), $T = 0.7$ K (nablas) and $T = 0.025$ K (diamonds); the circles obscure the nablas and the diamonds, showing that there is very little change at the lowest temperatures.

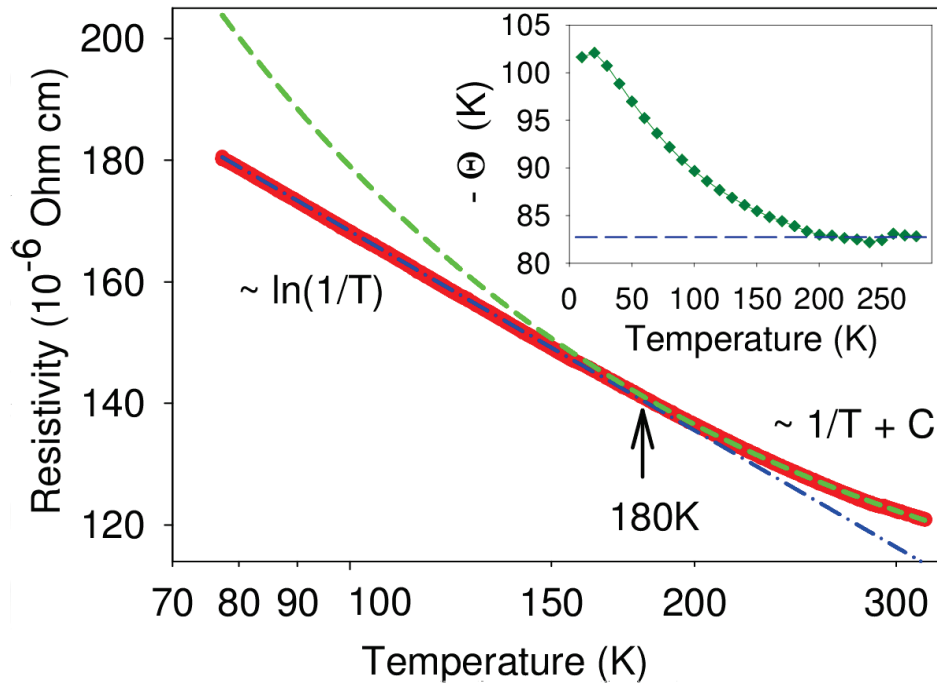


Figure B2.6: Temperature dependence of UBe_{13} electrical resistivity

Temperature dependence of the electrical resistivity of UBe_{13} (red: experimental points; green and blue dotted lines: fitting to corresponding functions). Inset: $\Theta(T)$ dependence extracted from magnetization measurements.

B.2.4. References for Appendix B.2

- [B2.1] Moriya, T. Spin Fluctuations in Itinerant Electron Magnetism. (Springer, New York, 1985).
- [B2.2] Coleman, P. Heavy Fermions: Electrons at the Edge of Magnetism in Handbook of Magnetism and Advanced Magnetic Materials. (ed. Kronmuller, H. & Parkin, S.) **1** (Wiley, New York, 2007).
- [B2.3] Basov D. N. & Timusk, T. Electrodynamics of high- T_c superconductors. *Rev Mod Phys* **77**, 721 (2005).
- [B2.4] Wiebe C. R., et al. Gapped itinerant spin excitations account for missing entropy in the hidden-order state of URu_2Si_2 . *Nature Physics* **3**, 96 (2007).
- [B2.5] Fisk, Z., et al. Heavy-Electron Metals: New Highly Correlated States of Matter. *Science* **239**, 33 (1988).

- [B2.6] Pfleiderer, C. Superconducting phases of f–electron compounds. *Rev Mod Phys* **81**, 1551 (2009).
- [B2.7] Coad, S. et al. Magnetic response in UBe_{13} . *Physica B* **276–278**, 764 (2000).
- [B2.8] Ott, H. R., Rudigier, H., Fisk, Z. & Smith, J. L. UBe_{13} : An Unconventional Actinide Superconductor. *Phys Rev Lett* **50**, 1595 (1983).
- [B2.9] Brison, J. P., et al. Normal and superconducting properties of UBe_{13} . *J Phys France* **50**, 2795 (1989).
- [B2.10] Oeschler, N., et al. UBe_{13} : Prototype of a Non–Fermi–Liquid Superconductor. *Acta Physica Polonica B* **34**, 255 (2003).
- [B2.11] Gegenwart, P., et al. Non–Fermi liquid normal state of the heavy–fermion superconductor UBe_{13} . *Physica C* **408–410**, 157 (2004).
- [B2.12] Flouquet, J. On the Heavy Fermion Road. *Prog Low Temp Phys* **15**, 139 (2005).
- [B2.13] Stewart, G. R. Non–Fermi–liquid behavior in d– and f–electron metals. *Rev Mod Phys* **73**, 797 (2001).
- [B2.14] Brown Holden, A. A., Wardlaw, G. M., Reedyk, M. & Smith, J. L. Emergence of Coherent Transport in UBe_{13} : An Optical Investigation in both the Normal and Superconducting States. *Phys Rev Lett* **91**, 136401 (2003).
- [B2.15] Liu, S. H. Electronic polaron model for the non–Fermi–liquid behavior of heavy fermion alloys. *Physica B* **240**, 49 (1997).
- [B2.16] Kasuya, T. f–f Magnetic polaron Wigner glass and anomalous superconductivity in $U_{1-x}Th_xBe_{13}$. *J Magn Magn Mater* **213**, 164 (2000).
- [B2.17] Majumdar, P. & Littlewood, P. B. Magnetoresistance in Mn Pyrochlore: Electrical Transport in a Low Carrier Density Ferromagnet. *Phys Rev Lett* **81**, 1314 (1998).
- [B2.18] Majumdar, P. & Littlewood, P. B. Dependence of magnetoresistivity on charge–carrier density in metallic ferromagnets and doped magnetic semiconductors. *Nature* **395**, 479 (1998).
- [B2.19] Storchak, V. G., et al. Observation of magnetic polarons in the magnetoresistive pyrochlore $Lu_2V_2O_7$. *J Phys Cond Mat* **25**, 115601 (2013).
- [B2.20] Brewer, J. H. *Muon Spin Rotation/Relaxation/Resonance*. in Encyclopedia of Applied Physics **11** 23–53 (VCH Publishers, New York, 1994)
- [B2.21] Yaouanc, A. & Dalmas de Reotier, P. Muon Spin Rotation, Relaxation, and Resonance. (Oxford Univ Press, New York, 2011).

- [B2.22] Sonier, J., et al. Anomalous Knight shift in the superconducting state of UBe_{13} . *Physica B* **289–290**, 20 (2000).
- [B2.23] Sonier, J., et al. μ^+ -Knight shift in the superconducting state of $\text{U}_{1-x}\text{Th}_x\text{Be}_{13}$, $x = 0$ and 0.035 single crystals. *Physica B* **326**, 414 (2003).
- [B2.24] Storchak, V. G., et al. Direct observation of the magnetic polaron. *Phys Rev B* **80**, 235203 (2009).
- [B2.25] Storchak, V. G., et al. Magnetic polaron bound to the positive muon in SmS: Exchange-driven formation of a mixed-valence state. *Phys Rev B* **79**, 193205 (2009).
- [B2.26] Storchak, V. G., et al. Electron localization into a bound spin polaron in the quasi-one-dimensional $S=1/2$ antiferromagnet LiCu_2O_2 . *Phys Rev B* **79**, 220406(R) (2009).
- [B2.27] Storchak, V. G., et al. Spin Polarons in the Correlated Metallic Pyrochlore $\text{Cd}_2\text{Re}_2\text{O}_7$. *Phys Rev Lett* **105**, 076402 (2010).
- [B2.28] Storchak, V. G., Brewer, J. H., Lichti, R. L., Lograsso, T. A. & Schlager, D. L. Electron localization into spin-polaron state in MnSi. *Phys Rev B* **83**, 140404(R) (2011).
- [B2.29] Storchak, V. G., Brewer, J. H., Lichti, R. L., Hu, R. & Petrovic, C. Thermal destruction of spin-polaron bands in the narrow-gap correlated semiconductors FeGa_3 and FeSb_2 . *J Phys Cond Mat* **24**, 185601 (2012).
- [B2.30] Nagaev, E. L. Colossal Magnetoresistance and Phase Separation in Magnetic Semiconductors. (Imperial College, London, 2002).
- [B2.31] de Gennes, P. G. Effects of Double Exchange in Magnetic Crystals. *Phys Rev* **118**, 141 (1960).
- [B2.32] Storchak, V. G., et al. Antiferromagnetism in the spin-gap system NaV_2O_7 : Muon spin rotation measurements. *Phys Rev B* **85**, 094406 (2012).
- [B2.33] Yaresko, A. N., Antonov, V. N. & Harmon, B. N. Electronic structure and x-ray magnetic circular dichroism in uranium compounds, III, Heavy-fermion compounds. *Phys. Rev. B* **68**, 214426 (2003).
- [B2.34] Storchak, V. G., Parfenov, O. E., Brewer, J. H. & Eshchenko, D. G. Reply to Comment on Direct observation of the magnetic polaron. *Phys Rev B* **83**, 077202 (2011).
- [B2.35] Felten, et al. Observation of a Schottky Anomaly in the Specific Heat of the Heavy-Fermion Compound UBe_{13} . *Europhys Lett* **2**, 323 (1986).

- [B2.36] Clark, W. G., et al. Observation of high-temperature spin fluctuations in UBe_{13} by nuclear-spin relaxation. *J Appl Phys* **63**, 3890 (1988).
- [B2.37] Kasuya, T. Electrical Resistance of Ferromagnetic Metals. *Prog Theor Phys* **16**, 58 (1956).
- [B2.38] de Gennes, P. G. & Friedel, J. Anomalies de resistivite dans certains metaux magniques. *J Phys Chem Solids* **4**, 71 (1958).
- [B2.39] Kondo, J. Resistance Minimum in Dilute Magnetic Alloys. *Prog Theor Phys* **32**, 37 (1964).
- [B2.40] Andraka, B., Kim, W. W., Kim, J. S. & Stewart, G. R. Resistivity and magnetoresistance of $(\text{U}_{1-x}\text{M}_x\text{Be}_{13})$ (M=La, Th, Y, Sc, Hf) *Phys Rev B* **44**, 5040 (1991).
- [B2.41] Abrikosov, A. A. Fundamentals of the Theory of Metals. (North-Holland, Amsterdam, 1988).
- [B2.42] Fulde, P. & Zwicknagl, G. Different routes to heavy fermion behaviour. *Physica B* **206**, 125 (1995).
- [B2.43] Mott, N. F. Polaron models of high-temperature superconductors. *J Phys Cond Mat* **5**, 3487 (1993).
- [B2.44] Storchak, V. G. & Prokof'ev, N. V. Quantum diffusion of muons and muonium atoms in solids. *Rev Mod Phys* **70**, 929 (1998).

B.3. MAGNETIC POLARONS IN $\text{Lu}_2\text{V}_2\text{O}_7$

IOP PUBLISHING

JOURNAL OF PHYSICS: CONDENSED MATTER

J. Phys.: Condens. Matter **25** (2013) 115601 (5pp)

doi:10.1088/0953-8984/25/11/115601

Observation of magnetic polarons in the magnetoresistive pyrochlore $\text{Lu}_2\text{V}_2\text{O}_7$

Vyacheslav G Storchak¹, Jess H Brewer², Dmitry G Eshchenko³,
Patrick W Mengyan⁴, Haidong Zhou^{5,6} and Christopher R Wiebe⁷

¹ Kurchatov NBICS Centre, National Research Centre 'Kurchatov Institute', Kurchatov Sq. 1, Moscow 123182, Russia

² Department of Physics and Astronomy, University of British Columbia, Vancouver, BC V6T 1Z1, Canada

³ Bruker BioSpin AG, Industriestrasse 26, 8117 Fällanden, Switzerland

⁴ Department of Physics, Texas Tech University, Lubbock, TX 79407-1051, USA

⁵ National High Magnetic Field Laboratory, Florida State University, Tallahassee, FL 32306-3016, USA

⁶ Department of Physics and Astronomy, University of Tennessee, Knoxville, TN 37996-1200, USA

⁷ Department of Chemistry, University of Winnipeg, Winnipeg, MB R3B2E9, Canada

E-mail: mussr@triumf.ca (Vyacheslav G Storchak)

Received 26 November 2012, in final form 28 January 2013

Published 14 February 2013

Online at stacks.iop.org/JPhysCM/25/115601

Abstract

Materials that exhibit colossal magnetoresistance (CMR) have attracted much attention due to their potential technological applications. One particularly interesting model for the magnetoresistance of low-carrier-density ferromagnets involves mediation by magnetic polarons (MP)—electrons localized in nanoscale ferromagnetic ‘droplets’ by their exchange interaction. However, MP have not previously been directly detected and their size has been difficult to determine from macroscopic measurements. In order to provide this crucial information, we have carried out muon spin rotation measurements on the magnetoresistive semiconductor $\text{Lu}_2\text{V}_2\text{O}_7$ in the temperature range from 2 to 300 K and in magnetic fields up to 7 T. Magnetic polarons with characteristic radius $R \approx 0.4$ nm are detected below about 100 K, where $\text{Lu}_2\text{V}_2\text{O}_7$ exhibits CMR; at higher temperature, where the magnetoresistance vanishes, these MP also disappear. This observation confirms the MP-mediated model of CMR and reveals the microscopic size of the MP in magnetoresistive pyrochlores.

(Some figures may appear in colour only in the online journal)

1. Background and introduction

Systems with strongly correlated electrons whose interaction energies exceed their kinetic energy may exhibit various subnanometer-sized inhomogeneous charge and spin states—lattice and magnetic polarons, droplet and stripe structures etc—that are believed to be intimately connected to remarkable cooperative phenomena such as metal–insulator transitions (MIT) and colossal magnetoresistance (CMR) [1–3] and are discussed in high- T_c superconductivity [4]. In the archetypal MIT and CMR materials—undoped perovskite manganites—the transition of the antiferromagnetic (AF) insulator state into the hole-doped ferromagnetic (FM) metallic state is found to occur through a phase-separated state. While collinear AF and FM states correspond to a

local minima in energy, a canted state [5] is unstable with respect to phase separation: the most energetically beneficial phase-separated state corresponds to FM spin (magnetic) polarons (MP) embedded in an AF matrix [3]. In manganites, strong interaction between electron and lattice subsystems via a combination of double-exchange (DE) and a Jahn–Teller distortion of the MnO_6 octahedra indicate that the lattice polaron effect plays an important role in the transport properties [6]. However, the remarkable sensitivity of the electron transport to the magnetization shows that electron localization into a magnetic polaron may be a key ingredient of MIT and CMR models in manganites.

The mixed-valence manganites share their properties, in particular MIT and/or CMR, with several other distinct families of magnetic semiconductors (MS). These include

the rare earth chalcogenides [1–3], Cr-based spinels [7] and diluted magnetic semiconductors. An impressive CMR in electron-doped EuO, on the order of 10^6 (as compared to several per cent in FM Fe and Ni or several dozen per cent in hole-doped manganites), clearly reflects a remarkable influence of the magnetic state on electron transport [1–3]. In general, the enormous MIT and CMR effects characteristic to non-degenerate Eu chalcogenides and Cr spinels obviously demand a model that goes beyond magnetic scattering theory [8]. Such a model of magnetic polarons, as deep levels which empty into a conduction band exhibiting giant band splitting, is employed to explain both huge MIT (up to 10^{14} -fold) and CMR (up to 10^6 -fold) in MS [1–3]. In fact, observations of MP in doped manganites [9] and cobaltites [10] as well as in Eu [11–13] and Sm [14] chalcogenides and Cr spinels [15, 16] support the MP model.

Recent discoveries reveal CMR in yet another distinct class of materials—frustrated magnetic pyrochlores [17–19]—which often adopt ground states that are macroscopically degenerate. Such degeneracy may promote different short-range alternatives to the long-range ordered ground state, producing exotic electronic and magnetic properties [20]. As in Eu- and Sm-based MS, and in marked contrast to manganites, there is no structural anomaly in the pyrochlores $Tl_2Mn_2O_7$ and $Lu_2V_2O_7$. The CMR discovered in these materials does not involve a lattice polaron; the DE model is also unsuitable, due to a single 3d valence state of Mn^{4+} and V^{4+} , respectively, and rather weak charge–lattice and spin–lattice couplings. In these pyrochlores and magnetic semiconductors (such as EuS, EuO or EuSe), the magnetic coupling is mediated instead (at least partly) by bound electrons (superexchange). In addition, the charge carriers in pyrochlores are electrons at very low density (0.001–0.005 per formula unit), rather than holes as in the perovskites (~ 0.2 per Mn atom) [18]. A model developed for low-carrier-density ferromagnets [21, 22] predicts the magnetoresistance to be dependent on the carrier density and that the narrowness of the conduction band may cause the carriers to self-trap as MP. In both the itinerant and the self-trapped regimes, the magnetoresistance appears to be large. At high temperature, the MP is confined to very few sites and its magnetization is saturated. Measurements of the magnetoresistance in the doped Tl_2MnO_7 [23, 24] show that the basic behavior is consistent with this model. However, a quantitative comparison with the experimental data is hampered by unknown carrier concentrations and uncontrolled disorder [22]. Nevertheless, the general approach of the MP model is supported by the basic trend of the magnetoresistance over various groups of materials ranging from doped magnetic semiconductors to intrinsic magnetic semiconductors and pyrochlores [22]. Direct observation of the MP and their co-evolution with the CMR is still needed to confirm this model.

Here, we present direct observation of the MP in the magnetoresistive pyrochlore, $Lu_2V_2O_7$. Magnetic polarons are detected in the temperature region where $Lu_2V_2O_7$ exhibits CMR, and disappear above 100 K where CMR is negligibly small.

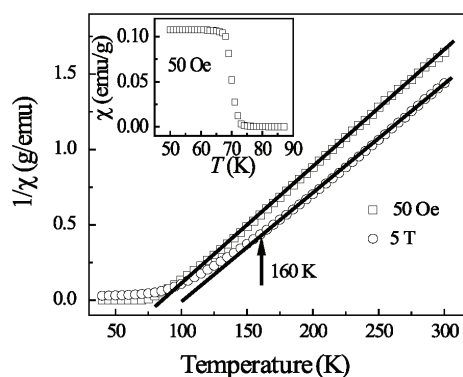


Figure 1. Temperature dependences of the inverse of the magnetic susceptibility of $Lu_2V_2O_7$ measured in applied magnetic fields 0.005 and 5 T. Inset: susceptibility of $Lu_2V_2O_7$ in magnetic field 0.005 T measured around 70 K.

2. Experiment details

Single crystals of $Lu_2V_2O_7$ for the current studies were grown by the traveling float zone technique. Details of the sample growth and characterization by x-ray diffraction, susceptibility (figure 1), resistivity, magnetoresistance, thermal expansion, specific heat and thermal conductivity are described in [19]. Time-differential muon spin rotation (μ^+ SR) experiments [25, 26] using 100% spin-polarized positive muons implanted into $Lu_2V_2O_7$ were carried out on the M15 muon channel at TRIUMF using the HiTime spectrometer.

3. Results and discussion

Within the temperature region (below about 100 K) of the CMR effect [19], Fourier transforms of the (μ^+ SR) time spectra measured in high magnetic field applied transverse to the muon spin (HTF) and along the (100) axis of the crystal consist of two lines (figure 2) shifted to lower frequencies relative to the reference frequency $\nu_\mu = \gamma_\mu B / 2\pi$ (where $\gamma_\mu = 2\pi \times 135.53879$ MHz T^{-1} is the muon gyromagnetic ratio and B is the magnetic field). HTF- μ^+ SR measurements in isostructural but non-magnetic $Lu_2Ti_2O_7$ reveal a single line at ν_μ .

A two-line spectrum is frequently attributed to two magnetically inequivalent positions of the bare muon in a magnetically ordered material. However, similar 2-line spectra are detected both below and well above $T_c = 69.5$ K (figure 3). Moreover, the two lines detected in the zero magnetic field μ^+ SR experiment do not follow the temperature dependence of the magnetization, which clearly indicates that the muon does not stay bare and does not act simply as a local magnetometer. Both latter observations are similar to those in $LiCu_2O_2$ where two-line spectra are identified as characteristic of MP [27]. Local magnetic fields acting on the muon at low temperature in the FM state of

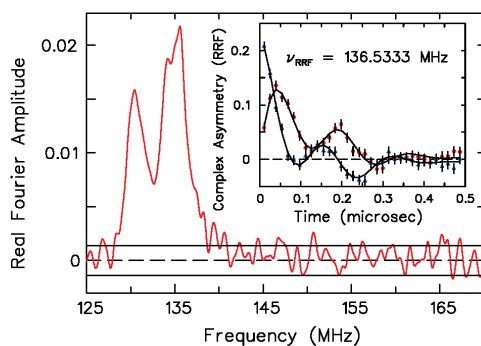


Figure 2. Frequency spectrum of muon spin precession in $\text{Lu}_2\text{V}_2\text{O}_7$ in a transverse magnetic field of $B = 1$ T at $T = 75$ K. Only the real part is shown. Inset: same spectrum in the time domain in a rotating reference frame at 136.5333 MHz (triangles—real part, circles—imaginary part). The two-frequency precession is characteristic of a localized electron state (MP) hyperfine-coupled to a muon.

$\text{Lu}_2\text{V}_2\text{O}_7$, extracted from 2-line spectra in a manner similar to that in [27], amount to ~ 0.08 T—typical for a muon in an interstitial site in various magnetic materials [25, 26]. Finally, a departure from linear magnetic field dependences of the two frequencies in $\text{Lu}_2\text{V}_2\text{O}_7$ allow one to rule out possible Knight shifts in the bare muon scenario.

Instead, observation of the 2-line spectrum with the characteristic overall FM shift is the fingerprint of an electron state hyperfine-coupled to the muon and confined into a FM ‘droplet’—a MP [12, 14, 16, 28, 29]. The HTF- μ^+ SR technique has long been used to reveal spectroscopic signatures of electron localization into the muonium ($\text{Mu} \equiv \mu^+e^-$) atom (a light analog of the H atom) [25, 26]. In HTF two classes of muon states can be distinguished by their characteristic precession signals: a diamagnetic charged state (usually a bare μ^+) and a paramagnetic neutral state (usually Mu). The former precesses at a frequency of ν_μ .

In weak magnetic field, the triplet (spin 1) state of Mu has a gyromagnetic ratio of 102.88349 times that of the bare muon. At higher magnetic field, the Mu precession splits into two lines following the Breit–Rabi Hamiltonian [25, 26], their separation determined by the muon–electron hyperfine constant, A . In very high magnetic field, the two observed Mu frequencies correspond to muon spin-flip transitions between states with the same electron spin orientation.

In magnetic semiconductors, Mu often turns into a more deeply bound MP. Any confinement of a carrier (mass m^*) raises its kinetic energy and is thus very unlikely, unless some local interaction compensates this increase. Such an increase in kinetic energy can be compensated by an exchange interaction, J , between local $d(f)$ moments of the magnetic ions mediated by the aforementioned electron [5]. The local character of such an interaction can cause spatial inhomogeneity. In a system of magnetic ions, the electron energy depends strongly on the magnetization, a minimum being achieved by ferromagnetic ordering. For this reason, the electron tends to establish and support this ordering, thus forming a FM ‘droplet’ over the extent of its wavefunction (typically, the first coordination sphere to maximize the exchange contribution) in a host that is otherwise AF or paramagnetic (PM) [3, 30]. The charge carrier coupled to its immediate FM environment behaves as a single quasiparticle—a magnetic polaron. In magnetic semiconductors, such a MP may be bound to a donor, whose Coulomb attraction provides important assistance to confinement, which is opposed by the entropy change, ΔS , due to ordering within the MP, so that the net change in the free energy

$$\Delta F = \frac{\hbar^2}{2m^*R^2} - J\frac{a^3}{R^3} - \frac{e^2}{\epsilon R} + T\Delta S \quad (1)$$

has a minimum as a function of R , thereby determining the radius of the confinement [12, 14, 16, 30].

Such MP with the electron confined in a 0.3–0.5 nm FM ‘droplet’ around a positive muon are found in PM states of EuS, EuO, EuSe, SmS and CdCr_2Se_4 [12, 31,

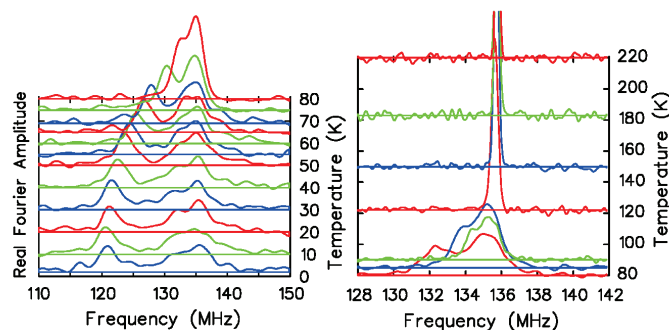


Figure 3. Fourier transforms of the muon spin precession signal in $\text{Lu}_2\text{V}_2\text{O}_7$ in a transverse external magnetic field $B = 1$ T at different temperatures. Characteristic MP lines appear below about 100 K and persist through the FM transition ($T_c = 69.5$ K) down to the lowest measured temperature.

14, 16], in the AF state of LiCu_2O_2 [27] or in metallic MnSi and $\text{Cd}_2\text{Re}_2\text{O}_7$ [28, 29]. In metals, an independently formed itinerant MP is captured by the muon to exhibit the characteristic $\mu^+ - e^-$ hyperfine splitting [28, 29]. The MP can be clearly distinguished from a simple Mu atom formed via electron capture by the muon in non-magnetic materials [32–34]. In a magnetic host, rapid spin exchange with the hosts spins would average the muon–electron hyperfine splitting to zero. By contrast, when the electron spin is strongly bound into a MP, the local FM ordering holds the electron spin fixed, revealing the hyperfine interaction [12, 28, 29]. In addition, a significant shift of the MP lines with respect to the reference signal reflects the FM internal field within a MP [12].

Figure 3 shows the evolution of the μ^+ SR spectra with temperature in magnetic field $B = 1$ T.

Above about 100 K, all spectra consist of a single line with a frequency coinciding with that observed in a reference sample (CaCO_3). This is taken as evidence that above 100 K the muon stays bare and a MP does not form in a high magnetic field $B = 1$ T. The CMR measured in a high magnetic field $B = 2$ and 5 T goes to zero in $\text{Lu}_2\text{V}_2\text{O}_7$ at about the same temperature (figure 4) [19]. On the other hand, both measurements of the magnetic susceptibility (in a low magnetic field $B = 0.005$ T) (figure 1) and resistivity (in a zero magnetic field) (figure 4) indicate that a MP starts to form at about 160 K [19]. However, these observations mark no contradiction as the binding energy of a MP is significantly reduced under an applied magnetic field [30, 19, 12, 16].

The CMR has a clear maximum at $T_{\text{max}} = 75$ K (figure 4) [19]. On the other hand, MP spectra do not have distinct peculiarities at T_{max} , which probably reflects the fact that μ^+ SR spectra only probe the MP after its capture by the muon and are insensitive to its transport prior to that capture. In contrast, the CMR is a measure of transport properties.

In the bulk FM state, the carrier is expected to be released from the MP and become delocalized, which would cause a sharp reduction of resistivity and disappearance of the characteristic MP two-line μ^+ SR spectra. However, in $\text{Lu}_2\text{V}_2\text{O}_7$, zero field resistivity decreases gradually through T_c down to 60 K and CMR decreases from T_{max} through T_c , still staying finite down to the lowest measured temperature of about 30 K [19]. Accordingly, μ^+ SR spectra exhibit characteristic lines down to the lowest measured temperature at 2 K (figure 3). These observations demonstrate that MP exist below the FM transition. MP and free carriers may coexist below T_c according to the model developed to describe CMR in $\text{Tl}_2\text{Mn}_2\text{O}_7$ [21, 22]. In fact, a similar picture of MP existence in the FM state is found in MnSi below its $T_c = 29.5$ K [29]. In the present case, the MP state is detected in $\text{Lu}_2\text{V}_2\text{O}_7$ within the region of significant CMR and vanishes when the CMR disappears.

Temperature and magnetic field dependences of the frequency splitting, $\Delta\nu$, provide information on the characteristic size, R , and composite spin, S , of the MP [12]. Within a mean field approximation, $\Delta\nu$ is proportional to a Brillouin function [35]. In $\text{Lu}_2\text{V}_2\text{O}_7$, $\Delta\nu$ follows a Brillouin function similar to those for magnetic polarons recently characterized

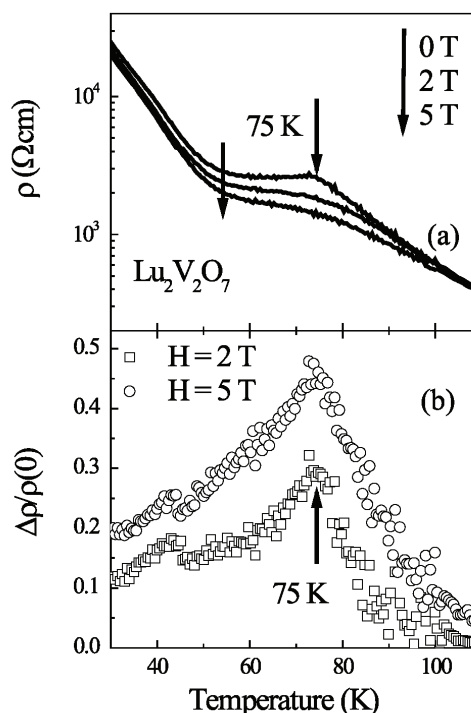


Figure 4. Temperature dependences of (a) resistivity and (b) magnetoresistance of $\text{Lu}_2\text{V}_2\text{O}_7$ in different magnetic fields.

in various other materials [12, 14, 16, 29]. For $g\mu_B B \ll k_B T$, this function [12] is linear in $B/(T - T_c)$:

$$\Delta\nu = A \left[\frac{g\mu_B B}{3k_B(T - T_c)} \right] (S + 1) \quad (2)$$

where μ_B is the Bohr magneton and k_B is Boltzmann's constant. At low T and high B , however, the composite MP spin, S , is fully polarized, resulting in saturation of $\Delta\nu$ at a value of A , from which the MP radius can be obtained [12]. In $\text{Lu}_2\text{V}_2\text{O}_7$, $\Delta\nu$ saturates as a function of both $1/T$ (at $B = 1$ T) and B (at $T = 2$ K) at the same value: $A = 13 \pm 1$ MHz (figure 5). Assuming an expanded hydrogen-like 1s MP wavefunction, the hyperfine coupling, A , scales as $A_{\text{vac}}(a_0/R)^3$; where $A_{\text{vac}} = 4463$ MHz is the hyperfine frequency of Mu in vacuum, $a_0 = 0.053$ nm is the Bohr radius of Mu (or the H atom) in vacuum and R is the characteristic radius of the MP electron wavefunction. Such an estimate gives $R \approx 0.4$ nm, corresponding to electron confinement within one unit cell of $\text{Lu}_2\text{V}_2\text{O}_7$. Depending on the muon site, a sphere of $R = 0.4$ nm contains from 8 to 12 V^{4+} ions with spin 1/2 each (Lu^{3+} being non-magnetic). Thus the fully polarized MP has $S = 5 \pm 1$. The value of the MP spin extracted from the slope of both linear dependences of $\Delta\nu$ and B at higher temperature and lower magnetic field using equation (2) amounts to $S = 3 \pm 1$, consistent with a partially polarized MP.

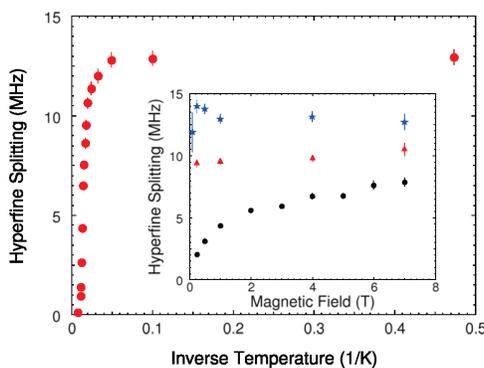


Figure 5. Temperature dependence of the MP frequency splitting, $\Delta\nu$, in $\text{Lu}_2\text{V}_2\text{O}_7$ in a magnetic field of $B = 1$ T. Inset: magnetic field dependences of $\Delta\nu$ at $T = 75$ K (circles), $T = 55$ K (triangles) and $T = 2$ K (stars). Both $\Delta\nu(1/T)$ and $\Delta\nu(B)$ saturate at the same value of $A = 13 \pm 1$ MHz.

The extracted value of $R \approx 0.4$ nm clearly indicates that MP do not overlap in this low-carrier-density (10^{-3}) ferromagnet. Such a characteristic size implies that the MP are completely decoupled below T_c —the same conclusion as that based on the CMR measurements [19].

At low temperature, the Zeeman energy of fully saturated MP having a magnetic moment of about $10 \mu_B$ obviously exceeds the thermal energy, which should lead to unequal spectral weights of the two MP lines [28]. However, both lines have nearly the same spectral weight (figure 3). This reflects a breakdown of the classical Boltzmann distribution of MP spin states, which suggests that in $\text{Lu}_2\text{V}_2\text{O}_7$ below T_c magnetic polarons are itinerant carriers as found in another correlated pyrochlore $\text{Cd}_2\text{Re}_2\text{O}_7$ [28] and MnSi [29]. This, in turn, suggests that the role of the muon as a localization center is almost negligible, which is consistent with the dominant role of the exchange interaction in the process of MP formation [28, 29].

4. Summary

We detect magnetic polarons in magnetoresistive $\text{Lu}_2\text{V}_2\text{O}_7$ exclusively within the region of CMR. This observation supports a model of magnetic-polaron-driven magnetoresistance in pyrochlores.

Acknowledgments

This work was supported by the NBICS Center of the Kurchatov Institute, NSERC of Canada, the US DoE (BES Grant DE-SC0001769), the Petroleum Fund of the ACS, the NSF (Grant DMR-0654118) and the State of Florida.

References

- [1] Coey J M D, Viret M and von Molnár S 1999 *Adv. Phys.* **48** 167
- [2] Dagotto E, Hotta T and Moreo A 2001 *Phys. Rep.* **344** 1

- [3] Nagaev E L 2002 *Colossal Magnetoresistance and Phase Separation in Magnetic Semiconductors* (London: Imperial College Press)
- [4] Emery V J, Kivelson S A and Lin H Q 1990 *Phys. Rev. Lett.* **64** 475
- [5] de Gennes P G 1960 *Phys. Rev.* **118** 141
- [6] Millis A J, Littlewood P B and Shraiman B I 1995 *Phys. Rev. Lett.* **74** 5144
- [7] Ramirez A P, Cava R J and Krajewski J 1997 *Nature* **386** 156
- [8] Fisher M E and Langer J S 1968 *Phys. Rev. Lett.* **20** 665
- [9] De Teresa J M, Ibarra M R, Algarabel P A, Ritter C, Marquina C, Blasco J, Garcia J, del Moral A and Arnold Z 1997 *Nature* **386** 256
- [10] Podlesnyak A *et al* 2008 *Phys. Rev. Lett.* **101** 247603
- [11] Rho H, Snow C S, Cooper S L, Fisk Z, Comment A and Ansermet J 2002 *Phys. Rev. Lett.* **88** 127401
- [12] Storchak V G *et al* 2009 *Phys. Rev. B* **80** 235203
- [13] Storchak V G *et al* 2010 *Phys. Rev. B* **81** 153201
- [14] Storchak V G, Brewer J H, Arseneau D J, Stubbs S L, Parfenov O E, Eshchenko D G, Morenzoni E and Aminov T G 2009 *Phys. Rev. B* **79** 193205
- [15] Yang Z, Xinyu B, Tan S and Zhang Y 2004 *Phys. Rev. B* **69** 144407
- [16] Storchak V G, Brewer J H, Russo P L, Stubbs S L, Parfenov O E, Lichti R L and Aminov T 2010 *J. Phys.: Condens. Matter* **22** 495601
- [17] Subramanian M A, Toby B H, Ramirez A P, Marshall W J, Sleight A W and Kwei G H 1996 *Science* **273** 81
- [18] Shimakawa Y, Kubo Y and Manako T 1996 *Nature* **379** 53
- [19] Zhou H D *et al* 2008 *Phys. Rev. B* **77** 020411
- [20] Gardner J S, Gingras M J P and Greedan J E 2010 *Rev. Mod. Phys.* **82** 53
- [21] Majumdar P and Littlewood P B 1998 *Phys. Rev. Lett.* **81** 1314
- [22] Majumdar P and Littlewood P B 1998 *Nature* **395** 479
- [23] Ramirez A P and Subramanian M A 1997 *Science* **277** 546
- [24] Martinez B, Senis R, Fontcuberta J, Obradors X, Cheikh-Rouhou W, Strobel P, Bougerol-Chailout C and Pernet M 1999 *Phys. Rev. Lett.* **83** 2022
- [25] Brewer J H 1994 *Encyclopedia of Applied Physics* vol 11 (New York: VCH) pp 23–53
- [26] Yaouanc A and Dalmas de Reotier P 2011 *Muon Spin Rotation, Relaxation, and Resonance: Applications to Condensed Matter* (New York: Oxford University Press)
- [27] Storchak V G, Brewer J H, Arseneau D J, Stubbs S L, Parfenov O E, Eshchenko D G and Bush A A 2009 *Phys. Rev. B* **79** 220406
- [28] Storchak V G, Brewer J H, Stubbs S L, Parfenov O E, Lichti R L, Mengyan P W, He J, Bredeson I, Hitchcock D and Mandrus D 2010 *Phys. Rev. Lett.* **105** 076402
- [29] Storchak V G, Brewer J H, Lichti R L, Lograsso T A and Schlager D L 2011 *Phys. Rev. B* **83** 140404
- [30] von Molnár S and Stampe P A 2007 *Handbook of Magnetism and Advanced Magnetic Materials* vol 5, ed H Kronmüller and S Parkin (Hoboken: Wiley)
- [31] Storchak V G *et al* 2009 *Physica B* **404** 899
- [32] Storchak V G, Cox S F J, Cottrell S P, Brewer J H, Morris G D, Arseneau D J and Hitti B 1997 *Phys. Rev. Lett.* **78** 2835
- [33] Storchak V G, Eshchenko D G, Brewer J H, Morris G D, Cottrell S P and Cox S F J 2000 *Phys. Rev. Lett.* **85** 166
- [34] Storchak V G, Eshchenko D G and Brewer J H 2004 *J. Phys.: Condens. Matter* **16** S4761
- [35] Smart J S 1966 *Effective Field Theories of Magnetism* (Philadelphia, PA: Saunders)

B.4. ANTIFERROMAGNETISM IN NaV_2O_5 PHYSICAL REVIEW B **85**, 094406 (2012)**Antiferromagnetism in the spin-gap system NaV_2O_5 : Muon spin rotation measurements**Vyacheslav G. Storchak,^{1,*} Oleg E. Parfenov,¹ Dmitry G. Eshchenko,² Roger L. Lichti,³ Patrick W. Mengyan,³ Masahiko Isobe,⁴ and Yutaka Ueda⁴¹National Research Centre, Kurchatov Institute, Kurchatov Square 1, Moscow 123182, Russia²Bruker BioSpin AG, Industriestrasse 26, 8117 Fällanden, Switzerland³Department of Physics, Texas Tech University, Lubbock, Texas 79409-1051, USA⁴Institute for Solid State Physics, University of Tokyo, Kashiwa, Chiba 277-8581, Japan

(Received 3 November 2011; revised manuscript received 18 January 2012; published 5 March 2012)

Muon spin rotation measurements have been carried out in a stoichiometric spin ladder compound NaV_2O_5 in the temperature range from 2 to 300 K, through the spin-gap transition at $T_c = 35$ K, in transverse magnetic fields from 0.3 to 7 T. Antiferromagnetic order with a local magnetic field at a muon site of about 0.17 T is detected coexisting with the spin-gap state below 15 K. Above 20 K, the signature of a spin-polaron state is observed, which persists to about 100 K.

DOI: 10.1103/PhysRevB.85.094406

PACS number(s): 75.45.+j, 71.38.Ht, 75.50.Ee, 76.75.+i

I. INTRODUCTION

Quasi-low-dimensional spin systems have attracted considerable attention due to the appearance of various nonmagnetic quantum states that can emerge when conventional long-range order is suppressed. In particular, in the quantum limit of spin 1/2, an antiferromagnetic (AF) state often has strong competition from a dimerized state (DS) of singlet bonds to become the ground state. Such a DS is characterized by zero average on-site spin and formation of a spin gap Δ of up to several hundred Kelvin, which separates the spin-singlet ground state from the first excited spin triplet. The prototypical systems include the Haldane and spin-Peierls compounds, spin chains, or spin ladders.¹⁻³

The absence of spectral weight at the Fermi level suggests that many of these systems are Mott insulators in which strong correlations are responsible for their insulating nature.⁴ However, even very low ($\sim 10^{-2}$) doping or the application of pressure can cause a remarkable collapse of the spin gap with emerging AF order or even metallic behavior and superconductivity.⁵ Impurities or defects in a spin-gap system may have profound effects on its magnetic state,⁶ triggering long-range AF ordering.⁷ A better-controlled way of altering the magnetic state of a quantum magnet from spin-singlet dimers to long-ranged AF order is achieved by the application of pressure altering the effect of spin fluctuations, thus, driving a quantum phase transition (QPT) between competing ground states.⁸ Distinct magnetic Bragg peaks observed by neutron spectroscopy in *stoichiometric* KCuCl_3 and TlCuCl_3 indicate the emergence of the ordered AF moments.^{9,10}

An even more delicate way to destroy a dimerized state in a *stoichiometric* spin-gap system is to drive it through a magnetic-field-induced QPT.¹¹ Typical examples include coupled spin ladders (such as TlCuCl_3 or KCuCl_3),¹² weakly coupled chains of $S = 1$ Ni atoms¹³ or planes of Cu dimers.¹⁴ In the presence of a magnetic field, the Zeeman energy reduces the gap to $\Delta(H) = \Delta - g\mu_B H$. At $T = 0$, a finite magnetization associated with AF order appears above the critical field $H_c = \Delta/g\mu_B$. The applied field, thus, acts like a chemical potential, and the Bose gas of triplets is populated above H_c .¹⁵ For most known systems, a rather high value of Δ drives H_c well above 100 T. Nevertheless, an exceptionally

low Δ on the order of several Kelvin in some quantum spin magnets indicated above makes it possible to observe magnetic-field-induced AF ordering above the corresponding $H_c = \Delta/g\mu_B$: In the canonical magnetic-field-induced QPT systems, TlCuCl_3 and KCuCl_3 Δ of 7.5 and 30 K correspond to H_c of 6 and 23 T, respectively.¹²

In contrast to all of the ways to destroy a DS mentioned above, in this paper, we present spectroscopic evidence for AF ordering below $T = 15$ K at *ambient pressure* in the *stoichiometric* spin-gap system NaV_2O_5 with $\Delta \approx 100$ K (Ref. 16) in a magnetic field of, at least, 2 orders of magnitude lower than H_c expected for a material with such a large Δ .

II. BACKGROUND

Highly anisotropic NaV_2O_5 has an orthorhombic structure (P_{mnn}) at room temperature.¹⁷ In the high-temperature phase, its magnetic susceptibility, χ , behaves similar to that expected for Heisenberg spin-1/2 chains. Below $T_c = 34$ K, a gap of $\Delta \sim 100$ K opens up in the spectrum of its magnetic excitations accompanied by a sharp reduction in χ due to dimerization and doubling of the lattice constants, characteristic of spin-Peierls systems.¹⁶ However, the strong suppression of T_c by a magnetic field inherent to spin-Peierls systems does not occur, whereas, $2\Delta/T_c$ is almost two times higher than that in genuine spin-Peierls systems.¹⁸ These facts, along with a very high jump in entropy at T_c , indicate that the driving force for the phase transition that results in an opening in a spin gap between the spin-singlet ground and spin-triplet excited states in NaV_2O_5 is the *charge ordering* of electrons in the quarter-filled vanadium ladders. Such a phase transition transforms a mixed-valence $V^{+4.5}$ state with one electron shared between two vanadium positions on a V-O-V rung above T_c to localized d electrons below T_c ,¹⁷ corresponding to charge ordering as revealed by x-ray diffraction,¹⁹ NMR,²⁰ and dielectric²¹ studies. It is suggested that a spin-singlet pair (dimer) is formed on adjacent rungs in a charge-ordered ladder.²²⁻²⁴ To the best of our knowledge, no AF phase transition has been reported in NaV_2O_5 down to 77 mK.⁶

Although a controversy over the number of inequivalent vanadium positions and their valences (V^{+4} , $V^{+4.5}$, and V^{+5})

has resulted in two theoretical models in which charge ordering occurs either in every vanadium ladder²² or in every other ladder,^{23,24} those models do explain most of the electronic and magnetic properties of NaV_2O_5 . However, several experiments, which reveal distinct anomalies well below T_c in the 10–15-K range, still require explanation. Those are an enormous increase in thermal conductivity peaked at about 15 K,²⁵ a steep increase in the electron spin resonance linewidth below about 15 K^{6,26} and static spin freezing around 11 K found by muon spin relaxation (μ^+ SR)²⁷ all of which disappear upon introduction of about 1% Na vacancies. Another μ^+ SR paper,²⁸ using samples from a different source, also shows increasing relaxation of muon spins with decreasing temperature characteristic of slowing spin fluctuations and suggests the possibility of magnetic ordering near 15 K, well below the spin-gap transition. These facts indicate that all of those effects are rather intrinsic and possibly reflect a magnetic phase transition unrevealed so far.

The muon experiments^{27,28} attract particular attention as, although having an unparalleled sensitivity to local magnetism, muons do not notice any sign of the spin-gap transition at T_c , clearly detected by many other techniques.^{16,19–21} In particular, the muon relaxation rate^{27,28} does not follow the sharp reduction in χ at T_c (Ref. 16), which clearly implies that the muon does not act as a local magnetometer in this temperature range. This fact may indicate that the local magnetic environment around the muon is fundamentally different from the rest of the host and that this local environment does not change around T_c . On the other hand, spin polarons (SPs) (which may form a local magnetic environment around the muon fundamentally different from that of the host) have long been predicted to persist around a magnetic transition.²⁹

III. THE EXPERIMENT

Time-differential muon spin rotation experiments,³⁰ using positive muons 100% spin-polarized transverse to the applied magnetic field and the c axis of single crystals of NaV_2O_5 (from the same source as those used in Ref. 27), were carried

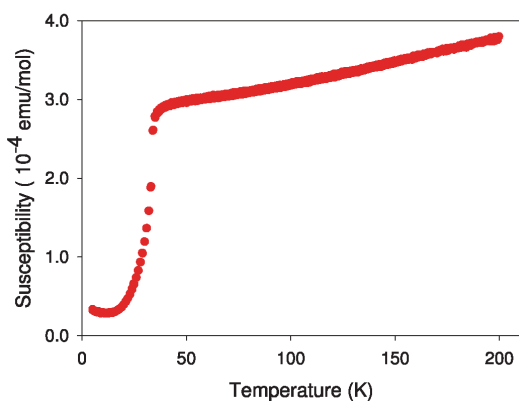


FIG. 1. (Color online) Temperature dependence of the magnetic susceptibility of NaV_2O_5 single crystals in magnetic fields at $H = 0.1$ T.

out on the M15 muon channel at TRIUMF using the *HiTime* spectrometer in magnetic fields up to 7 T and temperatures from 300 down to 2 K. X-ray diffraction and magnetic susceptibility (Fig. 1) measurements on these crystals and a polycrystalline pressed powder pellet of NaV_2O_5 (also examined) produce results consistent with the literature data.

IV. RESULTS AND DISCUSSION

At low temperatures, in magnetic fields transverse to the initial muon polarization, Fourier transforms of the μ^+ SR time spectra consist primarily of two satellite lines positioned symmetrically on either side of the central narrow line (Fig. 2), which appears precisely at the bare-muon Larmor frequency of $\nu_\mu = \gamma_\mu B/2\pi$ (where $\gamma_\mu = 2\pi \times 135.53879$ MHz/T is the muon gyromagnetic ratio and B is the magnetic field). The position of this central line is temperature independent and coincides with the single peak observed in a reference sample (CaCO_3); thus, it constitutes the signal from those muons whose immediate environments are *nonmagnetic*. Satellite lines represent signals from those muons that have different magnetic environments. Positions of the satellites with respect to the central line do not depend on a magnetic field and correspond to two characteristic local magnetic fields at

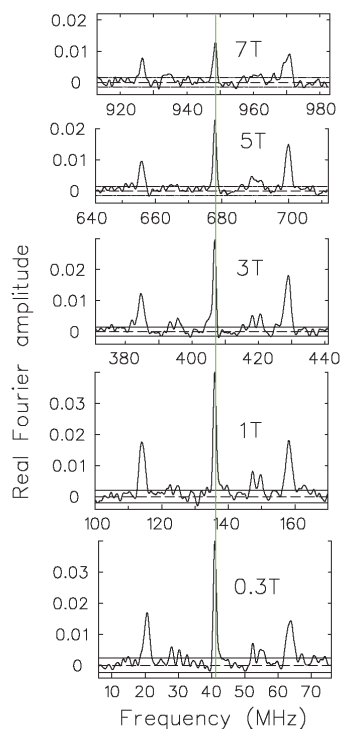


FIG. 2. (Color online) Frequency spectra of muon spin precession in NaV_2O_5 in different magnetic fields at $T = 2$ K. Each spectrum is offset horizontally to place the bare- μ^+ frequency on the same vertical line (green online).

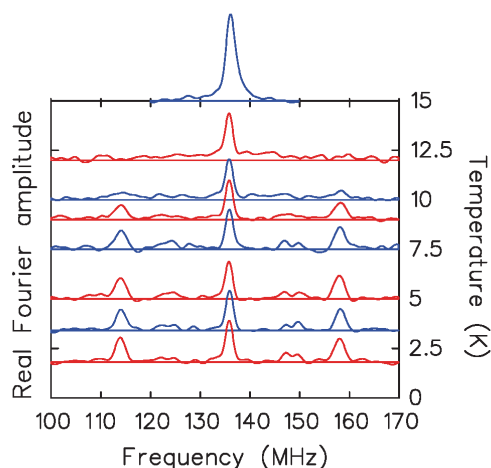


FIG. 3. (Color online) Frequency spectra of the muon spin precession signals in NaV_2O_5 in a magnetic field of 1 T at different temperatures. Characteristic AF lines disappear above 10 K.

$B_{\pm} = B \pm 0.17$ T. The local magnetic field of 0.17 T is typical for a muon at an interstitial position in various magnetic materials.³⁰

Figure 3 presents the evolution of μ^+ SR spectra with temperature. Satellite lines disappear above 10 K. Below 10 K, spectral weights of the satellite lines are identical at the lower fields, and each amounts to about 1/2 the spectral weight of the central line. Above 15 K, the spectral weight of the central line doubles at the expense of the satellite signals. We claim that such an evolution reflects an AF phase transition at about 15 K, which results in three magnetically inequivalent muon positions in the AF phase: 50% of muons in the *nonmagnetic* environment and the other 50% residing equally in the *magnetic* environment of the *two AF sublattices*. The three main lines can result from a single type of crystallographic muon site; the total spectral weight of other features in the frequency spectra do not exceed 10% of the overall spectral weight. Satellite lines are not seen in the polycrystalline sample, which is evidence for strong anisotropy of the local magnetic field. This latter fact and the results presented in Figs. 2 and 3 suggest that the local magnetic field is (anti)parallel to the *c* axis, which also is supported by the absence of muon spin precession in Ref. 27. Thus, the geometry chosen in the current experiment is the most convenient for the determination of the local magnetic field.

In NaV_2O_5 , the exchange interaction between vanadium ladders at high temperature $J_{\perp} \approx 35$ K is rather high,³¹ which might result in three-dimensional AF ordering. Nevertheless, the spin-gap state persists below T_c up to the highest applied field of 33 T as $\Delta \approx 100$ K is larger than J_{\perp} .³² However, formation of the spin-gap state in NaV_2O_5 is intimately connected to the charge ordering on the Trellis lattice (two-dimensional frustrated coupled ladders), which does not allow full charge ordering due to frustration.²⁴ This fact makes up the core of the model, which suggests charge ordering in every other vanadium ladder.²⁴ This results in differentiation

of the spin subsystem into magnetic and nonmagnetic ladders equally populated in NaV_2O_5 which is fully consistent with our experiment: Those muons, which reside within charge-ordered ladders, find themselves in the nonmagnetic environment of a spin-gap state, whereas, those muons that rest within charge-disordered ladders experience an AF transition at about $T_N \sim 15$ K as a result of a weak exchange interaction J_{\perp} between disordered ladders. At low temperatures, J_{\perp} is reduced with respect to its high-temperature value due to the intervening charge-ordered ladders and lattice doubling at T_c . According to the mean-field theory for a quasi-one-dimensional quantum AF system,³³ J_{\perp} can be estimated as $J_{\perp} \approx k_B T_N / [1.28 \sqrt{\ln(5.8J/k_B T_N)}] \approx 5$ K, where k_B is the Boltzmann constant and $J \approx 560$ K is the exchange interaction within the ladder.¹⁶ This value is consistent with $J_{\perp} \approx 2$ –4 K calculated for the low-temperature phase of NaV_2O_5 .²⁴

Thus, we find coexistence of spin-gap and AF phases in stoichiometric NaV_2O_5 below 15 K. As the muon is a local magnetic probe, we cannot determine if this AF ordering is a long-range transition or a local AF cluster formation. However, the experiments of Refs. 25–27 indicate a cooperative phenomenon rather than local clustering.

While staying bare and acting as a local magnetometer at low temperatures, the muon does not stay bare at a higher temperature: At temperatures above the AF transition, we observe the spectroscopic signature of spin polarons in NaV_2O_5 . As shown in Fig. 4 as a function of magnetic field at $T = 29$ K, the μ^+ SR spectra exhibit the characteristic two-frequency precession (doublet) in high magnetic fields^{34,35} (the low-frequency line is a background signal whose frequency coincides with that in CaCO_3). Such a doublet corresponds to two muon spin-flip transitions between states with fixed electron spin orientation within the SP.^{30,34,35} Amplitudes of the SP lines decrease very rapidly above 100 K implying significantly reduced SP formation probability in that temperature region. The characteristic widths of the polaron lines are consistent with the muon relaxation rate measured in a longitudinal magnetic field and are assigned to spin fluctuations associated with the spin gap.²⁷

In insulators and semiconductors, the positive muon can bind an electron to form a muonium (Mu) atom analogous to a hydrogen atom in which the proton is replaced by a muon.^{30,36} In the μ^+ SR experiments on insulators^{37,38} and semiconductors,^{39–42} each incoming 4-MeV muon injects a very low ($\sim 10^6$) concentration of free carriers liberated during its thermalization into the empty conduction band; one of those electrons can be captured by the muon. A positive muon, thus, acts as an attractive Coulomb center for electron localization.⁴³

In a magnetic system, the exchange interaction, I , between free electrons and localized spins creates yet another channel for electron localization—the charge carrier localizes into a ferromagnetic (FM) ‘droplet’ on the scale of the lattice spacing in a paramagnetic (PM) or AF ‘sea’—a spin polaron.⁴⁴ In this case, the long-range Coulomb interaction ensures initial electron capture, whereas, the short-range exchange interaction provides further localization into a bound SP (BSP) to the muon. Formation of a BSP around a positive muon was demonstrated recently in PM (Refs. 34 and 35) and AF (Ref. 45) hosts.

If a BSP were to form in a DS, the increase in the electron kinetic energy due to localization would have to be compensated by the on-site exchange interaction $IS/2$ of

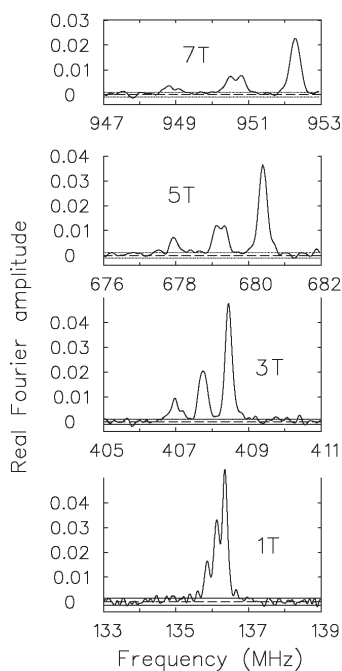


FIG. 4. Fourier transforms of the muon spin precession signal in NaV_2O_5 in different magnetic fields at $T = 29$ K. The low-frequency line of each spectrum is a background signal; two other lines represent two characteristic muon transitions (doublet) within a SP.

the electron with local spin S combined with the Coulomb potential of the muon versus the energy NJS^2 required to flip N local spins S with an effective exchange energy J to produce a FM droplet within the radius R plus the entropy change ΔW due to ordering within the SP so that the change in the free energy,

$$\Delta F = \frac{\hbar^2}{2mR^2} - I\frac{S}{2} - \frac{e^2}{\epsilon R} + NJS^2 + T\Delta W \quad (1)$$

has a minimum as a function of R —the radius of the electron's confinement.⁴⁵

The probability of SP formation around the muon depends on the last two terms of Eq. (1): In a DS with low J , the SP is expected to form, whereas, at higher J , the muon is expected to stay bare and, therefore, may be used as a local magnetic probe. In NaV_2O_5 , a rather high value of $J \approx 560$ K precludes SP formation in a fully developed DS. Instead, at low temperatures, the muon stays bare and sees either an AF or a DS environment (Figs. 2 and 3). By contrast, a SP bound to the muon is formed in NaV_2O_5 below about 100 K in the PM state and remains present through T_c down to 20 K, which is identified as the maximum temperature for a fully developed DS.²¹ Above 100 K, the increasing entropy within the SP reduces its stability and suppresses its formation, and the muon stays bare. Polaron spectra in a polycrystal are almost the same as in the single crystal, which indicates the 1s isotropic nature of the BSP electron.^{34,35}

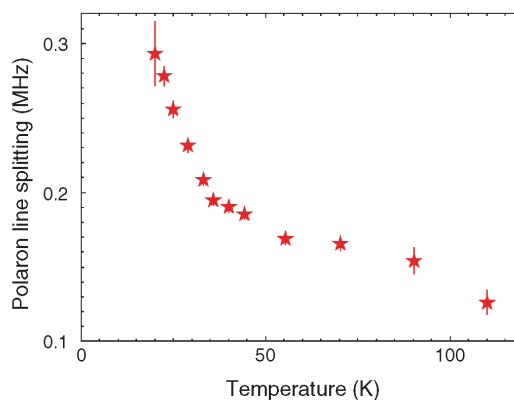


FIG. 5. (Color online) Temperature dependence of the SP lines splitting in a magnetic field of $H = 1$ T.

The observed splitting between the two SP lines in NaV_2O_5 is linear in H/T (Figs. 5 and 6), consistent with a Brillouin function in the small H/T regime and similar to observed dependences for SPs recently characterized in various other materials.^{34,35,45–49}

An alternative interpretation of these spectra as arising from a simple Mu atom can safely be ruled out as spin exchange with the host's spins³⁶ would result in rapid spin fluctuations of the bound electron, averaging the muon-electron hyperfine interaction to zero, which would cause effective doublet disappearance. By contrast, when the electron spin is bound strongly into a SP, the local FM ordering holds the electron spin fixed, which manifests itself as a characteristic doublet.^{34,35,45,46,48–50} Likewise, the insulating nature of NaV_2O_5 and a remarkable insensitivity to the spin-gap transition at T_c allows one to rule out possible Knight shifts within the bare-muon scenario. Finally, a strong shift in the SP lines to higher frequencies with respect to the background signal reflects the FM state within a SP.³⁴

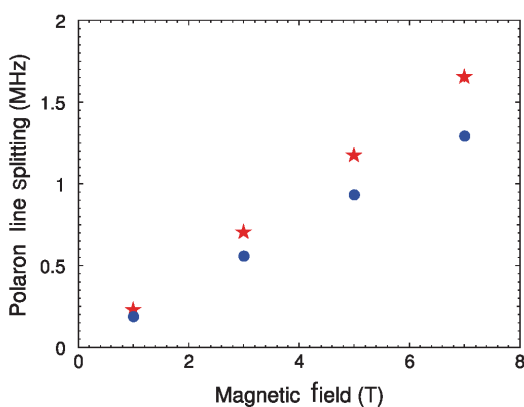


FIG. 6. (Color online) Magnetic-field dependences of the SP lines splitting at $T = 29$ K (stars, red online) and $T = 40$ K (circles, blue online).

V. SUMMARY

We have found a coexistence of spin-gap and AF states at low temperatures, $T \leq 15$ K, in NaV₂O₅. At higher temperatures, 20–100 K, we detected a SP bound to the muon.

ACKNOWLEDGMENTS

This work was supported by the NBIC Center of the Kurchatov Institute, NSERC of Canada, and the US DOE, Basic Energy Sciences (Grant No. DE-SC0001769).

- *mussr@triumf.ca
¹F. D. M. Haldane, *Phys. Rev. Lett.* **50**, 1153 (1983).
²M. Hase, I. Terasaki, and K. Uchinokura, *Phys. Rev. Lett.* **70**, 3651 (1993).
³E. Dagotto, *Rep. Prog. Phys.* **62**, 1525 (1999).
⁴G. T. Woods, G. P. Zhang, T. A. Callcott, L. Lin, G. S. Chang, B. Sales, D. Mandrus, and J. He, *Phys. Rev. B* **65**, 165108 (2002).
⁵T. Nagata, M. Uehara, J. Goto, J. Akimitsu, N. Motoyama, H. Eisaki, S. Uchida, H. Takahashi, T. Nakanishi, and N. Mōri, *Phys. Rev. Lett.* **81**, 1090 (1998).
⁶A. I. Smirnov, S. S. Sosin, R. Calemczuk, V. Villar, C. Paulsen, M. Isobe, and Y. Ueda, *Phys. Rev. B* **63**, 014412 (2000).
⁷Y. Uchiyama, Y. Sasago, I. Tsukada, K. Uchinokura, A. Zheludev, T. Hayashi, N. Miura, and P. Böni, *Phys. Rev. Lett.* **83**, 632 (1999).
⁸S. Sachdev, *Nat. Phys.* **4**, 173 (2008).
⁹K. Kakurai, T. Osakabe, K. Goto, A. Oosawa, M. Jujisawa, and H. Tanaka, *Physica B* **385-386**, 450 (2006).
¹⁰Ch. Rüegg, B. Normand, M. Matsumoto, A. Furrer, D. F. McMorro, K. W. Krämer, H.-U. Güdel, S. N. Gvasaliya, H. Mutka, and M. Boehm, *Phys. Rev. Lett.* **100**, 205701 (2008).
¹¹T. Giamarchi, Ch. Rüegg, and O. Tchernyshyov, *Nat. Phys.* **4**, 198 (2008).
¹²V. O. Garlea, A. Zheludev, T. Masuda, H. Manaka, L.-P. Regnault, E. Ressouche, B. Grenier, J.-H. Chung, Y. Qiu, K. Habicht, K. Kiefer, and M. Boehm, *Phys. Rev. Lett.* **98**, 167202 (2007); Ch. Rüegg, N. Cavadin, A. Furrer, H.-U. Güdel, K. Krämer, H. Mutka, A. Wildes, K. Habicht, and P. Vorderwisch, *Nature (London)* **423**, 62 (2003); A. Oosawa, T. Takamasu, K. Tatanii, H. Abe, N. Tsujii, O. Suzuki, H. Tanaka, G. Kido, and K. Kindo, *Phys. Rev. B* **66**, 104405 (2002).
¹³V. S. Zapf, D. Zocco, B. R. Hansen, M. Jaime, N. Harrison, C. D. Batista, M. Kenzelmann, C. Niedermayer, A. Lacerda, and A. Paduan-Filho, *Phys. Rev. Lett.* **96**, 077204 (2006).
¹⁴M. Jaime, V. F. Correa, N. Harrison, C. D. Batista, N. Kawashima, Y. Kazuma, G. A. Jorge, R. Stern, I. Heinmaa, S. A. Zvyagin, Y. Sasago, and K. Uchinokura, *Phys. Rev. Lett.* **93**, 087203 (2006); S. E. Sebastian, P. A. Sharma, M. Jaime, N. Harrison, V. Correa, L. Balicas, N. Kawashima, C. D. Batista, and I. R. Fisher, *Phys. Rev. B* **72**, 100404(R) (2005).
¹⁵T. Giamarchi and A. M. Tsvelik, *Phys. Rev. B* **59**, 11398 (1999).
¹⁶M. Isobe and Y. Ueda, *J. Phys. Soc. Jpn.* **65**, 1178 (1996); Y. Fujii, H. Nakao, T. Yoshizawa, M. Nishi, K. Nakajima, K. Kakurai, M. Isobe, Y. Ueda, and H. Sawa, *ibid.* **66**, 326 (1997).
¹⁷H. Smolinski, C. Gros, W. Weber, U. Peuchert, G. Roth, M. Weiden, and C. Geibel, *Phys. Rev. Lett.* **80**, 5164 (1998).
¹⁸W. Schnelle, Y. Grin, and R. K. Kremer, *Phys. Rev. B* **59**, 73 (1999).
¹⁹J. Lüdecke, A. Jobst, S. van Smaalen, E. Morré, C. Geibel, and H.-G. Krane, *Phys. Rev. Lett.* **82**, 3633 (1999); J. L. de Boer, A. Meetsma, J. Baas, and T. T. M. Palstra, *ibid.* **84**, 3962 (2000); H. Nakao, K. Ohwada, N. Takesue, Y. Fujii, M. Isobe, Y. Ueda, M. v. Zimmermann, J. P. Hill, D. Gibbs, J. C. Woicik, I. Koyama, and Y. Murakami, *ibid.* **85**, 4349 (2000).
²⁰Y. Fagot-Revurat, M. Mehring, and R. K. Kremer, *Phys. Rev. Lett.* **84**, 4176 (2000).
²¹A. I. Smirnov, M. N. Popova, A. B. Sushkov, S. A. Golubchik, D. I. Khomskii, M. V. Mostovoy, A. N. Vasil'ev, M. Isobe, and Y. Ueda, *Phys. Rev. B* **59**, 14546 (1999).
²²M. V. Mostovoy and D. I. Khomskii, *Solid State Commun.* **113**, 159 (2000).
²³N. Suaud and M.-B. Lepetit, *Phys. Rev. Lett.* **88**, 056405 (2002).
²⁴A. Bernert, P. Thalmeier, and P. Fulde, *Phys. Rev. B* **66**, 165108 (2002).
²⁵A. N. Vasil'ev, V. V. Pryadun, D. I. Khomskii, G. Dhalenne, A. Revcolevschi, M. Isobe, and Y. Ueda, *Phys. Rev. Lett.* **81**, 1949 (1998).
²⁶A. N. Vasil'ev, A. I. Smirnov, M. Isobe, and Y. Ueda, *Phys. Rev. B* **56**, 5065 (1997).
²⁷Y. Fudamoto, K. M. Kojima, M. I. Larkin, G. M. Luke, J. Merrin, B. Nachumi, Y. J. Uemura, M. Isobe, and Y. Ueda, *Phys. Rev. Lett.* **83**, 3301 (1999).
²⁸M. Ain, S. J. Blundell, J. Lord, J. Jegoudez, and A. Revcolevschi, *Physica B* **281-282**, 648 (2000).
²⁹T. Kasuya and A. Yanase, *Rev. Mod. Phys.* **40**, 684 (1968); E. L. Nagaev, *Magnetic Semiconductors* (Imperial College Press, London, 2002).
³⁰J. H. Brewer, *Encyclopedia of Applied Physics* (VCH, New York, 1994), Vol. 11, p. 23; A. Yaouanc and P. Dalmas de Reotier, *Muon Spin Rotation, Relaxation, and Resonance* (Oxford University Press, Oxford, New York, 2011).
³¹C. de Graaf, L. Hozoi, and R. Broer, *J. Chem. Phys.* **120**, 961 (2004).
³²T. Rööm, D. Hüvonen, U. Nagel, Y.-J. Wang, and R. K. Kremer, *Phys. Rev. B* **69**, 144410 (2004).
³³H. J. Schulz, *Phys. Rev. Lett.* **77**, 2790 (1996).
³⁴V. G. Storchak, O. E. Parfenov, J. H. Brewer, P. L. Russo, S. L. Stubbs, R. L. Lichti, D. G. Eshchenko, E. Morenzoni, T. G. Aminov, V. P. Zlomanov, A. A. Vinokurov, R. L. Kallaher, and S. von Molnár, *Phys. Rev. B* **80**, 235203 (2009).
³⁵V. G. Storchak, J. H. Brewer, D. J. Arseneau, S. L. Stubbs, O. E. Parfenov, D. G. Eshchenko, E. Morenzoni, and T. G. Aminov, *Phys. Rev. B* **79**, 193205 (2009).
³⁶B. D. Patterson, *Rev. Mod. Phys.* **60**, 69 (1988).
³⁷V. G. Storchak, J. H. Brewer, and G. D. Morris, *Phys. Rev. Lett.* **75**, 2384 (1995).
³⁸V. G. Storchak, D. G. Eshchenko, J. H. Brewer, G. D. Morris, S. P. Cottrell, and S. F. J. Cox, *Phys. Rev. Lett.* **85**, 166 (2000).
³⁹V. Storchak, S. F. J. Cox, S. P. Cottrell, J. H. Brewer, G. D. Morris, D. J. Arseneau, and B. Hitti, *Phys. Rev. Lett.* **78**, 2835 (1997).
⁴⁰D. G. Eshchenko, V. G. Storchak, J. H. Brewer, and R. L. Lichti, *Phys. Rev. Lett.* **89**, 226601 (2002).
⁴¹V. G. Storchak, D. G. Eshchenko, R. L. Lichti, and J. H. Brewer, *Phys. Rev. B* **67**, 121201 (2003).

VYACHESLAV G. STORCHAK *et al.*

PHYSICAL REVIEW B **85**, 094406 (2012)

- ⁴²D. G. Eshchenko, V. G. Storchak, S. P. Cottrell, and E. Morenzoni, *Phys. Rev. Lett.* **103**, 216601 (2009).
- ⁴³V. G. Storchak, D. G. Eshchenko, and J. H. Brewer, *J. Phys.: Condens. Matter* **16**, S4761 (2004).
- ⁴⁴P. G. de Gennes, *Phys. Rev.* **118**, 141 (1960).
- ⁴⁵V. G. Storchak, J. H. Brewer, D. J. Arseneau, S. L. Stubbs, O. E. Parfenov, D. G. Eshchenko, and A. A. Bush, *Phys. Rev. B* **79**, 220406 (2009).
- ⁴⁶V. G. Storchak, J. H. Brewer, S. L. Stubbs, O. E. Parfenov, R. L. Lichti, P. W. Mengyan, J. He, I. Bredeson, D. Hitchcock, and D. Mandrus, *Phys. Rev. Lett.* **105**, 076402 (2010).
- ⁴⁷V. G. Storchak, D. G. Eshchenko, E. Morenzoni, N. Ingle, W. Heiss, T. Schwarzl, G. Springholz, R. L. Kallaher, and S. von Molnár, *Phys. Rev. B* **81**, 153201 (2010).
- ⁴⁸V. G. Storchak, J. H. Brewer, P. L. Russo, S. L. Stubbs, O. E. Parfenov, R. L. Lichti, and T. G. Aminov, *J. Phys.: Condens. Matter* **22**, 495601 (2010).
- ⁴⁹V. G. Storchak, J. H. Brewer, R. L. Lichti, T. A. Lograsso, and D. L. Schlagel, *Phys. Rev. B* **83**, 140404(R) (2011).
- ⁵⁰V. G. Storchak, O. E. Parfenov, J. H. Brewer, and D. G. Eshchenko, *Phys. Rev. B* **83**, 077202 (2011).

094406-6

B.5. SPIN POLARONS IN $\text{Cd}_2\text{Re}_2\text{O}_7$

PRL 105, 076402 (2010)

PHYSICAL REVIEW LETTERS

week ending
13 AUGUST 2010**Spin Polarons in the Correlated Metallic Pyrochlore $\text{Cd}_2\text{Re}_2\text{O}_7$** Vyacheslav G. Storchak,^{1,*} Jess H. Brewer,² Scott L. Stubbs,² Oleg E. Parfenov,¹ Roger L. Lichti,³ Patrick W. Mengyan,³ Jian He,⁴ Isaac Bredeson,⁴ Dale Hitchcock,⁴ and David Mandrus⁵¹Russian Research center "Kurchatov Institute," Kurchatov Square 1, Moscow 123182, Russia²Department of Physics and Astronomy, University of British Columbia, Vancouver, British Columbia, Canada V6T 1Z1³Department of Physics, Texas Tech University, Lubbock, Texas 79409-1051, USA⁴Department of Physics and Astronomy, Clemson University, Clemson, South Carolina 29634, USA⁵Materials Science and Technology Division, Oak Ridge National Lab, Oak Ridge, Tennessee 37831, USA

(Received 14 January 2010; published 13 August 2010)

Muon spin rotation spectroscopy reveals localized electron states in the geometrically frustrated metallic pyrochlore $\text{Cd}_2\text{Re}_2\text{O}_7$ at temperatures from 2 to 300 K in transverse magnetic fields up to 7 T. Two distinctive types of localized states, with characteristic radii of about 0.5 and 0.15 nm, are detected at high and low temperature, respectively. These states may be spin polarons, formed due to strong exchange interaction between itinerant electrons and the magnetic $5d$ electrons of Re ions, which may determine the peculiar electronic and magnetic properties of $\text{Cd}_2\text{Re}_2\text{O}_7$.

DOI: 10.1103/PhysRevLett.105.076402

PACS numbers: 71.70.Gm, 71.30.+h, 71.38.Ht, 76.75.+i

Frustrated magnetic systems have been the focus of extensive research for many years. In particular, there has been a great deal of interest in systems where the magnetic ions occupy the vertices of edge- or corner-sharing triangular units [1]. In a 3D network of corner-sharing tetrahedra, the spins occupy the corners of a tetrahedron and two antiferromagnetic (AFM) bonds are broken when collinear spins try to arrange themselves on the corners. Such 3D networks occur for many spinel, Laves, and pyrochlore compounds.

Insulating pyrochlore compounds $A_2B_2O_7$, where B is a $3d/4d$ transition metal, form ideal local moment systems in which to study geometrical frustration. These studies have revealed a variety of exotic ground states, including cooperative paramagnetism at low temperatures [2], spin freezing [3], or novel "spin ice" states [4,5].

Most recently, however, there has been growing interest in the interplay between itinerant and local moments in $5d$ transition metal $A_2B_2O_7$ systems. These are typically metallic because the $5d$ orbitals are much less localized than $3d/4d$ electrons. In fact, most of the unique electronic and magnetic properties of $5d$ pyrochlores $\text{Cd}_2\text{Os}_2\text{O}_7$ and $\text{Cd}_2\text{Re}_2\text{O}_7$ are believed to originate from interaction between itinerant carriers and local electrons of the same d type [6–8].

To appreciate electron correlation effects, one has to take into account the exchange interaction J between itinerant carriers and localized spins. Such an exchange interaction may dramatically modify the electron state via electron localization into a spin polaron (SP) [9] which markedly affects the effective mass of the carrier. In particular, recent muon spin relaxation studies of the $3d$ spinel CdCr_2Se_4 did reveal severe electron localization into a SP [10]. On the other hand, the electron transport in $\text{Cd}_2\text{Re}_2\text{O}_7$ is believed to be governed by magnetic scattering [7], which causes a large mass enhancement, suggesting

anomalous correlations [8]. In addition, NMR and nuclear quadrupole resonance (NQR) studies have revealed a significant ferromagnetic enhancement while ruling out any magnetic order in $\text{Cd}_2\text{Re}_2\text{O}_7$ [11]. However, the mechanism by which such correlations lead to a large carrier mass and ferromagnetic enhancement has not been identified until now.

In this Letter we present spectroscopic evidence for electron confinement in metallic $\text{Cd}_2\text{Re}_2\text{O}_7$, which can result in a mass enhancement accompanied by a ferromagnetic enhancement. We propose that such an electron state may be a spin polaron, which may help explain the electronic and magnetic properties of the metal.

Any confinement of an electron raises its kinetic energy relative to that of a free carrier and is therefore very unlikely unless some local interaction compensates for such an increase. A well-known example is the attractive long-range Coulomb potential of a positive donor ion (or a positive muon) in semiconductors or insulators. In a metal, the Coulomb potential is effectively screened; nonetheless, electron confinement is still possible if the metal contains an array of magnetic ions between which the electron mediates a ferromagnetic (FM) exchange interaction. In such a system, an electron's energy depends strongly on the magnetization, with the minimum electron energy being achieved by FM ordering [12]: the electron will then localize and form a FM "droplet" over the extent of its wave function (typically on the order of the lattice spacing) in a host that is otherwise AFM, frustrated, or disordered—e.g., paramagnetic (PM). The charge carrier coupled to its immediate FM environment behaves as a single entity—the spin polaron.

In magnetic semiconductors (MS), the increase in the kinetic energy of the electron (effective mass m^* , charge $-e$) due to localization plus the entropy change ΔS due to ordering within the SP is compensated by the exchange

interaction J and the Coulomb interaction with the corresponding donor, so that the change in the free energy

$$\Delta F = \frac{\hbar^2}{2m^*R^2} - J\frac{a^3}{R^3} - \frac{e^2}{\epsilon R} + T\Delta S \quad (1)$$

(where a is the lattice constant and ϵ is the dielectric constant) yields a minimum in F as a function of R —the radius of the electron confinement into a bound spin polaron [12,13]. Such electron confinement in MS profoundly modifies their magnetic, electrical, and optical properties. In particular, the SP thus formed determines most of the transport properties of MS, leading to resistivity changes of up to 13 orders of magnitude [12].

For magnetic metals, one can neglect the third (Coulomb) term in the right-hand side of Eq. (1), thus recovering the original idea of de Gennes [9] about carrier confinement into a free SP. In this case, the length scale of the problem is significantly reduced: in MS the long-range Coulomb attraction of a positive donor ion ensures initial electron capture while the short-range exchange interaction provides further localization into a SP bound to the donor, whereas in a metal, electron capture into a free SP is ensured solely by the exchange interaction.

Bound SP have recently been detected in $4f$ [14] and $3d$ MS [10], via muon spin rotation (μ^+ SR) [15] spectroscopy analogous to earlier studies of nonmagnetic semiconductors [16], which revealed the details of electron capture to form a muonium ($\text{Mu} \equiv \mu^+e^-$) atom (a light analogue of the H atom) [17].

The current results constitute observation of a confined electron state in a metal. The stoichiometric pyrochlore $\text{Cd}_2\text{Re}_2\text{O}_7$ is a rather poor metal near room temperature. It exhibits at least 2 phase transitions below 300 K: a continuous transition from cubic to tetragonal structure at $T^* = 200$ K, which is accompanied by a continuous resistivity drop by about 2 orders of magnitude towards low temperature [7,8,18], and a superconducting transition below about 1 K [19]. Below about 60 K, its resistivity follows a T^2 dependence characteristic of a Fermi-liquid regime [7] with an electron mean free path of 81 nm at 2 K [8], suggesting very weak electron scattering in the conduction band. The number of such electrons, however, does not exceed 6% of the Re electrons [8]. The states of the remaining majority of electrons still need to be identified. (Various band structure calculations [20] do not appear to imply any anomalous correlation effects.)

Single crystals of $\text{Cd}_2\text{Re}_2\text{O}_7$ for the current study were grown by a vapor-transport technique; details of the synthesis and initial characterization are described elsewhere [21]. Time-differential μ^+ SR experiments using 100% spin-polarized positive muons implanted into these crystals were carried out on the M15 surface muon channel at TRIUMF using the HiTime μ^+ SR spectrometer.

At high temperature, in magnetic fields transverse to the initial muon polarization, Fourier transforms of the μ^+ SR time spectra exhibit two broad peaks, one on either side of

a narrow line [Fig. 1(a)]. The position of this central narrow line does not depend on temperature and occurs exactly at the bare muon frequency $\nu_\mu = \gamma_\mu B/2\pi$ (where $\gamma_\mu = 2\pi \times 135.53879$ MHz/T is the muon gyromagnetic ratio and B is the magnetic field); this is the background signal from muons that stop outside the sample. The two broader lines split about the background signal constitute a characteristic signature of the muon-electron bound state [10,14–16]. The solution of the Breit-Rabi Hamiltonian which governs a μ^+e^- (Mu) spin system yields 4 eigenvalues (due to 4 possible combinations of μ^+ and e^- spins) corresponding to 4 energy levels with different allowed transitions. In high magnetic field, the two allowed transitions correspond to two muon spin-flip transitions between states with fixed electron spin orientation [15,16]. The frequency splitting between these two transitions grows with the field until the muon Zeeman splitting greatly exceeds the muon-electron hyperfine coupling constant A , then the splitting between these two lines saturates at A [10,14]. For a $1s$ Mu atom in vacuum, with $R = R_{\text{Bohr}} = 0.053$ nm, $A_{\text{vac}} = 4463$ MHz; for “shallow” Mu atoms in solids, $A \ll A_{\text{vac}}$ and the value of A scales as $1/R^3$, which gives a measure of the characteristic radius R of the electron confinement [15,16]. In $\text{Cd}_2\text{Re}_2\text{O}_7$ at around 150 K, we find $A = 5 \pm 0.5$ MHz, implying $R = 0.51 \pm 0.02$ nm, which corresponds to electron confine-

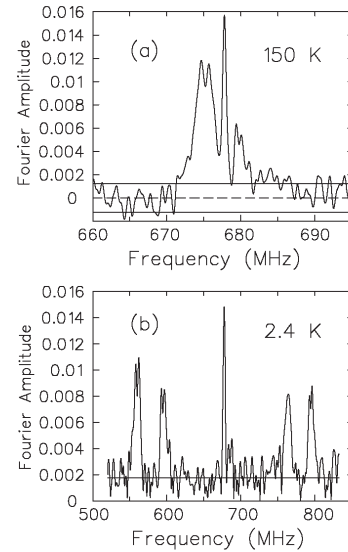


FIG. 1. Frequency spectra of muon spin precession in $\text{Cd}_2\text{Re}_2\text{O}_7$ in a transverse magnetic field of $H = 5$ T at $T = 150$ K (a) and $T = 2.4$ K (b). The two-frequency or four-frequency precession patterns characteristic of the electron bound state occur at frequencies on either side of the narrower background signal. Note different frequency scales for (a) and (b).

ment within one unit cell of $\text{Cd}_2\text{Re}_2\text{O}_7$ (lattice constant $a = 1.022$ nm). At higher temperature these two Mu lines exhibit a smaller splitting following the $1/T$ behavior observed in MS [14].

Similar states with the electron confined in a 0.3–0.5 nm FM droplet around a positive muon (large SP) are found in PM states of CdCr_2Se_4 , EuS, and SmS [10,14], or in the AFM state of LiCu_2O_2 [22], all of which have been identified as magnetic (spin) polarons. However, these materials are either semiconductors or insulators, where the Coulomb interaction has an important role in electron localization. In $\text{Cd}_2\text{Re}_2\text{O}_7$, the high ($\sim 10^{20}$ – 10^{21} cm^{-3}) concentration of itinerant carriers [8] ensures that the exchange interaction dominates electron localization, thus reducing the role of the positive muon to that of an “innocent bystander.” Nevertheless, in both cases the observed species are believed to be magnetic polarons. In a PM and/or metallic environment, the strong pair exchange interaction of the Mu electron with the host’s itinerant spins (so-called “spin exchange” [16]) would result in rapid spin fluctuations of the Mu electron, averaging the hyperfine interaction to zero, if some stronger interaction did not hold the Mu electron spin “locked.” That stronger interaction is in this case the exchange interaction of the Mu (SP) electron with the host’s local spins. The mere observation of Mu-like lines in the μ^+ SR spectra of a magnetically disordered metal is strong evidence for SP formation.

At low temperature, the μ^+ SR spectra consist of 5 signals—inner and outer pairs roughly centered on the background (“bare” μ^+) signal [Fig. 1(b)]. The splittings of both pairs of lines are dramatically increased with respect to that of the high temperature lines. The evolution of these signals is shown in Fig. 2: above about 20 K, all 4 lines begin to approach the central line, decreasing the splittings (Fig. 3), while each line broadens until it disappears above 60 K.

Two pairs of lines may mean formation of two kinds of SP in $\text{Cd}_2\text{Re}_2\text{O}_7$ at low temperature; an alternative possibility is discussed below. In the high-field limit at 2.4 K, these splittings level off at corresponding hyperfine frequencies [10,14] of $A_1 = 233 \pm 5$ MHz and $A_2 = 168 \pm 5$ MHz (see Fig. 4). Assuming a $1s$ state for the confined electron (neither p nor d electron states can produce a significant hyperfine field on the muon), the corresponding radii of electron confinement are $R_1 = 0.14 \pm 0.01$ nm and $R_2 = 0.16 \pm 0.01$ nm, respectively. These radii are a factor of 3 smaller than that of the proposed large SP in $\text{Cd}_2\text{Re}_2\text{O}_7$ at high T , suggesting that the electron state found below 60 K is fundamentally different from that at higher temperature. It is noteworthy that $T = 60$ K has been identified by both transport and susceptibility measurements as a “critical temperature” below which the itinerant electron density of states is significantly reduced [7,11]. We propose that the “missing” itinerant carriers are being “dressed” by Re spins into small SP states.

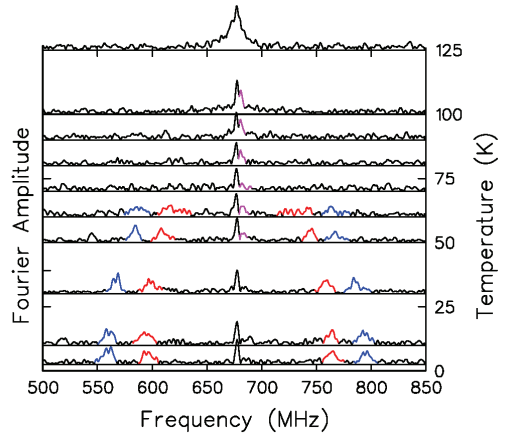


FIG. 2 (color online). Frequency spectra of muon spin precession in $\text{Cd}_2\text{Re}_2\text{O}_7$ in a transverse magnetic field of $H = 5$ T at different temperatures. The large splitting decreases towards high T and disappears above about 60 K.

Extensive studies of spin polarons in magnetoresistive perovskites, MS, and related compounds by different techniques [14,23–25] have revealed that the SP expands at low T . Therefore, the appearance of a much smaller SP in $\text{Cd}_2\text{Re}_2\text{O}_7$ below 60 K requires explanation. Stronger electron confinement at low temperature is impossible unless some very local interaction compensates for the increase of the carrier kinetic energy, and yet the SP radius of about 0.15 nm is consistent with its accommodation within the Re tetrahedron. Indeed, the Re-Re distance of 0.317 nm [21] might ensure a maximum overlap of the $1s$ SP electron with a $5d$ Re electron having a typical span of $r = 0.058$ nm [26], which would provide the maximum J . If an AFM Re-Re singlet bond is broken by a Re spin flip to form a FM Re-Re triplet bond, the corresponding reduction of energy might then stabilize the SP electron within the tetrahedron.

As the exchange coupling between itinerant carriers and local spins of the same $5d$ type within the SP is the dominant interaction leading to electron confinement, the role of the muon as a localization center seems to be quite modest. We suggest that at low temperature the host lattice is populated by small SP which form an extremely narrow SP band where the transport of the carrier is accompanied by deviations of Re spins [9,12,27] (hence the unexpectedly large NQR T_1^{-1} of Re [11]). The large SP [Fig. 1(a)] is expected to be static, the population of the electron spin-up and spin-down Breit-Rabi states being determined by a thermal (Boltzmann) distribution. In that case, the Zeeman splitting of the giant aggregate spin of the large SP (about 30 spins of Re, each carrying 2.8 Bohr magnetons) amounts to about 280 K in $H = 5$ T. Therefore, even high temperature is unable to equilibrate the unequal populations of spin-up and spin-down states as manifest in

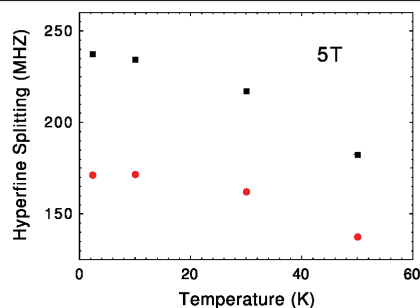


FIG. 3 (color online). Temperature dependences of hyperfine splittings in $\text{Cd}_2\text{Re}_2\text{O}_7$ at $H = 5$ T.

the strong amplitude difference between the two lines [Fig. 1(a)]. By contrast, at low temperature, the classical Boltzmann distribution breaks down and is replaced by a uniform distribution among different quantum states within the small SP band, making the spectral weight of different lines about the same [see Fig. 1(b)]. Formation of such a narrow SP band could explain the peculiar electronic and magnetic properties of $\text{Cd}_2\text{Re}_2\text{O}_7$: a large electron mass enhancement [28] and ferromagnetic enhancement [8,11] are both consistent with the formation of ferromagnetic SP.

Finally, we would like to offer an alternative interpretation of the 4-signal spectra at low temperature [Figs. 1(b) and 2]: while one pair of lines may reflect formation of a SP, two pairs might be a spectroscopic signature of a spin bipolaron (SBP). Such a SBP cannot form as a singlet: capture of the second electron to make a singlet with the first one would destroy the FM droplet (eradicating the energy reduction thereof), so that an opposite-spin electron avoids localization. It may, however, form in a triplet state, making the FM droplet larger, which decreases the muon-electron hyperfine interaction with respect to that in a simple SP, so that the splitting between the two lines

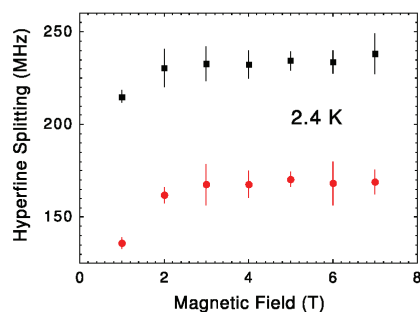


FIG. 4 (color online). Magnetic field dependence of hyperfine splittings at $T = 2.4$ K, from fast Fourier transform. Error bars represent apparent peak widths.

becomes smaller (see Figs. 1 and 2). Bose condensation of such SBPs [27,29] might cause the superconductivity detected below 1 K [19]. On the other hand, spatial anisotropy of the SP electron wave function might also explain the 4-signal pattern [16].

This work was supported by the Natural Sciences and Engineering Research Council of Canada and the U.S. Department of Energy (Grant No. DE-SC0001769). The work at Clemson University is supported by a DOE/EPSCoR Implementation Grant (No. DE-FG02-04ER-46139).

*mussr@triumf.ca

- [1] A. P. Ramirez, in *Handbook of Magnetic Materials*, edited by H. J. Buschlow (Elsevier Science, Amsterdam, 2001), Vol. 13.
- [2] J. S. Gardner *et al.*, *Phys. Rev. Lett.* **82**, 1012 (1999).
- [3] M. J. P. Gingras *et al.*, *Phys. Rev. Lett.* **78**, 947 (1997).
- [4] M. J. Harris *et al.*, *Phys. Rev. Lett.* **79**, 2554 (1997).
- [5] S. Bramwell and M. Gingras, *Science* **294**, 1495 (2001).
- [6] D. Mandrus *et al.*, *Phys. Rev. B* **63**, 195104 (2001).
- [7] R. Jin *et al.*, *J. Phys. Condens. Matter*, **14**, L117 (2002).
- [8] Z. Hiroi *et al.*, *J. Phys. Soc. Jpn.* **72**, 21 (2003).
- [9] P. G. de Gennes, *Phys. Rev.* **118**, 141 (1960).
- [10] V. G. Storchak *et al.*, arXiv:1003.1851v1.
- [11] O. Vyaselev *et al.*, *Phys. Rev. Lett.* **89**, 017001 (2002).
- [12] E. L. Nagaev, in *Magnetic Semiconductors* (Imperial College Press, London, 2002).
- [13] S. von Molnár and P. A. Stampel, in *Handbook of Magnetism and Advanced Magnetic Materials*, edited by H. Kronmüller and S. Parkin (John Wiley & Sons, New York, 2007).
- [14] V. G. Storchak *et al.*, *Phys. Rev. B* **80**, 235203 (2009); **79**, 193205 (2009).
- [15] J. H. Brewer, *Encyclopedia of Applied Physics* (VCH, New York, 1994), Vol. 11, pp. 23–53.
- [16] B. D. Patterson, *Rev. Mod. Phys.* **60**, 69 (1988).
- [17] V. G. Storchak *et al.*, *Phys. Rev. Lett.* **78**, 2835 (1997); *J. Phys. Condens. Matter* **16**, S4761 (2004).
- [18] J. P. Castellán *et al.*, *Phys. Rev. B* **66**, 134528 (2002).
- [19] M. Hanawa *et al.*, *Phys. Rev. Lett.* **87**, 187001 (2001); R. Jin *et al.*, *Phys. Rev. B* **64**, 180503 (2001); H. Sakai *et al.*, *J. Phys. Condens. Matter* **13**, L785 (2001).
- [20] S.-W. Huang *et al.*, *J. Phys. Condens. Matter* **21**, 195602 (2009); D. J. Singh *et al.*, *Phys. Rev. B* **65**, 155109 (2002).
- [21] J. He *et al.*, *J. Electron. Mater.* **36**, 740 (2007).
- [22] V. G. Storchak *et al.*, *Phys. Rev. B* **79**, 220406(R) (2009).
- [23] J. M. De Teresa *et al.*, *Nature (London)* **386**, 256 (1997).
- [24] H. Rho *et al.*, *Phys. Rev. Lett.* **88**, 127401 (2002).
- [25] A. Comment *et al.*, *Phys. Rev. B* **72**, 014428 (2005).
- [26] *Lange's Handbook of Chemistry*, edited by J. A. Dean (McGraw-Hill, New York, 1999), 15th ed.
- [27] N. F. Mott, *Metal-Insulator Transitions* (Taylor & Francis, Bristol, 1990).
- [28] N. L. Wang *et al.*, *Phys. Rev. B* **66**, 014534 (2002).
- [29] N. F. Mott, *J. Phys. Condens. Matter* **5**, 3487 (1993).